

MODELING, ESTIMATION, AND ANALYSIS OF UNRESOLVED SPACE  
OBJECT TRACKING AND IDENTIFICATION

by

LAURA SUAREZ HENDERSON

Presented to the Faculty of the Graduate School of  
The University of Texas at Arlington in Partial Fulfillment  
of the Requirements  
for the Degree of

DOCTOR OF PHILOSOPHY

THE UNIVERSITY OF TEXAS AT ARLINGTON

August 2014

Copyright © by LAURA SUAREZ HENDERSON 2014  
All Rights Reserved

I would like to dedicate this work to  
God for being a never ending source of strength,  
Dad for inspiring me to dream about the stars,  
Mom for cultivating my creativity,  
and most of all to my dear Michael for your unconditional  
love, support, and encouragement through the endless days and nights of work.

I love you all dearly.

## Acknowledgements

I would like to begin by thanking my committee chairman, Dr. Kamesh Subbarao, for his invaluable guidance during these years. I am so grateful for his wisdom and patience.

Likewise, I want to thank and acknowledge my committee members Dr. Atilla Dogan, Dr. Ben Harris, Dr. Donald Wilson, and Dr. Gaik Ambartsoumian for their teachings and advice. I have been very fortunate to have these and many other teachers and professors advise me and spur me on since my early years in grade school through graduate school.

Moreover, I would like to thank the administrative staff of the Mechanical and Aerospace Engineering Department, specially Debi, Sally, and Lanie, for their amazing support and dedication. Without you nothing would ever get done and we would never graduate.

I could have never gotten here without the encouragement of my family and friends. I so grateful for having parents who planted and nurtured my love for space and my creativity. Mom and Dad, thank you for your love and encouragement. To my big brother Yeye, thank you for being an example of following your passion and never giving up. I know I can always count on you. I also want to thank my grandmothers, Hilda and Gina, for being examples of strength and faith, and for their unconditional love.

To my labmates and schoolmates, thank you for walking with me during the many years of school. I am honored to have had you next to me during all the endless

hours of classes and homework. I am so grateful for your friendship, help, laughs, and of course, food.

Most of all, I want to thank my dearest husband Michael for his daily support, encouragement, and love. Thank you for never letting me give up and pushing me to complete this work. I would have never finished without your fortitude and confidence.

August 6, 2014

Abstract

MODELING, ESTIMATION, AND ANALYSIS OF UNRESOLVED SPACE  
OBJECT TRACKING AND IDENTIFICATION

LAURA SUAREZ HENDERSON, Ph.D.

The University of Texas at Arlington, 2014

Supervising Professor: Kamesh Subbarao

The problem of orbit determination along with shape determination is significant. The orbit determination problem has been tackled for centuries by some of the greatest mathematicians and physicists. The issue of shape determination of space objects, although more recent, has also been addressed quite extensively. Nevertheless, these problems remain of great interest in the scientific and engineering community, and are addressed in this work. The greatest motivation for the tracking and identification of Earth orbiting objects is the ever-increasing population of space assets and man-made debris. It is of interest to implement new and better techniques to track and identify new debris and new orbiting bodies. The precise mathematical modeling of the space object's motion, along with the estimation of its position, velocity, attitude, angular velocity, shape, and size object is presented here.

The first step is the development of mathematical model of the equations of motion of the orbiting body. The translational equations of motion are based on the orbiting two-body equations. In addition, rigid-body rotational equations are developed. This mathematical framework also includes models for perturbations. These

perturbations are based on phenomena which affect the object as it orbits Earth. In order to acquire information regarding the object, astrometric and photometric measurement models are developed. These models emulate stations in the Space Surveillance Network.

Special consideration is given to the development of the photometric model (i.e. the light curve model). The light curve measurement has only recently been used for this application and an extensive analysis of the information it carries is done. This study involves a sensitivity and observability analysis, which provide insight into the information contained in the light curve regarding the orientation, spin, shape, and size of the object. In addition, several mathematical models of the light reflectance phenomena are implemented in the light curve model. Their performance is evaluated and compared in order to choose which is the most effective one.

The orbit determination and shape and size estimation is performed by implementing several estimation techniques. The first is the unscented Kalman filter (UKF). This filter has been shown to be effective in dealing with nonlinear systems and measurement models, which are inherent in the work presented here. The filter employs the dynamical model, measurement model, and noisy measurements to produce estimates of its location, orientation, shape, size, and future intentions. The second technique is a batch estimation within the UKF. This was implemented to improve the estimation of the shape and size parameters of the object. This estimates the states via the UKF and the shape/size parameters via a batch estimation algorithm. The batch algorithm minimizes a cost function to yield an updated estimate of the parameters. The third estimation technique uses a bootstrap particle filter (BPF), which is the first developed functioning particle filter. This filter draws a large number of samples from the distribution of the state in order to approximate the probability density function (pdf). In particular, the BPF uses importance

sampling and weights. This filter is effective in dealing with nonlinear systems and non-Gaussian distributions.

All three estimation techniques are applied to the combined direct and inverse problem. The UKF and UKF-batch experiments demonstrate the UKF performs well when dealing with the estimation of all the states and parameters. The UKF-batch, which implemented the Gauss-Newton algorithm to improve the estimates of the shape/size parameters, performs better than the other two UKF methods, but at a high computational cost. The BPF performs well for the estimation of the velocity, angular velocity, and shape/size parameters. Nevertheless, it is not able to estimate the position and attitude as well as the UKF schemes. Moreover, the estimation of the shape/size parameters via the BPF are not as good as the ones yielded by the UKF. This is attributed to insufficient number of particles given the number of states and parameters being estimated. It should also be noted that the BPF has a high computational cost compared to the UKF. The UKF is the method which is the least computationally expensive and yields good estimates across all states and parameters.

## Table of Contents

Acknowledgements . . . . .	iv
Abstract . . . . .	vi
List of Illustrations . . . . .	xiii
List of Tables . . . . .	xix
Chapter	Page
1. Executive Summary . . . . .	1
1.1 Introduction and Motivation . . . . .	1
1.2 Background . . . . .	1
1.2.1 Orbit Determination and Estimation Techniques . . . . .	1
1.2.2 Light Curve Measurements and the Inverse Problem . . . . .	4
1.3 Objectives and Contributions . . . . .	6
2. Problem Formulation . . . . .	11
2.1 Combined Direct and Inverse Problem . . . . .	11
2.2 Governing Equations of Motion . . . . .	13
2.2.1 Translational Dynamics . . . . .	13
2.2.2 Rigid Body Rotational Kinematics . . . . .	14
2.2.3 Rigid Body Rotational Dynamics . . . . .	16
2.3 Measurement Models . . . . .	16
2.3.1 Astrometric Measurement . . . . .	16
2.3.2 Light Curve Measurement . . . . .	17
2.4 Coordinate Frames . . . . .	17
2.4.1 Earth Centered Inertial Frame . . . . .	17

2.4.2	Body Fixed Frame . . . . .	18
2.4.3	Up-East-North Frame . . . . .	18
3.	Perturbation Models . . . . .	20
3.1	Drag Acceleration . . . . .	20
3.2	Aspherical Gravitational Field Acceleration . . . . .	21
3.3	Solar Radiation Pressure Acceleration . . . . .	22
3.4	Solar Radiation Pressure Torque . . . . .	23
3.5	Gravity Gradient Torque . . . . .	24
4.	Measurement Models . . . . .	26
4.1	Astrometric Measurements . . . . .	26
4.2	Light Curve Measurement . . . . .	28
5.	The Unscented Kalman Filter . . . . .	31
6.	Observability and Sensitivity Analysis . . . . .	36
6.1	Position and Velocity . . . . .	36
6.2	Attitude, Angular Velocity, Shape and Size . . . . .	37
6.3	Bidirectional Reflectance Distribution Function Comparison and Analysis . . . . .	38
6.3.1	Ward Model (1992, abbr. Wa) . . . . .	41
6.3.2	Ward-Dür Model (2004, abbr. Wa-Dü) . . . . .	41
6.3.3	Blinn-Phong Model (1977, abbr. Bl-Ph) . . . . .	42
6.3.4	Lafortune et al. Model (1997, abbr. La) . . . . .	42
6.3.5	Cook-Torrance Model (1981, abbr. Co-To) . . . . .	43
6.3.6	He et al. Model (1991, abbr. He) . . . . .	44
6.3.7	Ashikhmin-Shirley Model (2000, abbr. As-Sh) . . . . .	45
6.3.8	Material Selection . . . . .	46
6.4	Sensitivity Analysis . . . . .	46

6.4.1	Numerical Observation Matrix . . . . .	48
6.4.2	Unscented Kalman Filter Derived Observation Matrix . . . . .	48
6.4.3	Error Analysis and Observability Gramian . . . . .	49
6.5	Observability Analysis . . . . .	50
6.6	Sensitivity and Observability Results . . . . .	52
6.7	Discussion and Model Selection . . . . .	73
6.8	Light Reflectance Model Comparison . . . . .	73
7.	Inverse Problem . . . . .	77
7.1	Inverse Crime . . . . .	78
7.1.1	Numerical Setup . . . . .	78
7.1.2	Results and Discussion . . . . .	79
7.2	Inverse Problem Solution via Unscented Kalman Filter . . . . .	83
7.2.1	Numerical Setup . . . . .	83
7.2.2	Results . . . . .	83
8.	Joint Estimation via Unscented Kalman Filter . . . . .	92
8.1	UKF-Batch Estimation . . . . .	93
8.2	Numerical Setup . . . . .	95
8.3	Results and Discussion . . . . .	96
8.3.1	UKF Estimation Results . . . . .	101
8.3.2	UKF-Batch Estimation Results . . . . .	106
8.3.3	Discussion and Comparison . . . . .	106
9.	Joint Estimation via Bootstrap Particle Filter . . . . .	115
9.1	Bootstrap Recursive Algorithm . . . . .	116
9.1.1	Prediction Step . . . . .	118
9.1.2	Update Step . . . . .	119
9.1.3	Resampling . . . . .	119

9.2 Numerical Setup . . . . .	121
9.3 Results and Discussion . . . . .	126
10. Summary and Closing Remarks . . . . .	133
Appendix	
A. Light Curve BRDF Analysis Tables and Plots . . . . .	137
References . . . . .	161
Biographical Statement . . . . .	168

## List of Illustrations

Figure	Page
2.1 Earth Centered Inertial Frame . . . . .	17
2.2 Body Fixed Frame . . . . .	18
2.3 Up-East-North Frame . . . . .	19
3.1 Solar Radiation Model Geometry . . . . .	23
4.1 Geometry of Earth, Observer, and Object . . . . .	26
4.2 Resident Space Object Model with Light Curve Model Vectors . . . . .	28
5.1 Unscented Kalman Filter Algorithm . . . . .	35
6.1 Depiction of Observability Degree for a Three Dimensional Vector . . . . .	52
6.2 Specular Component of Light for Case 1 . . . . .	54
6.3 Specular Component of Light for Case 2 . . . . .	55
6.4 Diffuse Component of Light for Case 1 . . . . .	55
6.5 Diffuse Component of Light for Case 2 . . . . .	56
6.6 Magnitude of Light for Case 1 . . . . .	56
6.7 Magnitude of Light for Case 2 . . . . .	57
6.8 Ward Model Angular Velocity Sensitivity . . . . .	59
6.9 Ward Model Attitude Sensitivity . . . . .	60
6.10 Ward Model Shape/Size Parameters Sensitivity . . . . .	60
6.11 Cook-Torrance Model Angular Velocity Sensitivity . . . . .	61
6.12 Cook-Torrance Model Attitude Sensitivity . . . . .	61
6.13 Cook-Torrance Model Shape/Size Parameters Sensitivity . . . . .	62
6.14 Error Parameter for Attitude . . . . .	62

6.15	Error Parameter for Shape/Size Parameter . . . . .	63
6.16	Ward Model Numerical based Gramian for Case 1 . . . . .	65
6.17	Ward Model UKF based Gramian for Case 1 . . . . .	65
6.18	Ward Model Numerical based Gramian for Case 2 . . . . .	66
6.19	Ward Model UKF based Gramian for Case 2 . . . . .	66
6.20	Cook-Torrance Model Numerical based Gramian for Case 1 . . . . .	67
6.21	Cook-Torrance Model UKF based Gramian for Case 1 . . . . .	67
6.22	Cook-Torrance Model Numerical based Gramian for Case 2 . . . . .	68
6.23	Cook-Torrance Model UKF based Gramian for Case 2 . . . . .	68
6.24	Observability Degree of Attitude States for Case 1 . . . . .	71
6.25	Observability Degree of Attitude States for Case 2 . . . . .	71
6.26	Observability Degree of Shape/Size Parameters for Case 1 . . . . .	72
6.27	Observability Degree of Shape/Size Parameters for Case 2 . . . . .	72
7.1	Light Curve Error Comparison . . . . .	81
7.2	Shape/Size Parameter Estimation Error Comparison . . . . .	82
7.3	Inverse Problem True Object Position . . . . .	85
7.4	Inverse Problem True Object Velocity . . . . .	85
7.5	Inverse Problem True Object Angular Velocity . . . . .	86
7.6	Inverse Problem True Object Euler Angles . . . . .	86
7.7	Inverse Problem Perturbation Accelerations . . . . .	87
7.8	Inverse Problem Perturbation Torques . . . . .	87
7.9	Inverse Problem Estimation Angular Velocity . . . . .	89
7.10	Inverse Problem Estimation of Attitude (MRPs) . . . . .	89
7.11	Inverse Problem Estimation of Attitude (Euler Angles) . . . . .	90
7.12	Inverse Problem Estimation of Shape/Size Parameters . . . . .	90
7.13	Inverse Problem Estimation of Shape/Size Parameter (no $3\sigma$ bounds) .	91

7.14	Inverse Problem Acquired vs. Estimated Light Curve Measurement . . .	91
8.1	UKF-Batch Estimation Algorithm . . . . .	94
8.2	UKF Joint Estimation True Object Position . . . . .	97
8.3	UKF Joint Estimation True Object Position . . . . .	98
8.4	UKF Joint Estimation True Object Velocity . . . . .	98
8.5	UKF Joint Estimation True Object Euler Angles . . . . .	99
8.6	UKF Joint Estimation True Object Angular Velocity . . . . .	99
8.7	UKF Joint Estimation Perturbation Accelerations . . . . .	100
8.8	UKF Joint Estimation Perturbation Torques . . . . .	100
8.9	UKF Joint Estimation of Position . . . . .	102
8.10	UKF Joint Estimation of Velocity . . . . .	102
8.11	UKF Joint Estimation of Attitude (MRPs) . . . . .	103
8.12	UKF Joint Estimation of Attitude (Euler Angles) . . . . .	103
8.13	UKF Joint Estimation of Angular Velocity . . . . .	104
8.14	UKF Joint Estimation of Shape/Size Parameters . . . . .	104
8.15	UKF Joint Estimation of Shape/Size Parameter (no $3\sigma$ bounds) . . . .	105
8.16	UKF Levenberg Marquardt Batch Estimation of Position . . . . .	107
8.17	UKF Levenberg Marquardt Batch Estimation of Velocity . . . . .	108
8.18	UKF Levenberg Marquardt Batch Estimation of Attitude (MRPs) . . .	109
8.19	UKF Levenberg Marquardt Batch Estimation of Attitude (Euler Angles)	109
8.20	UKF Levenberg Marquardt Batch Estimation of Angular Velocity . . .	110
8.21	UKF Levenberg Marquardt Batch Estimation of Shape/Size Parameters	110
8.22	UKF Levenberg Marquardt Batch Cost . . . . .	111
8.23	UKF Gauss Newton Batch Estimation of Position . . . . .	111
8.24	UKF Gauss Newton Batch Estimation of Velocity . . . . .	112
8.25	UKF Gauss Newton Batch Estimation of Attitude (MRPs) . . . . .	112

8.26	UKF Gauss Newton Batch Estimation of Attitude (Euler Angles) . . .	113
8.27	UKF Gauss Newton Batch Estimation of Angular Velocity . . . . .	113
8.28	UKF Gauss Newton Batch Estimation of Shape/Size Parameters . . .	114
8.29	UKF Gauss Newton Batch Cost . . . . .	114
9.1	BPF Joint Estimation True Object Position . . . . .	123
9.2	BPF Joint Estimation True Object Velocity . . . . .	123
9.3	BPF Joint Estimation True Object Euler Angles . . . . .	124
9.4	BPF Joint Estimation True Object Angular Velocity . . . . .	124
9.5	BPF Joint Estimation Perturbation Accelerations . . . . .	125
9.6	BPF Joint Estimation Perturbation Torques . . . . .	125
9.7	BPF Joint Estimation of Position . . . . .	127
9.8	BPF Joint Estimation of Velocity . . . . .	127
9.9	BPF Joint Estimation of Attitude (MPRs) . . . . .	128
9.10	BPF Joint Estimation of Attitude (Euler Angles) . . . . .	129
9.11	BPF Joint Estimation of Angular Velocity . . . . .	130
9.12	BPF Joint Estimation of Shape/Size Parameters . . . . .	130
9.13	BPF Joint Estimation of Shape/Size Parameter (no $3\sigma$ bounds) . . . .	131
9.14	BPF Joint Estimation Importance Weights . . . . .	131
A.1	Ward Model Angular Velocity Sensitivity . . . . .	140
A.2	Ward Model Attitude Sensitivity . . . . .	141
A.3	Ward Model Shape/Size Parameters Sensitivity . . . . .	141
A.4	Ward Model Numerical based Gramian . . . . .	142
A.5	Ward Model UKF based Gramian . . . . .	142
A.6	Ward-Dür Model Angular Velocity Sensitivity . . . . .	143
A.7	Ward-Dür Model Attitude Sensitivity . . . . .	143
A.8	Ward-Dür Model Shape/Size Parameters Sensitivity . . . . .	144

A.9	Ward-Dür Model Numerical based Gramian . . . . .	145
A.10	Ward-Dür Model UKF based Gramian . . . . .	145
A.11	Blinn-Phong Model Angular Velocity Sensitivity . . . . .	146
A.12	Blinn-Phong Model Attitude Sensitivity . . . . .	146
A.13	Blinn-Phong Model Shape/Size Parameters Sensitivity . . . . .	147
A.14	Blinn-Phong Model Numerical Based Gramian . . . . .	148
A.15	Blinn-Phong Model UKF based Gramian . . . . .	148
A.16	Lafortune et al. Model Angular Velocity Sensitivity . . . . .	149
A.17	Lafortune et al. Model Attitude Sensitivity . . . . .	149
A.18	Lafortune et al. Model Shape/Size Parameters Sensitivity . . . . .	150
A.19	Lafortune et al. Model Numerical based Gramian . . . . .	151
A.20	Lafortune et al. Model UKF based Gramian . . . . .	151
A.21	Cook-Torrance Model Angular Velocity Sensitivity . . . . .	152
A.22	Cook-Torrance Model Attitude Sensitivity . . . . .	152
A.23	Cook-Torrance Model Shape/Size Parameters Sensitivity . . . . .	153
A.24	Cook-Torrance Model Numerical based Gramian . . . . .	154
A.25	Cook-Torrance Model UKF based Gramian . . . . .	154
A.26	He Model Angular Velocity Sensitivity . . . . .	155
A.27	He Model Attitude Sensitivity . . . . .	155
A.28	He Model Shape/Size Parameters Sensitivity . . . . .	156
A.29	He Model Numerical based Gramian . . . . .	157
A.30	He Model UKF based Gramian . . . . .	157
A.31	Ashikhmin-Shirley Model Angular Velocity Sensitivity . . . . .	158
A.32	Ashikhmin-Shirley Model Attitude Sensitivity . . . . .	158
A.33	Ashikhmin-Shirley Model Shape/Size Parameters Sensitivity . . . . .	159
A.34	Ashikhmin-Shirley Model Numerical based Gramian . . . . .	160

A.35 Ashikhmin-Shirley Model UKF based Gramian . . . . .	160
--	-----

## List of Tables

Table	Page
6.1 BRDF Characteristics Comparison . . . . .	39
6.2 Common Notation for BRDF Model Comparison . . . . .	40
6.3 Initial Conditions for Sensitivity and Observability Analysis . . . . .	53
6.4 Observability Results for Case 1 . . . . .	70
6.5 Observability Results for Case 2 . . . . .	70
6.6 Light Reflectance Model Comparison . . . . .	75
7.1 Initial Conditions for Inverse Crime . . . . .	79
7.2 Initial Error and Error Covariance for Inverse Crime . . . . .	79
7.3 Model Combinations . . . . .	79
7.4 Initial Conditions for Inverse Problem . . . . .	84
7.5 Initial Error and Error Covariance for Inverse Problem . . . . .	84
8.1 Initial Conditions for UKF and UKF-Batch Joint Estimation . . . . .	96
8.2 Initial Error and Error Covariance for UKF and UKF-Batch Joint Es- timation . . . . .	96
8.3 Shape/Size Parameter Final UKF Estimation Error (cm) Comparison	107
9.1 Initial Conditions for BPF Joint Estimation . . . . .	122
9.2 Initial Error and Error Covariance for BPF Joint Estimation . . . . .	122
9.3 Shape/Size Parameter Final Estimation Error (cm) Summary . . . . .	129
A.1 Brushed Aluminium Experimental Data Model Parameters [1] . . . . .	138
A.2 Black Oxidized Steel Experimental Data Model Parameters [1] . . . . .	138
A.3 Black Plastic Experimental Data Model Parameters [1] . . . . .	139

## Chapter 1

### Executive Summary

#### 1.1 Introduction and Motivation

Space is one of the important national assets. Satellites are vital to the economy, national security, and global connectivity. Space can also be one of our most unexpected vulnerabilities. Space assets like the International Space Station, GPS satellites, and private and military communication satellites must all be protected from accumulating space debris [2–4] and enemy threat. The accumulation of space debris is becoming critical as new satellites are being placed in orbit, while old defunct satellites slowly decay. Furthermore, recent collisions have caused dangerous debris clouds, which pose a great risk for neighboring satellites [3–6].

It is of great importance to address the issue of identifying orbital debris, as well as, predicting the debris' location, and the risk it poses to other orbiting bodies. It is crucial to detect, track, identify, and predict future intentions, actions, and location of resident space objects at various altitudes with known accuracy and precision. It is necessary to know the location and trajectory of a space object and to identify its origin, detect changes in its orbital state, determine its orientation, and predict its intentions and capabilities. These challenges provide the motivation for this work.

#### 1.2 Background

##### 1.2.1 Orbit Determination and Estimation Techniques

The problem of orbit determination is defined as the process of obtaining the values of parameters which specify the motion of the orbiting object given a set of

observations of that body [7–9]. These observations are often obtained from ground-based tracking systems. The determination of the parameters which describe the orbit is often performed by means of an estimator. The estimator takes into account the measurement and process noise and yields a best-fit approximation of the orbit parameters. Because these parameters are time-varying, they must be updated often.

The process of orbit determination consists of several components. The first of these components is the mathematical model of the system. In other words, the system of equations that describe the dynamics and kinematics of the orbiting body, Earth’s rotation, and perturbation models. The dynamics are described by the orbital two-body motion. This motion can be parametrized by several different sets such as classical orbital elements, Keplerian orbital elements, and inertial coordinates, to name a few. In addition to the dynamics, an important component which affects the motion of the orbiting body is orbital perturbations. Perturbations are deviations from the ‘normal’ or ‘idealized’ motion of the object [10]. They are often caused by the presence of naturally occurring phenomena such as atmospheric drag, aspherical gravitational field, third-body perturbations, and solar radiation pressure.

The second component of orbit determination is the measurement models. These models correspond to the measurements used for this particular application. These measurements give information about the orbiting body’s position, velocity, attitude, angular velocity, shape, size, and mass. Measurements can be obtained via observers on Earth such as the Space Surveillance Network. Some of the most common measurements are range, range rate, azimuth, elevation, and Earth landmark tracking. Measurements can also be acquired from other satellites (satellite-to-satellite tracking) or from vehicle mounted sensors [9].

The third and final component of orbit determination is the estimator. Gauss first approached this problem in 1795 by using least squares approximation tech-

niques [9]. Later on, Kalman utilized an estimation filter (i.e. Kalman filter) which is more accurate, efficient, and numerically stable [7, 9]. Since the development of this filter, there have been numerous alterations and improvements.

For the purpose of orbit determination, linear and nonlinear techniques have been employed. The extended Kalman filter (EKF) and the unscented Kalman filter (UKF) are the most widely used and have both shown to produce reliable results [11–13]. These two estimators have been used due to their capacity for handling the nonlinearity of the equations of motion and nonlinear measurement models. Nevertheless, the UKF produces better estimates than the EKF for nonlinear systems in general. This is due to the fact that the EKF linearizes the nonlinear dynamics and measurement models of the system to yield estimates. Consequently, this filter neglects the higher order Taylor series truncation terms [13]. Unlike the EKF, the UKF relies on the premise that with a fixed number of parameters, approximating the Gaussian distribution would be better than approximating the nonlinear functions. Furthermore, the UKF has the advantages of having a lower expected error than the EKF, it can be applied to non-differentiable functions, and it bypasses the need of the Jacobian matrix derivation [11]. The UKF has been shown to be an effective filter for the application of orbit determination and other orbiting body related estimations [11–13].

Another popular filter is the particle filter (PF). The goal of this particular filter is to reconstruct the posterior probability density function (pdf) of the state and parameter vector. Particle filters have the ability to handle nonlinear systems with non-Gaussian statistics, by approximating a continuous distribution via a large finite number of weighed random samples (particles) in the state space [14]. The bootstrap particle filter (BPF) is the first operational particle filter developed by Gordon, Salmond, and Smith [14, 15]. The BPF is a flavor of PF which uses a

Bayesian approach to construct the pdf of the state and parameter vector based on all available information. The performance of this filter is superior to that of the EKF. This is a consequence of the EKF assuming the pdf can be well approximated by a Gaussian distribution, which can lead filter divergence [15].

Once all the components of the orbit determination problem are combined, the estimator will use the mathematical models of the dynamics, perturbations, noisy measurements, along with initial conditions, and any other a priori knowledge regarding the orbiting body to produce an estimate of the object's time-varying states and parameters. The literature on this type of problem is extensive, as it has been addressed for several decades. Orbit determination has been used for Viking-Mars and Voyager-Jupiter missions [9,16], GPS aided aircraft navigation, as well as, aircraft and missile tracking [9], to name a few applications.

### 1.2.2 Light Curve Measurements and the Inverse Problem

The estimation of the shape of orbiting bodies has been a topic of interest for several decades. One of the most commonly used measurements to estimate the shape of a space object is the light curve measurement. The light curve is the time history of an object's observed brightness [12]. This measurement is a major source of information not only about near-Earth objects but for asteroids [17]. The problem that arises with the use of light curves is the light curve inversion. Light curves from space resident objects are ruled by the object's physical characteristics: attitude, angular velocity, shape, size, and photometric behavior of the surface, as well as the geometric arrangement of observation: location of light source, observer, and body. The light curve inversion problem is defined as finding the best possible fit between an observed light curve and a synthetic light curve generated by a model [18] without any a priori knowledge of the shape or size of the orbiting body. The work done in this area

over the past decades has established that light curve measurements contain a wealth of information regarding the mentioned properties of near-Earth asteroids [17–20]. These works have utilized the light curve measurement from asteroids to obtain their approximate shape and rotational rates. The estimation of the shape of these asteroids involves recovering information from the light curves such as: a convex representation of a non-convex original body, sidereal period, and pole direction along with a shape solution, and non-convex description of the original object [17]. This is often done by minimizing the number of free parameters by placing more constraints on the shape being evaluated. This can be addressed by modifying a generic tri-axial ellipsoid until the light curve matches that of the object [17]. Other works have been successful in demonstrating that the non-trivial shape of the object can be obtained from the use of acquired and synthetic light curves, by means of fitting the optical light curves [19,20].

In addition to the progress done in estimating the shape of near-Earth asteroids, light curves have also been utilized to estimate the attitude and angle variation of objects orbiting Earth [12,21–24]. This process has been evaluated by implementing a variety of Kalman filters and other estimation techniques. Some of this work was performed via data fusion of the light curve with the azimuth and elevation measurements to obtain more accurate estimations [12]. Moreover, other approaches use known ephemerides of the orbiting objects in combination with optical observations [22,24]. Most of these works have shown that the light curve measurement is a good source of information for the attitude and angle variation of Earth orbiting objects. Furthermore, light curves have also been used to estimate the shape of some of these objects [22,24]. These works have focused on matching the particular light curve of an existing object with that of a synthetic light curve.

### 1.3 Objectives and Contributions

#### Primary Objectives:

- I. Develop a realistic mathematical model of the short-term and long-term evolution of a resident space object orbiting Earth.
- II. Generate a set of synthetic measurements yielded by observers on Earth emulating the Space Surveillance Network.
- III. Estimate properties of the unresolved space object and its orbit. More specifically, its shape and size, attitude, angular velocity, position, and velocity.
- IV. Infer object's future intentions or possible threat to space assets.

The above mentioned objectives are the principal objectives of the work presented here. Nevertheless, these objectives imply the development and investigation of several secondary topics. These secondary objectives are listed below.

#### Secondary Objectives:

- V. Analysis of the observability and sensitivity of the light curve measurement with respect to the shape and size parameters, as well as, attitude and angular velocity of the resident space object.
- VI. Light reflectance mathematical models survey and comparison.
- VII. Investigation of the “inverse crime.”
- VIII. Investigation of better estimation techniques.

#### List of Published Works

(a) Objectives I–III:

K. Subbarao and L. Henderson, “Inverse problems in unresolved space object identification,” in AAS/AIAA Space Flight Mechanics Meeting, no. AAS 11-149, 2011. [25].

(b) Objectives I–III, VIII:

L. S. Henderson, P. Goyal, and K. Subbarao, “Inverse problem formulation cou-

pled with unscented kalman filtering for state and shape estimation of space objects,” in AAS/AIAA Space Flight Mechanics Meeting, no. AAS 12-115, 2012. [26].

(c) Objectives I–III, VIII:

P. Goyal, L. Henderson, and K. Subbarao, “A preliminary study in state and shape estimation for space objects in leo using the unscented kalman filter,” *Adventures on the Interface of Mechanics and Control*, pp. 299–325, 2012, in Honor of Prof. John L. Junkins on the occasion of his being awarded the ICCES Life-Time Achievement Medal. [27].

(d) Objectives V,VI:

L. S. Henderson, and K. Subbarao, “Sensitivity Analysis of the Lightcurve Measurement Model for Use in Attitude and Shape Estimation of Resident Space Objects,” in AAS/AIAA Space Flight Mechanics Meeting, no. AAS 13-430, 2013. [28].

(e) Objective VII:

L. S. Henderson, and K. Subbarao, “ ‘Inverse Crime’ and Model Integrity in Unresolved Space Object Identification,” in AAS/AIAA Space Flight Mechanics Meeting, no. AAS 14-205, 2014. [29]

The work presented here focuses in the area of low observables. More specifically, the short-term and long-term evolution of space objects are studied. For any individual object, a realistic mathematical time evolution model is developed, based on a system of stochastic nonlinear differential equations. These equations include perturbation forces due to the Earth’s gravitational pull (including  $J_2$ ), atmospheric drag, and solar radiation pressure. Other unmodeled effects are lumped together and represented as stochastic disturbing forces and torques. The atmospheric drag

and solar radiation pressure models are constructed as functions of the shape/size parameters of the space object.

In this work, the combination of two distinct problems is addressed: the direct problem and the inverse problem. The direct problem is orbit determination of the resident space object. Moreover, it focuses on estimating the orbiting body's position, velocity, attitude, and angular velocity given an accurate mathematical model of the object's dynamics [11, 30, 31]. The direct problem usually has a priori knowledge of the object's initial conditions, size, shape, and mass properties. Along with this knowledge, the orbit determination problem utilizes measurements such as azimuth, elevation, or radar. The combination of the modeled dynamics, a priori information, and noisy measurements are used by a filter to produce estimates of the object's states. The inverse problem focuses on estimating the shape, size, and spin rates of the space object [12, 17–19, 32, 33]. This problem is approached with a priori knowledge of the object's orbit. In this case, the measurements used are light curve or CCD arrays. Similarly to the first problem, a filter or a fitting algorithm is used to find the properties of the object.

The combined direct and inverse problem to be addressed in this work consists of determining the shape/size parameters that appear in the system of stochastic nonlinear differential equations so that an accurate description of the position, velocity, attitude, angular velocity, and shape/size parameters of the object can be obtained [25–27, 34]. The parameters that appear in the system of differential equations characterize the object, which is assumed to be a cuboid. In other words, the parameters are the length, width, and height of the object. To estimate these parameters, the system of equations include the translational dynamics and rigid body rotational dynamics with varying mass and moment of inertia terms, so that a complete description of the position and orientation of the object is obtained. The simulated

measurements will emulate information from the Space Surveillance Network. Light curve measurements are used to determine shape/size, attitude, and angular velocity, while elevation and azimuth information is used for position and velocity [35, 36].

A detailed study of the light curve measurement is also presented in this work. The information contained in this measurement is crucial to evaluate the model's effectiveness in characterizing the attitude, angular velocity, and shape parameters of an object. This evaluation is performed using synthetic measurements generated for a representative object attitude maneuver. A computer graphics light reflection model is used to describe how the rays of light from the Sun impinge upon the object and are then reflected to an observer on Earth [25, 26, 34, 37, 38]. For this study, several light reflectance functions are evaluated. The best performing models are chosen for the remaining work. The computer graphics models are based on work which compares experimentally obtained bidirectional reflectance distribution functions (BRDFs) with synthetic BRDFs from mathematical models [1]. The work in reference [1] extensively explores different materials and the behavior of the models compared to experimental data. These BRDF models are integrated into the light curve model and are tested via a sensitivity and observability analyses. Numerical sensitivities (observation matrix) are computed and a detailed study is conducted to analyze the information present in this measurement regarding the attitude, spin, and shape/size.

When evaluating the observability of a state variable it is often necessary to go beyond testing whether it is observable or not; it is often of more importance to establish the degree of observability that the state variable has. This type of analysis has been done for linear time-varying systems for the purpose of determining the efficiency of a Kalman filter designed to estimate the state of the system. Reference [39] expands on the observability analysis of time-varying systems which can be approxi-

mated as piece-wise constant systems with little loss in accuracy and without any loss in the behavior of the system. This approximation is possible because the focus of the observability analysis is the characteristics of the system rather than its time response. Moreover, references [40] and [41] evaluate the observable degree via a singular value decomposition (SVD). This method allows the evaluation of the observability degree of all state variables. The analysis presented in the previously mentioned references is evaluated for the system in question. The observability analysis will focus mainly in the object's orientation and shape/size parameters.

The final secondary objective is the investigation of alternative approaches for the estimation of the state and parameters of the object. This is done to inquire if other estimation techniques, besides the UKF, yield better estimates of the states for this particular application. The first of these attempts involves a UKF-batch estimation implementation. In this scheme the states are estimated via the UKF while the parameters are estimated via a batch algorithm which minimizes a cost function. This approach is used to improve the estimation of the shape/size parameters. In addition to this approach, a particle filter is also implemented. This particular filter, referred to as the bootstrap particle filter (BPF), reconstructs the posterior probability density function (pdf) of the state and parameter vector. The BPF makes no assumption regarding the system's linearity or statistics. This is of benefit, as the dynamics of the space object are nonlinear and the statistics have been assumed to be Gaussian for the implementation of the UKF.

## Chapter 2

### Problem Formulation

Given a time series of astrometric and photometric measurements from the Space Surveillance Network as explicit and implicit functions of position, velocity, attitude, angular velocity, and resident space object's shape and size, in addition to governing equations for the system dynamics and appropriate measurement models the combined direct and inverse problem is addressed:

- Direct Problem [11, 30, 31]

Estimate the resident space object's position, velocity, attitude, and angular velocity. The initial conditions, shape, size, and mass of the object are known.

- Inverse Problem [12, 17–19, 32, 33]

Determine the resident space object's shape, size, and spin rate. The orbit of the object is known.

- Combined Direct + Inverse Problem [25, 26, 34]

Estimate the resident space object's position, velocity, angular velocity, attitude, and shape and size.

#### 2.1 Combined Direct and Inverse Problem

Let  $\mathbf{x}$  be the vector with entries consisting of the positions, velocities, angular displacements, and angular velocities of a resident space object. The corresponding nonlinear differential equations governing the time evolution of  $\mathbf{x}$  are,

$$\dot{\mathbf{x}} = \mathbf{f}(\mathbf{x}, \mathbf{p}, t) \tag{2.1}$$

Given the previous expression, the direct problem is to determine  $\mathbf{x}(t)$  when all the system parameters and initial conditions are known. The inverse problem for a single space object here deals with the estimation of the orbit state, object attitude, angular velocity, and shape parameters (dimensions) at some epoch based on measurements from sensors such as radar or optical sensor arrays. The problem is then posed as,

$$\begin{aligned} \min \quad & \sum_j \|\mathbf{y}_m(j) - \hat{\mathbf{y}}(j)\|^2 \\ \text{subject to} \quad & \dot{\hat{\mathbf{x}}}(t) = \mathbf{f}(\hat{\mathbf{x}}, \hat{\mathbf{p}}, t) \\ & \dot{\hat{\mathbf{p}}}(t) = \mathbf{g}(\hat{\mathbf{p}}) \end{aligned} \tag{2.2}$$

where  $\dot{\hat{\mathbf{x}}}(t) = \mathbf{f}(\hat{\mathbf{x}}, \hat{\mathbf{p}}, t)$  is the same as the model in Equation (2.1).  $\mathbf{y}_m(j)$  is the vector of measurements or the available data and  $\hat{\mathbf{y}}(j)$  is the predicted output at the  $j^{\text{th}}$  sample instant. The solution approach adopted in this case involves the development of an analogous dynamical system model that estimates the system states and provides estimates for the orbit states and the parameters. For the above, the proposed approach in solving the combined direct and inverse problem consists of three steps:

1. Obtaining the expected value of the orbit as a function of time
2. Analyzing the time dependence of the covariance for the orbit
3. Estimating the system parameters and related error terms.

All of this is accomplished within an estimation algorithm framework.

It is of importance to estimate the physical parameters together with the spin rates of the objects, as they are key indicators of the nature of the object. For example, objects that are determined to have constant angular rates, regular geometries, and are estimated to be in closed orbits with perigee larger than radius of the Earth can be classified as Earth orbiting satellites. Additionally, if the angular rates are not constant but bounded and everything else remains the same, as with the earlier case,

they can be classified as being defunct satellites that contribute to space debris. For the most part, these already form a large portion of the US Space Catalog.

## 2.2 Governing Equations of Motion

The governing equations of motion for combined translation and rotation for the space object are given by a system of nonlinear ordinary differential equations as shown in Equation (2.3).

$$\begin{aligned}
 \dot{\mathbf{r}} &= \mathbf{v} \\
 \dot{\mathbf{v}} &= -\frac{\mu}{|\mathbf{r}|^3}\mathbf{r} + \mathbf{a}_{J_2} - \alpha(\mathbf{p})|\mathbf{v}_{rel}|\mathbf{v}_{rel} + \mathbf{a}(\mathbf{p})_{SRP} + \mathbf{\Gamma} \\
 \dot{\mathbf{g}} &= \mathbf{A}(\mathbf{g})\boldsymbol{\omega} \\
 \mathbf{I}(\mathbf{p})\dot{\boldsymbol{\omega}} &= -[\tilde{\boldsymbol{\omega}}]\mathbf{I}(\mathbf{p})\boldsymbol{\omega} + \boldsymbol{\tau}_{SRP} + \boldsymbol{\tau}_{gg} + \boldsymbol{\gamma}
 \end{aligned} \tag{2.3}$$

### 2.2.1 Translational Dynamics

The dynamics of an object orbiting Earth can be described by the two-body equation of motion. These equations are derived from Newton's law of universal gravitation, Newton's laws of motions, along with Kepler's laws. In addition to the two-body motion, perturbation effects and unmodeled stochastic effects have been included.

$$\dot{\mathbf{r}} = \mathbf{v} \tag{2.4}$$

$$\dot{\mathbf{v}} = -\frac{\mu}{|\mathbf{r}|^3}\mathbf{r} + \mathbf{a}_{J_2} - \alpha(\mathbf{p})|\mathbf{v}_{rel}|\mathbf{v}_{rel} + \mathbf{a}(\mathbf{p})_{SRP} + \mathbf{\Gamma} \tag{2.5}$$

The first equation is the derivative of the object's position  $\mathbf{r}$  with respect to time, which by definition is the object's velocity  $\mathbf{v}$ .

The second equation is the derivative of velocity with respect to time, acceleration. In this equation all accelerations acting on the body due to external forces are

included. The first term  $-\frac{\mu}{|\mathbf{r}|^3}\mathbf{r}$  accounts for the (deterministic) acceleration due to the Earth’s gravitational pull. This term contains Earth’s gravitational constant  $\mu$  ( $3.896 \times 10^5 \text{ km}^3/\text{s}^2$ ). The second term  $\mathbf{a}_{J_2}$ , captures the effects of the acceleration due to higher order gravity effects. This acceleration is a result of the Earth not being a perfect sphere, and consequently having an aspherical gravitational potential. The model used to represent this effect is zonal harmonics.  $J_2$  is the strongest perturbation due to Earth’s shape, and it accounts for most of the difference between a perfect spherical gravitational field [10]. The third term  $\alpha(\mathbf{p})$ , describes the effect of atmospheric drag. This term is a function of the projected area of the object perpendicular to the direction of the velocity. The dependence on the area is in turn a dependence on the shape and size parameters  $\mathbf{p}$ . It is also a function of atmospheric density, and the coefficient of drag. The term  $\mathbf{v}_{rel} = \mathbf{v} - \boldsymbol{\omega}_E \times \mathbf{r}$  is the relative velocity, where  $\boldsymbol{\omega}_E$  is the angular velocity of the Earth. The fifth term  $\mathbf{a}_{SRP}$ , is the acceleration due to solar radiation pressure (SRP). Similarly to drag, SRP is a non-conservative force. It develops as a consequence of the pressure felt by the object due the incoming radiation from the Sun [10]. This term is also a function of the shape/size parameters as the pressure exerted on the object depends on the cross-sectional area exposed to the Sun [10]. The final term  $\boldsymbol{\Gamma}$  is the (stochastic) acceleration due to composite unmodeled forces.

### 2.2.2 Rigid Body Rotational Kinematics

The resident space object is considered to be a rigid body. To model the attitude of the object Modified Rodrigues Parameters (MRPs) are used [42]. The use of these parameters allows for almost non-singular, bounded, minimal attitude representation. These three attitude parameters are stereographic projections of the Euler-Rodrigues symmetric parameters sphere [43]. For this application we use the

positive form of the parameters as shown in Equation (2.10). For an uncontrolled tumbling object,  $\mathbf{g}$  and  $\boldsymbol{\omega}$  denote the orientation and the angular velocity vectors of the object respectively. Here  $\mathbf{A}(\mathbf{g})$  is a matrix consisting of functions that depend nonlinearly on the orientation  $\mathbf{g}$ .

$$\dot{\mathbf{g}} = \mathbf{A}(\mathbf{g})\boldsymbol{\omega} \quad (2.6)$$

The initial condition is given using a quaternion  $\mathbf{q}$ , parametrization which is then is transformed to MRPs,  $\mathbf{g}$ . Equations (2.7) through (2.9) show the quaternion parametrization. The conversion to MRPs can be done using Equation (2.10) [44]. Note that the vector portion of the quaternion is  $\boldsymbol{\rho}$  and the scalar part is  $q_4$ . The vector portion is listed before the scalar portion.

$$\mathbf{q} \equiv \begin{bmatrix} \boldsymbol{\rho} \\ q_4 \end{bmatrix} \quad (2.7)$$

$$\boldsymbol{\rho} = [q_1 \ q_2 \ q_3]^T = \hat{\mathbf{e}} \sin\left(\frac{\nu}{2}\right) \quad (2.8)$$

$$q_4 = \cos\left(\frac{\nu}{2}\right) \quad (2.9)$$

$$g_i = \frac{q_i}{1 + q_4} \quad i = 1, 2, 3 \quad (2.10)$$

The attitude matrix can be written as a function of the MRP as shown in Equation (2.11).

$$\mathbf{A}_E^B(\mathbf{g}) = I_{3 \times 3} - \frac{4(1 - \mathbf{g}^T \mathbf{g})}{(1 + \mathbf{g}^T \mathbf{g})^2} [\mathbf{g} \times] + \frac{8}{(1 + \mathbf{g}^T \mathbf{g})^2} [\mathbf{g} \times]^2 \quad (2.11)$$

$$[\mathbf{g} \times] = \begin{bmatrix} 0 & -g_3 & g_2 \\ g_3 & 0 & -g_1 \\ -g_2 & g_1 & 0 \end{bmatrix} \quad (2.12)$$

Finally, the MRPs attitude kinematics are given by Equation (2.13).

$$\dot{\mathbf{g}} = \frac{1}{2} \left[ I_{3 \times 3} \left( \frac{1 - \mathbf{g}^T \mathbf{g}}{2} \right) + [\mathbf{g} \times] + \mathbf{g} \mathbf{g}^T \right] \boldsymbol{\omega} \quad (2.13)$$

### 2.2.3 Rigid Body Rotational Dynamics

The rotational dynamics describe the change in angular velocity with respect to time. This equation includes terms which account for torques caused by perturbations. It also takes into account the moment of inertia  $\mathbf{I}(\mathbf{p})$  as a function of the shape/size parameters of the object. For the purpose of this work, the density of the object is assumed constant.

$$\mathbf{I}(\mathbf{p})\dot{\boldsymbol{\omega}} = -[\boldsymbol{\omega} \times] \mathbf{I}(\mathbf{p})\boldsymbol{\omega} + \boldsymbol{\tau}_{SRP} + \boldsymbol{\tau}_{gg} + \boldsymbol{\gamma} \quad (2.14)$$

$[\tilde{\boldsymbol{\omega}}]$  is the skew-symmetric vector cross product operator of the angular velocity. The perturbation effects considered for the translational motion are the same considered here. The term  $\boldsymbol{\tau}_{gg}$  is the external torque due to the gravity gradient.  $\boldsymbol{\tau}_{SRP}$  is the external torque due to solar radiation pressure. The final term is the stochastic acceleration due to composite unmodeled torques. It is assumed that the object does not have any control torques acting on it.

## 2.3 Measurement Models

There are three measurements used for the estimation of all states and parameters. The astrometric measurements are azimuth and elevation angles. The photometric measurement is the light curve.

### 2.3.1 Astrometric Measurement

It is assumed the observer on Earth has capacity of measuring azimuth  $\Theta$  and elevation  $\Phi$  angles. These measurements are defined from the relative position of the object with respect to the observer in the Up-East-North frame defined in the following section. The following expressions will be used to obtain the measurements.

$$\Theta = \tan^{-1} \left( \frac{\rho_e}{\rho_n} \right)$$

$$\Phi = \sin^{-1} \left( \frac{\rho_u}{\|\boldsymbol{\rho}\|} \right)$$

### 2.3.2 Light Curve Measurement

This measurement model is based on a reflectance distribution function. It takes into account each of the object's faces, along with the position of the observer, and the Sun. This model can be tuned for the type of surface the object is made of. The final measurement describes the amount of sunlight reflected from the object toward the observer.

$$m_{app} = -m_{app,sun} - 2.5 \log_{10} \left| \sum_i^6 \frac{F_{obs,i}}{C_{sun,vis}} \right|$$

## 2.4 Coordinate Frames

### 2.4.1 Earth Centered Inertial Frame

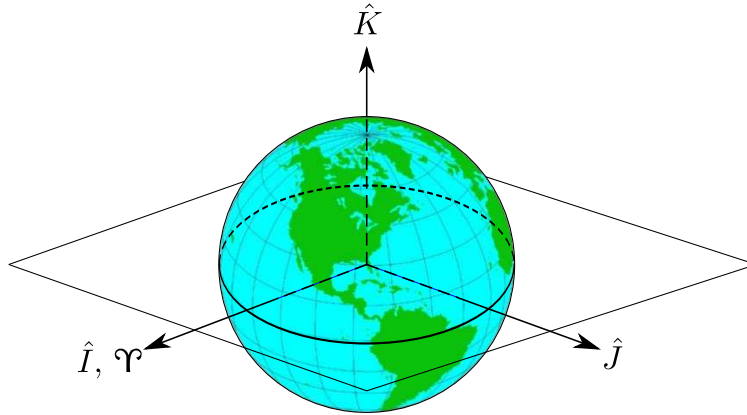


Figure 2.1. Earth Centered Inertial Frame.

The Earth centered inertial (ECI) frame has its origin at the center of the Earth. The  $\hat{I}\hat{J}$ -plane lies on the equatorial plane. The  $\hat{I}$  axis points to the vernal equinox, the  $\hat{K}$  goes through the north pole, and the  $\hat{J}$  completes the triad. Although

the equinox and equatorial plane do move over time [10], they are considered to be static for the purpose of this application. The ECI frame is shown in Figure 2.1. This frame is represented as  $[\hat{I}\hat{J}\hat{K}]$ . Vectors represented in this frame have a subscript  $E$ .

#### 2.4.2 Body Fixed Frame

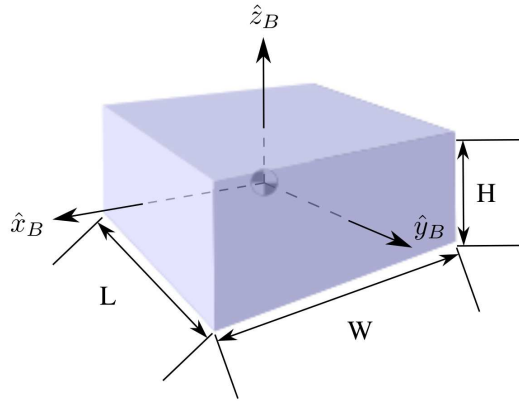


Figure 2.2. Body Fixed Frame.

The body fixed frame has its origin at the geometrical center of the space object as shown in Figure 2.2. Because the object is considered to have a constant density, the geometric center coincides with the center of mass. The shape/size parameters are defined so that the width ( $W$ ) is along the  $x_B$  axis, the length  $L$  is along the  $y_B$  axis, and the height  $H$  lies along the the  $z_B$  axis. Vectors represented in this frame have a subscript  $B$ .

#### 2.4.3 Up-East-North Frame

The Up-East-North (UEN) frame is defined by the geometry of the location of an observer on Earth. The position vector of the observer is  $\mathbf{R}$ , with  $\theta$  as the sidereal time and  $\lambda$  the as the latitude of the observer. The up direction  $\hat{\mathbf{u}}$  points in the

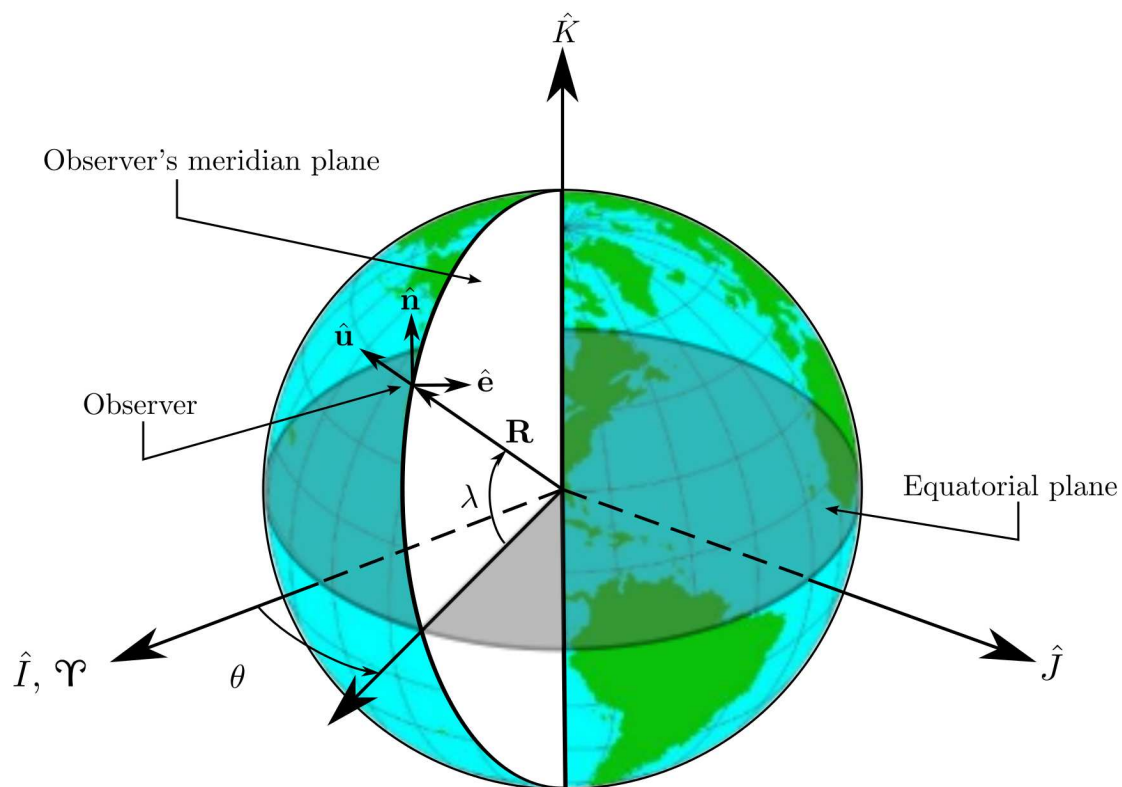


Figure 2.3. Up-East-North Frame.

direction of the position vector. The other two directions point to the local north  $\hat{n}$  and local east  $\hat{e}$  directions. Figure 2.3 shows the ECI frame and UEN frame.

## Chapter 3

### Perturbation Models

#### 3.1 Drag Acceleration

Equation (3.1) is used to describe the drag experienced by the resident space object as it orbits the Earth. The ballistic coefficient (BC) is set up as a function of the area projected on a plane perpendicular to the body's velocity vector. As the object tumbles, this area will change and so will the ballistic coefficient. The model used is an exponential atmospheric model [10]. This model assumes a spherically symmetrical distribution of particles where the density varies exponentially according to Equation (3.3). The superscript  $E$  refers to the vectors referenced to the ECI frame.

$$\mathbf{a}_{drag}^E = -\frac{1}{2} \frac{\rho_{atm} \|\mathbf{v}_{rel}^E\|}{BC} \mathbf{v}_{rel}^E \quad (3.1)$$

$$BC = \frac{m}{C_D A_p} \quad (3.2)$$

$$\rho_{atm} = \rho_{atm,0} \exp \left[ -\frac{h_{ellp} - h_0}{H} \right] \quad (3.3)$$

In the previous equation,  $\rho_{atm}$  refers to the atmospheric density,  $BC$  is the ballistic coefficient,  $A_p$  is the projected area,  $m$  is the mass of the object,  $C_D$  is the drag coefficient,  $\rho_{atm,0}$  is the reference density,  $h_{ellp}$  is the altitude of the object from the surface of the Earth, and  $h_0$  is the reference altitude. The exponential model is used for density as in Reference [10]. Note, it is assumed the object's density and the drag coefficient are constant, while  $A_p$  and  $m$  are computed based on the instantaneous estimates of the object dimensions.

### 3.2 Aspherical Gravitational Field Acceleration

For most applications, the assumption that Earth is a sphere is sufficient. For a more comprehensive model, it is necessary to account for the accelerations due to the non-spherical nature of Earth. An aspherical-potential function must be derived in order to determine the gravitational attraction on the space object. In this case, a simplification of the accelerations along each of the axis is used. The disturbing function  $R_2$  is shown in Equation (3.4), where  $J_2$  indicates that this approximation is using the second order zonal harmonics ( $J_2 = 0.0010826269$ ). Furthermore,  $\mu$  is Earth's gravitational parameter,  $R_E$  is Earth's mean equatorial radius ( $R_E = 6,378 \text{ km}$ ),  $r$  is the norm of position vector of the object measured from the center of the Earth  $\mathbf{r}$ , and  $\phi_{gc}$  is the latitude of the object.

$$R_2 = -\frac{3J_2\mu}{2r} \left( \frac{R_E}{r} \right) \left( \sin^2(\phi_{gc}) - \frac{1}{3} \right) \quad (3.4)$$

Using  $\sin(\phi_{gc}) = r_k/r$  where  $r_k$  is the component of  $\mathbf{r}$  along the z-axis, the following expression can be obtained.

$$R_2 = -\frac{3J_2\mu R_E^2}{2r^3} \left( \frac{r_K^2}{r^2} \right) + \frac{J_2\mu R_E^2}{2r^3} \quad (3.5)$$

Now Equation (3.5) can be differentiated with respect to each of the components of  $\mathbf{r}$  to obtain the corresponding accelerations. As an example, Equation (3.6) shows the partial derivative of  $R_2$  with respect to the component about the x-axis  $r_I$ :

$$\frac{\partial R_2}{\partial r_I} = -\frac{3J_2\mu R_E^2 r_I}{2r^5} \left( -\frac{5r_K^2 + 1}{r^2} \right) \quad (3.6)$$

Following the same procedure Equations (3.8) and (3.9) can be obtained for components  $r_J$  and  $r_K$  respectively. This yields all three accelerations for this model [10].

$$\mathbf{a}_I = -\frac{3J_2\mu R_E^2 r_I}{2r^5} \left( 1 - \frac{5r_K^2}{r^2} \right) \quad (3.7)$$

$$\mathbf{a}_J = -\frac{3J_2\mu R_E^2 r_J}{2r^5} \left(1 - \frac{5r_K^2}{r^2}\right) \quad (3.8)$$

$$\mathbf{a}_K = -\frac{3J_2\mu R_E^2 r_K}{2r^5} \left(3 - \frac{5r_K^2}{r^2}\right) \quad (3.9)$$

### 3.3 Solar Radiation Pressure Acceleration

Solar radiation pressure is a nonconservative disturbance, much like drag. This model will arrive at an expression for the acceleration due to this disturbance. The force exerted on the object is a function of the object's visible area from the Sun. Furthermore, the pressure experienced by the object is the force divided by the incident area exposed to the Sun. The first factor to be considered is the intensity of the energy of the Sun's incoming radiation. The following expression gives the solar flux ( $W/m^2$ ) which varies over a year [10]. Because the simulation is short, compared to the time it takes Earth to complete a rotation about the Sun, the solar flux is set to be  $SF = 1353 W/m^2$ .

$$SF = \frac{1358}{1.004 + 0.0334 \cos(D_{\text{aphelion}})} \quad (3.10)$$

In the above expression  $D_{\text{aphelion}}$  is  $2\pi$  times the days from the time the Earth is at aphelion denoted as a fraction of the whole year. The change in momentum or the solar pressure per unit area is shown below where  $c$  is the speed of light.

$$p_{SR} = \frac{SF}{c} \quad (3.11)$$

Most surfaces reflect some portion of the incoming radiation and absorb the other portion.  $R_{\text{abs}}$  is used to determine the percentage of absorption,  $R_{\text{diff}}$  is used to denote the percentage of diffused light and finally  $R_{\text{specular}}$  is the percentage of specular light for a surface  $A_f$  which has incident solar radiation. The normal to the surface makes an incidence angle with the Sun-object line of  $\phi_{\text{inc}}$  as shown on Figure 3.1. The

reflective angle  $\phi_{\text{ref}}$  is equal to the incident angle. Assuming a Lambertian diffusion, the following expressions can be used to describe the diffusive and specular radiation forces [10]. As seen in Figure 3.1  $\hat{\mathbf{s}}$  points in the direction of the Sun and  $\hat{\mathbf{n}}$  points in the direction normal to the facet.

$$\mathbf{F}_a = -p_{SR}R_{\text{abs}}A_f \cos(\phi_{\text{inc}})\hat{\mathbf{s}} \quad (3.12)$$

$$\mathbf{F}_{rs} = -2p_{SR}R_{\text{spec}}A_f \cos^2(\phi_{\text{inc}})\hat{\mathbf{n}} \quad (3.13)$$

$$\mathbf{F}_{rd} = -p_{SR}R_{\text{diff}}A_f \cos(\phi_{\text{inc}}) \left( \frac{2}{3}\hat{\mathbf{n}} + \hat{\mathbf{s}} \right) \quad (3.14)$$

The total acceleration contribution from all the facets of the object is given by Equation (3.15). If  $\phi_{\text{inc}}$  for a particular facet does not lie between  $[-\pi/2, \pi/2]$ , then contribution of that facet to the net acceleration produced is assumed to be zero.

$$\mathbf{a}_{SRP} = - \sum_{i=1}^6 \frac{p_{SR}A_i \cos(\phi_{\text{inc}})}{m} \left[ 2 \left( \frac{R_{\text{diff}}}{3} + R_{\text{spec}} \cos(\phi_{\text{inc}}) \right) \hat{\mathbf{n}} + (1 - R_{\text{spec}}) \hat{\mathbf{s}} \right] \quad (3.15)$$

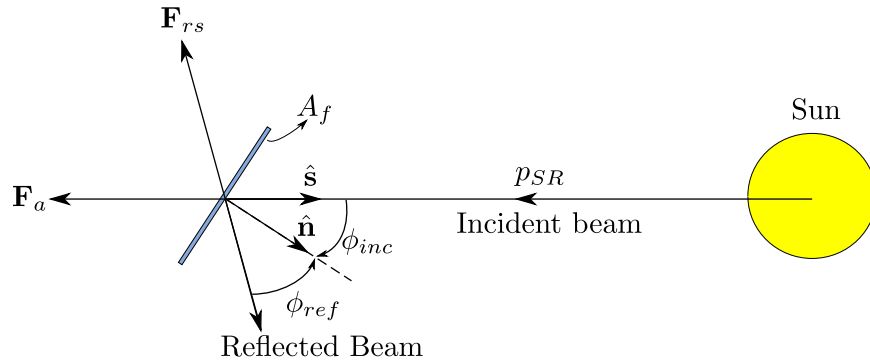


Figure 3.1. Solar Radiation Model Geometry.

### 3.4 Solar Radiation Pressure Torque

The force due to the solar radiation pressure acting on each face of the space object can be calculated by taking the vector sum of forces defined in Equations

(3.12)–(3.14). The net force is assumed to be acting on the center of the facet and so the torque produced is calculated using  $\mathbf{r}_c \times \mathbf{F}$ , where  $\mathbf{r}_c$  is the vector from the center of the space object to the center of the facet. Equation (3.16) shows the expression used to calculate the net torque due to solar radiation pressure.

$$\boldsymbol{\tau}_{SRP} = \sum_{i=1}^6 \mathbf{r}_{c,i} \times \mathbf{F}_i \quad (3.16)$$

$\boldsymbol{\tau}_{SRP}^E$  can be obtained by using the direction cosine matrix from from the body fixed frame to the ECI frame.

### 3.5 Gravity Gradient Torque

The orbiting object will not experience the same gravitational attraction on all points of its body. In order to account for this phenomena, a gravity gradient torque model has been introduced. Portions that are closer to Earth will experience a stronger attraction compared to the portions of the object that are further away. To calculate the net gravity gradient torque Equation (3.17) is used [45]. The size of the object considered for this study is quite small for this to be significant. Nevertheless, these models are included for modeling the true data and for possible applications wherein these torques are not negligible.

$$\boldsymbol{\tau}_{gg} = \int_B \mathbf{r}_b \times d\mathbf{F}_g \quad (3.17)$$

For the above equation  $\mathbf{r}_b$  is the position vector of the infinitesimal body element with respect to the center of mass of the space object.  $d\mathbf{F}_g$  is the infinitesimal gravitational force experienced by the body element and can be calculated using Equation (3.18).  $M_e$  is the mass of the Earth,  $dm$  is the body element mass, and  $\mathbf{r}$  is the inertial

relative position vector from the center of the Earth to the space object's center of mass.

$$d\mathbf{F}_g = -\frac{G M_e}{|\mathbf{r}|^3} \mathbf{r} dm \quad (3.18)$$

Substituting Equation (3.18) into (3.17) the following expression can be obtained.

$$\boldsymbol{\tau}_{\text{gg}} = G M_e \mathbf{R}_c \times \int_B \frac{\mathbf{r}}{|\mathbf{r}|^3} dm \quad (3.19)$$

This equation can be generalized as shown in Equation (3.20). This formulation uses the truncation of the binomial series as an approximation, where  $R_c$  is the inertial position vector relative to the center of the Earth and  $\mathbf{I}(\mathbf{p})$  is the inertia matrix.

$$\boldsymbol{\tau}_{\text{gg}}^{\mathbf{E}} = \frac{3 G M_e \mathbf{R}_c}{R_c^5} \times \mathbf{I}(\mathbf{p}) \mathbf{R}_c \quad (3.20)$$

## Chapter 4

### Measurement Models

#### 4.1 Astrometric Measurements

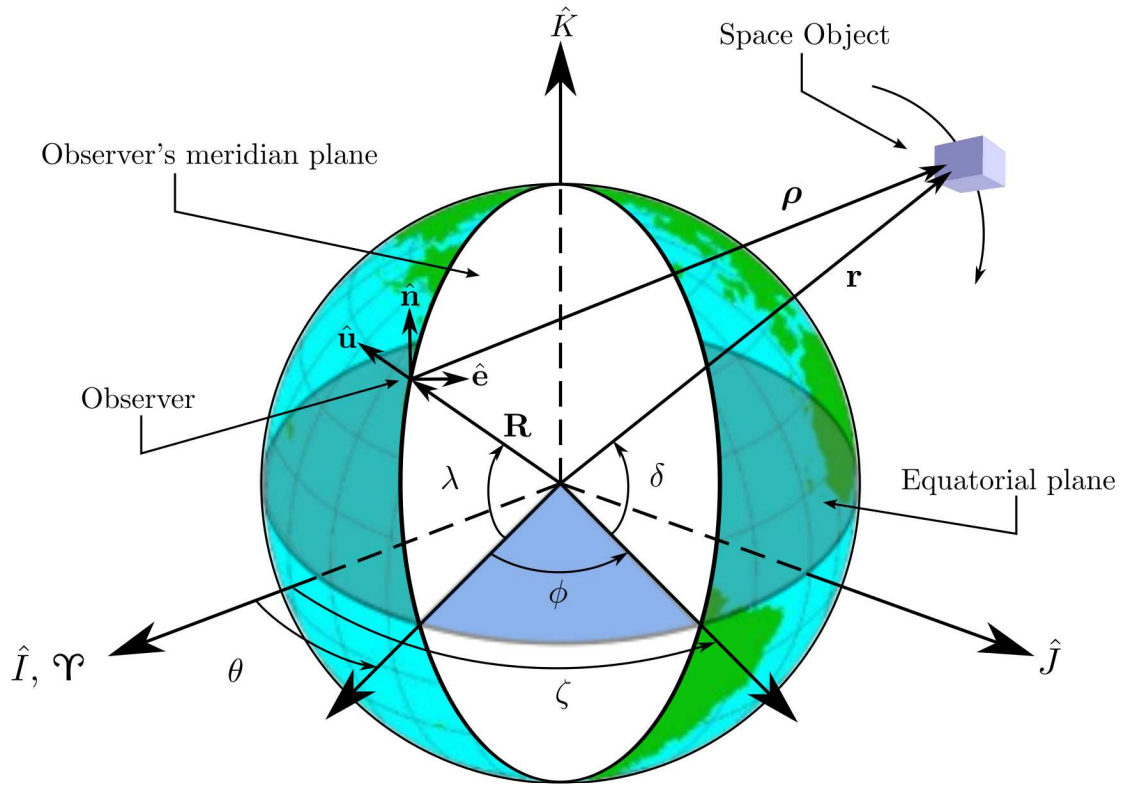


Figure 4.1. Geometry of Earth, Observer, and Object.

For this model, a radar site is deemed as the observer. This observer can measure range, azimuth, and elevation of the space object. Figure 4.1 shows the associated geometry and terminology used for this model. The slant range is  $\boldsymbol{\rho}$ , the radius vector of the object is  $\mathbf{r}$ , the radius vector of the observer is  $\mathbf{R}$ , the right

ascension and the declination of the body are  $\zeta$  and  $\delta$  respectively, the sidereal time of the observer is  $\theta$ , the latitude of the observer is  $\lambda$ , and the east longitude from the observer to the object is  $\phi$  [46]. The fundamental range observation is given by Equation (4.1) [46].

$$\boldsymbol{\rho} = \mathbf{r} - \mathbf{R} \quad (4.1)$$

For the ECI frame  $\boldsymbol{\rho}$  is given by the following expression, where  $\|\mathbf{R}\|$  is the norm of the observer position and  $[x \ y \ z]$ .

$$\boldsymbol{\rho}^E = \begin{bmatrix} x - \|\mathbf{R}\| \cos \lambda \cos \theta \\ y - \|\mathbf{R}\| \cos \lambda \sin \theta \\ z - \|\mathbf{R}\| \sin \lambda \end{bmatrix} \quad (4.2)$$

The range vector is represented in the Up-East-North frame by rotating the range vector represented in the ECI frame through the sidereal time and latitude angles as shown below.

$$\begin{bmatrix} \rho_u \\ \rho_e \\ \rho_n \end{bmatrix} = \begin{bmatrix} \cos \lambda & 0 & \sin \lambda \\ 0 & 1 & 0 \\ -\sin \lambda & 0 & \cos \lambda \end{bmatrix} \begin{bmatrix} \cos \theta & \sin \theta & 0 \\ -\sin \theta & \cos \theta & 0 \\ 0 & 0 & 1 \end{bmatrix} \boldsymbol{\rho}^E \quad (4.3)$$

The measurements the observer can obtain are azimuth  $\Theta$  and elevation  $\Phi$  angles.

The following expressions will be used to model the measurements.

$$\Theta = \tan^{-1} \left( \frac{\rho_e}{\rho_n} \right) \quad (4.4)$$

$$\Phi = \sin^{-1} \left( \frac{\rho_u}{\|\boldsymbol{\rho}\|} \right) \quad (4.5)$$

For the problem being addressed, only one optical sensor is used and only the azimuth and elevation measurements are considered.

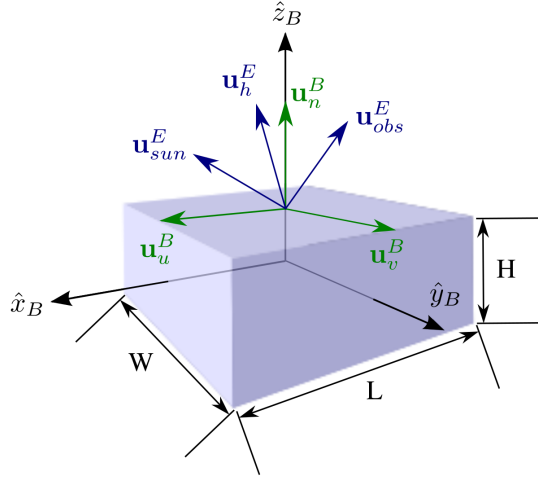


Figure 4.2. Resident Space Object Model with Light Curve Model Vectors.

#### 4.2 Light Curve Measurement

This model was constructed using a bidirectional reflectance distribution function (BRDF). This function is used to model the light distribution from a surface under incident light. As its name indicates, it is a function of two directions: first is the direction towards the light source and the second is towards the direction of the observer. This function can be tuned for specific types of materials the observer believes the orbiting body is composed of. Further analysis and selection of the reflectance model will be done in the chapter 6. Reflectance models will yield two components of light: the specular component  $\rho_{spec}$  and the diffusive component  $\rho_{diff}$ . The first component describes the light that is focused in a specific direction (mirror-like). The second component describes the light that is diffused or scattered equally in all directions (Lambertian).

$$\rho_{total} = \rho_{spec} + \rho_{diff} \quad (4.6)$$

A simplified model for flat surfaces will be used to develop the light curve observation model, where the total observed brightness of the object is the summation of the

brightness of each facet. Figure 4.2 illustrates a six facet model with vectors shown on the top facet. The shape model used for this work is composed by a finite number of facets. Each of these facets has a set of corresponding unit vectors  $\mathbf{u}_n^B$ ,  $\mathbf{u}_u^B$ , and  $\mathbf{u}_v^B$ . The unit vector  $\mathbf{u}_n^B$  is normal to the facet while  $\mathbf{u}_u^B$  and  $\mathbf{u}_v^B$  are in the plane of the facet. These vectors are expressed in the body frame and therefore do not change since the object is considered to be a rigid body. The following rotation matrix can be used to express the vectors in the ECI frame. It is necessary to rotate these vectors to the ECI frame so they can be used in the light curve model.

$$\mathbf{u}_i^E = A(\mathbf{g}_B^E)\mathbf{u}_i^B, \quad i = u, v, n \quad (4.7)$$

$A(\mathbf{g}_B^E)$  is the attitude matrix obtained from MRPs. In addition to these basis vectors, there are three unit vectors that must be considered for each of the body's facets. The first vector is the unit vector pointing in the direction of the Sun  $\mathbf{u}_{sun}^E$ . The second is  $\mathbf{u}_{obs}^E$  which points from the object to the observer. Third, the vector  $\mathbf{u}_h^E$  is the normalized half-angle vector between  $\mathbf{u}_{sun}^E$  and  $\mathbf{u}_{obs}^E$ . The last element of the shape model is the area of each of the facets denoted  $A_i$ . The shape and size of the orbiting object is defined once the number of facets is chosen, the set of six vectors, and the corresponding area for each facet has been obtained.

To calculate the apparent magnitude of the object, the fraction of visible sunlight impinging on the object must be calculated in combination with the total BRDF. This is a result of sunlight reflecting from the object's facets in the direction of the line-of-sight to the observer. The power per square meter affecting it caused by visible light striking the facets is  $C_{sun,vis} = 455 \text{ W/m}^2$  [37]. The dot product shown in Equation (4.8) is added to account for the visibility of the reflection towards the observer. If the angle between the observer's direction and the surface normal or the

angle between the Sun direction and the surface normal are greater than  $\pi$  then there is no light reflected in the direction of the observer and  $F_{sun}$  will be zero [37].

$$F_{sun} = C_{sun,vis} \rho_{total} \mathbf{u}_n^E \cdot \mathbf{u}_{sun}^E \quad (4.8)$$

The fraction of sunlight affecting the body that is then reflected can be calculated using Equation (4.9). Where  $\mathbf{R}$  is the position vector of the observer and  $A_i$  is the area of the facet.

$$F_{obs,i} = \frac{F_{sun} A_i \mathbf{u}_n^E \cdot \mathbf{u}_{obs}^E}{\|\mathbf{R}\|^2} \quad (4.9)$$

Now the apparent magnitude for each facet can be calculated. The apparent magnitude of the Sun is -26.7. Finally, the apparent magnitude of the object is taken to be the summation of the apparent magnitudes of all the facets.

$$m_{app} = -m_{app,sun} - 2.5 \log_{10} \left| \sum_i^6 \frac{F_{obs,i}}{C_{sun,vis}} \right| \quad (4.10)$$

## Chapter 5

### The Unscented Kalman Filter

The Unscented Kalman Filter was chosen as one of the estimation schemes because the expected error is lower than the Extended Kalman Filter (EKF) and it avoids the derivation of Jacobian matrices. The UKF works based on the notion that with a fixed number of parameters the Gaussian distribution can be estimated with more ease than with arbitrary nonlinear functions. The states to be approximated are position, velocity, rotation rate, and orientation. The parameters to be estimated are the object dimensions. The state for the UKF is shown in Equation (5.1).

$$\mathbf{x}^T = [\mathbf{r}^T \ \mathbf{v}^T \ \boldsymbol{\omega}_{B/E}^T \ \mathbf{g}^T \ \mathbf{p}^T] \quad (5.1)$$

where the shape/size parameters are defined as  $\mathbf{p} = [L \ W \ H]^T$ , (length, width, and height) the dimensions of the object. The system model will incorporate the orbital and attitude dynamics together with the model for the parameters  $\mathbf{p}$ . Additionally,  $\mathbf{w}(t)$  is a Gaussian white noise process term with zero mean and  $Q(t)$  is the covariance [46]

$$\dot{\mathbf{x}}(t) = \mathbf{f}(\mathbf{x}, \mathbf{p}, t) + G(t)\mathbf{w}(t) \quad (5.2)$$

For a discrete-time nonlinear system model the equation are is given as:

$$\mathbf{x}_{k+1} = \mathbf{f}(\mathbf{x}_k, \mathbf{w}_k, \mathbf{u}_k, k) \quad (5.3)$$

$$\tilde{\mathbf{y}}_k = \mathbf{h}(\mathbf{x}_k, \mathbf{u}_k, \mathbf{v}_k, k) \quad (5.4)$$

where the measurement is  $\tilde{\mathbf{y}}_k$  and the measurement noise is  $\mathbf{v}_k$  which has a zero mean Gaussian process with covariance  $R_k$ .

The propagation of this filter uses sigma points. These points are selected to be along the principal axis directions of the Gaussian state distribution. For a given  $n \times n$  state error-covariance matrix  $P_k$ , a set of  $2n$  symmetric points is created:

$$\sigma_k \leftarrow 2n \text{ columns from } \pm \gamma \sqrt{P_k} \quad (5.5)$$

The first point is taken to be the estimation of the state while the rest of the sigma points are taken to be the positive and negative summations of the square root of the covariance, weighted by the parameter  $\gamma$  given by Equation (5.9), where  $L$  is the size of the vector  $\hat{\mathbf{x}}_k$ .

$$\boldsymbol{\chi}_k(0) = \hat{\mathbf{x}}_k \quad (5.6)$$

$$\boldsymbol{\chi}_k(i) = \boldsymbol{\sigma}_k(i) + \hat{\mathbf{x}}_k \quad (5.7)$$

$$P_k = P_k^+ \quad (5.8)$$

$$\gamma = \sqrt{L + \lambda} \quad (5.9)$$

$$\lambda = \alpha^2(L + \kappa) - L \quad (5.10)$$

The composite scaling parameter  $\lambda$  is given by Equation (5.10). The spread of the sigma points is determined by  $\alpha$ , which is set to be a small positive number ( $1 \times 10^{-4} \leq \alpha \leq 1$ ). The parameter  $\kappa$  is used to apply the knowledge about higher moments for the given distribution [46].  $\beta$  is used to include prior knowledge of the distribution. For a Gaussian distribution  $\beta = 2$ . The weights are used to calculate the predicted mean and predicted covariance in Equation (5.14) and (5.15) respectively.

$$W_0^{mean} = \frac{\lambda}{L + \lambda} \quad (5.11)$$

$$W_0^{cov} = \frac{\lambda}{L + \lambda} + (1 - \alpha^2 + \beta) \quad (5.12)$$

$$W_i^{mean} = W_i^{cov} = \frac{1}{2(L + \lambda)}, \quad i = 1, 2, \dots, 2L \quad (5.13)$$

The predicted mean of the state estimate is found using the weights shown in Equations (5.11)–(5.13), where the values of the sigma points are weighted and summed.

$$\hat{\mathbf{x}}_{k+1}^- = \sum_{i=0}^{2L} W_i^{mean} \boldsymbol{\chi}_{k+1}^x(i) \quad (5.14)$$

Similarly, the predicted covariance is obtained by taking the difference of each calculated sigma point and the estimated value of the state at  $k + 1$ . The weighted sum of these values yields the predicted covariance.

$$P_{k+1}^- = \sum_{i=0}^{2L} W_i^{cov} [\boldsymbol{\chi}_{k+1}^x(i) - \hat{\mathbf{x}}_{k+1}^-] [\boldsymbol{\chi}_{k+1}^x(i) - \hat{\mathbf{x}}_{k+1}^-]^T + \Gamma Q_{k+1} \Gamma^T \quad (5.15)$$

The mean observation is given by the following expression, where the measurements obtained for each of the sigma points  $\boldsymbol{\gamma}_{k+1}$  are obtained via the measurement models, and are summed and weighted.

$$\hat{\mathbf{y}}_{k+1}^- = \sum_{i=0}^{2L} W_i^{mean} \boldsymbol{\gamma}_{k+1}(i) \quad (5.16)$$

$$\boldsymbol{\gamma}_{k+1}(i) = \mathbf{h}(\boldsymbol{\chi}_{k+1}^x(i), k + 1) \quad (5.17)$$

The output covariance  $P^{yy}$  is given by Equation (5.18). This covariance is obtained by obtaining the error between the mean observation and the measurement obtained from each sigma point. Similarly to the previous covariances, the difference is also weighted.

$$P_{k+1}^{yy} = \sum_{i=0}^{2L} W_i^{cov} [\boldsymbol{\gamma}_{k+1}(i) - \hat{\mathbf{y}}_{k+1}^-] [\boldsymbol{\gamma}_{k+1}(i) - \hat{\mathbf{y}}_{k+1}^-]^T \quad (5.18)$$

The innovation  $\mathbf{v}$  is defined as the difference between the mean observation and the acquired measurement. The innovations covariance defined as the output covariance plus the measurement noise covariance.

$$\mathbf{v}_{k+1} \equiv \tilde{\mathbf{y}}_{k+1} - \hat{\mathbf{y}}_{k+1}^- \quad (5.19)$$

$$P_{k+1}^{vv} = P_{k+1}^{yy} + R_{k+1} \quad (5.20)$$

The cross-correlation covariance  $P^{xy}$  is calculated by the weighted difference between each sigma point and the estimated state, and the measurement from each sigma point and the mean observation.

$$P_{k+1}^{xy} = \sum_{i=0}^{2L} W_i^{cov} [\mathcal{X}_{k+1}^x(i) - \hat{\mathbf{x}}_{k+1}^-] [\boldsymbol{\gamma}_{k+1}(i) - \hat{\mathbf{y}}_{k+1}^-]^T \quad (5.21)$$

Now the Kalman gain can be computed using the cross-correlation covariance and the innovations covariance.

$$K_{k+1} = P_{k+1}^{xy} (P_{k+1}^{vv})^{-1} \quad (5.22)$$

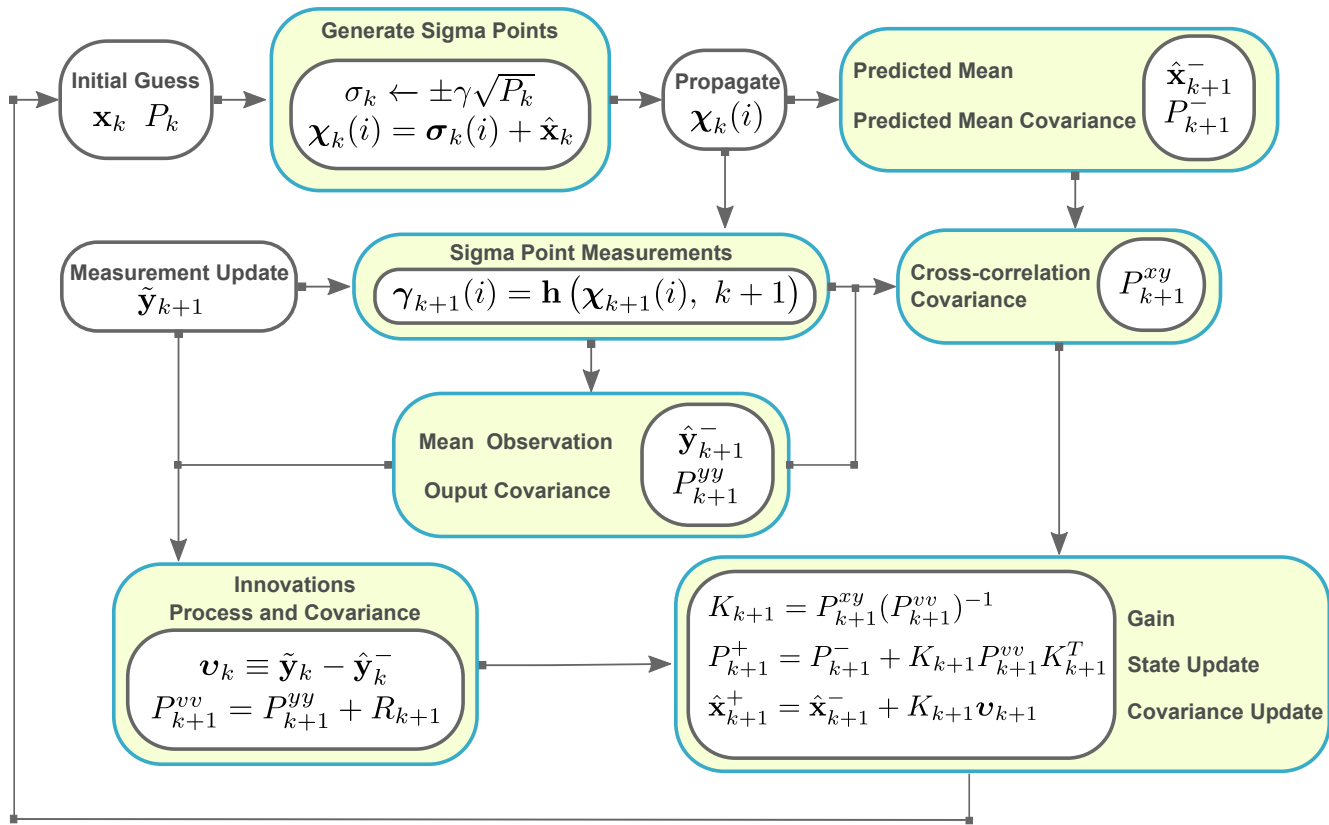
Finally, the state and error covariance updates can be obtained as shown Equation (5.23) and (5.24).

$$\hat{\mathbf{x}}_{k+1}^+ = \hat{\mathbf{x}}_{k+1}^- + K_{k+1} \mathbf{v}_{k+1} \quad (5.23)$$

$$P_{k+1}^+ = P_{k+1}^- + K_{k+1} P_{k+1}^{vv} K_{k+1}^T \quad (5.24)$$

The process of the UKF is depicted in Figure 5.1. The process begins with an initial guess of the state and covariance. Then the sigma point are generated from the covariance. The sigma points are then propagated using the dynamic model and measurements are obtained using the measurement models. In addition, the estimated states are also propagated and the corresponding measurements are obtained. The mean observation and output covariance, innovation covariance, and cross correlation covariance are calculated by using an acquired measurement. This then allows the calculation of the predicted mean and predicted covariance. Finally, the Kalman gain is calculated, yielding the updated state and covariance. The process is repeated after all measurements are obtained or the filter converges.

Figure 5.1. Unscented Kalman Filter Algorithm.



## Chapter 6

### Observability and Sensitivity Analysis

#### 6.1 Position and Velocity

For the purpose of this work, the radar measurement has been neglected. This makes for the estimation of an ‘unresolved’ object. Nevertheless, the astrometric data, azimuth and elevation, provide enough information to estimate its position and velocity. The orbit determination via these two measurements is referred to as angles-only orbit determination. This type of problem has been addressed for hundreds of years and the literature on it is extensive. To give a few historical references, the first documented attempt was done by Laplace in 1780. He implemented the now termed Laplace’s Method, to estimate the position and velocity vectors of comets and minor planets [10,47]. Another method for angles-only observation was developed by Gauss [9]. This method assumes the object’s position vectors, at three different epochs, all lie on the same plane. A newer implementation of orbit determination with angles-only would be via a Kalman filter [47]. The availability of high accuracy angle measurements and improved methods for estimation have produced accurate orbit determination. These methods have been implemented with real and synthetic data by several authors, and has proven to be successful [47–49].

Because of the work and advances in this particular area, the observability and sensitivity of the position and velocity with respect to the azimuth and elevation measurements will not be performed. It has been established for a long period of time, by numerous authors, and with several techniques, that these astrometric measurements contain sufficient information to produce accurate estimates of the position and veloc-

ity. Consequently, the efforts of this study will focus on the light curve measurement, attitude, angular velocity states and shape/size parameters.

## 6.2 Attitude, Angular Velocity, Shape and Size

The light curve model is one of the essential components in the estimation of the shape/size parameters, attitude, and angular velocity of the resident space object. Therefore, the level of information carried in this measurement is key. The mathematical models used to represent the light reflections from the object are borrowed from computer graphics models. These models can be adapted to represent the amount of light from the Sun reflected by the object and received by an observer on Earth. These light reflection functions used in computer graphics, range from the very complex to the simplistic, physically accurate, or created for computational speed. Therefore, a detailed examination of these models and their properties is necessary to determine which one will best suit the application of estimating parameters and states of a space object. This chapter presents the work done to address this.

First, a comparison of the BRDFs will be presented in common nomenclature along with performance comparisons performed in the area of computer graphics rendering. Furthermore, all BRDFs are be applied to the space object problem via the light curve model and a sensitivity and observability analysis is performed. The sensitivity analysis determines if the measurement contains information regarding the attitude, angular velocity, and shape/size parameters. The observability analysis determines whether the states and parameters are observable from the light curve measurement, and if so, to what degree.

### 6.3 Bidirectional Reflectance Distribution Function Comparison and Analysis

This section will present the light reflection functions being considered. Seven models are analyzed: Ward [50], Ward-Dür [51], Blinn-Phong [52], Lafortune et al. [53], Cook-Torrance [54], He et al. [55], and Ashikhmin-Shirley [38]. The models are presented in the next section with common nomenclature for easy comparison. Reference [1] evaluates these models in terms of their ability to fit measured BRDFs. These authors have utilized a high-resolution data set of one hundred isotropic materials and four anisotropic materials and have computed the best approximation for each of the mentioned models. The results for all materials and all models is presented in reference [1]. The results suggest that the Cook-Torrance, Ashikhmin-Shirley, and He models perform well for the isotropic materials. Another characteristic noted on the investigation, is the way in which the specular lobe is represented. One formulation uses the dot product between the half-angle vector and the facet normal, while the other, uses the dot product between the viewer and the mirror reflection of the light vector. The models using the first dot product have a smaller error when compared with the measured BRDFs, while the models that use the second dot product are visually inaccurate when rendering an image. Although image rendering is not part of the work presented here, accurate reflection of light is of importance. Finally, it should be noted that the Ashikhmin-Shirley was deemed as the best model for isotropic materials [1].

Table 6.1 contains the main characteristics of each of those models. The first aspect is the specular lobe representation. This can either be done using the dot product between the half-angle vector and the facet normal, while the other uses the dot product between the unit vector pointing to the observer and the direction of mirror reflection of the unit vector pointing light source. The second characteristic shows whether the model can handle isotropic and/or anisotropic materials. Isotropic ma-

materials reflect light in the same matter regardless of direction. Anisotropic materials, on the other hand, have different reflectivity properties depending on the direction in which light is striking the surface. The third characteristic is if the model accounts for the polarization of light. The fourth aspect is the way in which the surface roughness is quantified. Some models utilize a simplification parameters, while others use the Fresnel factor or an approximation of the Fresnel factor (Ashikhmin-Shirley). The last attribute is whether the model accounts for conservation of energy, i.e. the amount of energy impinging upon the object is the same that is being absorbed and reflected back.

Table 6.1. BRDF Characteristics Comparison

Model	Specular Lobe		Materials		Light Pol.	Surface Roughness		Energy Conserv.
	$\mathbf{u}_h \cdot \mathbf{u}_n$	$\mathbf{u}_{obs} \cdot \mathbf{u}_{sun}$	Isotrop.	Aniso.		Simplif. Param.	Fresnel Factor	
Wa	x		x			x		x
Wa-Dü	x		x			x		x
Bl-Ph	x		x					
La	x		x			x		
Co-To	x		x	x	x		x	
He		x	x		x		x	
As-Sh	x		x	x			x	x

The light reflection models will be integrated as shown in section 4.2. Each model will yield a specular  $\rho_{spec}$  and diffusive  $\rho_{diff}$  component of reflected light. Furthermore, the materials selected for the object will be chosen from the work in reference [1], as each model contains different parameters to describe materials and their properties. The investigation by these authors was geared towards computer rendering; therefore, each of the models contain information regarding color spectrum. This means each color channel: red, green, and blue, will have values for specular

and diffuse amounts of light. As only the amount of light is considered, these values will be summed to obtain a singular value for ‘white’ light. Finally, all models will have the same diffuse component model as shown in Equation (6.1).  $\rho_d$  is the factor for diffusive light; it is material dependent and describes the amount of light that is diffusive. This model is referred to as Lambertian and is the most commonly used. This model essentially distributes the amount of light that is diffusive in all directions equally; Unless the observer is behind the facet being evaluated, and therefore cannot see the light being reflected (i.e. negative dot product), in which case the value would be zero [52]. Table 6.2 contains the nomenclature used to describe all seven models.

$$\rho_{diff} = \rho_d \max(0, \mathbf{u}_n \cdot \mathbf{u}_{sun}) \quad (6.1)$$

Table 6.2. Common Notation for BRDF Model Comparison

Notation	Definition
$\mathbf{u}_n$	unit vector normal to facet
$\mathbf{u}_{obs}, (u_{obs,x}, u_{obs,y}, u_{obs,z})$	unit vector pointing towards the observer
$\mathbf{u}_{sun}, (u_{sun,x}, u_{sun,y}, u_{sun,z})$	unit vector pointing towards the Sun
$\mathbf{u}_r$	mirror reflection of $\mathbf{u}_{sun}$
$\mathbf{u}_h$	half vector between $\mathbf{u}_{obs}$ and $\mathbf{u}_{sun}$
$\delta_{lobe}$	angle between $\mathbf{u}_n$ and $\mathbf{u}_h$
$\rho_{spec}$	specular component of light
$\rho_{diff}$	diffuse component of light
$\rho_s$	specular reflectance of material
$\rho_d$	diffuse reflectance of material
$p_0, p_1, p_2$	model specific parameters

### 6.3.1 Ward Model (1992, abbr. Wa)

This model was first presented by Ward in [50]. According to the author, the aim of this mathematical model was to provide a simple yet physically accurate model that would reflect measured data accurately. For the sake of simplicity, the Ward model does not explicitly contain any information regarding the wavelength or polarization of light. Furthermore, the author has used a single normalization factor which has replaced the Fresnel coefficient, geometrical attenuation factors, and arbitrary constants used in other models. These factors account for the assumptions taken regarding the statistics of a surface height function. This particular model also yields correct energy balance, due to the normalization [50]. Equation (6.2) shows the specular component developed by Ward, where  $\alpha$  is the standard deviation (RMS) of the surface slope. Tables A.1-A.3 in Appendix A contain the values for each corresponding material and are listed as  $p_0 = \alpha$ .

$$\rho_{spec} = \frac{\rho_s}{\sqrt{(\mathbf{u}_n \cdot \mathbf{u}_{sun})(\mathbf{u}_n \cdot \mathbf{u}_{sun})}} \frac{\exp[-\tan^2 \delta_{lobe}/\alpha^2]}{4\pi\alpha^2} \quad (6.2)$$

### 6.3.2 Ward-Dür Model (2004, abbr. Wa-Dü)

This model is very similar to the Ward model. The author has re-assessed a new normalization for the bidirectional reflection distribution function proposed by Ward [56]. This model produces higher peaks in the direction of the half-vector. The author points out this is closer to measured BRDFs. The values for the materials are listed as  $p_0 = \alpha$  on tables A.1-A.3 in Appendix A.

$$\rho_{spec} = \frac{\rho_s}{(\mathbf{u}_n \cdot \mathbf{u}_{sun})(\mathbf{u}_n \cdot \mathbf{u}_{sun})} \frac{\exp[-\tan^2 \delta_{lobe}/\alpha^2]}{4\pi\alpha^2} \quad (6.3)$$

### 6.3.3 Blinn-Phong Model (1977, abbr. Bl-Ph)

This model is based on experimental measurements on how light reflects from real surfaces. This model introduced the concept of maximum highlight direction. The model uses the fact that more light is reflected in the direction making an equal angle of incidence with the reflectance direction. The light reflected in this direction is termed as specular. The model defines this direction as  $\mathbf{u}_h$ . Other models have adopted this concept, often calling it the half-angle vector between the incoming light vector and viewer vector. The cosine of the angle between  $\mathbf{u}_h$  and  $\mathbf{u}_n$ , denoted as  $\delta_{lobe}$ , is used as a measure of the distance a particular surface is away from the maximum specular direction [52]. The sharpness of the highlight is then adjusted by raising the cosine of the angle to some power  $n$ . This value is provided according to the material in Tables A.1-A.3 as  $p_0 = n$  in Appendix A.

$$\mathbf{u}_h = \frac{\mathbf{u}_{sun} + \mathbf{u}_{obs}}{|\mathbf{u}_{sun} + \mathbf{u}_{obs}|} \quad (6.4)$$

$$\rho_{spec} = \rho_s \frac{n+2}{2\pi} \cos^n \delta_{lobe} \quad (6.5)$$

### 6.3.4 Lafortune et al. Model (1997, abbr. La)

The model described in reference [53] uses functions with nonlinear parameters to represent the light reflectance model. This model is based on the cosine lobe model shown in Equation (6.5). The model shown in Equation (6.6) uses the generalized cosine lobe model by means of creating a matrix transformation along with a normalization factor. This allows the use of nine different parameters that can be used to tune the model [53]. These parameters are limited by physical restrictions and

simplify to the equation shown below. The parameters are shown in Tables A.1-A.3 as  $p_0 = C_{xy}$ ,  $p_1 = C_z$ , and  $p_2 = n$  in Appendix A.

$$\rho_{spec} = \rho_s [C_{xy}(u_{sun,x}\mathbf{u}_{obs,x} + \mathbf{u}_{sun,y}\mathbf{u}_{obs,y}) + C_z\mathbf{u}_{sun,z}\mathbf{u}_{obs,z}]^n \frac{n+2}{2\pi [\max(|C_z|, |C_{xy}|)]^n} \quad (6.6)$$

### 6.3.5 Cook-Torrance Model (1981, abbr. Co-To)

This model is based on geometrical optics. It defines the reflection of light by relating the brightness of an object to the intensity and size of the light source which is illuminating it. Additionally, it can predict the directional distribution and spectral composition of the reflected light. This is possible by describing the spectral composition of the light source, as well as, the wavelength-selective reflection of the surface. Similarly to the Blinn-Phong model, it uses the half-angle vector for the direction of the specular light. The intensity of the light is defined by the use of a solid angle, which is the projected area of the light source divided by the square of the distance to the light source (constant for distant sources) [54]. Furthermore, this model describes the distribution function of the directions of the faces in  $D$ , and the amount by which the facets shadow and mask one another in  $G$  [52]. Finally, this model introduces the Fresnel factor. This factor gives the fraction of light that is incident on a facet which is being reflected as opposed to absorbed. This factor is a function of the angle of incidence on the facet and the index of refraction on the surface. The Fresnel equation for unpolarized light is shown in Equation (6.8),

where  $n$  is the index of refraction. The parameters in Tables A.1-A.3 can be found as  $p_0 = F_0$  and  $p_1 = m$  in Appendix A.

$$\begin{aligned}\rho_{spec} &= \frac{\rho_s}{\pi} \frac{DG}{(\mathbf{u}_n \cdot \mathbf{u}_{sun})(\mathbf{u}_n \cdot \mathbf{u}_{sun})} \text{Fresnel}(F_0, (\mathbf{u}_{obs} \cdot \mathbf{u}_h)) \\ G &= \min \left\{ 1, \frac{2(\mathbf{u}_n \cdot \mathbf{u}_h)(\mathbf{u}_n \cdot \mathbf{u}_{obs})}{(\mathbf{u}_{obs} \cdot \mathbf{u}_h)}, \frac{2(\mathbf{u}_n \cdot \mathbf{u}_h)(\mathbf{u}_n \cdot \mathbf{u}_{sun})}{(\mathbf{u}_{obs} \cdot \mathbf{u}_h)} \right\} \\ D &= \frac{1}{m^2 \cos^4 \delta_{lobe}} \exp - [\tan \delta_{lobe}/m]^2\end{aligned}\tag{6.7}$$

$$\begin{aligned}\text{Fresnel}(F_0, (\mathbf{u}_{obs} \cdot \mathbf{u}_h)) &= \frac{1}{2} \left( \frac{g-c}{g+c} \right)^2 \left[ 1 + \frac{(c(g+c)-1)^2}{(c(g-c)+1)^2} \right] \\ n &= \frac{1 + \sqrt{F_0}}{1 - \sqrt{F_0}} \\ c &= \mathbf{u}_{sun} \cdot \mathbf{u}_h \\ g &= \sqrt{n^2 + c^2 - 1}\end{aligned}\tag{6.8}$$

### 6.3.6 He et al. Model (1991, abbr. He)

The authors of this model based it on physical optics. Unlike other models, this one includes a component for specular, directional diffuse, and uniform diffuse. This model also includes information regarding the polarization, wavelength, incidence angle, roughness parameters, and surface refractive index. The specular component is due to the specular reflection by the mean surface, while the directional diffuse is due to the diffraction scattering by the surface roughness. In the Equation (6.14) below  $n$  is the index of refraction,  $|F|^2$  is the Fresnel reflectivity for unpolarized light at the bisecting angle  $\phi_b$ ,  $\mathcal{S}$  is the shadowing/masking factor,  $g$  is the surface roughness function,  $\theta_r$  is the angle of reflection,  $\theta_i$  is the angle of incidence, and  $\sigma$  is

the standard deviation of the surface height [1, 55]. The parameters for this model are listed in Tables A.1-A.3 as  $p_0 = \tau$ ,  $p_1 = \sigma$ , and  $p_2 = n$  in Appendix A.

$$\Lambda(\theta) = \frac{1}{2} \left[ \frac{2\sigma}{\sqrt{\pi}\tau \cot \theta} - \operatorname{erfc} \left( \frac{\tau \cot \theta}{2\sigma} \right) \right] \quad (6.9)$$

$$S(\theta) = \left[ 1 - \frac{1}{2} \operatorname{erfc} \left( \frac{\tau \cot \theta}{2\sigma} \right) \right] \frac{1}{\Lambda(\theta) + 1} \quad (6.10)$$

$$\mathcal{S} = S(\theta_i)S(\theta_r) \quad (6.11)$$

$$g = \left[ \frac{2\pi\sigma}{\lambda} ((\mathbf{u}_n \cdot \mathbf{u}_{sum}) + (\mathbf{u}_n \cdot \mathbf{u}_r)) \right]^2 \quad (6.12)$$

$$\phi_h = \arccos \left( \frac{|\mathbf{u}_{sun} - \mathbf{u}_r|}{2} \right) \quad (6.13)$$

$$\phi_b = \arcsin \left( \frac{\sin \phi_h}{n} \right) \quad (6.14)$$

$$|F|^2 = \frac{1 \sin^2(\phi_h - \phi_b)}{2 \sin^2(\phi_h + \phi_b)} \left( 1 - \frac{\cos^2(\phi_h + \phi_b)}{\cos^2(\phi_h - \phi_b)} \right) \quad (6.15)$$

$$\rho_s = |F|^2 e^{-g} \mathcal{S} \quad (6.16)$$

$$\rho_{spec} = \frac{\rho_s}{\cos(\theta_i)} \quad (6.17)$$

### 6.3.7 Ashikhmin-Shirley Model (2000, abbr. As-Sh)

This model is inspired by the Ward model [50], along with other popular models. This model obeys the energy conservation laws and allows the analysis of anisotropic materials. Similarly to other models, it uses the Fresnel behavior, but uses an approximation rather than the equations used in the previous models. As the creation of this model was motivated by practical applications, it has a simplistic appearance when compared to other models. The parameters are listed as  $p_0 = F_0$  and  $p_1 = n$  in Tables A.1-A.3 in Appendix A.

$$\rho_{spec} = \frac{n+1}{8\pi} \frac{(\mathbf{u}_n \cdot \mathbf{u}_h)^n}{(\mathbf{u}_{obs} \cdot \mathbf{u}_h) \max((\mathbf{u}_n \cdot \mathbf{u}_{sun}), (\mathbf{u}_n \cdot \mathbf{u}_{obs}))} \operatorname{Fresnel}(\rho_s, (\mathbf{u}_{obs} \cdot \mathbf{u}_h)) \quad (6.18)$$

$$\operatorname{Fresnel}(\rho_s, (\mathbf{u}_{obs} \cdot \mathbf{u}_h)) = \rho_s + (1 - \rho_s) (1 - (\mathbf{u}_{obs} \cdot \mathbf{u}_h))^5 \quad (6.19)$$

### 6.3.8 Material Selection

The material selection was done based the experimental work in reference [1]. This study covers a wide range of materials. These materials are categorized by the way in which they reflect light. Isotropic materials are those which reflect light in the same matter regardless of direction. Anisotropic materials on the other hand have different reflectivity properties based on the direction in which light is striking the material. Two of the materials chosen for the object are isotropic: black oxidized steel and black plastic. The third material is anisotropic: brushed aluminum. These materials would have a similar reflectivity behavior to that of a man-made space object. Most man-made objects orbiting Earth contain aluminum, solar panel structures, and composites. Unfortunately, composites and solar panels were not part of the experimental work performed in the previously mentioned work. Consequently, materials with similar reflectivity properties the above mentioned were chosen. The isotropic materials are black oxidized steel and black plastic. Tables A.1-A.3 in Appendix A show the parameters obtained experimentally for the chosen materials for all models.

### 6.4 Sensitivity Analysis

The sensitivity analysis will be carried out using the numerically computed Jacobian of the measurements with respect to the system state vector and the UKF derived observer matrix. For this analysis, the only measurement considered is the light curve magnitude,  $\tilde{y} = m_{app} + v$ , where  $v \sim \mathcal{N}(0, \sigma_m^2)$  ( $\sigma_m^2$  is the measurement error variance). Furthermore, a reduced state vector is considered as  $\mathbf{x} = [\mathbf{g}^T \boldsymbol{\omega}^T \mathbf{p}^T]^T$  with only the attitude (MRP), angular velocity, and vector of parameters that characterizes the shape and size. For the purpose of this study, the object's rotational motion will be simulated assuming the translational position and velocity fixed at

some representative epoch. For a non-rotating Earth, this will translate to measuring the object brightness and its variation only due to the attitude changes while everything else that could affect the light curve has been kept fixed (i.e. no translation or perturbation effects). This enables to clearly study the amount of attitude and shape/size information present in the light curve.

Given the notion that the true state is sufficiently close to the estimated state, the dynamics of the system can be well approximated by a linearization using a first-order Taylor series expansion. The nonlinear governing equations of motion and measurement models are shown in Equation (6.20). The linearization is done about a nominal state  $\bar{\mathbf{x}}_k$ , where the measurement is  $\tilde{\mathbf{y}}_k$ .

$$\begin{aligned}\mathbf{x}_{k+1} &= \mathbf{f}(\mathbf{x}_k, k) \\ \tilde{\mathbf{y}}_k &= \mathbf{h}(\mathbf{x}_k, k)\end{aligned}\tag{6.20}$$

The first order expansions of  $\mathbf{f}(\mathbf{x}_k, k)$  and  $\mathbf{h}(\mathbf{x}_k, k)$  about the nominal state are as follows:

$$\mathbf{f}(\mathbf{x}_k, k) \cong \mathbf{f}(\bar{\mathbf{x}}_k, k) + \left. \frac{\partial \mathbf{f}}{\partial \mathbf{x}} \right|_{\bar{\mathbf{x}}_k} (\mathbf{x}_k - \bar{\mathbf{x}}_k)\tag{6.21}$$

$$\mathbf{h}(\mathbf{x}_k, k) \cong \mathbf{h}(\bar{\mathbf{x}}_k, k) + \left. \frac{\partial \mathbf{h}}{\partial \mathbf{x}} \right|_{\bar{\mathbf{x}}_k} (\mathbf{x}_k - \bar{\mathbf{x}}_k)\tag{6.22}$$

The system Jacobian  $\mathbf{F}(\bar{\mathbf{x}}_k, k)$  is obtained numerically. The measurement Jacobian  $\mathbf{H}(\bar{\mathbf{x}}_k, k)$  (also denoted the observation matrix) is obtained as described in the subsequent sections.

$$\mathbf{F}(\bar{\mathbf{x}}_k, k) \equiv \left. \frac{\partial \mathbf{f}}{\partial \mathbf{x}} \right|_{\bar{\mathbf{x}}_k}\tag{6.23}$$

$$\mathbf{H}(\bar{\mathbf{x}}_k, k) \equiv \left. \frac{\partial \mathbf{h}}{\partial \mathbf{x}} \right|_{\bar{\mathbf{x}}_k}\tag{6.24}$$

### 6.4.1 Numerical Observation Matrix

It can be seen from the light curve model described in section 4.2 that an analytical calculation of the observation matrix is impractical. Rather a numerical approximation is utilized to obtain the measurement Jacobian with respect to the state variables. The numerical Jacobian is computed by perturbing the state vector, one component at a time, to obtain one row of the measurement Jacobian matrix.

$$\frac{\partial \tilde{y}_k}{\partial x_i} \approx \frac{\tilde{y}(\mathbf{x}_k + \Delta x_i) - \tilde{y}(\mathbf{x}_k)}{\Delta x_i} \quad i = 1, 2, \dots, n \quad (6.25)$$

where  $\mathbf{x} = [x_1, x_2, \dots, x_n]$ . Then the numerical Jacobian can be defined as

$$\mathbf{H}_N(\mathbf{x}_k) \equiv \left[ \frac{\partial \tilde{y}_k}{\partial x_1} \quad \frac{\partial \tilde{y}_k}{\partial x_2} \quad \dots \quad \frac{\partial \tilde{y}_k}{\partial x_n} \right] \quad (6.26)$$

### 6.4.2 Unscented Kalman Filter Derived Observation Matrix

The observation matrix can also be inferred from the the unscented Kalman filter (UKF) formulation as shown in chapter 5. Using the cross-covariance matrix between the states  $\mathbf{x}_k$  and the measurement  $\tilde{\mathbf{y}}_k$  and the state covariance matrix as defined in the UKF derivation in Equation (5.21),

$$\mathbf{P}_{xy} = E \{ \mathbf{x}_k \tilde{\mathbf{y}}_k^T \} \quad (6.27)$$

where  $E \{ \}$  denotes the expectation operator. For a linear system the measurements can be modeled as  $\tilde{\mathbf{y}}_k = \mathbf{H}\mathbf{x}_k$  so that

$$\begin{aligned} \mathbf{P}_{xy} &= E \{ \mathbf{x}_k (\mathbf{H}\mathbf{x}_k)^T \} \\ &= E \{ \mathbf{x}_k \mathbf{x}_k^T \} \mathbf{H}^T \\ &= \mathbf{P}_k \mathbf{H}^T \end{aligned} \quad (6.28)$$

where  $E \{ \mathbf{H}(\bar{\mathbf{x}}_k, k) \} = \mathbf{H}(\bar{\mathbf{x}}_k, k)$  and  $E \{ \mathbf{x}_k \mathbf{x}_k^T \} = \mathbf{P}_k$ . Thus the observation matrix can be inferred from the UKF formulation as

$$\mathbf{H}_{UKF}(\mathbf{x}_k) \equiv (\mathbf{P}_k^{-1} \mathbf{P}_{xy})^T \quad (6.29)$$

To study the filter performance, as well as, the observability of the states, the observation matrices obtained via the numerical approximation and the UKF are compared.

#### 6.4.3 Error Analysis and Observability Gramian

To study the filter performance as well as the observability of the states, the observation matrices obtained via the numerical approximation and the UKF are compared. In order to better assess the sensitivity results the error parameter shown in the equation below will be used to determine whether the UKF derived observation matrix and the numerically derived Jacobian carry the same information. If  $\epsilon$  is close to one, this means the values for both matrices are the same. As the value decreases the information the matrices carry differs.

$$\epsilon = \frac{\mathbf{H}_{NUM}\mathbf{H}_{UKF}^T}{\|\mathbf{H}_{NUM}\|\|\mathbf{H}_{UKF}\|} \quad (6.30)$$

In addition to the error parameter, the observability Gramian is utilized to assess the information carried by the numerical and UKF observation matrix. The observability Gramian for a linear system is defined as shown in Equation (6.31). It is assumed that at each discrete point in time  $t_k$ , the measurement matrix is approximated by the observation matrix,  $\mathbf{C}(t_k) \approx \mathbf{H}(t_k)$ . Moreover,  $\mathbf{A}(t)$  is taken to be the system Jacobian  $\mathbf{F}$  defined in Equation (6.23). Consequently, the Gramian for the numerical observation matrix is denoted  $\mathbf{W}_{NUM}$  and the Gramian for the UKF observation matrix is denoted  $\mathbf{W}_{UKF}$ . The rank of the Gramian indicates how many states and parameters are observable.

$$\mathbf{W}(0, t_f) = \int_0^{t_f} \exp^{\mathbf{A}(t)^T t} \mathbf{C}(t)^T \mathbf{C}(t) \exp^{\mathbf{A}(t)t} dt \quad (6.31)$$

## 6.5 Observability Analysis

This analysis will focus on the observability of the MRPs ( $\mathbf{g}$ ) and the shape/size parameters ( $\mathbf{p}$ ) with respect to light curve measurement. To apply the methodology outlined in references [39, 41] we first linearize the system dynamics to obtain the system Jacobian as shown in Equation (6.21)-(6.24).  $\delta\mathbf{x}_k = \mathbf{x}_k - \bar{\mathbf{x}}_k$  and  $\delta\mathbf{y}_k = \mathbf{y}_k - \bar{\mathbf{y}}_k$  are defined as small perturbations for the state and measurement respectively. A segment of time  $j$  is defined, where  $n$  measurements are collected.  $\bar{\mathbf{x}}_k$  denotes the nominal state, which is considered to be the estimated state at time  $k$ .

$$\begin{aligned}\delta\mathbf{x}_{k+1} &= \mathbf{F}(\bar{\mathbf{x}}_k)\delta\mathbf{x}_k \\ \delta\tilde{\mathbf{y}}_{j,k} &= \mathbf{H}(\bar{\mathbf{x}}_k)\delta\mathbf{x}_k\end{aligned}\tag{6.32}$$

The obtained measurements can be expressed as a function of  $\delta\mathbf{x}_1$  as follows

$$\begin{aligned}\delta\tilde{\mathbf{y}}_{j,1} &= \mathbf{H}(\bar{\mathbf{x}}_1)\delta\mathbf{x}_1 \\ \delta\tilde{\mathbf{y}}_{j,2} &= \mathbf{H}(\bar{\mathbf{x}}_2)\mathbf{F}(\bar{\mathbf{x}}_1)\delta\mathbf{x}_1 \\ \delta\tilde{\mathbf{y}}_{j,3} &= \mathbf{H}(\bar{\mathbf{x}}_3)\mathbf{F}(\bar{\mathbf{x}}_2)\mathbf{F}(\bar{\mathbf{x}}_1)\delta\mathbf{x}_1 \\ &\vdots \\ \delta\tilde{\mathbf{y}}_{j,n} &= \mathbf{H}(\bar{\mathbf{x}}_n)\mathbf{F}(\bar{\mathbf{x}}_{n-1})\mathbf{F}(\bar{\mathbf{x}}_{n-2})\dots\mathbf{F}(\bar{\mathbf{x}}_1)\delta\mathbf{x}_1\end{aligned}\tag{6.33}$$

This can be written in matrix form as

$$\tilde{\mathbf{Y}}_j = \mathbf{Q}_j\delta\mathbf{x}_1\tag{6.34}$$

where  $\tilde{\mathbf{Y}}_j = [\delta\tilde{\mathbf{y}}_{j,1}^T, \delta\tilde{\mathbf{y}}_{j,2}^T, \dots, \delta\tilde{\mathbf{y}}_{j,n}^T]^T$  and

$$\mathbf{Q}_j = \begin{bmatrix} \mathbf{H}(\bar{\mathbf{x}}_1) \\ \mathbf{H}(\bar{\mathbf{x}}_2)\mathbf{F}(\bar{\mathbf{x}}_1) \\ \mathbf{H}(\bar{\mathbf{x}}_3)\mathbf{F}(\bar{\mathbf{x}}_2)\mathbf{F}(\bar{\mathbf{x}}_1) \\ \vdots \\ \mathbf{H}(\bar{\mathbf{x}}_n)\mathbf{F}(\bar{\mathbf{x}}_{n-1})\mathbf{F}(\bar{\mathbf{x}}_{n-2}) \dots \mathbf{F}(\bar{\mathbf{x}}_1) \end{bmatrix} \quad (6.35)$$

Now the single value decomposition (SVD) can be performed on the observability matrix  $\mathbf{Q}_j$  during the time segment  $j$  to asses the degree of observability of the state variables [40]. The SVD of the observability matrix is as follows:

$$\mathbf{Q}_j = \mathbf{U}\mathbf{\Sigma}\mathbf{V}^T = \sum_{i=1}^r \mathbf{u}_i s_i \mathbf{v}_i^T \quad (6.36)$$

where for any given  $\mathbf{Q}_j \in \mathfrak{R}^{p \times q}$  whose rank is  $r$  and  $p \geq q$  where the left singular vector matrix is  $\mathbf{U}_{p \times p} = [\mathbf{u}_1, \mathbf{u}_2, \dots, \mathbf{u}_p]$ , the right singular vector matrix is  $\mathbf{V}_{q \times q} = [\mathbf{v}_1, \mathbf{v}_2, \dots, \mathbf{v}_q]$ , and the singular value matrix is  $\mathbf{\Sigma} = \text{diag}(\mathbf{S}, 0)$ ,  $\mathbf{S} = [s_1, s_2, \dots, s_r]$ ,  $s_1 \geq s_2 \geq \dots, s_r$ . These singular values are related to the system's initial states. When the observation vector  $\tilde{\mathbf{Y}}_j$  has a constant norm, the initial state vector  $\bar{\mathbf{x}}_1$  of the given time segment is located in an ellipsoid in  $r$ -dimensions with equation as shown below:

$$|\tilde{\mathbf{Y}}_j|^2 = \sum_{i=1}^r (s_i \mathbf{v}_i^T \delta \mathbf{x}_1 \mathbf{u}_i)^2 \quad (6.37)$$

The length of each of the  $n$  axes of the ellipsoid is  $1/s_i$ . Consequently, a large singular value would indicate a smaller ellipsoid. In other words, the initial state variable has a small numeric area and a high observability. A small singular value indicates a large ellipsoid and a state variable with low observability. Furthermore, a singular value of zero indicates the state variable is unobservable. Figure 6.1 depicts the ellipsoid for a three dimensional vector, where the second variable has a small singular value

and consequently a larger axis and a smaller observability. On the contrary, the second variable with axis  $1/s_1$  has a larger singular value, a smaller axis, and larger observability.

The observability degree of a state variable is defined as the singular value related to that state variable. The singular value of a state variable is the one that makes the state variable maximum. As in reference [40], if one of the components of the state vector related to the singular value is larger than the other components, this particular singular value is the observability degree of the state variable on the corresponding component of the state vector. The state vector related to the singular value  $s_i$  is shown below.

$$\mathbf{x}_{s,i} = \frac{\mathbf{u}_i^T \tilde{\mathbf{Y}}_j \mathbf{v}_i^T}{s_i} \quad (6.38)$$

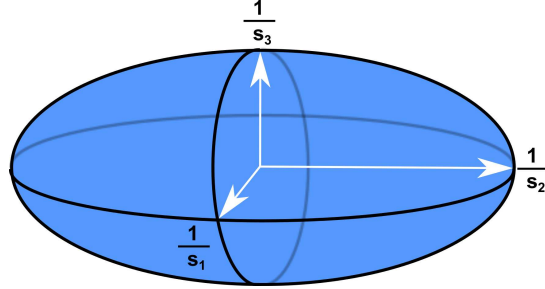


Figure 6.1. Depiction of Observability Degree for a Three Dimensional Vector.

## 6.6 Sensitivity and Observability Results

Two cases were performed for the observability and sensitivity analyses. Case 1 begins with the object body frame and the ECI frame aligned, as the object rotates about the x-axis only, the observer can only see the face in the yz-plane. Case 2 on the other hand, begins with the object tilted, where three faces are visible to the

observer. Both cases have the same initial position, velocity, and angular velocity for the resident space object. The dimensions of the object are the same for both cases. Table 6.3 below show the chosen initial conditions.

Table 6.3. Initial Conditions for Sensitivity and Observability Analysis

State/Parameter		(unit)	Initial Value
Position	$\mathbf{r}_0$	( <i>km</i> )	$[6737 \ 0 \ 0]^T$
Velocity	$\mathbf{v}_0$	( <i>km/s</i> )	$[0 \ 7.4293 \ 1.9907]^T$
Angular Velocity	$\boldsymbol{\omega}$	( <i>rad/s</i> )	$[0.00524 \ 0 \ 0]^T$
Attitude			
(Case 1)	$\mathbf{q}_0$		$[0 \ 0 \ 0 \ 1]^T$
	$[\phi_0 \ \theta_0 \ \psi_0]$	( <i>deg</i> )	$[0 \ 0 \ 0]^T$
(Case 2)	$\mathbf{q}_0$		$[0.23929 \ 0.18930 \ 0.03813 \ 0.95154]^T$
	$[\phi_0 \ \theta_0 \ \psi_0]$	( <i>deg</i> )	$[30 \ 20 \ 10]^T$
Shape/Size	$\mathbf{p}_0$	( <i>m</i> )	$[5 \ 3 \ 4]^T$

Each of the BRDF models were implemented into the light curve model. In addition, both cases were produced for each reflectance model. This was done to evaluate the individual performance of each of the models on a low observability case 1 and a higher observability case 2.

Figure 6.2 shows a comparison of the specular component for all the models for case 1. Because the observer can only see one face of the object, the specular component is zero, as only diffusive light is visible. Figure 6.4 shows the diffusive component for all models for case 1. The behavior of this component is very similar for all cases. This is expected, as the same model was used for the diffusive component, only the material parameters changed from one model to another. Figure 6.6 shows the resulting light curve magnitude. The light curve for all the models remains close

to constant. This is a consequence of the object's visibility remaining constant as it is observed.

Results for the second case are shown in Figures 6.3, 6.5, and 6.7. The specular component exhibits higher peaks as the object rotates. The Cook-Torrance and Ashikhmin-Shirley models exhibit large peaks, while Ward-Dürer and Ward exhibit small peaks. The He model exhibits a square wave, rather than a smooth curve. Lafortune and Blinn-Phong exhibit very little change. The diffuse component is very similar to the first case. This is to be expected, as the value of this component does not depend upon the geometry of the observation. Moreover, the light curve magnitude for the second case shows defined peaks for those models which also showed peaks in the specular component. The light curve exhibits a smoother behavior for the models which did not produce specular peaks.

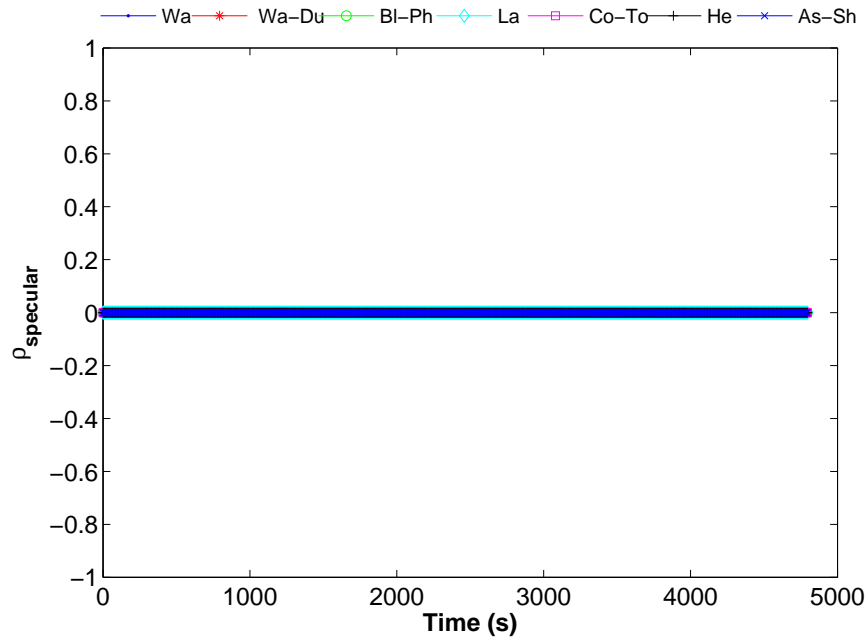


Figure 6.2. Specular Component of Light for Case 1.

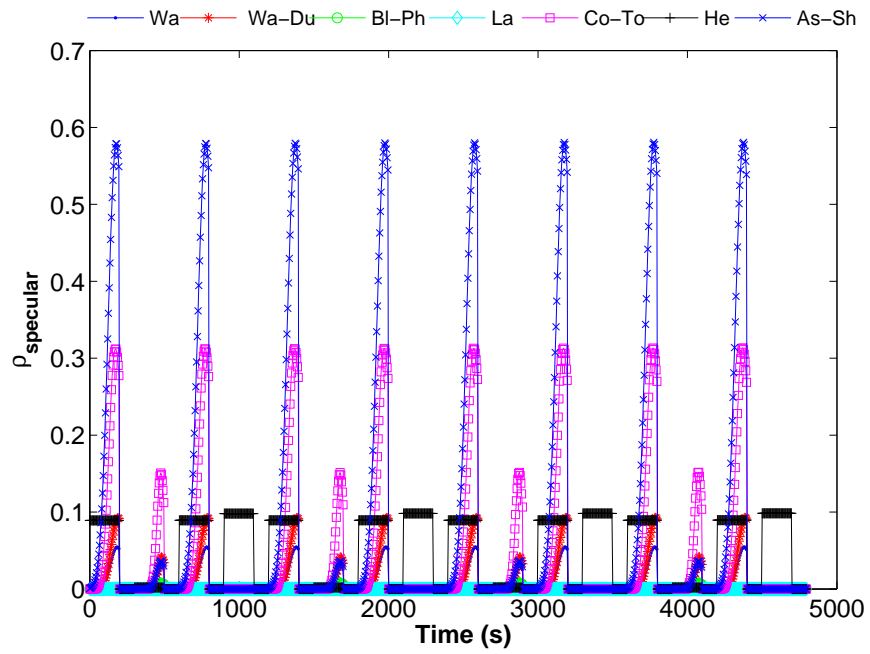


Figure 6.3. Specular Component of Light for Case 2.

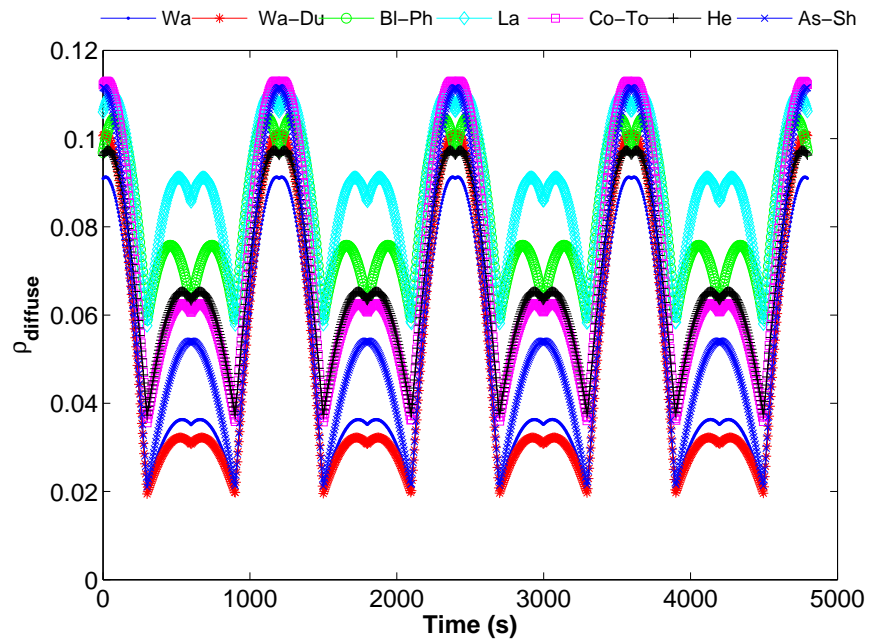


Figure 6.4. Diffuse Component of Light for Case 1.

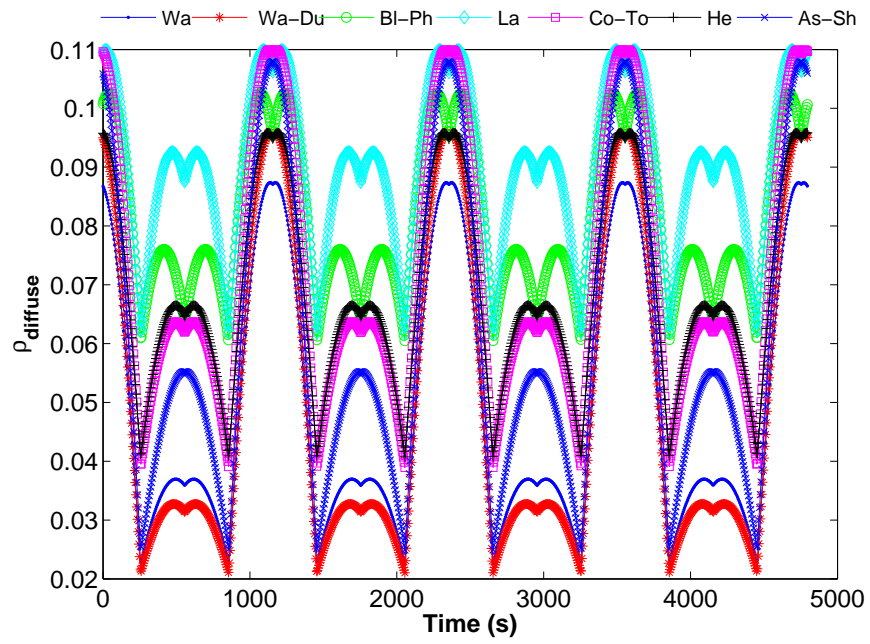


Figure 6.5. Diffuse Component of Light for Case 2.

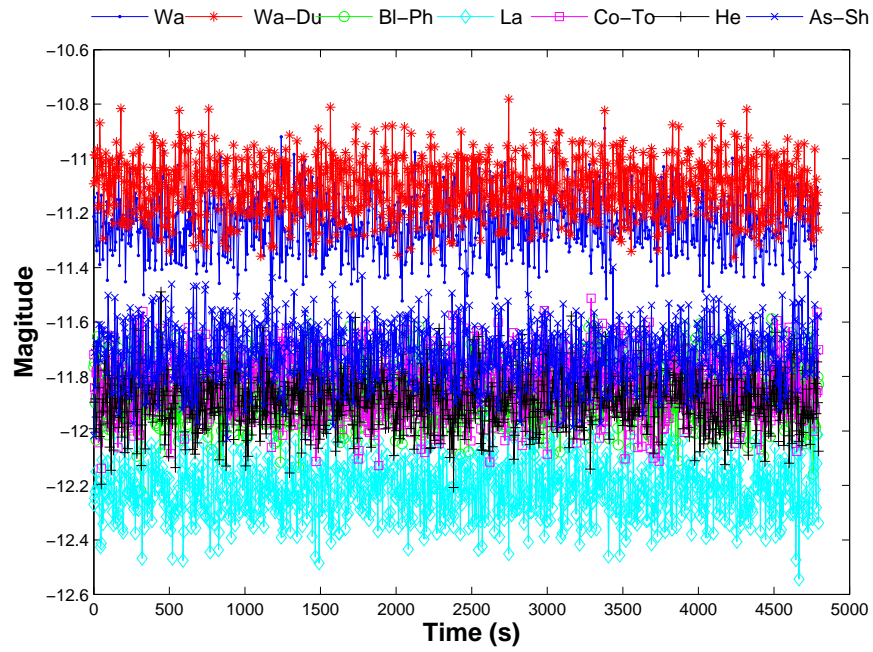


Figure 6.6. Magnitude of Light for Case 1.

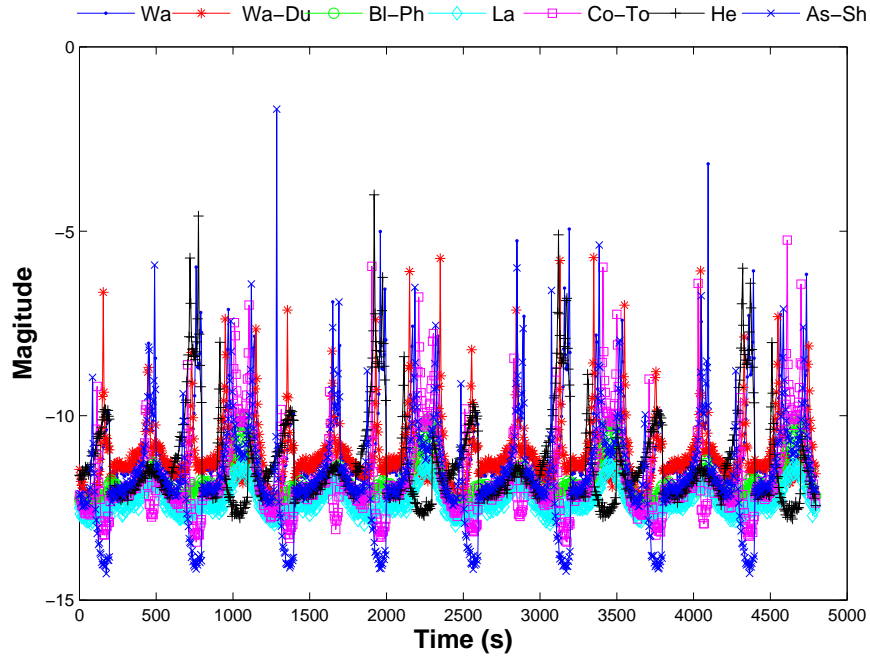


Figure 6.7. Magnitude of Light for Case 2.

The sensitivity analysis is performed by calculating the numerically computed Jacobian, denoted  $\mathbf{H}_{NUM}$ , and the UKF derived observation matrix, denoted  $\mathbf{H}_{UKF}$ . These matrices will show whether a measurement is sensitive to the change of a state. It will also show whether the numerical Jacobian and the UKF observation matrix carry the same information. For this analysis the sensitivity of the light curve will be analyzed with respect to the angular velocity, attitude, and shape/size parameters. This analysis was performed for the cases mentioned in the previous section and for each of the models presented in Appendix A.

Figures A.1, A.6, A.11, A.16, A.21, A.26, and A.31 in Appendix A, compare the obtained observation matrices for the angular velocity state for both cases. For brevity, only results for Ward and Cook-Torrance are shown in this section in Figures 6.8 and 6.11 for both cases. These figures show the sensitivity of the angular velocity with respect to the light curve measurement. It can be seen that the numer-

ical Jacobian produces no sensitivity to the angular velocity state. Nevertheless, the UKF derived observation matrix is highly sensitive to this state. The same behavior is observed for the other models as shown in the above mentioned figures. This is a clear indication that the information regarding this state does not improve with any of the models. Consequently, it is safe to assume that this measurement does not carry any information regarding angular velocity, as the values for  $\mathbf{H}_{NUM}$  remain zero for all cases. Nevertheless, the  $\mathbf{H}_{UKF}$  values clearly show there is some information. This can only be a consequence of the information the UKF obtains from the rotational dynamics model. This reinforces the notion that there is no information about the angular velocity regardless of the position of the object or reflectance model.

The error parameter results for the attitude and shape/size parameter are shown in Figure 6.14 and 6.15. The observation matrix results for these states and parameters for all models are shown in Appendix A in Figures A.2, A.7, A.12, A.17, A.22, A.27, and A.32 for the attitude and in Figures A.3, A.8, A.13, A.18, A.23, A.28, and A.33 for the shape/size parameters. The the results for the Ward and Cook-Torrance are shown in this section. As shown in Figure 6.9 and 6.10, the Ward model shows little information for case 1 for the attitude and shape/size for  $\mathbf{H}_{NUM}$  or  $\mathbf{H}_{UKF}$ . On the contrary, there is significantly more information carried in the  $\mathbf{H}_{NUM}$  and slightly more information in  $\mathbf{H}_{UKF}$  for case 2. This behavior is observed in the Ward-Dür, Cook-Torrance, Ashikhmin-Shirley, and He models. Nevertheless, the error parameter for these models shows that less than 60% of the points coincide for the two observation matrices. This is an indication that the error parameter should not be taken as a measurement of ‘quality’ of information but rather whether the information is the same for both matrices. Another example of this behavior are the results for the Lafortune model. This model shows little information for the attitude or shape/size parameter for either case and either matrix. However, the error pa-

parameter shows that the observation matrices coincide in their values (which are both close to zero for both cases as shown in Figures A.17 and A.18). The behavior of the Blinn-Phong is very similar to the Lafortune model as shown in Figure A.12 and A.13. It should be noted that the error parameter should only be used as an aid when analyzing the data of the observation matrices. In addition, the models that have shown to carry the most information for case 2 are the Cook-Torrance, He, and Ashikhmin-Shirley as shown in Figures A.22, A.27, and A.32 for the attitude and Figures A.23, A.28, and A.33 for the shape/size parameters.

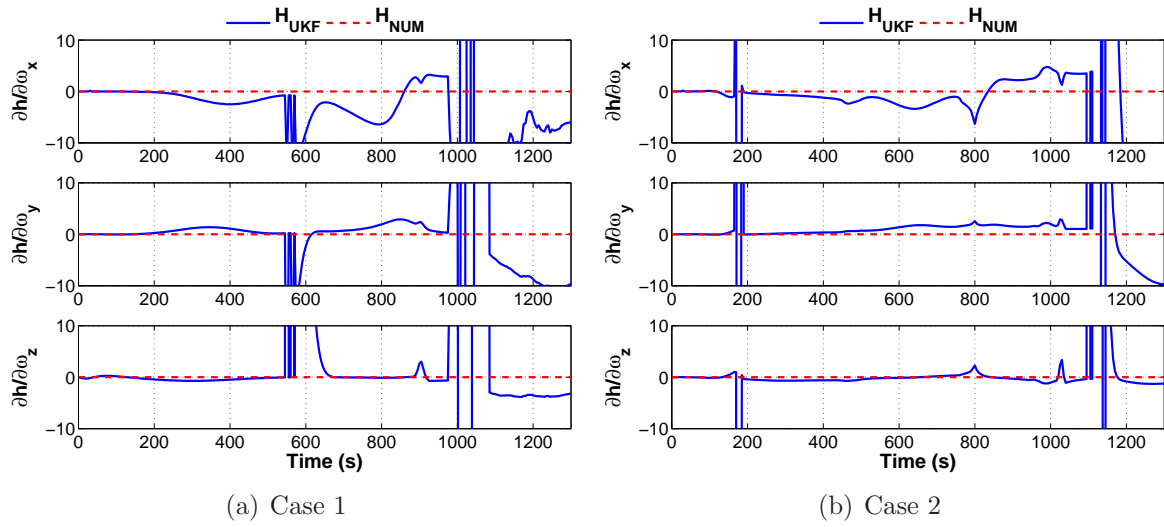


Figure 6.8. Ward Model Angular Velocity Sensitivity.

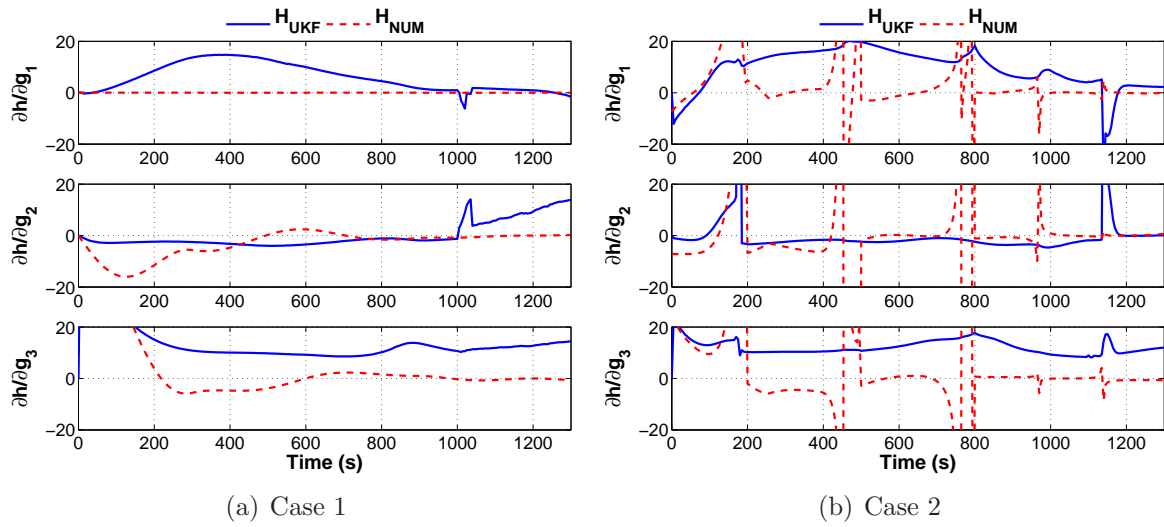


Figure 6.9. Ward Model Attitude Sensitivity.

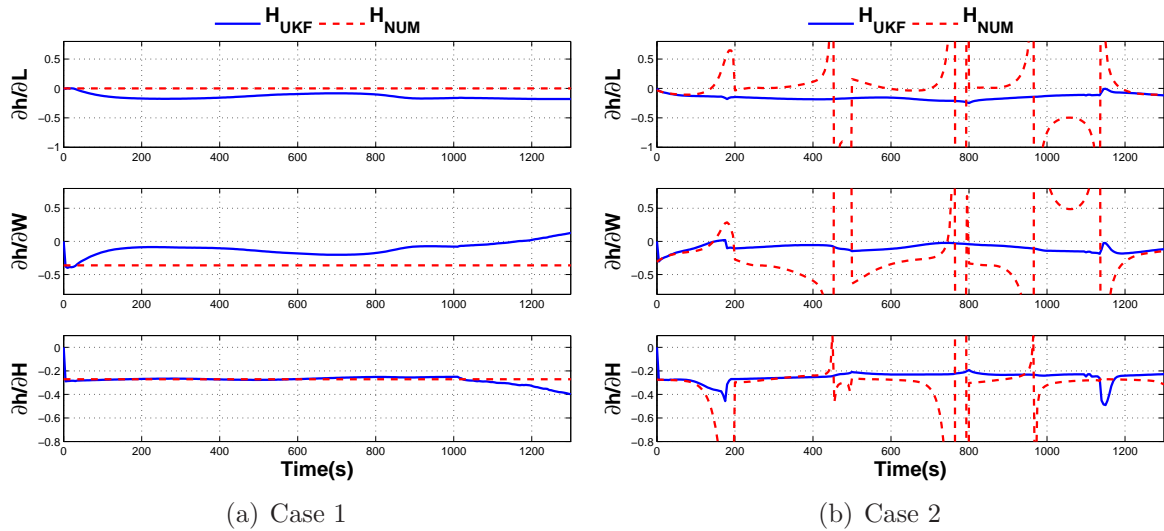


Figure 6.10. Ward Model Shape/Size Parameters Sensitivity.

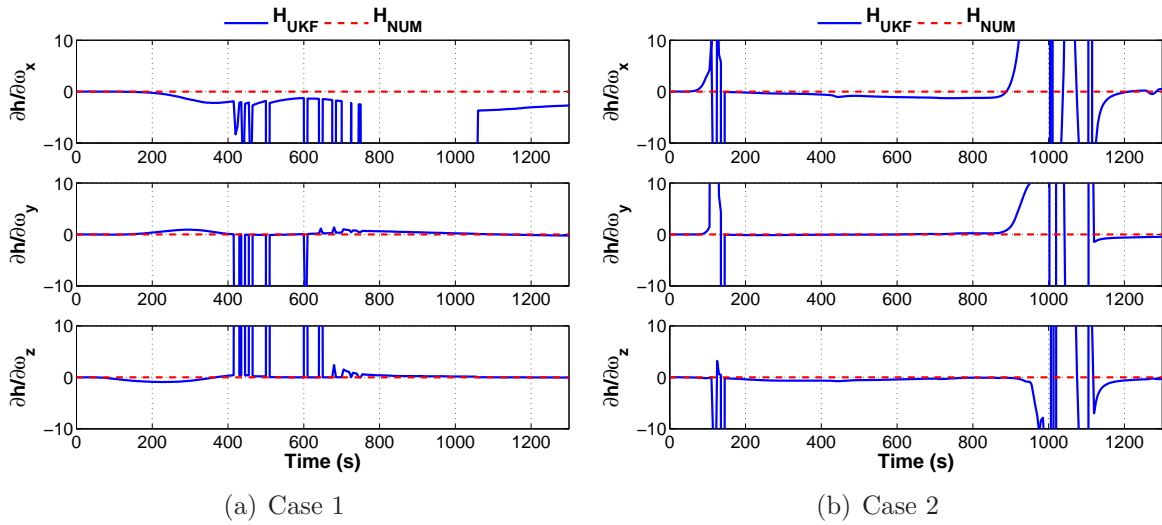


Figure 6.11. Cook-Torrance Model Angular Velocity Sensitivity.

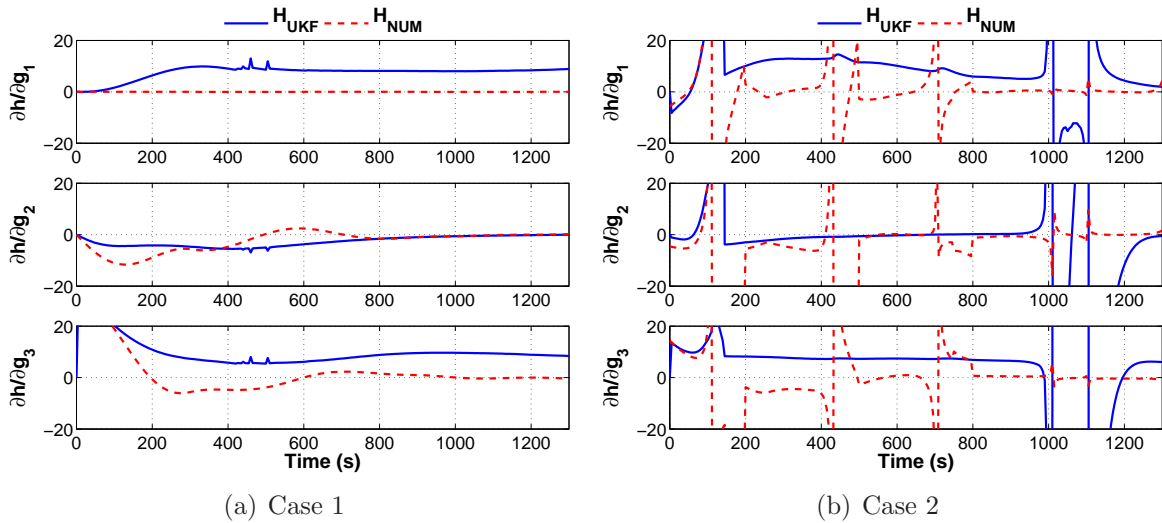


Figure 6.12. Cook-Torrance Model Attitude Sensitivity.

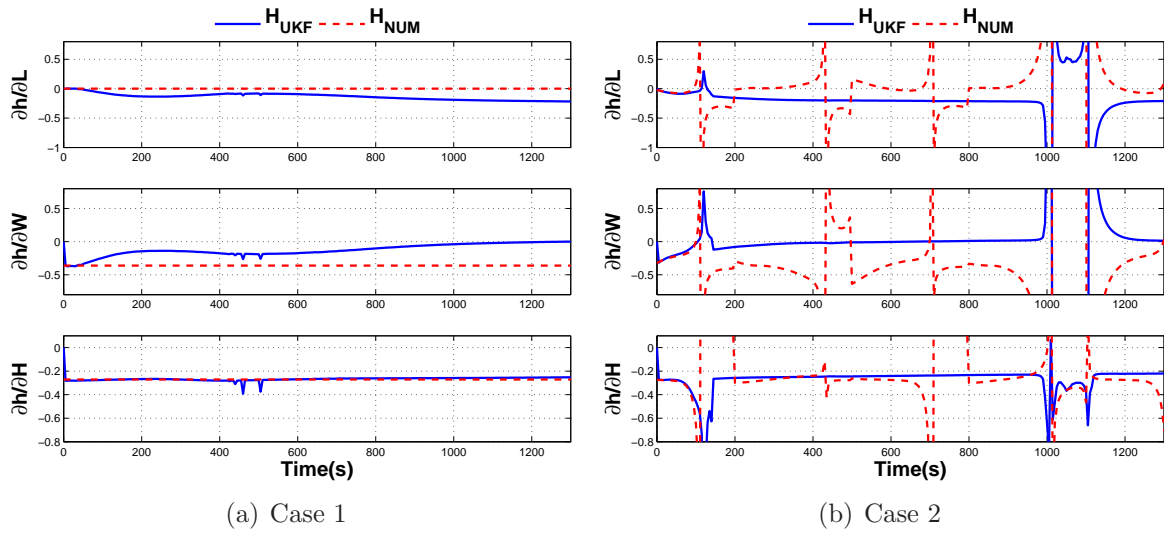


Figure 6.13. Cook-Torrance Model Shape/Size Parameters Sensitivity.

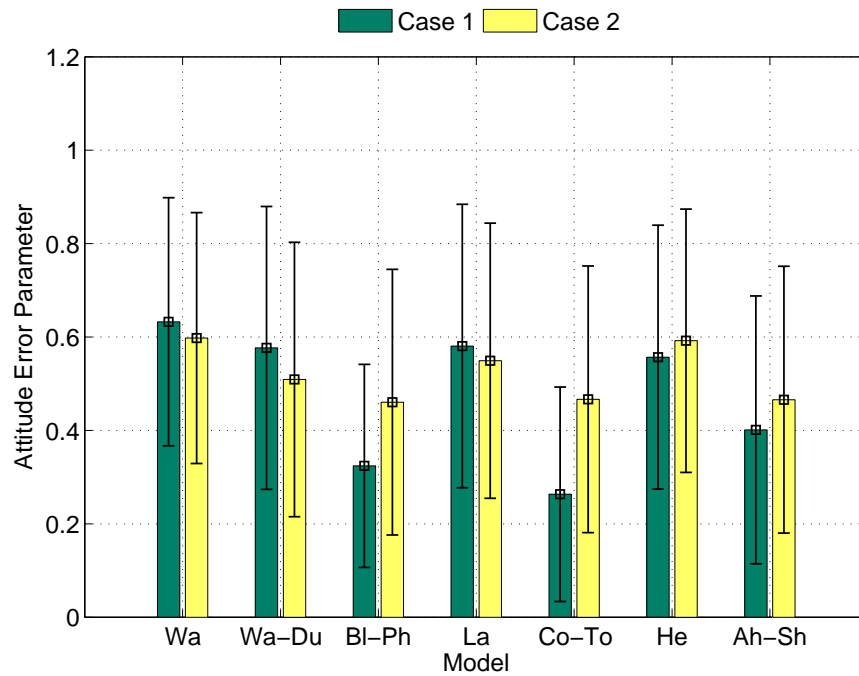


Figure 6.14. Error Parameter for Attitude.

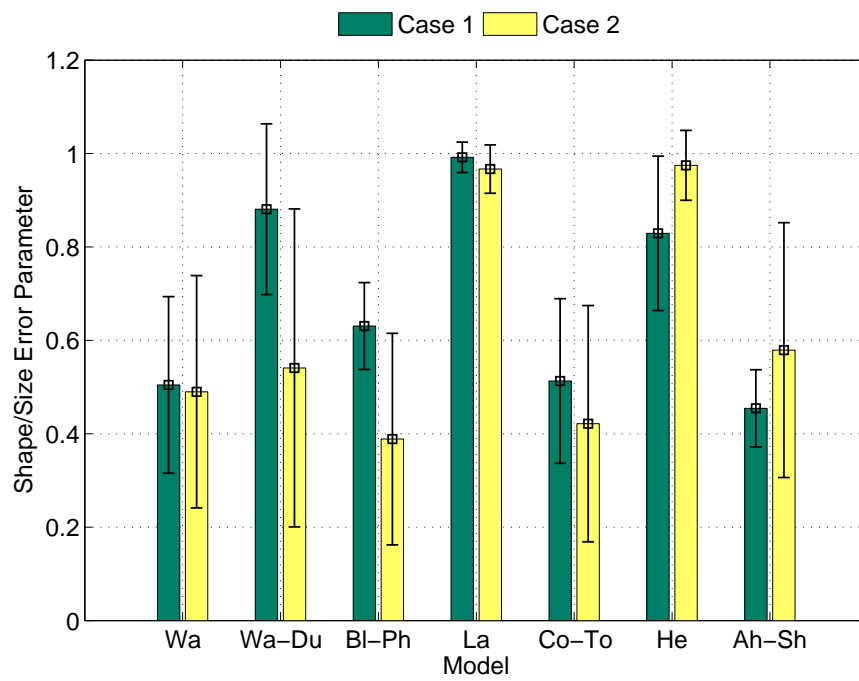


Figure 6.15. Error Parameter for Shape/Size Parameter.

The Gramian was calculated for both the numerical and UKF observation matrices for all cases. Only the results for the Ward and Cook-Torrance are shown in this section, the plots for the rest of the models are shown in Appendix A in Figures A.4, A.9, A.14, A.19, A.24, A.29, and A.34 for the numerical based Gramian and Figures A.5, A.10, A.15, A.20, A.25, A.30, and A.35 for the UKF based Gramian. These plots show the Gramian, along with, the attitude MPRs and the light curve measurement. The x-axis shows the number of rotations of the object during the simulation.

The results of the Ward model for case 1 are shown in Figures 6.16 and 6.17. The Gramian maintains a rank of 2 regardless of the values for the attitude and the light curve. This indicates that there are only two states and/or parameters are observable for this case. Conversely, the Gramian changes from rank 2 to 3 for case 2. This jump happens when the information in the attitude and the information in the light curve change, close to the end of the first rotation and the third, where the peaks of the MPRs and the light curve coincide. Moreover, the results are nearly identical between the numerical and UKF matrices, except for some bouncing between rank 2 and 3 before the third rotation for case 2.  $\mathbf{H}_{NUM}$  has more of these jumps, which can be attributed to the numerical computation of this matrix. The higher rank for case 2 is consistent with the observer having a better view of the object as it rotates and the light curve being richer in information compared to case 1. Moreover, the results for the Cook-Torrance are nearly identical to those of the Ward model as shown in Figures 6.20 and 6.23. The same is true for the remaining model results as shown in Appendix A.

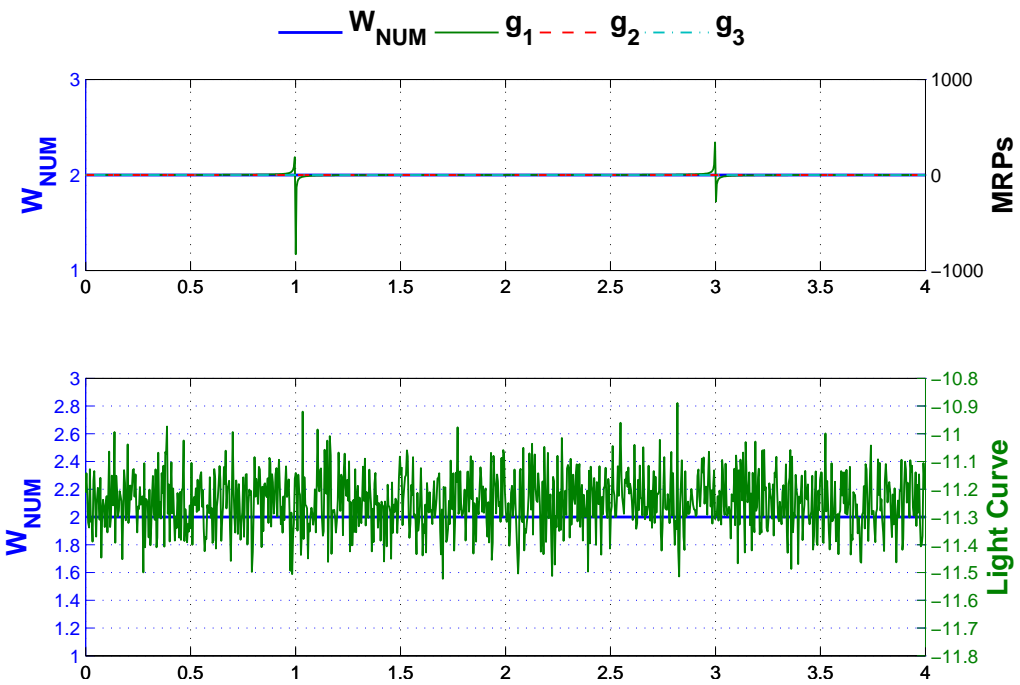


Figure 6.16. Ward Model Numerical based Gramian for Case 1.

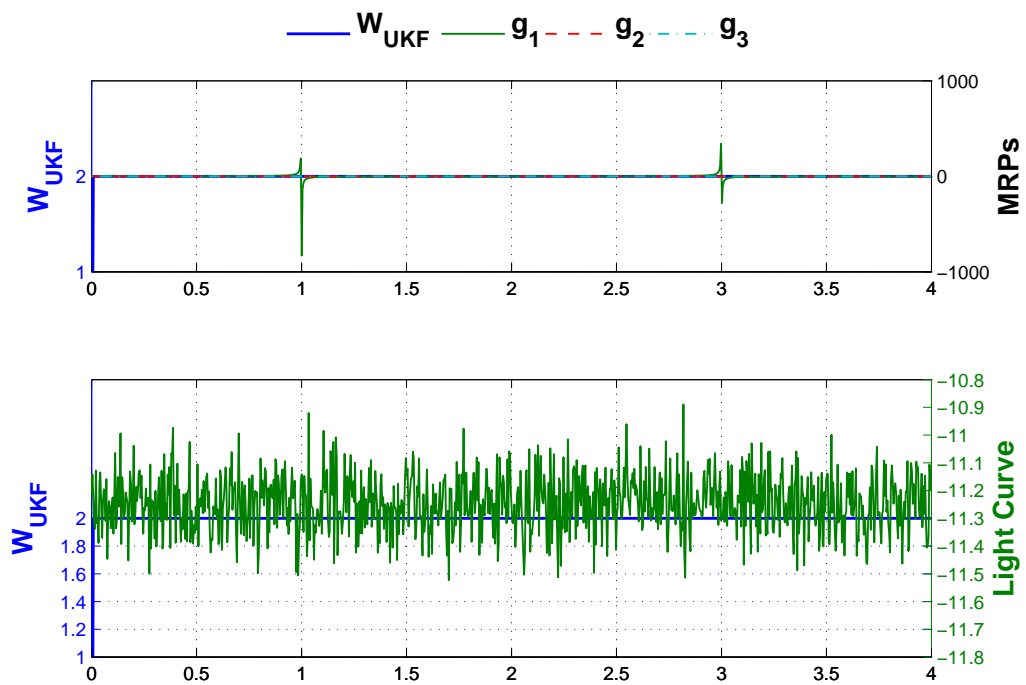


Figure 6.17. Ward Model UKF based Gramian for Case 1.

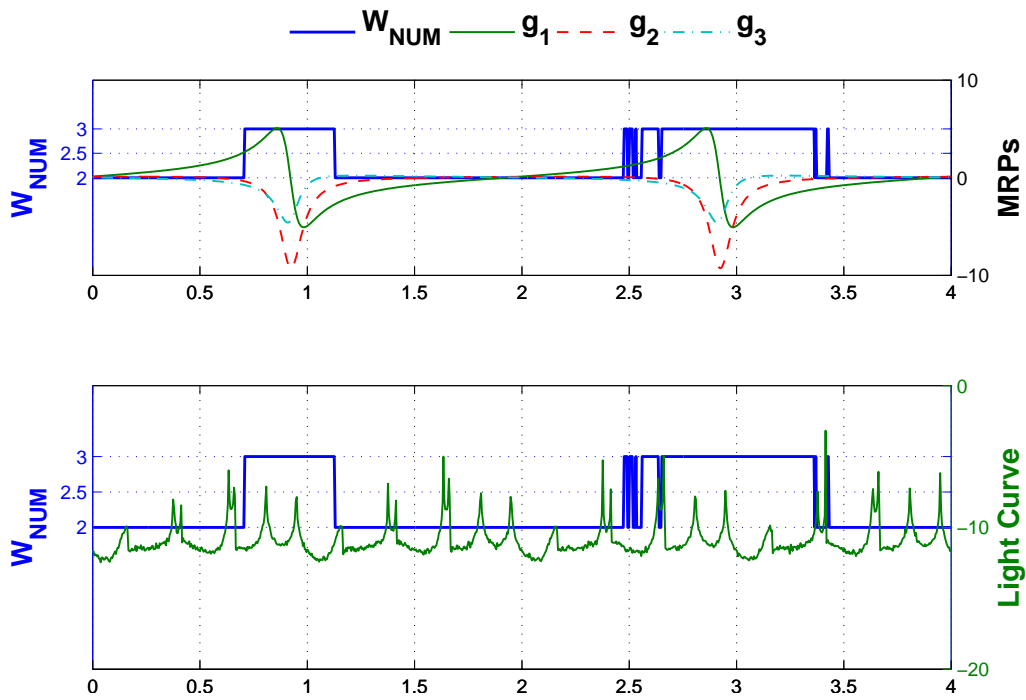


Figure 6.18. Ward Model Numerical based Gramian for Case 2.

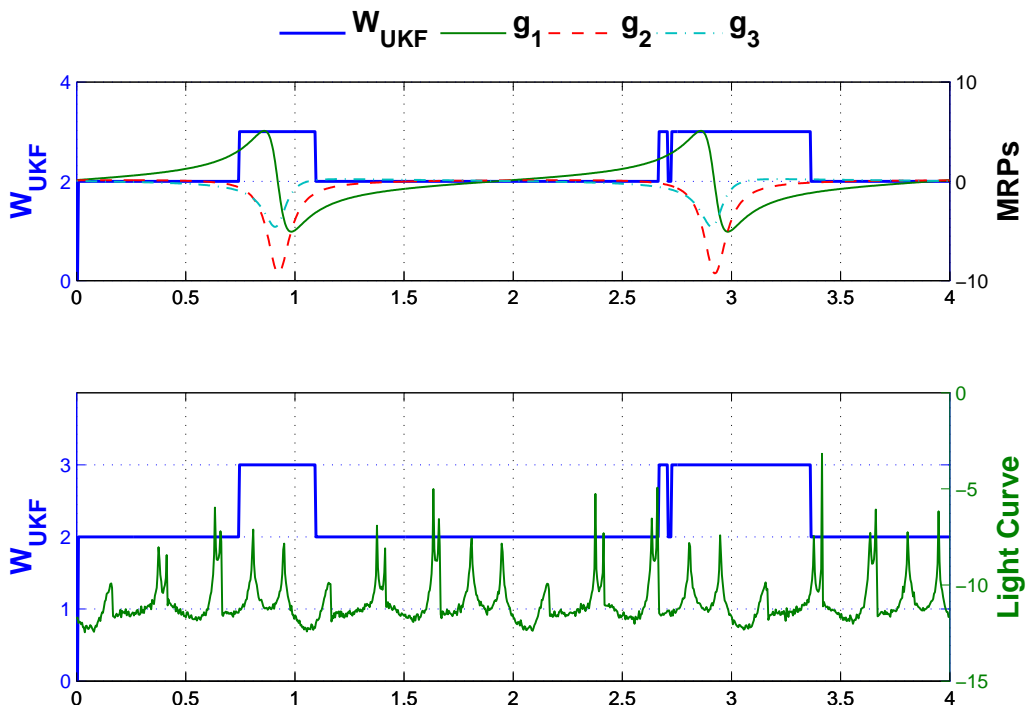


Figure 6.19. Ward Model UKF based Gramian for Case 2.

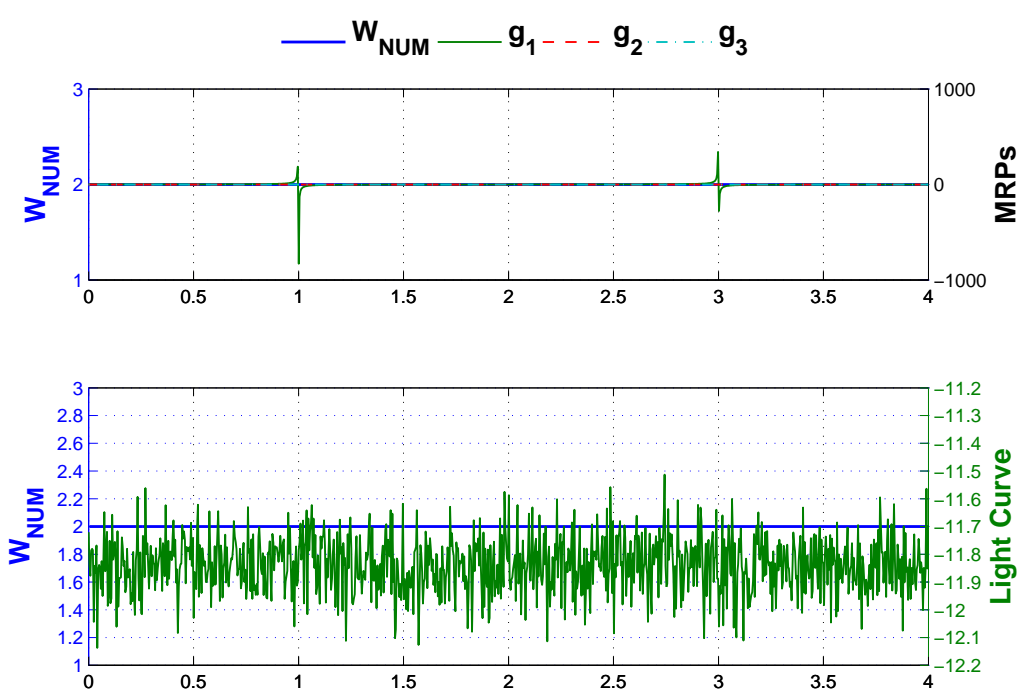


Figure 6.20. Cook-Torrance Model Numerical based Gramian for Case 1.

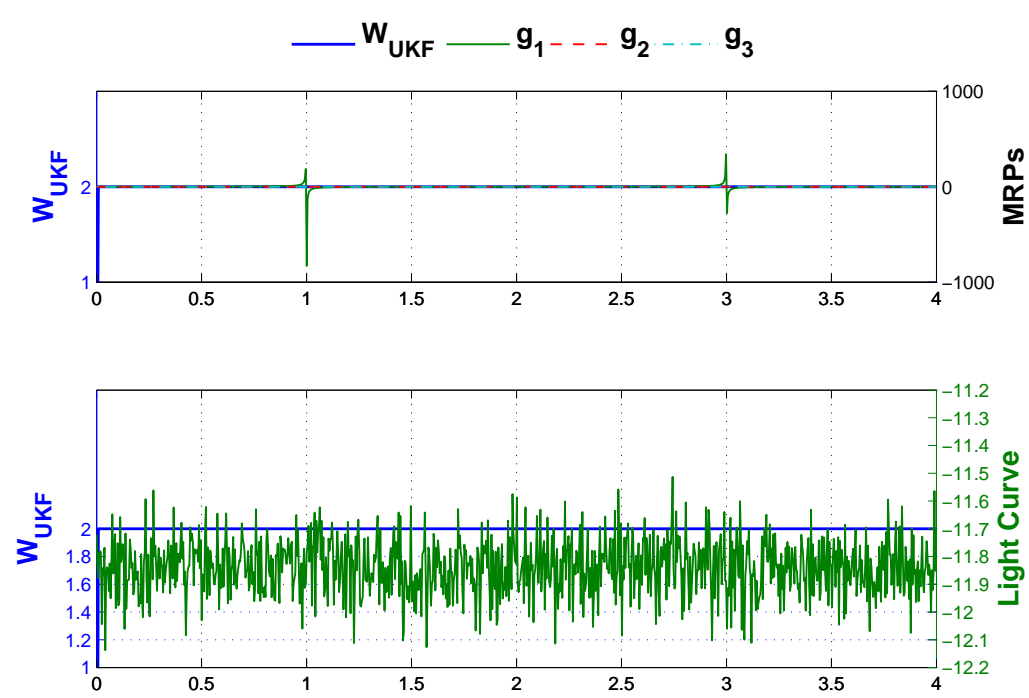


Figure 6.21. Cook-Torrance Model UKF based Gramian for Case 1.

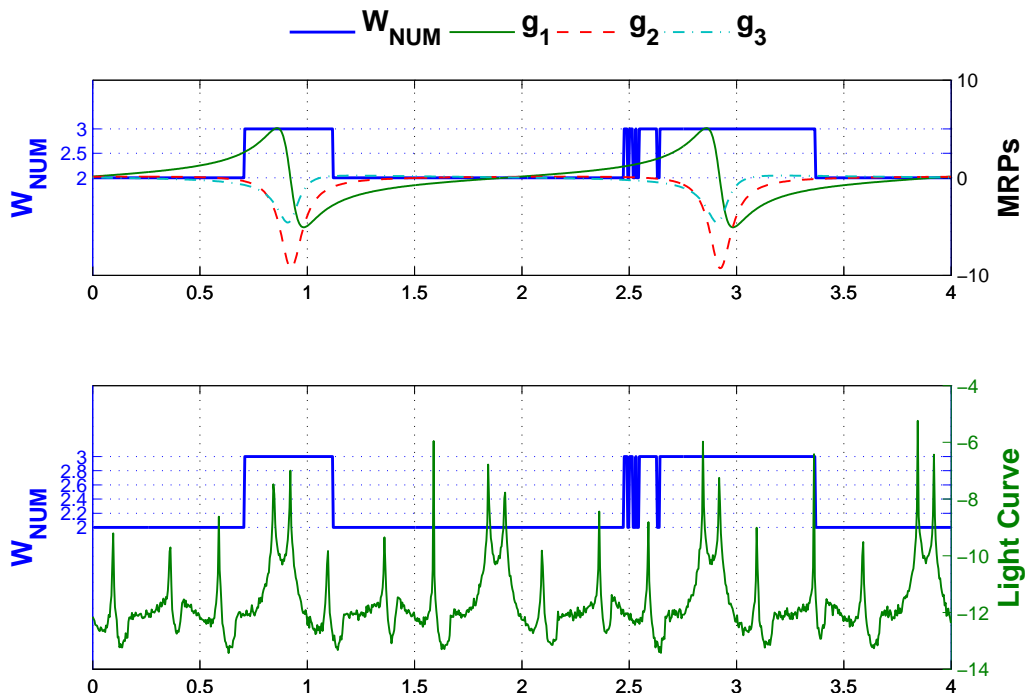


Figure 6.22. Cook-Torrance Model Numerical based Gramian for Case 2.

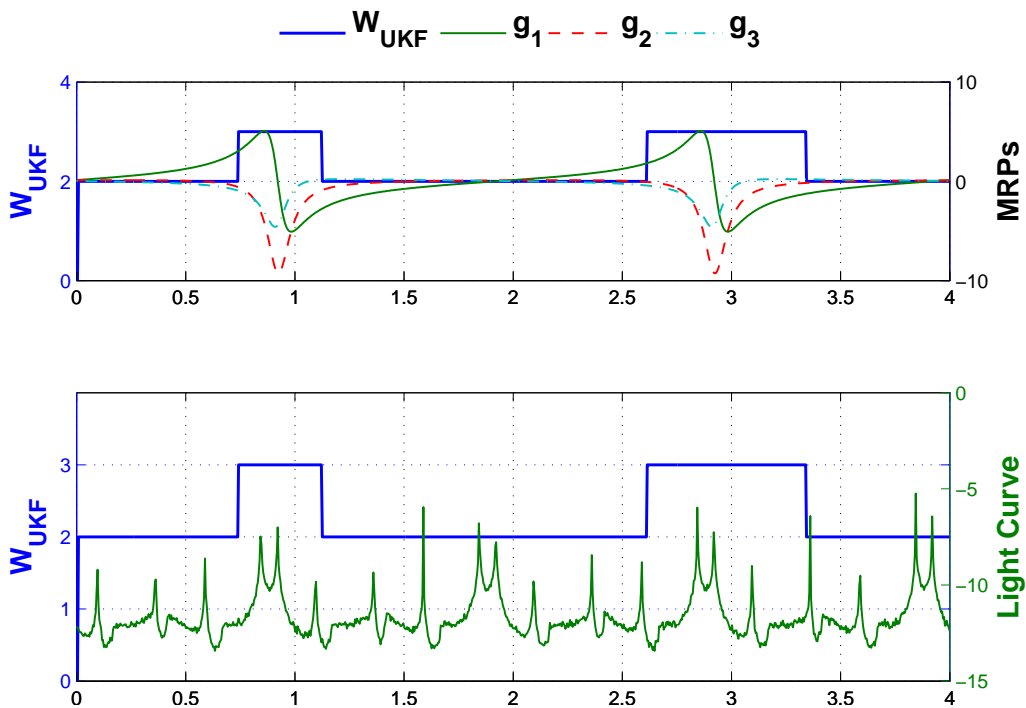


Figure 6.23. Cook-Torrance Model UKF based Gramian for Case 2.

For the observability analysis the same two cases mentioned at the beginning of this section are used. Both the attitude and shape/size parameters have been evaluated to obtain an observability degree as described in previous section. Given the results of the sensitivity analysis, which determined there is no information regarding the angular velocity in the light curve measurement, no observability analysis is performed for this state. Table 6.5 and 6.4 summarize the obtained observability degree for both cases and all states. Figures 6.24–6.27 show these same values in bar plots. The logarithmic scale has been used so that the greatly varying values are well displayed. The greater the value of the observability, the state or parameter is regarded as being more observable. If the observability degree for a state or parameter shows a zero, it is not observable.

The observability of the attitude for the first case, shows similar behavior for all models as seen in Figure 6.24. With only one of the MRP states having a large observability. This result is to be expected, as the observer has a limited view of the object as it orbits. The observer can only see one face of the object, and therefore determining attitude is very difficult. The observability of the shape/size for case 1 shows that for most models, only two parameters are visible as shown in Figure 6.26. The He model stands out as it has slightly larger observability values. Nevertheless, these values are significantly small, meaning the observability degree of these states is very low for all cases.

The observability values for the attitude for case 2 are significantly larger for all models and all three attitude parameters as shown in Figure 6.25. All models show a higher observability for all three attitude states. It should be noted that the Ward, Ward-Dür, Cook-Torrance, and Ashikhmin-Shirley models show the largest observability for all three states. The He model, although it shows a large observability for one state, has almost no observability for the last attitude parameter. Moreover,

the observability values for the shape/size parameters also improve for the second case. Only the Ward-Dür, Lafortune, Cook-Torrance, and He show observability for all three shape/size parameters. Nevertheless, the Cook-Torrance and Ward model show that the observability is larger when compared to the other models.

Table 6.4. Observability Results for Case 1

Model	$g_1$	$g_2$	$g_3$	$L$	$W$	$H$
Wa	10.416	0.65339	0.084212	0.018936	0.082608	0
Wa-Dü	7.1035	1.1373	0.054290	0.0054239	0.085041	0
Bl-Ph	19.359	0.19628	0.019130	0.0056528	0	0
La.	7.1111	0.12140	0.026330	0.016973	0	0
Co-To	13.742	0.27325	0.036670	0.0061527	0	0
He.	8.2358	0.20290	0.048711	0.021404	0.025973	0
As-Sh	13.691	0.32947	0.047498	0.0056414	0	0

Table 6.5. Observability Results for Case 2

Model	$g_1$	$g_2$	$g_3$	$L$	$W$	$H$
Wa	914.53	90.462	8.0650	0.62753	0.51546	0
Wa-Dü	403.52	7.2345	4.1746	0.18034	0.065995	0.057633
Bl-Ph	20.009	0.30492	0.048960	0.061122	0.021422	0
La.	16.135	0.087610	0.062459	0.047921	0.052074	0.00021999
Co-To	134.44	3.7042	2.0685	0.20721	0.092301	0.0056346
He	6503.9	29.258	0.079639	0.19235	0.013681	0.024759
As-Sh	1833.0	9.8100	3.5378	0.26654	0.42050	0

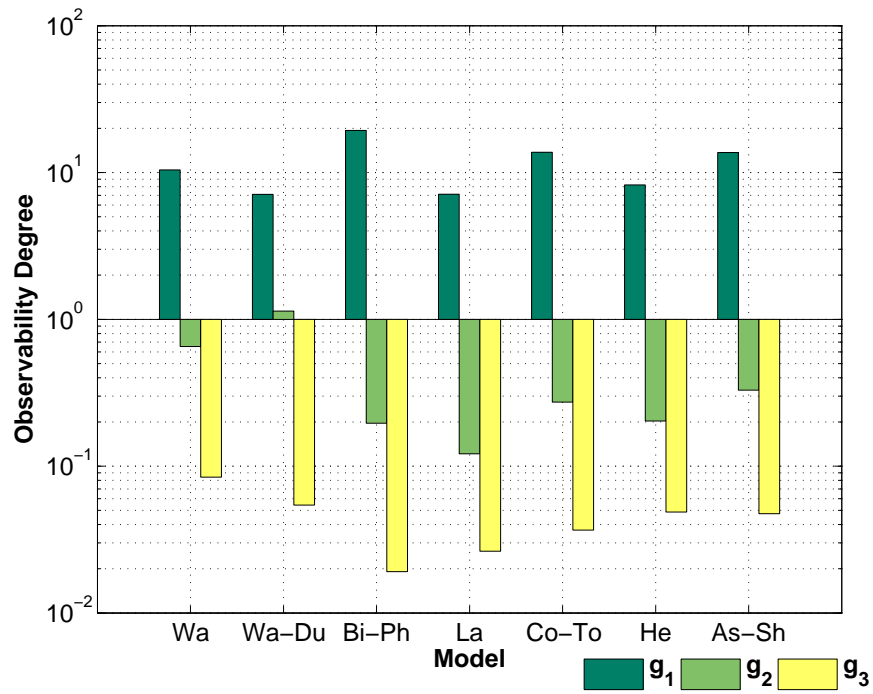


Figure 6.24. Observability Degree of Attitude States for Case 1.

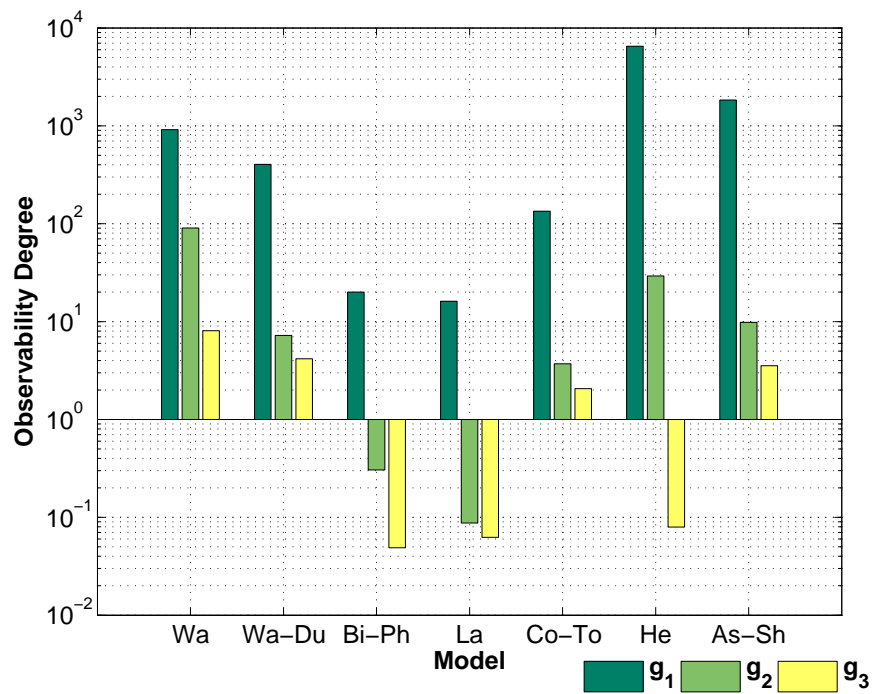


Figure 6.25. Observability Degree of Attitude States for Case 2.

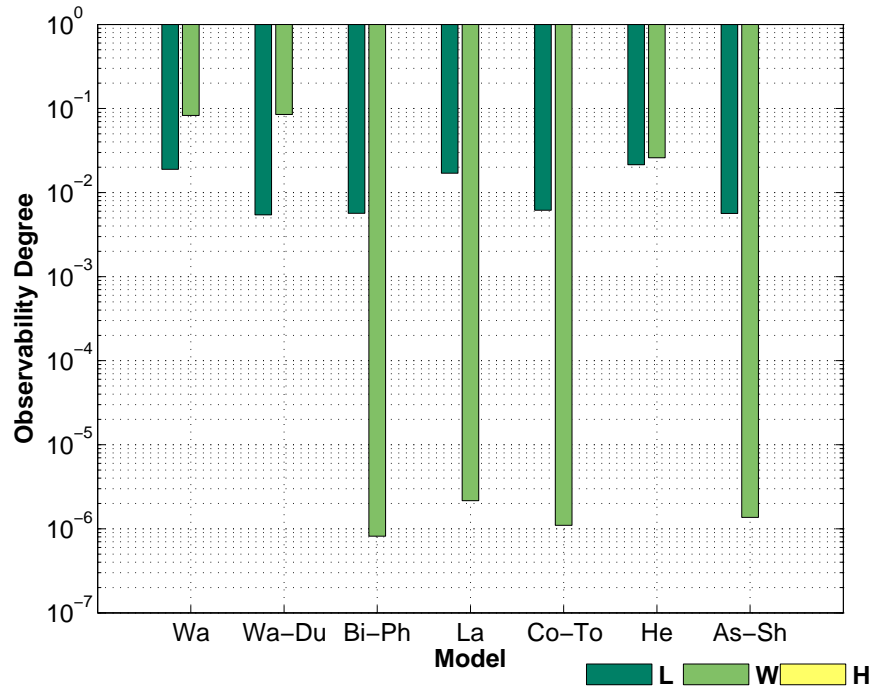


Figure 6.26. Observability Degree of Shape/Size Parameters for Case 1.

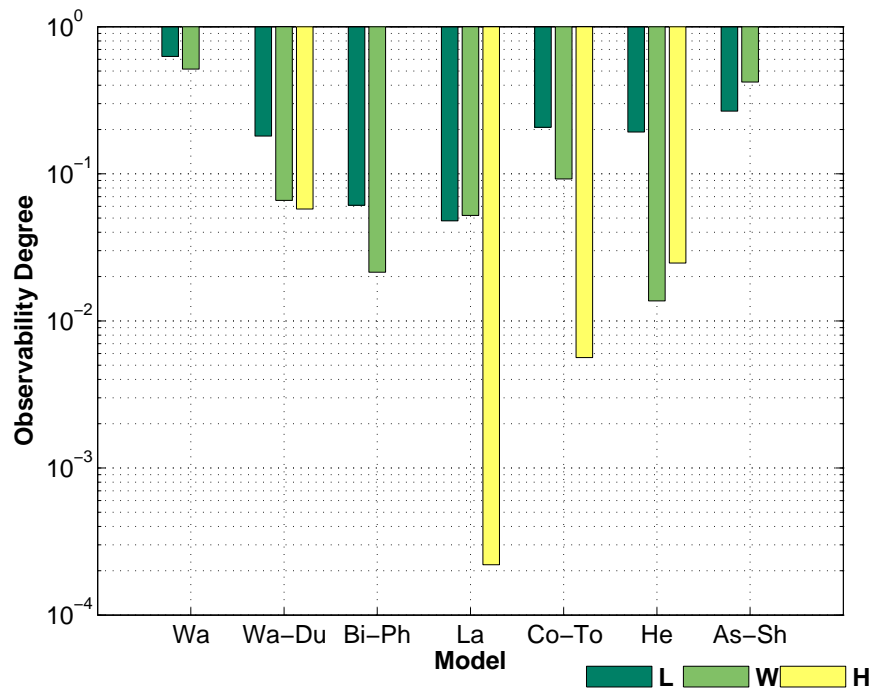


Figure 6.27. Observability Degree of Shape/Size Parameters for Case 2.

## 6.7 Discussion and Model Selection

Given the results for the observability and sensitivity, it can be concluded that for the purpose of this study, not all models perform equally, and careful consideration should be placed in selecting a model. The Ward and Ward-Dür models performed average in the observability analysis. Nevertheless, the sensitivity analysis showed that the observation matrices are not sensitive to the change in the attitude and shape/size parameters. The Blinn-Phong and Lafortune models performed poorly across both analyses and both cases. It was shown that the observation matrices carry no information for the attitude or shape/size. The Cook-Torrance, He, and Ashikhmin-Shirley performed well in the sensitivity for both cases and both models. Moreover, these models did well in the observability study. Given these results the Cook-Torrance, He, and Ashikhmin-Shirley are the models that perform the best for this particular application. Given these results the Cook-Torrance and Ashikhmin-Shirley are compared in the following sections and are selected as the primary models for the remainder of this work.

## 6.8 Light Reflectance Model Comparison

Both the Cook-Torrance and Ashikhmin-Shirley light reflectance models uses different mathematical expressions to describe each of the physical phenomena affecting the reflection of light off a surface. Nevertheless, both models contain components which describe the same physical phenomena. Moreover, both light reflectance models can be expressed using the common notation as defined on Equation (6.39). Table 6.6 shows a comparison of each of these components for both of the models.

$$\rho_{spec} = cFGD \tag{6.39}$$

The components are defined as follows:  $c$  is a constant,  $F$  represents the Fresnel function or its approximation,  $G$  is the geometrical attenuation factor, and  $D$  is the facet slope distribution function. The constant contains information regarding the reflectivity of the specified material of the surface. The Fresnel function describes the way in which light is reflected from a smooth facet.  $G$  accounts for the shadowing or masking effects of one facet onto another. Finally,  $D$  describes the facets which are oriented in the direction of the half-angle vector  $\mathbf{u}_h$ .

From Table 6.6 it can be seen that both the Ashikhmin-Shirley and Cook-Torrance use significantly different mathematical models to describe each of the characteristics of the light reflection model. The first evident difference is observed in the constant  $c$ . The Ashikhmin-Shirley model in the original publication uses a function of ‘phong-like’ exponents to quantify the reflectivity qualities of the specified material [38]. The version of this component used in reference [1], which is being used in this work, is modified and instead uses the refraction index of the material. In the Cook-Torrance model, the denominator is the qualification of the percentage of specular reflectance the specified material has. Both these components are then scaled by  $\pi$ . In addition, the Ashikhmin-Shirley model further scales the constant by 8. The second notable difference is the Fresnel function. The Ashikhmin-Shirley model uses a 5<sup>th</sup> order polynomial to approximate the original function, while the Cook-Torrance model uses the original function. The Fresnel function uses the index of refraction and the angle between the light and the half-angle vector to obtain a 7<sup>th</sup> order polynomial to describe the quantity of light reflected and absorbed. Because the Cook-Torrance model uses a higher fidelity function it is expected it will yield more accurate results. Furthermore, the geometrical attenuation factor  $G$  somewhat differs between the two models. This function is used to determine whether the geometry of the facet’s position is interfering with the amount of light that is actually

Table 6.6. Light Reflectance Model Comparison

	Ashikhmin-Shirley	Cook-Torrance
c	$\frac{n + 1}{8\pi}$ <p>index of refraction corresponding to specified material scaled by <math>8\pi</math>. In original publication denominator is a function of ‘phong-like’ exponents [1].</p>	$\frac{\rho_s}{\pi}$ <p>specular reflectance of specified material scaled by <math>\pi</math></p>
F	$F_0 + (1 - F_0) (1 - (\mathbf{u}_{obs} \cdot \mathbf{u}_h))^5$ <p>approximation of Fresnel function with 5<sup>th</sup> order polynomial of <math>\mathbf{u}_{obs} \cdot \mathbf{u}_h</math></p>	$\frac{1}{2} \left( \frac{g - c}{g + c} \right)^2 \left[ 1 + \frac{(c(g + c) - 1)^2}{(c(g - c) + 1)^2} \right]$ <p>Fresnel function for un-polarized incident light</p>
G	$\frac{b}{\max \{(\mathbf{u}_n \cdot \mathbf{u}_{obs}), (\mathbf{u}_n \cdot \mathbf{u}_{sun})\}}$ $b = \frac{(\mathbf{u}_n \cdot \mathbf{u}_h)}{(\mathbf{u}_{obs} \cdot \mathbf{u}_h)}$ <p>function of inverse of maximum angle between normal and observer or normal and light</p>	$a \min \left\{ \frac{(\mathbf{u}_{obs} \cdot \mathbf{u}_h)}{2(\mathbf{u}_n \cdot \mathbf{u}_h)}, (\mathbf{u}_n \cdot \mathbf{u}_{obs}), (\mathbf{u}_n \cdot \mathbf{u}_{sun}) \right\}$ $a = \frac{2(\mathbf{u}_n \cdot \mathbf{u}_h)}{(\mathbf{u}_{obs} \cdot \mathbf{u}_h)(\mathbf{u}_n \cdot \mathbf{u}_{obs})(\mathbf{u}_n \cdot \mathbf{u}_{sun})}$ <p>function of minimum of angle between normal and observer, normal and light, or function of angle between observer and normal and half angle</p>
D	$(\mathbf{u}_n \cdot \mathbf{u}_h)^{n-1}$ <p>angle between normal and half-angle vector to the power of the index of refraction minus one [1]. In original publication <math>n = n_u \cos^2 \phi + n_v \sin^2 \phi</math>, where <math>\phi</math> is the angle between the projection of <math>\mathbf{u}_h</math> onto the plane perpendicular to <math>N</math>, and <math>n_u</math> and <math>n_v</math> are ‘phong-like’ exponents [1].</p>	$\frac{\exp \{ - [(\tan \delta)/m]^2 \}}{m^2 \cos^4 \delta}$ <p>exponential function with information about facet slope <math>m</math> and angle between <math>\mathbf{u}_n</math> and <math>\mathbf{u}_h</math> <math>\delta</math></p>

striking them. The final component, is the facet slope distribution  $D$ . This particular component is significantly different for both models. The Ashikhmin-Shirley model uses a polynomial of the angle between the normal and the half-angle vector, while Cook-Torrance uses a exponential of this angle in combination with the root mean square facet slope  $m$ .

## Chapter 7

### Inverse Problem

The inverse problem is defined as determining the resident space object's shape, size, attitude, and spin rate when the orbit of the object is known. As previously stated, one of the most commonly used measurements to estimate the shape and spin of a space object is the light curve measurement. This measurement is a major source of information, not only for near-Earth objects but also for asteroids [17] and man-made orbiting objects (See references. 22, 24, 34, 37, 25, and 26). Most of the mentioned works have shown that the light curve measurement is a reliable source of information for the attitude and angle variation of Earth orbiting objects. In addition, light curves have also been used to estimate the shape of some of these objects [22,24].

The problem that arises with the use of light curves to estimate the shape and spin of the object is the light curve inversion. The light curve inversion problem is defined as finding the best possible fit between an observed light curve and a synthetic light curve generated by a model [18], without any a priori knowledge of the shape or size of the orbiting body. As shown in the previous chapter, these synthetic measurements are produced by a mathematical model that aims to describe the physical phenomena given a particular observation. These synthetic measurements are then used to estimate the states and parameters of a given object. Thus, model integrity (the choice of an appropriate mathematical representation of the observed data) is critical to the success of the observability of states and parameters in the measurements. However, it is in the choice of the measurement model to generate the synthetic data and use of the same model in the inversion process (estimation),

where the “inverse crime” is committed [57, 58]. The following section expands on this concept.

## 7.1 Inverse Crime

Simply stated, the “inverse crime” is an expression that denotes the act of using the same model to generate and later invert synthetic data [57]. In doing so, the inverse problem is presented in such a way where it becomes *less* ill-posed than it actually is, consequently leading to solutions which can be unrealistically optimistic [59]. The authors of reference [58] warn against committing the inverse crime as to avoid a “trivial inversion” [57, 58]. Furthermore, they state that it is of great importance that the synthetic data does not have a “connection” to the inverse solver models. The goal of this section is to investigate the consequences of the inverse crime in the context of light curve inversion for unresolved space object identification and tracking. This will be achieved by using two distinct models for the light curve, one for the synthetic measurement creation and another for the inversion.

### 7.1.1 Numerical Setup

In order to fully investigate the inverse crime, four cases were developed as shown in Table 7.3. Each of the presented light curve models were used to produce the synthetic measurements and/or for the UKF measurement model. These cases use identical initial conditions, UKF set-up, and equations of motion. Initial conditions are shown on Table 7.1. Table 7.2 shows the initial state and covariance error for the UKF. Measurements were created using zero-mean white noise process error with standard deviation of 0.1 magnitude for the light curve measurement. The time between measurements was set to be 10 seconds. The work presented here is the result of 100 averaged runs for each case.

Table 7.1. Initial Conditions for Inverse Crime

State/Parameter		Initial Value (unit)
Position	$\mathbf{r}_0$	$[4764 \ 4764 \ 0]^T$ (km)
Velocity	$\mathbf{v}_0$	$[-5.25 \ 5.25 \ 1.99]^T$ (km/s)
Angular Velocity	$\boldsymbol{\omega}$	$[0 \ 0.0262 \ 0]^T$ (rad/s)
Attitude	$\mathbf{q}_0$	$[0.239 \ 0.189 \ 0.038 \ 0.951]^T$
	$[\phi_0 \ \theta_0 \ \psi_0]$	$[30 \ 20 \ 10]^T$ (deg)
Shape/Size	$\mathbf{p}_0$	$[5 \ 3 \ 4]^T$ (m)

Table 7.2. Initial Error and Error Covariance for Inverse Crime

State/Parameter		Initial Error (unit)	Error Covariance (unit)
Position	$\mathbf{r}_0$	1 (km)	$1^2$ (km <sup>2</sup> )
Velocity	$\mathbf{v}_0$	0.001 (km/s)	$0.001^2$ (km <sup>2</sup> /s <sup>2</sup> )
Angular Velocity	$\boldsymbol{\omega}$	60 (deg/hr)	$60^2$ (deg <sup>2</sup> /hr <sup>2</sup> )
Attitude	$[\phi_0 \ \theta_0 \ \psi_0]$	0.15 (deg)	$0.15^2$ (deg <sup>2</sup> )
Shape/Size	$\mathbf{p}_0$	0.1 (m)	$0.1^2$ (m <sup>2</sup> )

Table 7.3. Model Combinations

Case No.	Synthetic Measurement Model	UKF Measurement Model	Type
1	Ashikhmin-Shirley	Cook-Torrance	No Inverse Crime
2	Cook-Torrance	Ashikhmin-Shirley	No Inverse Crime
3	Ashikhmin-Shirley	Ashikhmin-Shirley	Inverse Crime
4	Cook-Torrance	Cook-Torrance	Inverse Crime

### 7.1.2 Results and Discussion

The following figures show the results for all four cases. The cases are denoted by the model used to produce the synthetic measurements first and the UKF measurement model second. The first case shown in Figure 7.1 used the Ashikhmin-Shirley BRDF model for the creation of the synthetic measurements and the Cook-Torrance BRDF model for the UKF measurement model. A comparison of the two BRDF models is shown in section 6.8. Figure 7.1 shows the mean and standard deviation

of the error between the light curve produced by the synthetic measurement model and the UKF measurement model. The light curve error and standard deviation is smallest for the cases in which the inverse crime is committed (case 3 and 4). For case 4, the higher fidelity model (Co-To) was used for the production of the synthetic measurements as well as the estimation measurement model. Case 3, for which the lower fidelity model (As-Sh) is used for both models, shows a slightly larger error mean and standard deviation than case 4. For the cases where the inverse crime is not committed the error is much higher. Moreover, case 1 where the higher fidelity model is used for the estimation while the lower fidelity model is used for the synthetic measurements, shows a larger error and standard deviation when compared to case 2 for which the lower fidelity model is used in the estimation. Case 4 where the light curve is both produced and inverted using the same model, yields much better results than if a lower fidelity model is used to perform the estimation (case 2). The same is true when case 1 and case 3 are compared. This is an indication that the “inverse crime” does indeed affect the results of the estimation for the problem of light curve inversion.

Figure 7.2 shows the estimated shape/size parameter errors for each of the cases. Similarly to the previous figure, the best results are obtained in case 3 and 4, where the inverse crime is committed. For case 2, when the low fidelity As-Sh model is used for the inversion of measurements produced by the Co-To model, the results are less than desirable. This is a consequence of loss of information due to the lower fidelity model being used for the estimation. The results in case 4, where the Co-To model is used for both estimation and measurements, the results are significantly better than those of case 2. If one extrapolates these results to an experiment performed with ‘real’ measurements, case 2 illustrates the closest scenario: the measurements are generated by a the ‘highest’ fidelity model (a.k.a. nature), while a lower fidelity

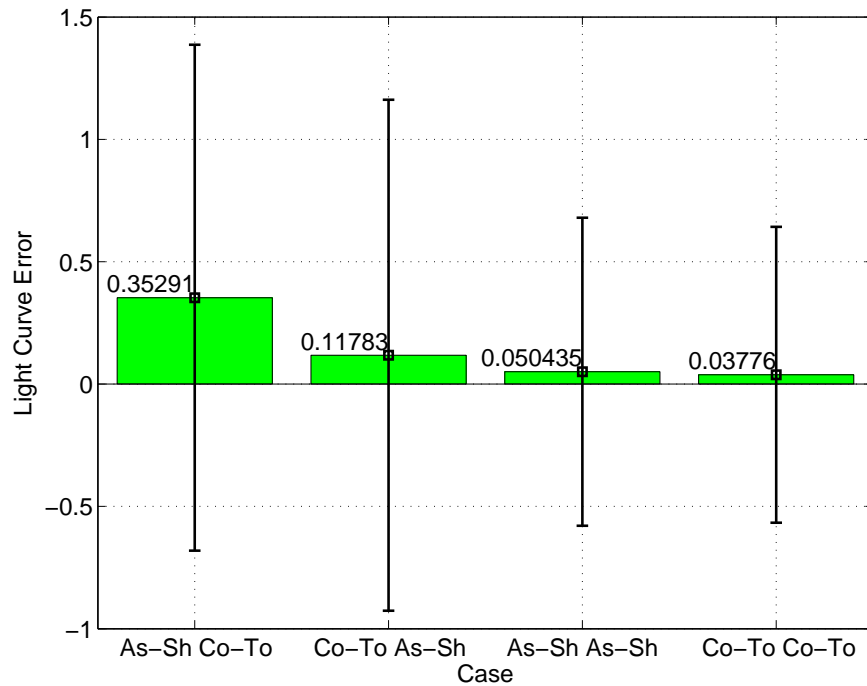


Figure 7.1. Light Curve Error Comparison.

model (mathematical approximation) is used to describe the phenomena. It can be clearly seen that if one does not consider this when performing experiments with synthetic data, results might be misleadingly optimistic, as case 4 shows.

The effective use of the light curve measurement to acquire information regarding unresolved space objects has been shown by several authors in many different publications. The investigation shown in this section aimed to examine the problem that arises when the same model is used for the creation of the synthetic light curve and the light curve inversion, otherwise known as the “inverse crime”. Four cases were investigated where two models were used to create the synthetic data and/or to perform the estimation of the shape parameters and states of an unresolved space object. The results showed that for this particular application the “inverse crime” indeed has an effect on the estimation of these shape parameters. When using a high

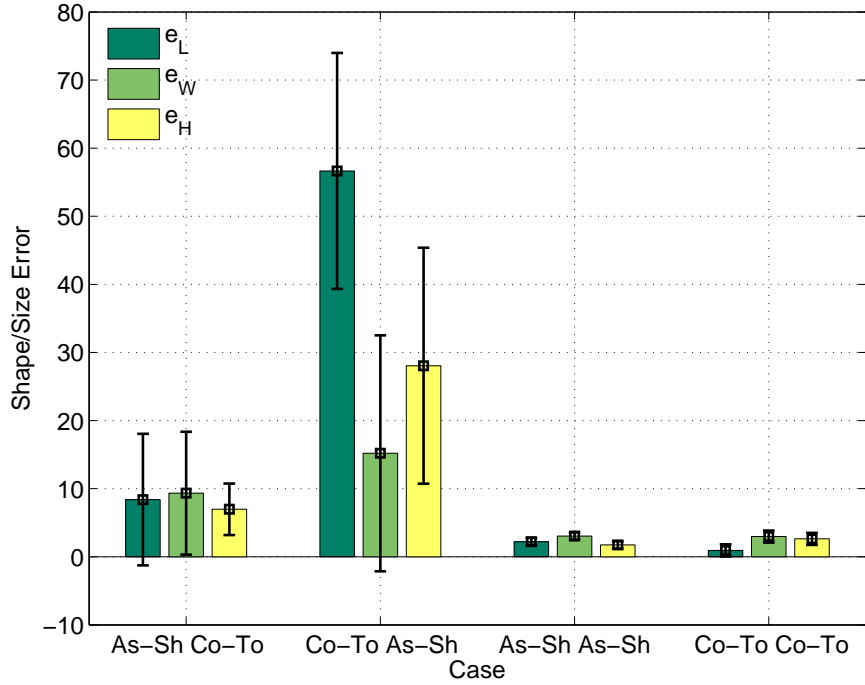


Figure 7.2. Shape/Size Parameter Estimation Error Comparison.

fidelity model for both the measurement creation and inversion the results of the estimation errors are significantly smaller than when using a lower fidelity model for the estimation, or for the measurement creation. Moreover, if a lower fidelity model is used for the measurement creation and a higher fidelity model is used for the estimation, the errors improve over the reverse case, as expected. This investigation focused on a specific application, nevertheless it might serve as a cautionary voice as to avoid the “inverse crime” when performing experiments which require synthetic data that will later be inverted to extract information. The comparison results have shown that the Cook-Torrance model is a higher fidelity model, as it contains the full Fresnel function, and a more complex geometrical attenuation component and slope distribution component when compared to those of the As-Sh model. Consequently, the Cook-Torrance has a higher capacity of capturing behavior which the

Ashikhmin-Shirley model might loose. This in turn affects the choice of which model is used to produce synthetic measurements and which model is used to solve the light curve inversion problem via the UKF. The next section will show a comparison of the estimation results of case 1 vs. 4 (i.e. no inverse crime vs. inverse crime).

## 7.2 Inverse Problem Solution via Unscented Kalman Filter

### 7.2.1 Numerical Setup

The solution to the inverse problem is presented here. The unscented Kalman filter as presented in chapter 5 is utilized. The solution of the inverse problem focuses on the estimation of the angular velocity, attitude, and shape/size parameters. A reduced state defined as  $\mathbf{x} = [\boldsymbol{\omega}^T \mathbf{g}^T \mathbf{p}^T]^T$ . The initial conditions, initial state error, and initial covariance are shown in Table 7.4. Measurements were created using zero-mean white noise process error with standard deviation of 0.1 magnitude for the light curve measurement. The time between measurements was set to be 10 seconds. The two sets results shown here will compare the effects of the inverse crime. For the first scenario the Cook-Torrance model is used to produce the measurements, while the Ashikhmin-Shirley model is used for the estimation. The second scenario uses the Cook-Torrance for both the synthetic measurement creation and the estimation measurement model. The results shown here are the result of one hundred averaged runs.

### 7.2.2 Results

Figure 7.3–7.6 show the true position, velocity, angular velocity, and attitude of the object. The orbit is assumed to be known for the inverse problem, and therefore the position and velocity are not estimated. Figure 7.7 and 7.8 show the perturbation accelerations and torques experienced by the object as it orbits. Perturbations due

Table 7.4. Initial Conditions for Inverse Problem

State/Parameter		Initial Value (unit)
Position	$\mathbf{r}_0$	$[4764 \ 4764 \ 0]^T$ (km)
Velocity	$\mathbf{v}_0$	$[-5.25 \ 5.25 \ 1.99]^T$ (km/s)
Angular Velocity	$\boldsymbol{\omega}_0$	$[0 \ 0.0262 \ 0]^T$ (rad/s)
Attitude	$\mathbf{q}_0$	$[0.239 \ 0.189 \ 0.038 \ 0.951]^T$
	$[\phi_0 \ \theta_0 \ \psi_0]$	$[30 \ 20 \ 10]^T$ (deg)
Shape/Size	$\mathbf{p}_0$	$[5 \ 3 \ 4]^T$ (m)

Table 7.5. Initial Error and Error Covariance for Inverse Problem

State/Parameter		Initial Error (unit)	Error Covariance (unit)
Angular Velocity	$\boldsymbol{\omega}_0$	60 (deg/hr)	$60^2$ (deg <sup>2</sup> /hr <sup>2</sup> )
Attitude	$[\phi_0 \ \theta_0 \ \psi_0]$	0.15 (deg)	$0.15^2$ (deg <sup>2</sup> )
Shape/Size	$\mathbf{p}_0$	0.1 (m)	$0.1^2$ (m <sup>2</sup> )

to drag, aspherical Earth, solar radiation pressure, and gravity gradient are shown.

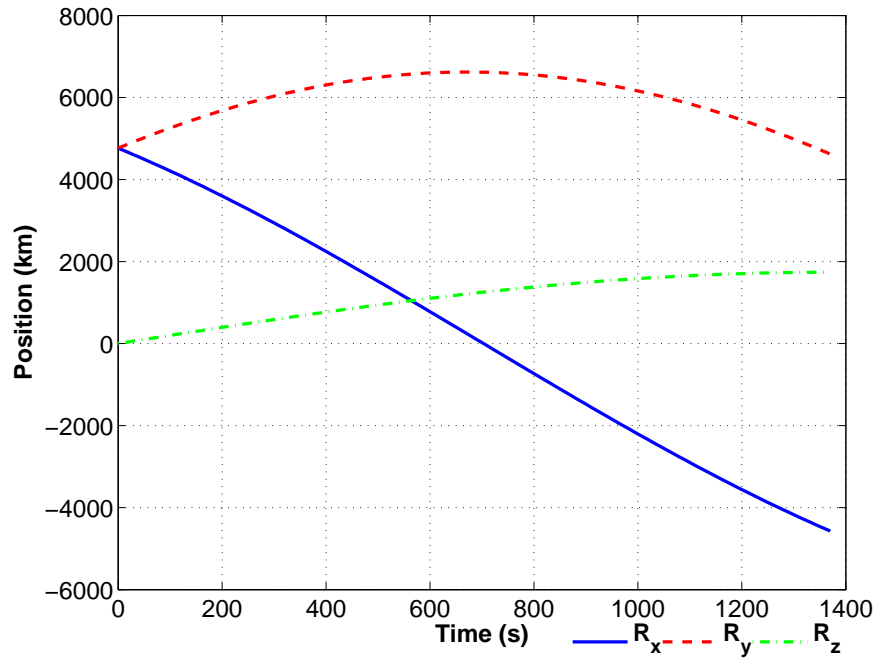


Figure 7.3. Inverse Problem True Object Position.

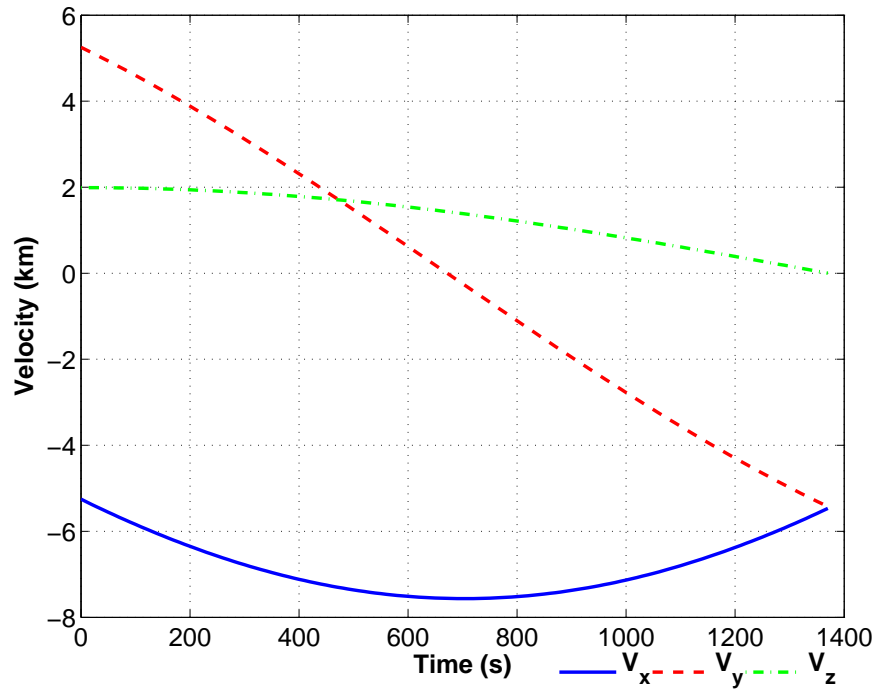


Figure 7.4. Inverse Problem True Object Velocity.

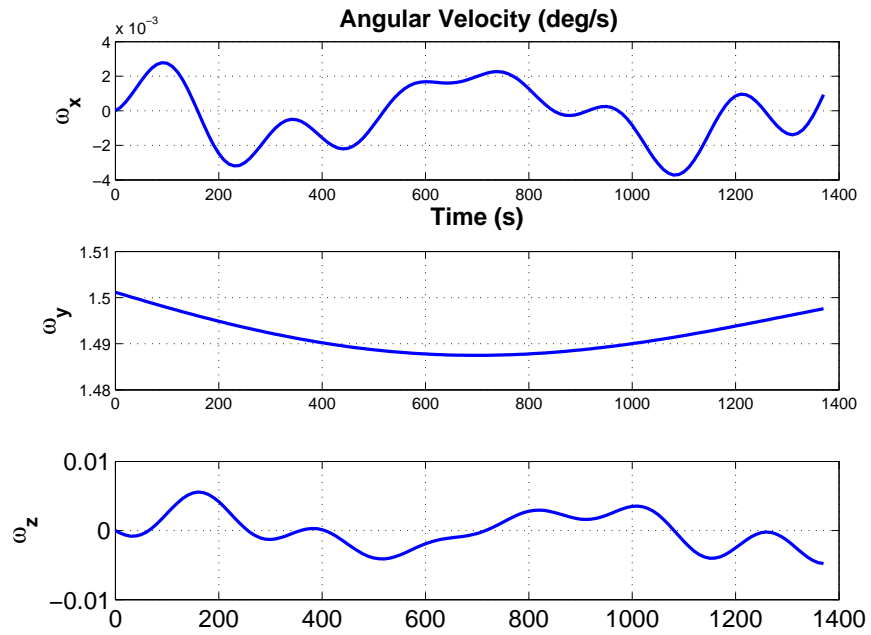


Figure 7.5. Inverse Problem True Object Angular Velocity.

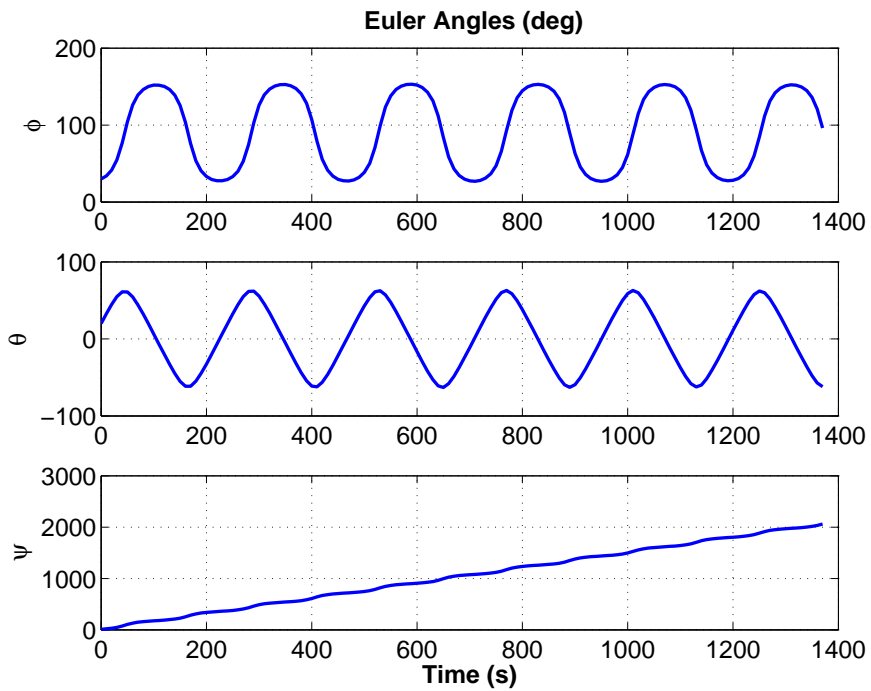


Figure 7.6. Inverse Problem True Object Euler Angles.

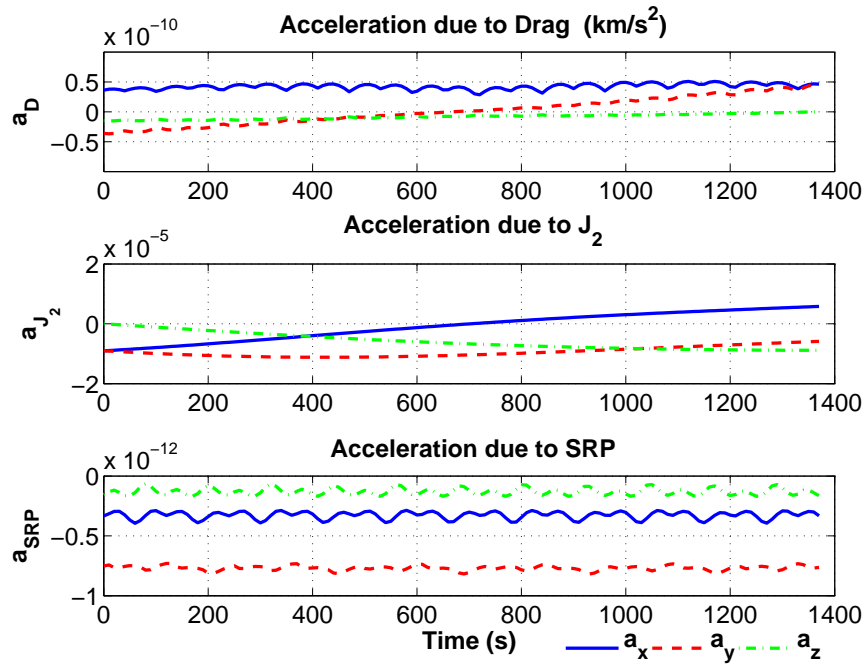


Figure 7.7. Inverse Problem Perturbation Accelerations.

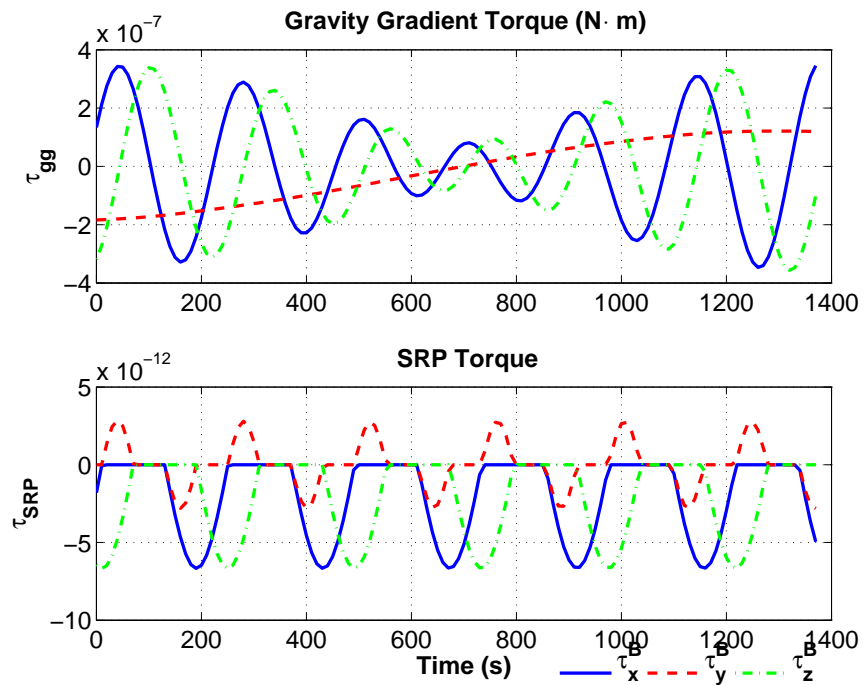
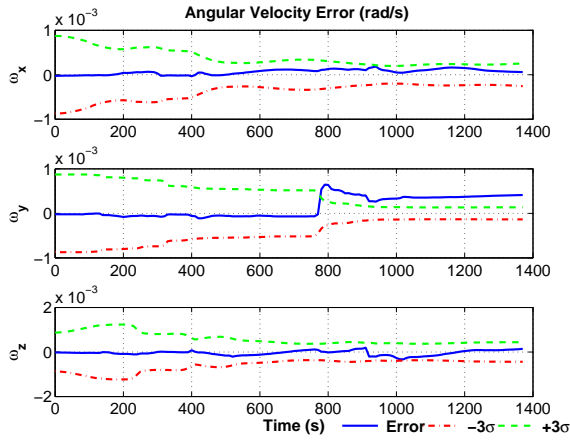
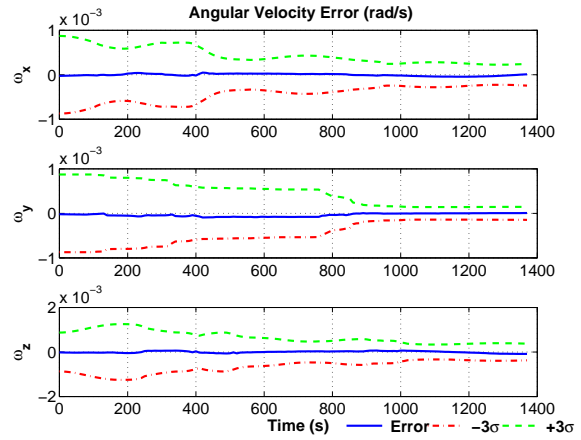


Figure 7.8. Inverse Problem Perturbation Torques.

The estimation of the angular velocity for both cases is shown in Figure 7.9. It can clearly be seen that the inverse crime solution results in a far better estimation of this state. The jump in the error for the no-inverse crime case can be attributed to the difference between the light curve measurements at 800 seconds in Figure 7.14. Similarly, the estimation of the attitude shown in Figures 7.10 and 7.11 demonstrates the effect of the inverse crime: The error for the MRP in the Co-To As-Sh case increases with each phase change of the states, while the Co-To Co-To case decreases. This reflects with increasing errors for the Euler angles for the first case, while the second case shows decreasing errors and  $3\sigma$  bounds. Figures 7.12 and 7.13 show the estimation error of the shape/size parameters. The first shows the error along with  $3\sigma$  bounds. The bounds decrease for all three states, the error for the width leaves the three sigma bounds but then returns. A jump in all three estimations can be observed, similarly to the estimation of the angular velocity. On the contrary, the errors for the inverse crime case remain bounded and decrease for all three parameters. As previously mentioned, the estimated light curve and synthetic light curve also have discrepancies at this same time as shown in Figure 7.14 for the no inverse crime case, while the error remains negligible for the inverse crime. This is further evidence that the inverse crime has significant influence on the estimation of the angular velocity, attitude, and shape/size for a resident space object.

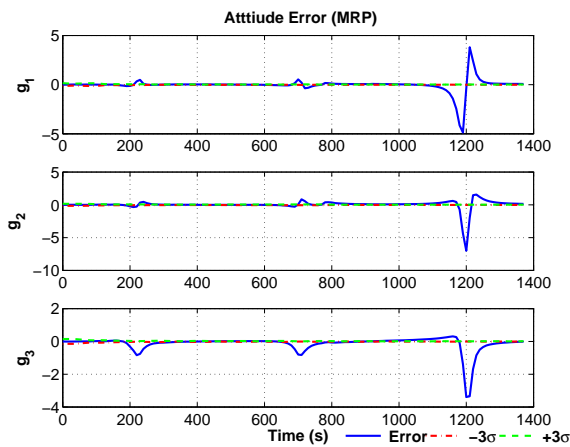


(a) Co-To As-Sh

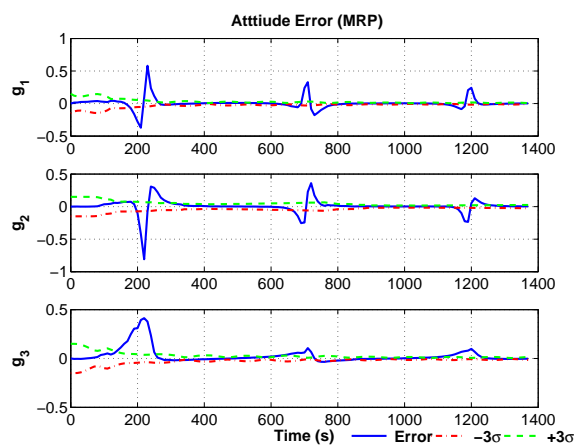


(b) Co-To Co-To

Figure 7.9. Inverse Problem Estimation Angular Velocity.

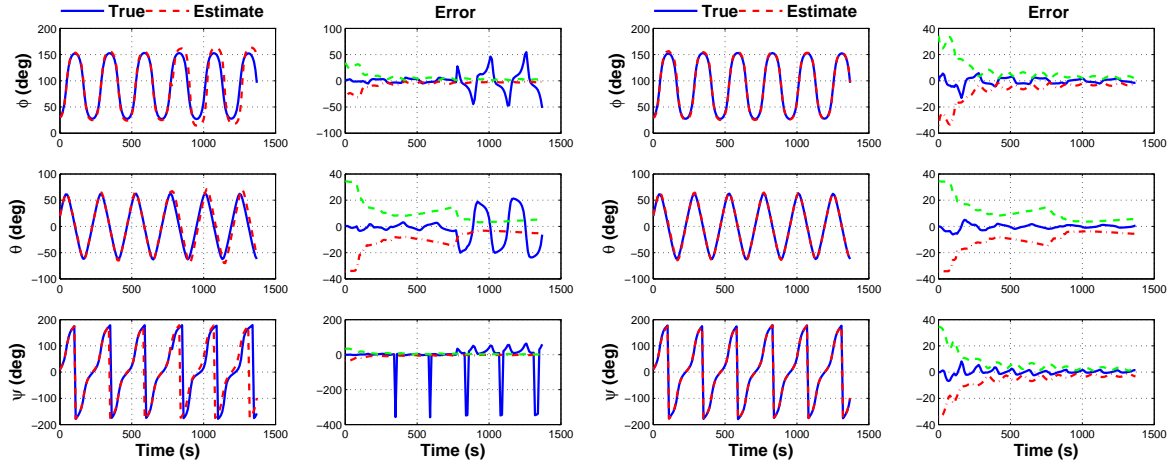


(a) Co-To As-Sh



(b) Co-To Co-To

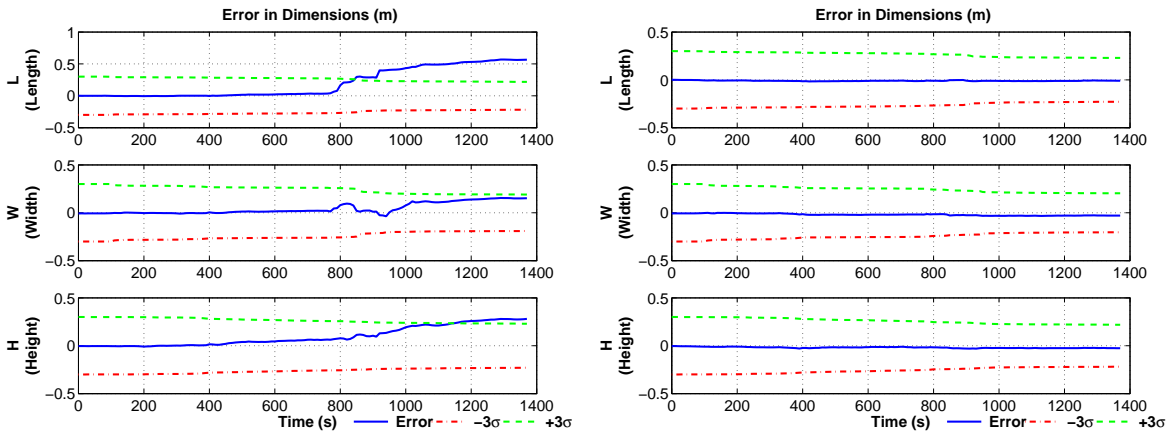
Figure 7.10. Inverse Problem Estimation of Attitude (MRPs).



(a) Co-To As-Sh

(b) Co-To Co-To

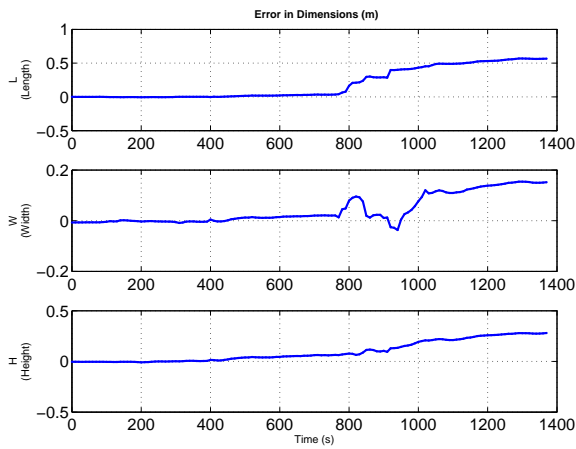
Figure 7.11. Inverse Problem Estimation of Attitude (Euler Angles).



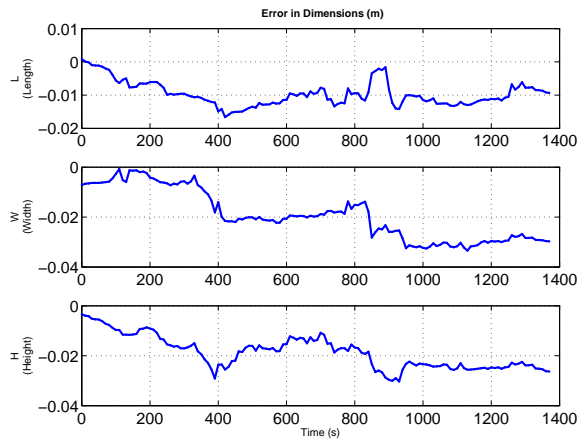
(a) Co-To As-Sh

(b) Co-To Co-To

Figure 7.12. Inverse Problem Estimation of Shape/Size Parameters.

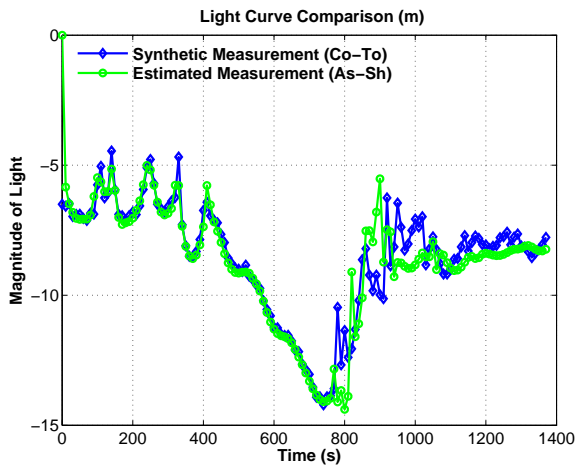


(a) Co-To As-Sh

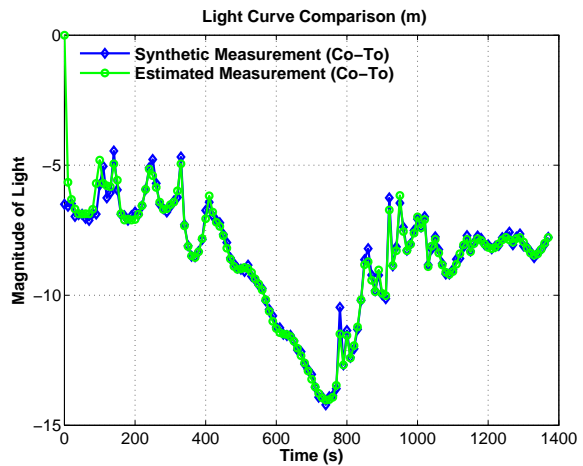


(b) Co-To Co-To

Figure 7.13. Inverse Problem Estimation of Shape/Size Parameter (no  $3\sigma$  bounds).



(a) Co-To As-Sh



(b) Co-To Co-To

Figure 7.14. Inverse Problem Acquired vs. Estimated Light Curve Measurement.

## Chapter 8

### Joint Estimation via Unscented Kalman Filter

This chapter introduces the first solution approach to the combined direct and inverse problem. The estimation is referred to as ‘joint’ estimation of the states all states and parameters. Two approaches have been implemented for the estimation of the object’s states and parameters involving the unscented Kalman filter (UKF). The first is a joint estimation where all states and parameters are simultaneously estimated using a UKF. The second approach estimates the states by means of the UKF and stores these values until a fixed batch size criterion is met. Then these estimated state values are passed to the batch estimation algorithm which produces a new updated value for the parameters by reducing a cost function. This is done until all the measurements are used.

The batch estimation has been implemented in an effort to improve the estimation of the shape/size parameters. As it was shown in the observability and sensitivity analysis, the shape/size parameters are observable from the light curve measurement. Nevertheless, this observability is good only for one of the parameters in the low observability case and two parameters are observable for the high observability case. The remaining parameter(s) have a low observability. In addition, the light curve measurement is also used to aid in the estimation of the attitude. This leads to the estimation of three states and three parameters from one measurement. Therefore, it is the objective of the batch estimation to aid in the process of the estimation of the parameters. Results for both the UKF estimation and UKF-batch estimations

will be shown and discussed in this chapter. The UKF is implemented as shown in chapter 5. The following section expands on the UKF-batch implementation.

## 8.1 UKF-Batch Estimation

For the batch estimation of the object parameters, the maximum likelihood estimation approach is used. This method minimizes the following cost function:

$$J(\hat{\mathbf{p}}) = \frac{1}{2} \sum_{k=1}^N (\tilde{\mathbf{y}}_k - \hat{\mathbf{y}}_k)^T (\tilde{\mathbf{y}}_k - \hat{\mathbf{y}}_k) \quad (8.1)$$

where  $\hat{\mathbf{y}}_k$  is the estimated value of the measurement  $\mathbf{y}$  at the time  $t_k$  and  $N$  is the total number of measurements in a particular batch. For an iteration number  $i$ , the estimate of  $\mathbf{p}$  at  $i + 1$  is  $\hat{\mathbf{p}}$  obtained from the  $i^{th}$  estimate by

$$\hat{\mathbf{p}}_{i+1} = \hat{\mathbf{p}}_i - [\nabla_{\hat{\mathbf{p}}}^2 J(\hat{\mathbf{p}})]^{-1} [\nabla_{\hat{\mathbf{p}}} J(\hat{\mathbf{p}})] \quad (8.2)$$

where the gradients are obtained using the following expressions.

$$[\nabla_{\hat{\mathbf{p}}} J(\hat{\mathbf{p}})] = - \sum_{k=1}^N [\nabla_{\hat{\mathbf{p}}} \hat{\mathbf{y}}_k]^T (\tilde{\mathbf{y}}_k - \hat{\mathbf{y}}_k) \quad (8.3)$$

$$[\nabla_{\hat{\mathbf{p}}}^2 J(\hat{\mathbf{p}})] \approx \sum_{k=1}^N [\nabla_{\hat{\mathbf{p}}} \hat{\mathbf{y}}_k]^T [\nabla_{\hat{\mathbf{p}}} \hat{\mathbf{y}}_k] \quad (8.4)$$

As shown in Figure 8.1, the UKF begins with an initial guess for the states and parameters. The UKF estimates both states and parameters until the number of measurements equals a predetermined batch size  $N$ . Next, the estimated values of the states and the parameters from the UKF is passed to the Batch loop. The parameters are iterated until either the cost function meets a specified tolerance or until a fixed number of iterations is met. The value of the parameters is then passed back to the UKF to continue the estimation process. For this study, this is done until all measurements are used.

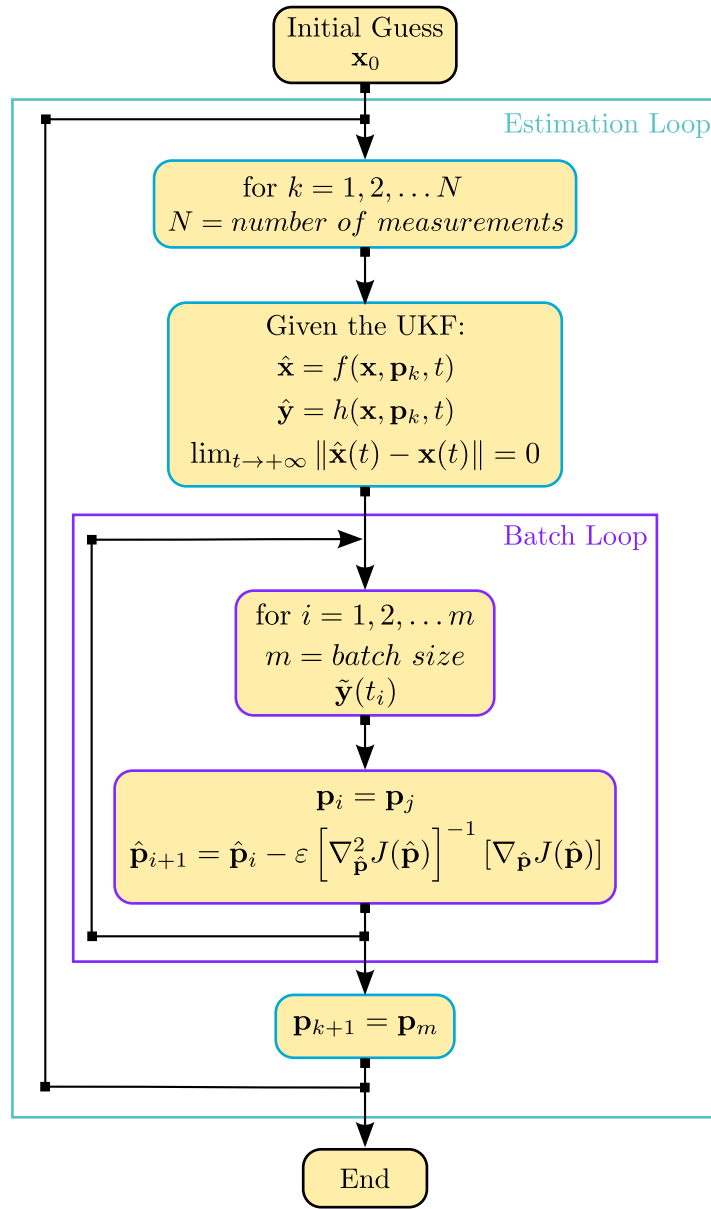


Figure 8.1. UKF-Batch Estimation Algorithm.

Two approaches were adopted for the update phase in the Batch loop. The first uses the Levenberg-Marquardt update as shown in Equation (8.5). The parameter  $\eta$  is heuristically chosen.  $\eta$  is taken to be large for the initial iteration and is reduced by a specified factor ( $f$ ) on each iteration.  $Z$  is a diagonal matrix with entries equal to the diagonal elements of  $\nabla_{\hat{\mathbf{p}}}^2 J(\hat{\mathbf{p}})$  and  $\varepsilon$  is a scaling factor [46].

$$\hat{\mathbf{p}}_{i+1} = \hat{\mathbf{p}}_i - \varepsilon [\nabla_{\hat{\mathbf{p}}}^2 J(\hat{\mathbf{p}}) + \eta Z]^{-1} [\nabla_{\hat{\mathbf{p}}} J(\hat{\mathbf{p}})] \quad (8.5)$$

$$\eta_{k+1} = \frac{\eta_k}{f} \quad (8.6)$$

The second approach uses a modified Gauss-Newton algorithm, where a scaling factor  $\varepsilon$  is used as shown in Equation (8.7).

$$\hat{\mathbf{p}}_{i+1} = \hat{\mathbf{p}}_i - \varepsilon [\nabla_{\hat{\mathbf{p}}}^2 J(\hat{\mathbf{p}})]^{-1} [\nabla_{\hat{\mathbf{p}}} J(\hat{\mathbf{p}})] \quad (8.7)$$

## 8.2 Numerical Setup

Both the UKF estimation and UKF-batch estimation experiments have the same experimental setup. For both cases, one hundred averaged runs have been executed. The results presented here are the mean of those 100 experiments. The object is selected to be at an attitude that will provide good observability as it orbits. As it was shown in the chapter 6, an initial condition which leads to the observer having visibility of all faces provides better observability for the attitude state and shape/size parameters. These true values are also used to produce synthetic measurements for azimuth, elevation, and light curve.

The initial conditions for the experiment are shown in Table 8.1. The estimator initial conditions were set as shown in Table 8.2. The synthetic measurements were created using zero-mean white noise error process with standard deviation of 2 *arcseconds* for elevation and azimuth. The light curve measurement has an error

process with standard deviation of 0.1 magnitude. The measurements were acquired every 10 seconds. The synthetic light curve measurements were created using the Ashikhmin-Shirley model. This model is also used for the UKF measurement model.

Table 8.1. Initial Conditions for UKF and UKF-Batch Joint Estimation

State/Parameter		Initial Value (unit)
Position	$\mathbf{r}_0$	$[4764.48 \ 4764.48 \ 0]^T$ ( $km$ )
Velocity	$\mathbf{v}_0$	$[-5.2533 \ 5.2533 \ 1.9906]^T$ ( $km/s$ )
Angular Velocity	$\boldsymbol{\omega}$	$[0 \ 0.00262 \ 0]^T$ ( $rad/s$ )
Attitude	$\mathbf{q}_0$	$[0.23929 \ 0.18930 \ 0.03813 \ 0.95154]^T$
	$[\phi_0 \ \theta_0 \ \psi_0]$	$[30 \ 20 \ 10]^T$ ( $deg$ )
Shape/Size	$\mathbf{p}_0$	$[5 \ 3 \ 4]^T$ ( $m$ )

Table 8.2. Initial Error and Error Covariance for UKF and UKF-Batch Joint Estimation

State/Parameter		Initial Error (unit)	Error Covariance (unit)
Position	$\mathbf{r}_0$	1 ( $km$ )	$1^2$ ( $km^2$ )
Velocity	$\mathbf{v}_0$	0.001 ( $km/s$ )	$0.001^2$ ( $km^2/s^2$ )
Angular Velocity	$\boldsymbol{\omega}$	20 ( $deg/hr$ )	$20^2$ ( $deg^2/hr^2$ )
Attitude	$[\phi_0 \ \theta_0 \ \psi_0]$	5 ( $deg$ )	$5^2$ ( $deg^2$ )
Shape/Size	$\mathbf{p}_0$	0.1 ( $m$ )	$0.1^2$ ( $m^2$ )

### 8.3 Results and Discussion

Figures 8.3–8.6 show the true states over time. The object is in a lower Earth orbit (LEO) with an inclination of 15 degrees. It is first observed South-West of the observer as it crosses over the Equatorial plane into the North-East portion of the

sky as shown in Figure 8.2. As the object orbits, it has an initial angular velocity along its y-axis. The object is affected by acceleration perturbations as shown in Figure 8.7, and torque perturbations as shown in Figure 8.8. Figure 8.6 shows the angular velocity changes due to these perturbations.

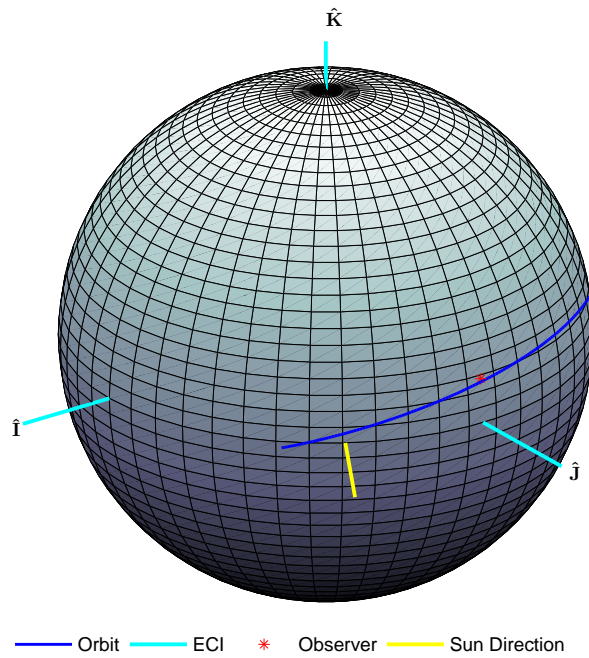


Figure 8.2. UKF Joint Estimation True Object Position.

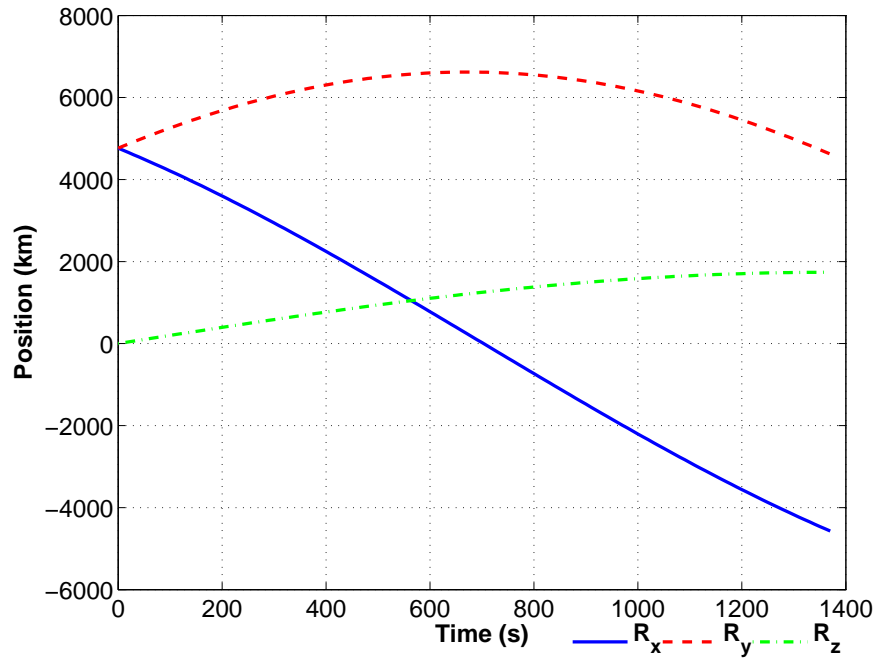


Figure 8.3. UKF Joint Estimation True Object Position.

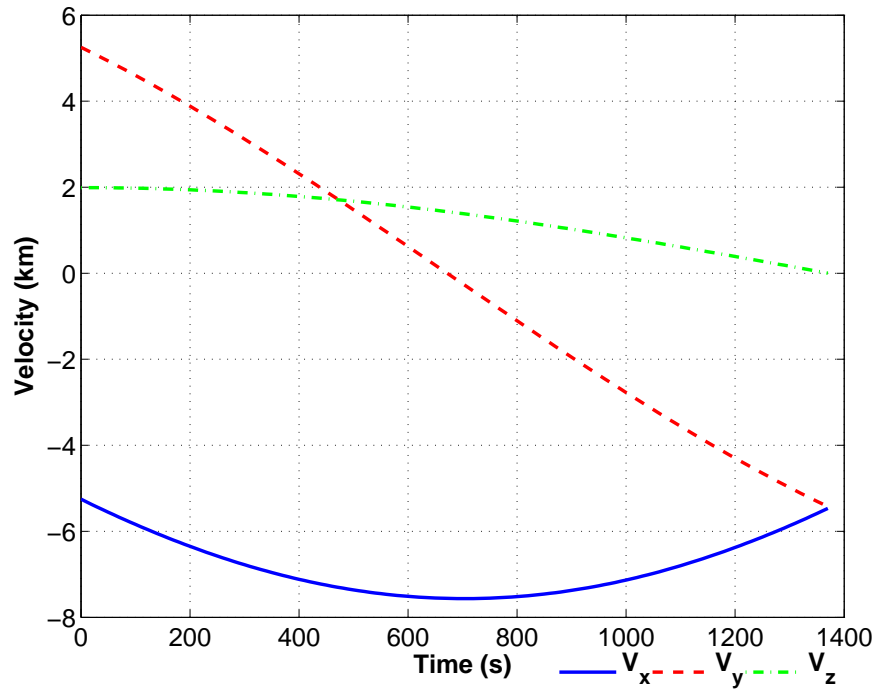


Figure 8.4. UKF Joint Estimation True Object Velocity.

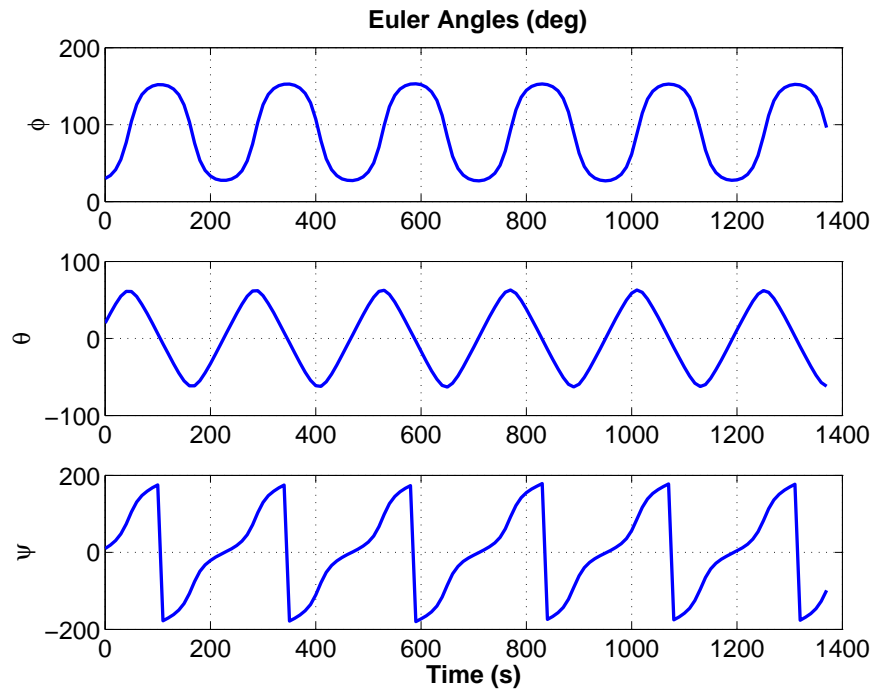


Figure 8.5. UKF Joint Estimation True Object Euler Angles.

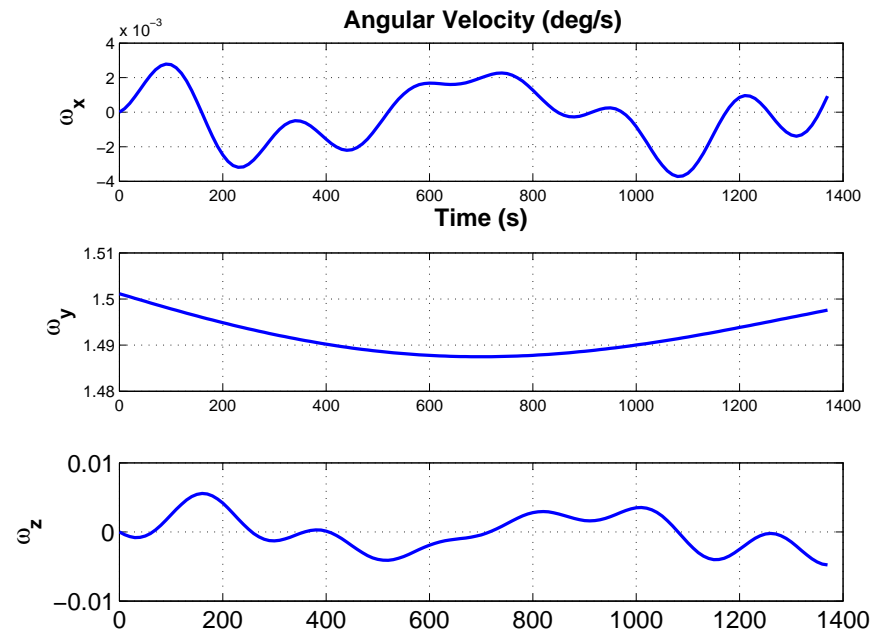


Figure 8.6. UKF Joint Estimation True Object Angular Velocity.

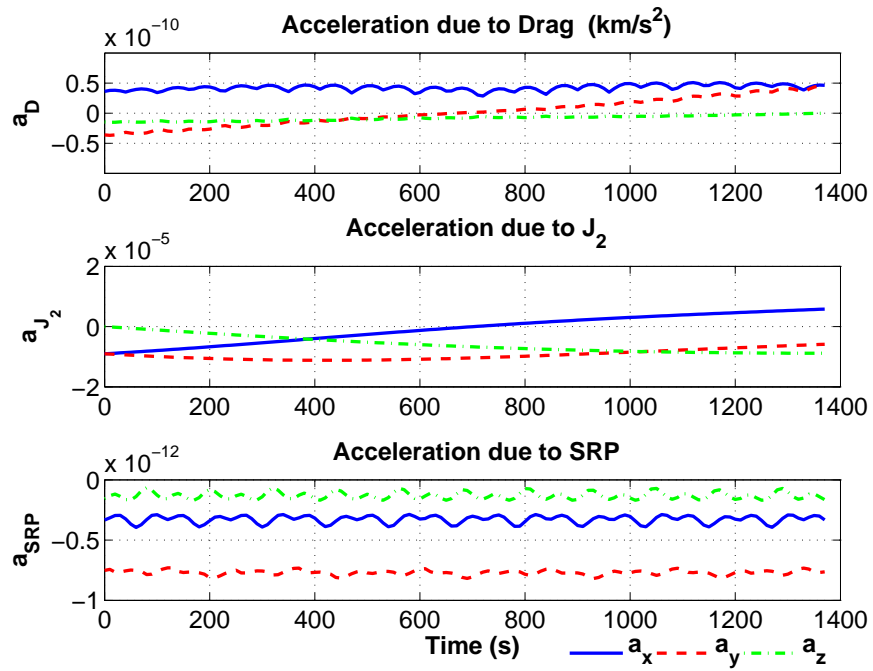


Figure 8.7. UKF Joint Estimation Perturbation Accelerations.

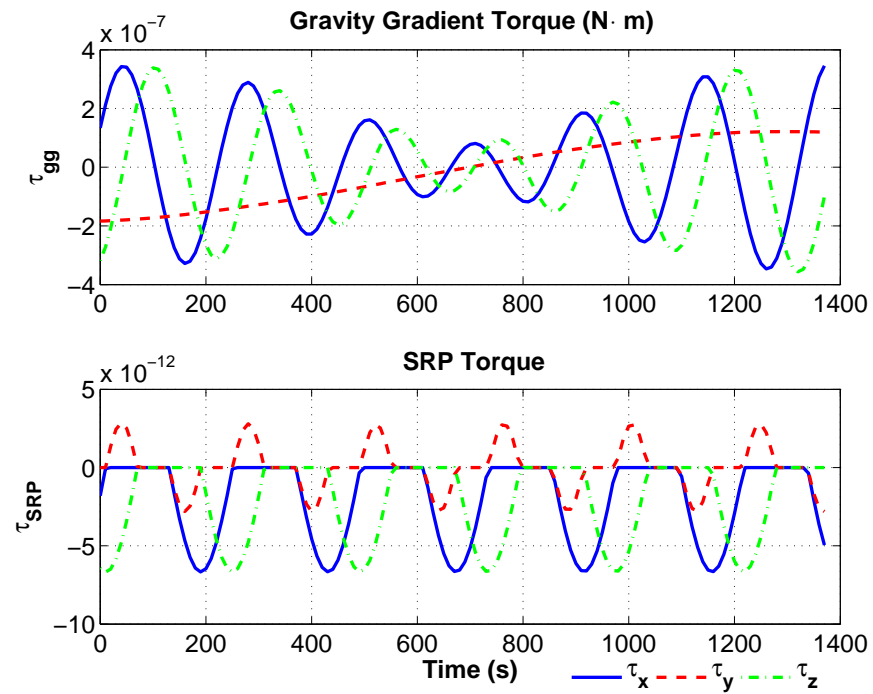


Figure 8.8. UKF Joint Estimation Perturbation Torques.

### 8.3.1 UKF Estimation Results

The estimation of the states and parameters was done via the UKF as described in chapter 5. Figure 8.9 shows the estimation of the position. The position of the space object is estimated within the first 600 seconds and the sigma bounds reduce significantly. The behavior of the velocity estimation is similar as shown in Figure 8.10. As stated many times, the estimation of the position and velocity based on the astrometric measurements has been done many times and is once again shown here.

Although the attitude states used in the UKF were Quaternions and MRPs, the estimation has been shown in MRPs and Euler angles to ease the interpretation of the results as shown in Figures 8.11 and 8.12. These figures show the attitude is well behaved, as the object tumbles and goes through change in angular velocity, the MRPs attitude error leaves the  $3\sigma$  bounds but quickly returns. In addition to the change in angular velocity, attitude parametrization contains singularities and this can lead to a change in phase for the MRPs. Nevertheless, once the UKF adapts to the change in behavior, the sigma bounds grow and later reduce, along with the error. Figures 8.12 shows the true and estimated Euler angles, where the estimated angles track the true values very close. The angular velocity estimates well, and the  $3\sigma$  bounds reduce around 400 seconds into the simulation.

Finally, the estimation of the shape/size parameters is shown in Figure 8.14. Figure 8.15 shows the same result as 8.14 without  $3\sigma$  bounds to give a more detailed evolution of the estimation of the parameters. The estimation stays well bounded through out the simulation. The initial error for the parameters was 20 centimeters, it is shown here to be reduced close to 2 centimeters for length, 2 centimeters for width, and 3 centimeters for height. This is a great reduction in the error for the shape/size parameters.

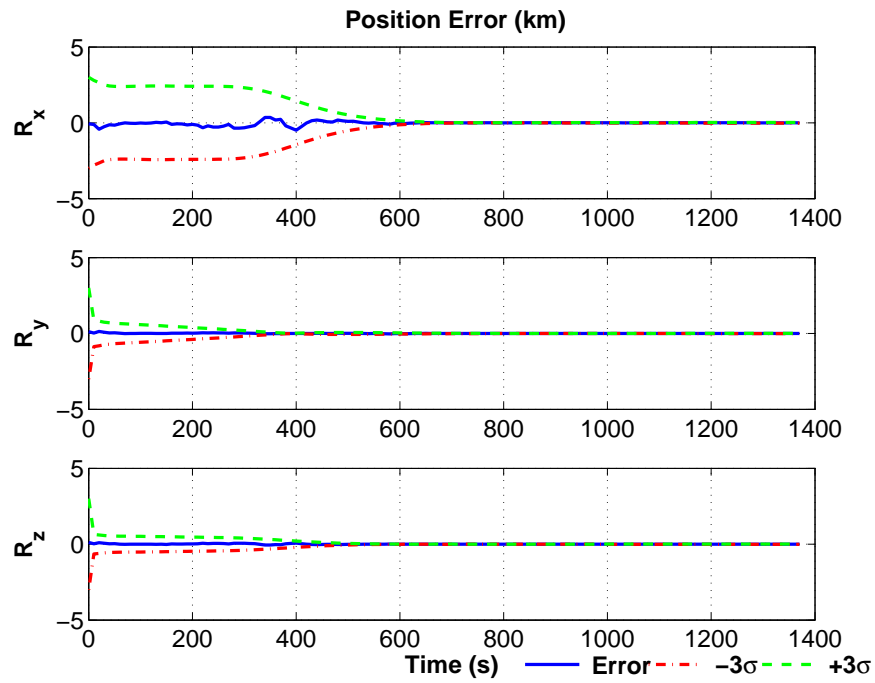


Figure 8.9. UKF Joint Estimation of Position.

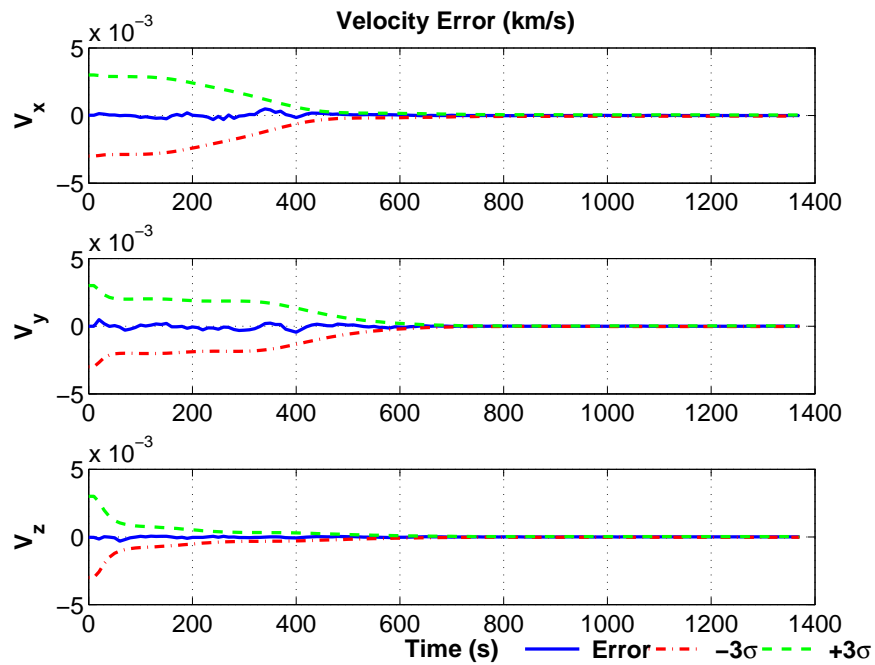


Figure 8.10. UKF Joint Estimation of Velocity.

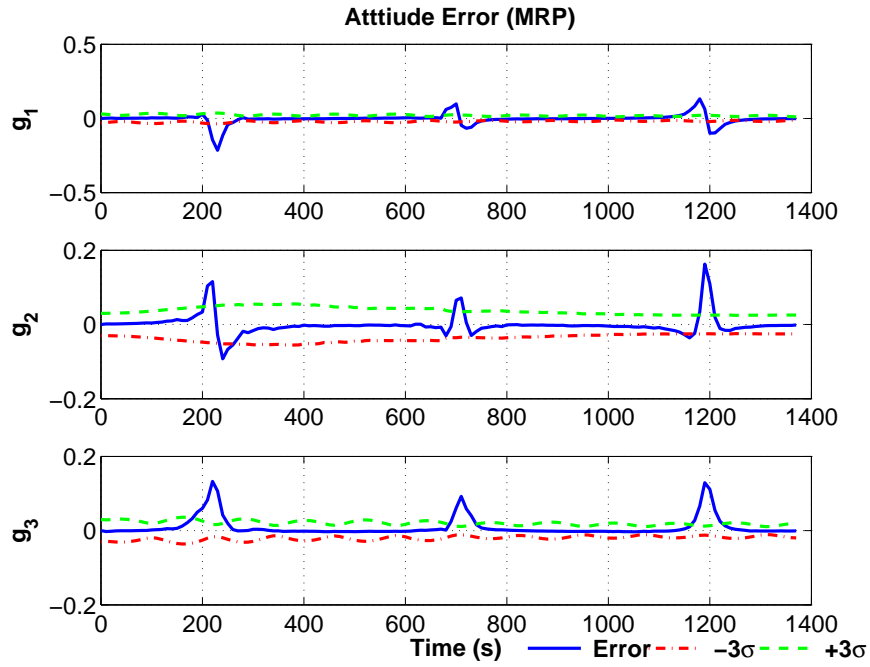


Figure 8.11. UKF Joint Estimation of Attitude (MRPs).

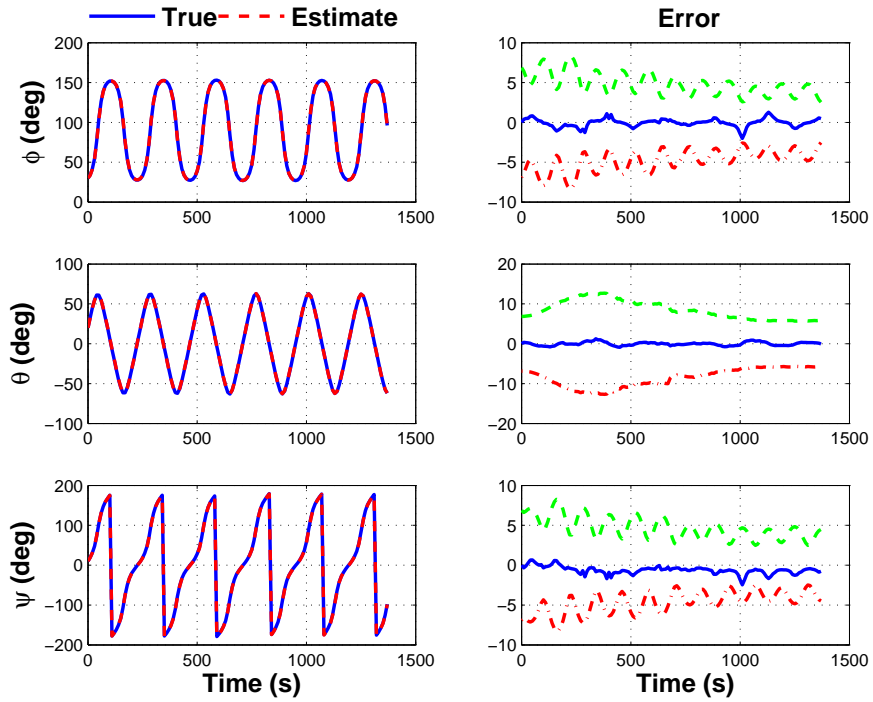


Figure 8.12. UKF Joint Estimation of Attitude (Euler Angles).

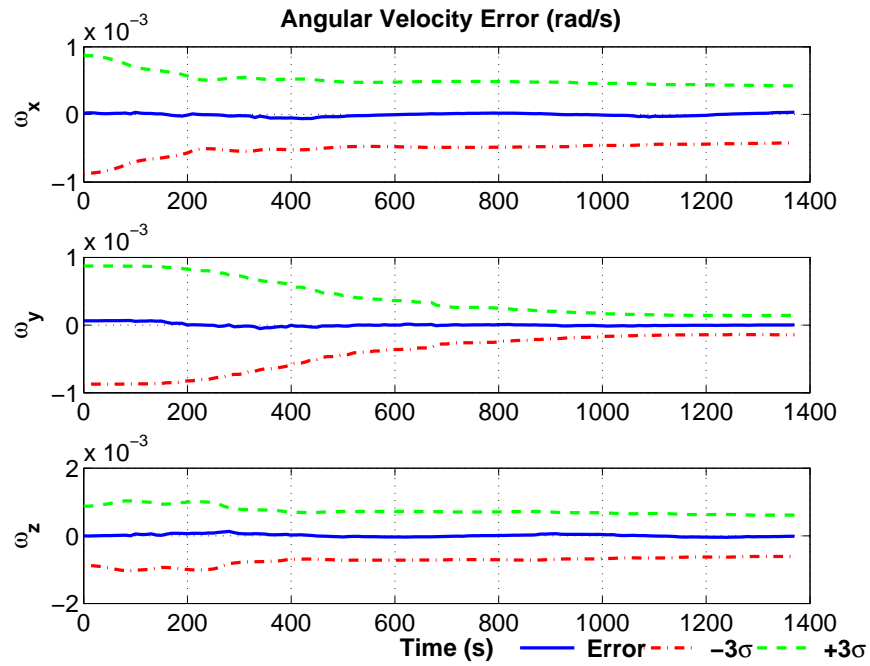


Figure 8.13. UKF Joint Estimation of Angular Velocity.

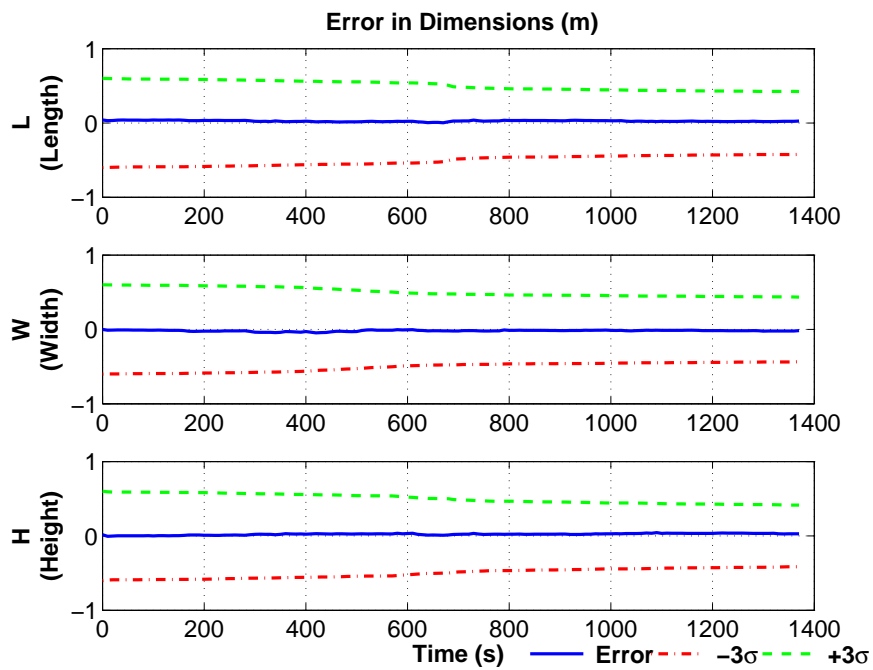


Figure 8.14. UKF Joint Estimation of Shape/Size Parameters.

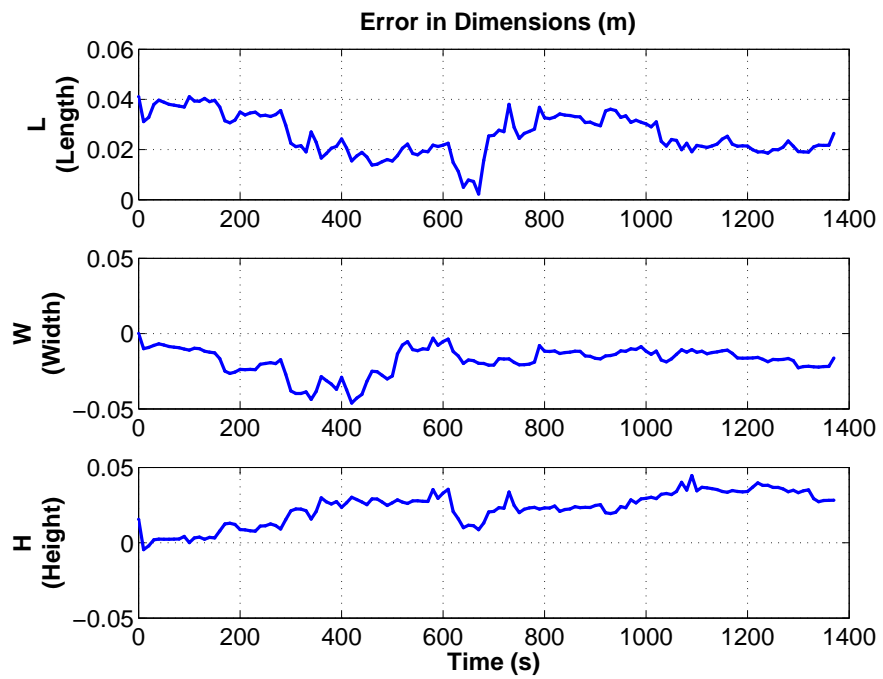


Figure 8.15. UKF Joint Estimation of Shape/Size Parameter (no  $3\sigma$  bounds).

### 8.3.2 UKF-Batch Estimation Results

The results for both the Levenberg-Marquardt (LM) and Gauss-Newton (GN) cost function approaches are shown in this section. The estimation procedure for the position, velocity, attitude, and angular velocity is the same for the UKF-batch estimation, as it is for the UKF estimation. The estimation of the position, velocity, angular velocity, and attitude be seen in Figures 8.16-8.20 for the Levenberg-Marquardt and Figures 8.23-8.27 for the Gauss-Newton approach. These results show that the estimation of these sates is very similar to the UKF estimation results. The position and velocity are estimated quickly and the errors stay bounded by the shrinking sigma bounds. The same behavior is observed for the angular velocity in the UKF-batch as the UKF estimation. The attitude estimation for both cases has similar results with the errors spiking out of the bounds and later returning for the MRPs and tracks well for the Euler angles.

The estimation of the shape/size parameters is also improves for the UKF-batch schemes. The Levenberg-Marquardt batch estimation and Gauss-Newton yielded a final error almost 4 centimeters for length, 0.6 centimeters for width, and 1.2 centimeters for height. This is an excellent estimation of the shape/size parameters. In addition to the error plots in Figure 8.21 and 8.28, the cost function reduction for each measurement batch has been shown in figures 8.22 and 8.29 for both approaches. Both these figures show the reduction of the cost for 30 iterations.

### 8.3.3 Discussion and Comparison

Table 8.3 shows a comparison of the shape/size final estimation error for all three experiments. This is the average error over the last 10 seconds of the estimation for 100 averaged runs. These results indicate that the estimation of the parameters was somewhat close for the three methods. The error is more evenly distributed for the

GN method, while the LM method has a large value for the length and small values for the width and height. This value was almost twice as much as the error obtained by both the batch estimations. The cost of obtaining this improvement is significant as the computational time for the batch estimation is substantially larger than the joint estimation.

Table 8.3. Shape/Size Parameter Final UKF Estimation Error (cm) Comparison

$\mathbf{p}$	UKF	UKF-Batch LM	UKF-Batch GN
Length	2.14	4.70	1.13
Width	2.02	0.618	1.06
Height	3.17	1.24	1.27
Norm	4.32	4.89	1.99

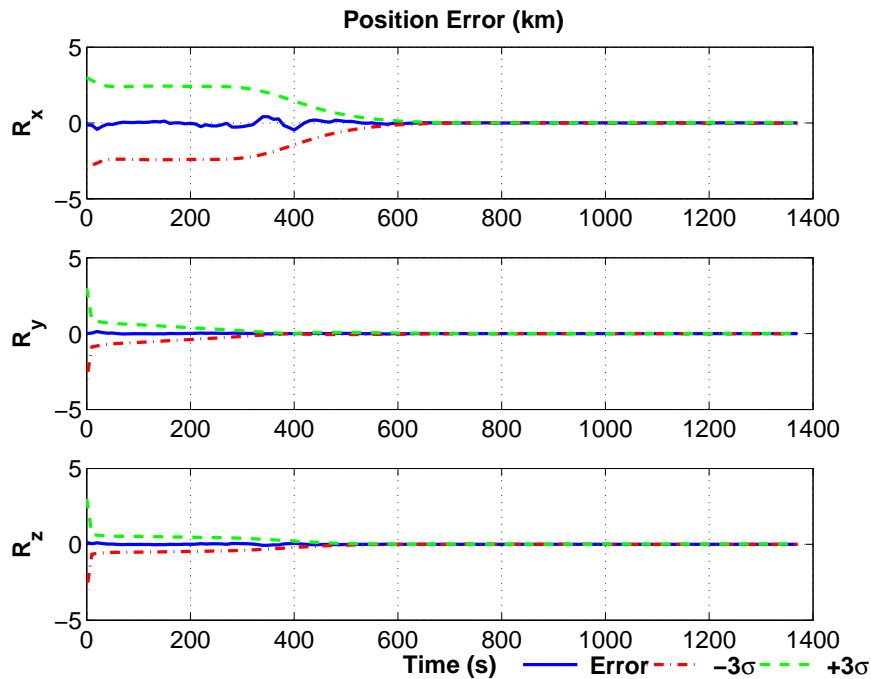


Figure 8.16. UKF Levenberg Marquardt Batch Estimation of Position.

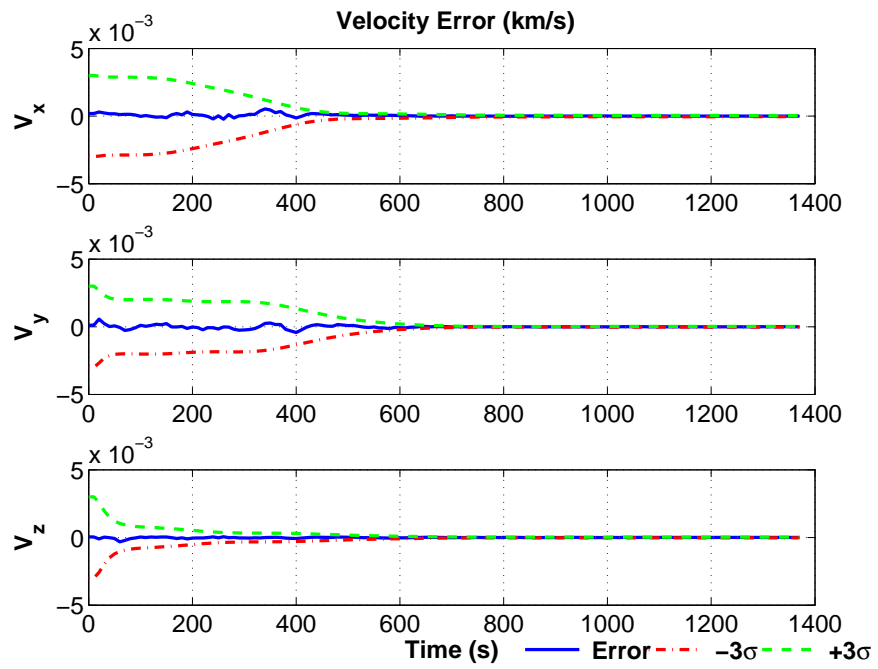


Figure 8.17. UKF Levenberg Marquardt Batch Estimation of Velocity.

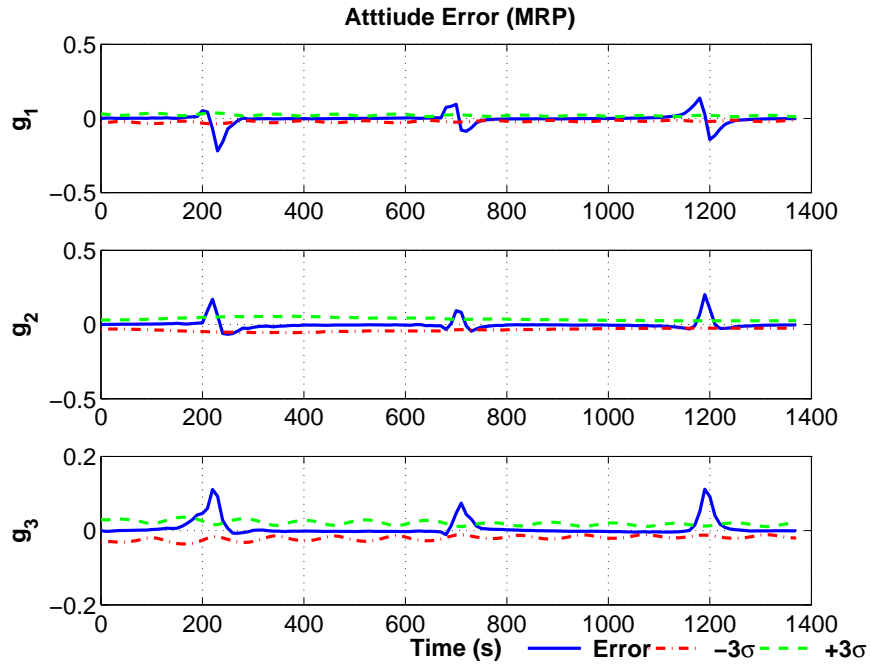


Figure 8.18. UKF Levenberg Marquardt Batch Estimation of Attitude (MRPs).

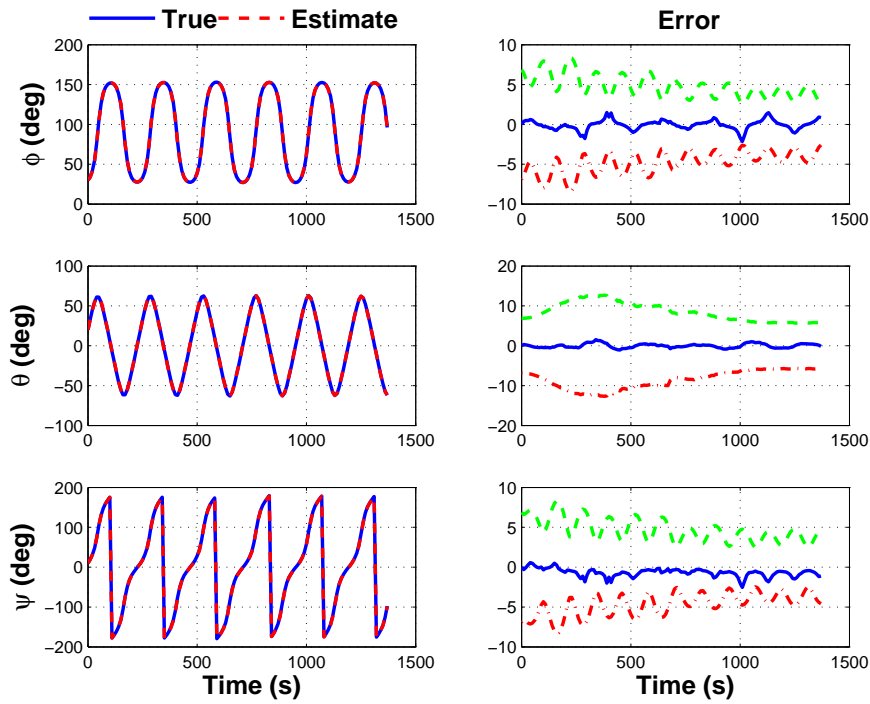


Figure 8.19. UKF Levenberg Marquardt Batch Estimation of Attitude (Euler Angles).

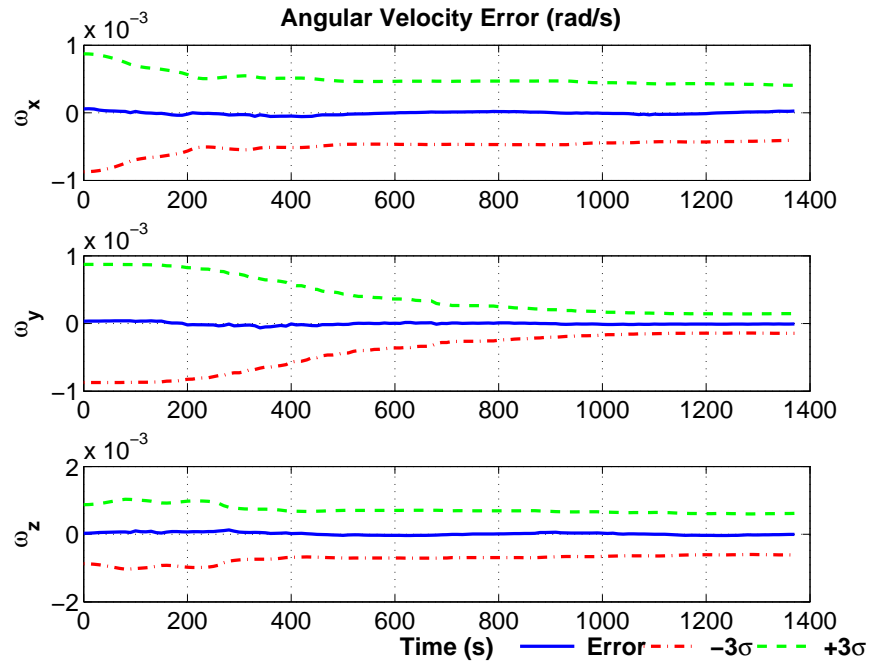


Figure 8.20. UKF Levenberg Marquardt Batch Estimation of Angular Velocity.

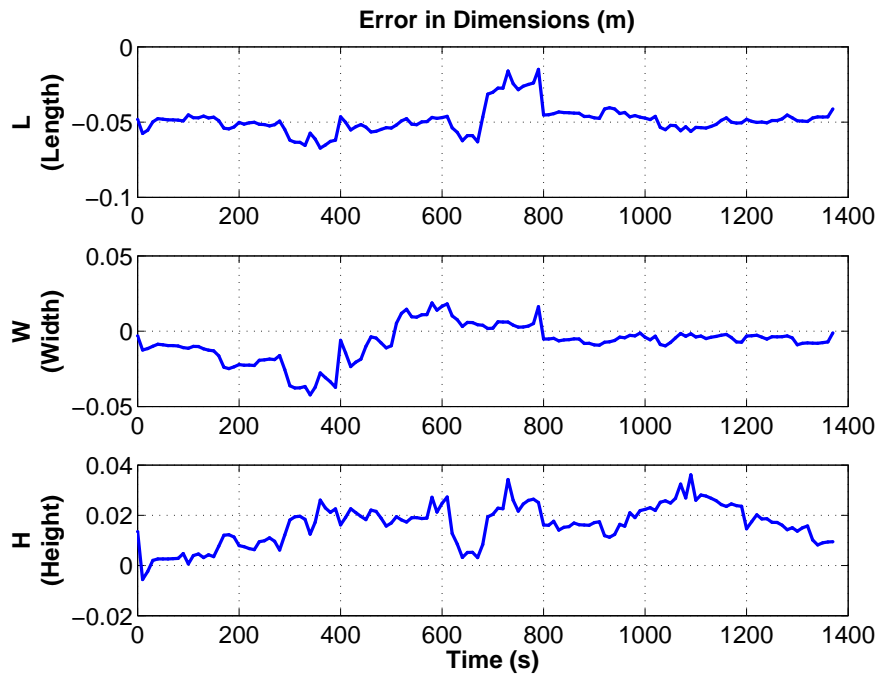


Figure 8.21. UKF Levenberg Marquardt Batch Estimation of Shape/Size Parameters.

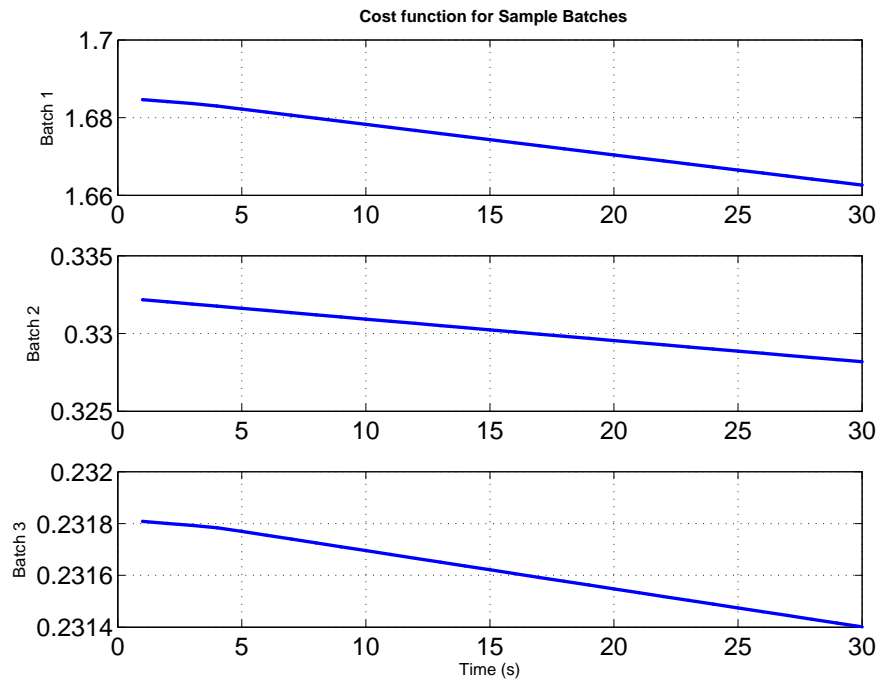


Figure 8.22. UKF Levenberg Marquardt Batch Cost.

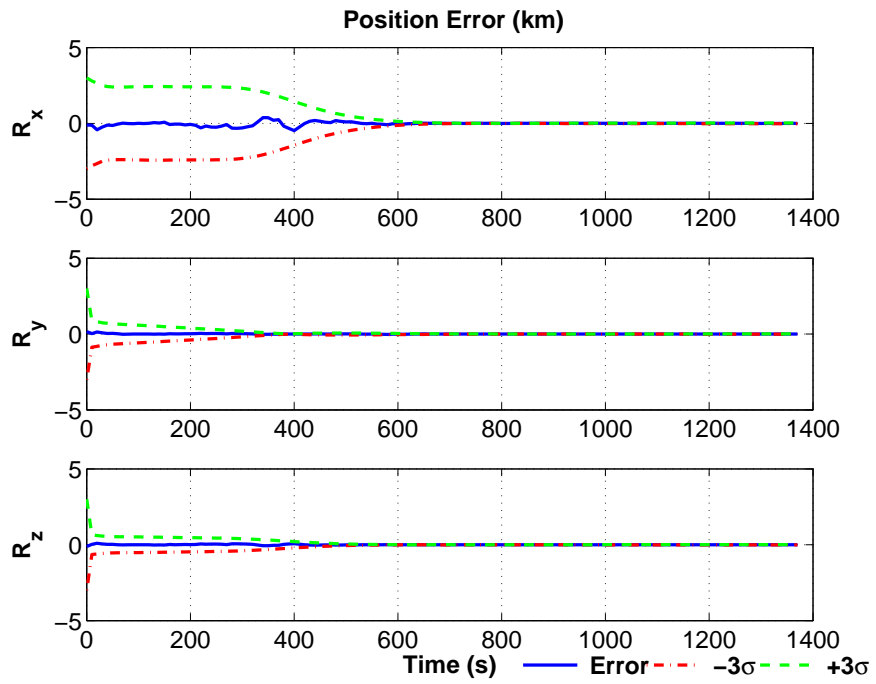


Figure 8.23. UKF Gauss Newton Batch Estimation of Position.

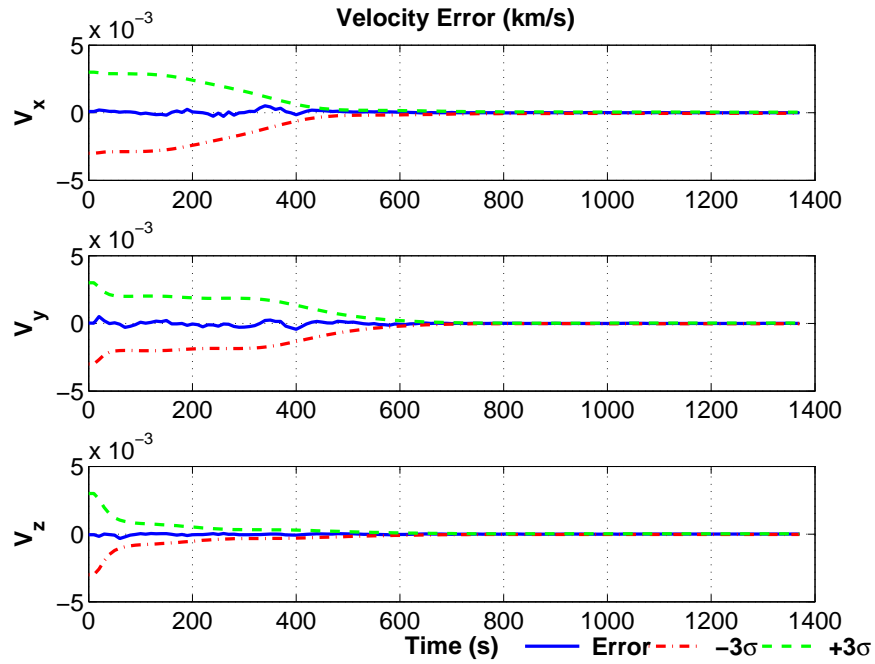


Figure 8.24. UKF Gauss Newton Batch Estimation of Velocity.

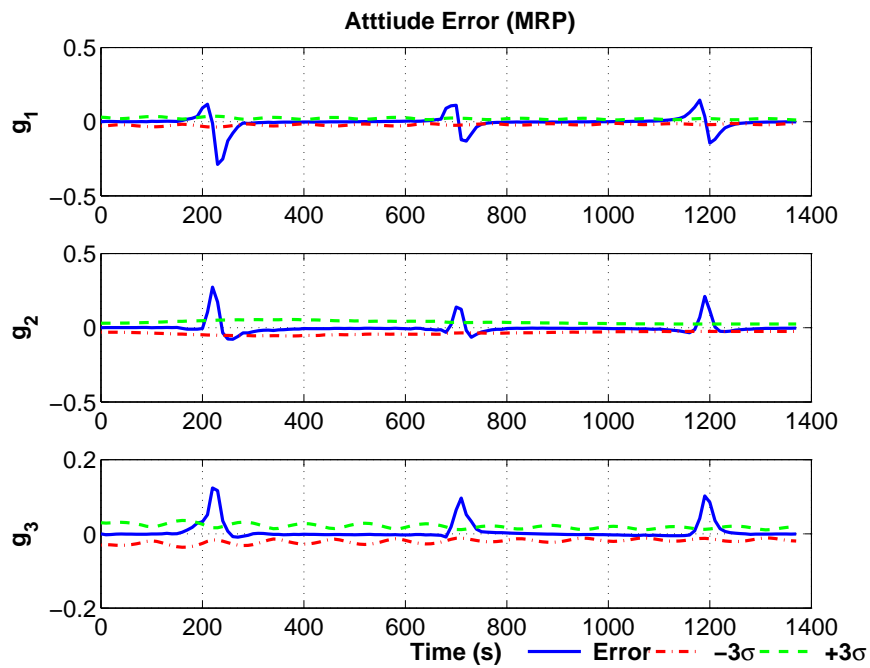


Figure 8.25. UKF Gauss Newton Batch Estimation of Attitude (MRPs).

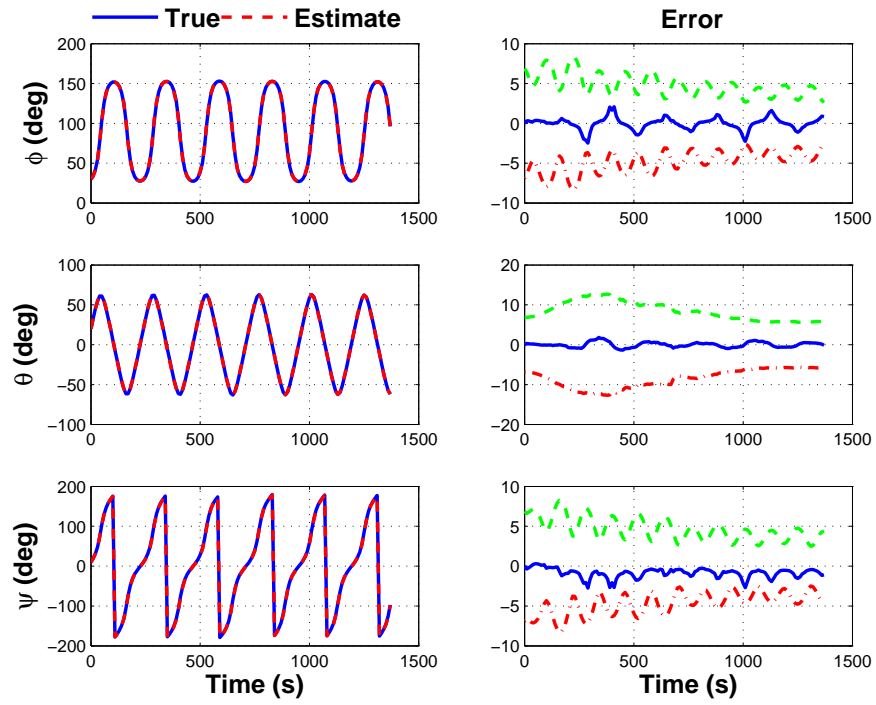


Figure 8.26. UKF Gauss Newton Batch Estimation of Attitude (Euler Angles).

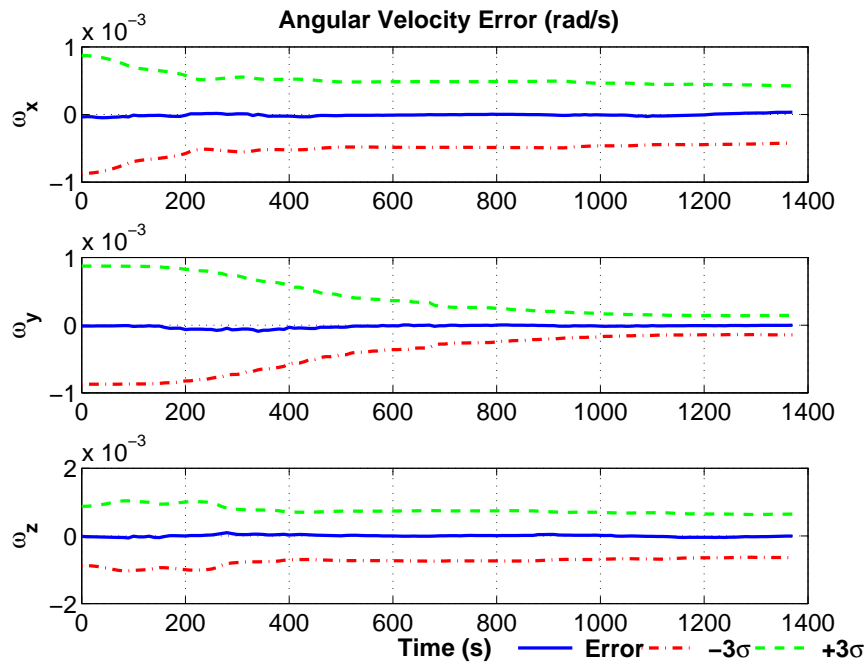


Figure 8.27. UKF Gauss Newton Batch Estimation of Angular Velocity.

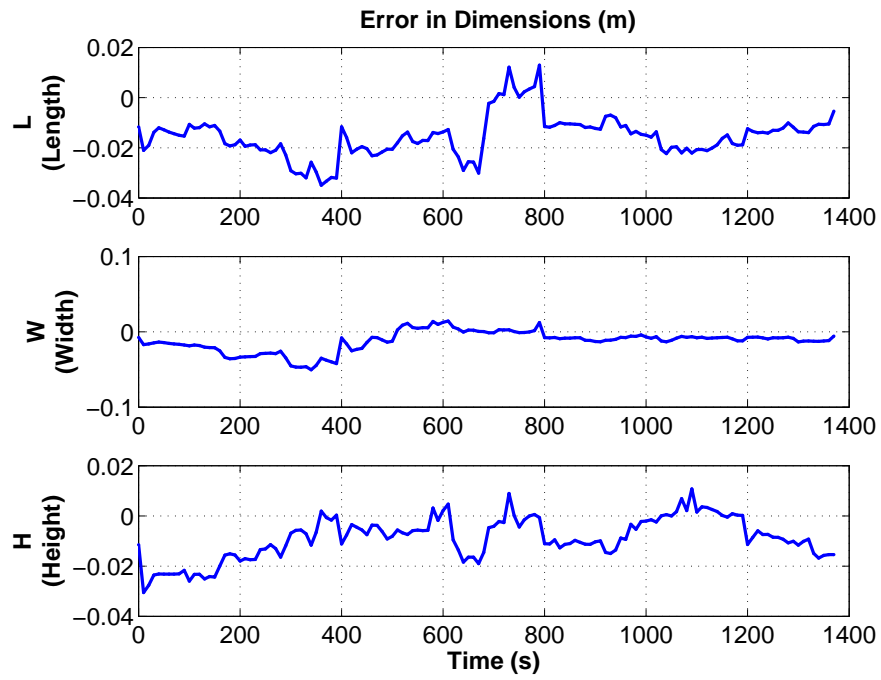


Figure 8.28. UKF Gauss Newton Batch Estimation of Shape/Size Parameters.

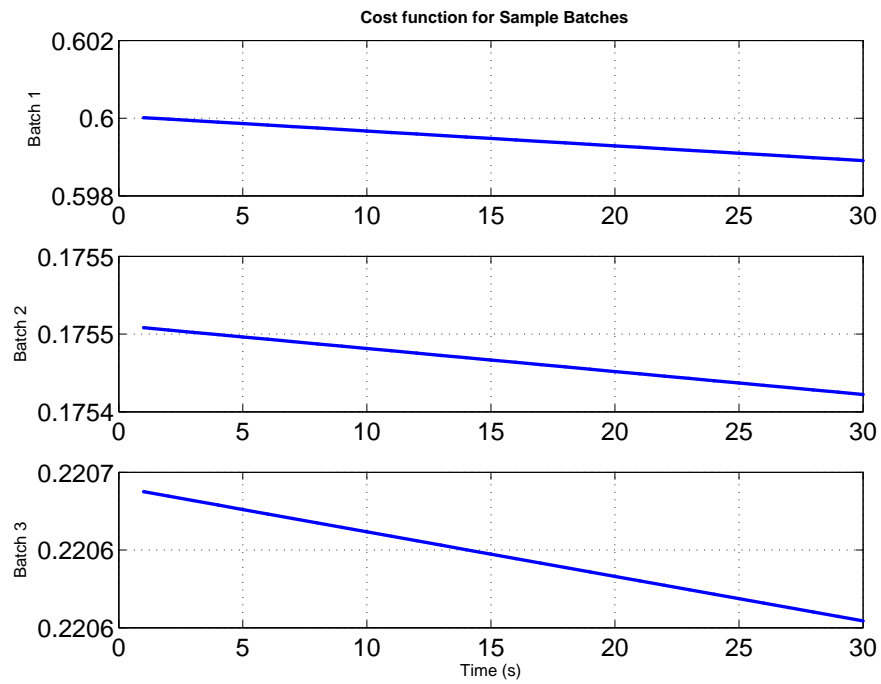


Figure 8.29. UKF Gauss Newton Batch Cost.

## Chapter 9

### Joint Estimation via Bootstrap Particle Filter

This chapter introduces the second solution approach to the combined direct and inverse problem. The bootstrap particle filter (BPF) uses Bayesian estimation to construct the probability density function (pdf) of the state based on all available information [15]. It uses a recursive algorithm where the required density of the state and parameter vector is represented with a set of random samples. These samples are updated and propagated by the filter. This particular filter is not restricted to systems which are nonlinear or with non-Gaussian distributions [15].

The same general description of the discrete-time nonlinear system used in chapter 5 in Equation (5.3) and (5.4) as shown below. Similarly,  $\mathbf{w}(t)$  is a Gaussian white noise process term with zero mean and  $Q(t)$  is the covariance, where the measurement is  $\tilde{\mathbf{y}}_k$  and the measurement noise is  $\mathbf{v}_k$  which has a zero mean Gaussian noise with covariance  $R_k$ . The distributions of the mutually independent  $\mathbf{x}_0$ ,  $\mathbf{w}_k$ , and  $\mathbf{v}_k$ , are denoted  $p(\mathbf{x}_0)$ ,  $p(\mathbf{w}_k)$ , and  $p(\mathbf{v}_k)$  respectively. All three distributions are assumed to be known [14, 15].

$$\begin{aligned}\mathbf{x}_{k+1} &= \mathbf{f}(\mathbf{x}_k, \mathbf{w}_k, \mathbf{u}_k, k) \\ \tilde{\mathbf{y}}_k &= \mathbf{h}(\mathbf{x}_k, \mathbf{u}_k, \mathbf{v}_k, k)\end{aligned}$$

Based on the Bayesian approach, the central idea of this algorithm is to build the posterior density function  $p(\mathbf{x}_{k+1}|\tilde{\mathbf{Y}}_{k+1})$ , where  $\tilde{\mathbf{Y}}_{k+1} = \{\tilde{\mathbf{y}}_0, \tilde{\mathbf{y}}_1, \dots, \tilde{\mathbf{y}}_{k+1}\}$  is the set of acquired measurement from time  $t_0$  up to and including time  $t_{k+1}$ . This pdf can be found recursively by two steps: prediction and update. It is assumed that the pdf

$p(\mathbf{x}_{k-1}|\tilde{\mathbf{Y}}_{k-1})$  at the previous time  $t_{k-1}$  is known. It is possible then, to find the prior pdf of the state at time  $t_k$  by means of the system model.

$$p(\mathbf{x}_k|\tilde{\mathbf{Y}}_{k-1}) = \int p(\mathbf{x}_k|\mathbf{x}_{k-1})p(\mathbf{x}_{k-1}|\tilde{\mathbf{Y}}_{k-1})d\mathbf{x}_{k-1} \quad (9.1)$$

where  $p(\mathbf{x}_k|\mathbf{x}_{k-1})$  is the probabilistic model of the state evolution. It is a Markov model and is defined by the system equations and the known statistics of  $\mathbf{w}_{k-1}$

$$p(\mathbf{x}_k|\mathbf{x}_{k-1}) = \int p(\mathbf{x}_k|\mathbf{x}_{k-1}, \mathbf{w}_{k-1})p(\mathbf{w}_{k-1}|\mathbf{x}_{k-1})d\mathbf{w}_{k-1} \quad (9.2)$$

It is assumed that  $p(\mathbf{w}_{k-1}|\mathbf{x}_{k-1}) = p(\mathbf{w}_{k-1})$ , so that the following expression is obtained, where  $\delta(\cdot)$  is the Dirac delta function. The delta function results because if  $\mathbf{x}_{k-1}$  and  $\mathbf{w}_{k-1}$  are known, then  $\mathbf{x}_k$  can be obtained by Equation (5.3).

$$p(\mathbf{x}_k|\mathbf{x}_{k-1}) = \int \delta(\mathbf{x}_k - \mathbf{f}_{k-1}(\mathbf{x}_{k-1}, \mathbf{w}_{k-1})) \times p(\mathbf{w}_{k-1})d\mathbf{w}_{k-1} \quad (9.3)$$

When a measurement  $\tilde{\mathbf{y}}_k$  is received at time  $t_k$ , then it can be used to update the prior by means of Bayes rule. Equation (9.4) is the the update equation, where the measurement  $\mathbf{y}_k$  modifies the previously predicted prior to obtain the posterior state.

$$p(\mathbf{x}_k|\tilde{\mathbf{Y}}_{k-1}) = \frac{p(\mathbf{y}_k|\mathbf{x}_k)p(\mathbf{x}_k|\tilde{\mathbf{Y}}_{k-1})}{p(\mathbf{y}_k|\tilde{\mathbf{Y}}_{k-1})} \quad (9.4)$$

The normalizing denominator is given by Equation (9.5) and the conditional pdf  $p(\mathbf{x}_k|\mathbf{y}_k)$  is defined by the measurement model and the known statistics of  $\mathbf{v}_k$ .

$$p(\mathbf{y}_k|\mathbf{x}_k) = \int \delta(\mathbf{y}_k - \mathbf{h}_k(\mathbf{x}_k, \mathbf{v}_k))p(\mathbf{v}_k)d\mathbf{v}_k \quad (9.5)$$

## 9.1 Bootstrap Recursive Algorithm

The recursive prediction and update steps presented above have very few analytic solutions. The Kalman filter for instance provides a solution for a linear system

with Gaussian process and measurement noise of known variance [15]. The BPF provides an approximate solution based on Monte Carlo methods. This approximation uses a set of random samples to represent each probability density function. For a given set of random samples  $\mathbf{x}_{k-1}^{(j)}$  drawn from  $p(\mathbf{x})$ ,  $j = 1, \dots, N$ , the distribution can be approximated as shown in Equation (9.6).

$$p(\mathbf{x}) \approx \frac{1}{N} \sum_{j=1}^N \delta(\mathbf{x} - \mathbf{x}^{(j)}) \quad (9.6)$$

An arbitrary integral, or expectation, with respect to the pdf  $p(\mathbf{x})$  can be approximated by Equation (9.7).

$$\int \mathbf{f}(\mathbf{x})p(\mathbf{x})d\mathbf{x} \approx \sum_{j=1}^N \mathbf{f}(\mathbf{x}^{(j)}) \quad (9.7)$$

Because perfect Monte Carlo sampling assumes the samples to be drawn directly from the distribution  $p(\mathbf{x})$ , and this is seldom possible, the BPF uses a technique known as importance sampling. Importance sampling draws  $\mathbf{x}_{k-1}^{(j)}$ ,  $j = 1, \dots, N$  samples from an importance pdf  $q(\mathbf{x})$ . Each sample is weighed by a corresponding importance weight  $w^{(j)}$ . These weights simultaneously satisfy the relations shown in Equation (9.8) to account for the discrepancy between the importance function  $q(\mathbf{x})$  and the target distribution  $p(\mathbf{x})$ .

$$\begin{aligned} w^{(j)} &\propto \frac{p(\mathbf{x}^{(j)})}{q(\mathbf{x}^{(j)})} \\ \sum_{j=1}^N w^{(j)} &= 1 \end{aligned} \quad (9.8)$$

The importance integral is approximated as shown in Equation (9.9)

$$\int \mathbf{f}(\mathbf{x})p(\mathbf{x})d\mathbf{x} \approx \sum_{j=1}^N w^{(j)}\mathbf{f}(\mathbf{x}^{(j)}) \quad (9.9)$$

The importance function is assumed to be of the form shown in Equation (9.10), where  $\mathbf{X}_k^{(j)} = \{\mathbf{x}_0^{(j)}, \mathbf{x}_1^{(j)}, \dots, \mathbf{x}_k^{(j)}\}$  is the set of vectors up to and including  $t_k$ .

$$q(\mathbf{X}_{k+1}^{(j)}|\tilde{\mathbf{Y}}_{k+1}) = q(\mathbf{X}_k^{(j)}|\tilde{\mathbf{Y}}_k)q(\mathbf{x}_{k+1}^{(j)}|\mathbf{X}_{k+1}^{(j)}, \tilde{\mathbf{Y}}_{k+1}) \quad (9.10)$$

The particles at time  $t_{k+1}$  are drawn from the importance density function

$q(\mathbf{x}_{k+1}^{(j)} | \mathbf{X}_{k+1}^{(j)}, \tilde{\mathbf{Y}}_{k+1})$ . The importance weights on  $\mathbf{x}_{k+1}^{(j)}$  are evaluated using Bayes' rule [14]

$$\begin{aligned} p(\mathbf{X}_{k+1}^{(j)} | \tilde{\mathbf{Y}}_{k+1}) &= \frac{p(\tilde{\mathbf{y}}_{k+1} | \mathbf{X}_{k+1}^{(j)}, \tilde{\mathbf{Y}}_k) p(\tilde{\mathbf{X}}_{k+1}^{(j)} | \tilde{\mathbf{Y}}_k)}{p(\tilde{\mathbf{y}}_{k+1} | \tilde{\mathbf{Y}}_k)} \\ &\propto p(\tilde{\mathbf{y}}_{k+1} | \mathbf{x}_{k+1}^{(j)}) p(\mathbf{x}_{k+1}^{(j)} | \mathbf{x}_k^{(j)}) p(\mathbf{X}_k^{(j)} | \tilde{\mathbf{Y}}_k) \end{aligned} \quad (9.11)$$

Consequently, the weights at  $t_{k+1}$  are obtained from substituting Equation (9.11) into (9.8), to obtain the expression shown in Equation (9.12), where  $q(\mathbf{x}_{k+1}^{(j)} | \mathbf{X}_k^{(j)}, \tilde{\mathbf{Y}}_{k+1}) = q(\mathbf{x}_{k+1}^{(j)} | \mathbf{x}_k^{(j)}, \tilde{\mathbf{y}}_{k+1})$  for a Markov process.

$$w_{k+1}^{(j)} = w_k^{(j)} \frac{p(\tilde{\mathbf{y}}_{k+1} | \mathbf{x}_{k+1}^{(j)}) p(\mathbf{x}_{k+1}^{(j)} | \mathbf{x}_k^{(j)})}{q(\mathbf{x}_{k+1}^{(j)} | \mathbf{X}_k^{(j)}, \tilde{\mathbf{Y}}_{k+1})} \quad (9.12)$$

The importance function in the BPF is chosen to be the prior  $p(\mathbf{x}_{k+1} | \mathbf{x}_k^{(j)})$ , which is independent of the previous particle trajectories before  $t_k$  and the measurements. As a result, the importance weight relation shown in Equation (9.12) reduces to

$$w_{k+1}^{(j)} \propto w_k^{(j)} p(\tilde{\mathbf{y}} | \mathbf{x}_{k+1}^{(j)}) \quad (9.13)$$

### 9.1.1 Prediction Step

The prediction step takes the particles at time  $t_k$  and propagates them via the dynamics model, where  $N$  samples  $\mathbf{w}_k^{(j)}$  of the process noise are drawn according to  $p(\mathbf{w}_k)$ , denoted  $\mathbf{w}_k^{(j)} \sim p(\mathbf{w}_k), j = 1, \dots, N$ . In this step, the particle's importance weights remain unchanged.

$$\mathbf{x}_{k+1}^{(j)} = \mathbf{f}(\mathbf{x}_k^{(j)}, \mathbf{w}_k^{(j)}, \mathbf{u}_k, k) \quad (9.14)$$

### 9.1.2 Update Step

The update step consists of obtaining the new importance weights for each particle from the likelihood function, where  $\leftarrow$  denotes the replacement.

$$w_{k+1}^{(j)} = w_k^{(j)} p\left(\tilde{\mathbf{y}}_{k+1} | \mathbf{x}_{k+1}^{(j)}\right) \quad (9.15)$$

$$w_{k+1}^{(j)} \leftarrow \frac{w_{k+1}^{(j)}}{\sum_{j=1}^N w_{k+1}^{(j)}} \quad (9.16)$$

The likelihood function depends on the particular application, for this work the likelihood is shown in Equation (9.19), where

$$\mathbf{e}_{k+1}^{(j)} \equiv \tilde{\mathbf{y}}_{k+1} - \mathbf{h}(\hat{\mathbf{x}}_{k+1}^{(j)}) \quad (9.17)$$

$$P_{k+1}^{e(j)} \equiv E \left\{ \mathbf{e}_{k+1}^{(j)} (\mathbf{e}_{k+1}^{(j)})^T \right\} \quad (9.18)$$

$$p\left(\tilde{\mathbf{y}}_{k+1} | \mathbf{x}_{k+1}^{(j)}\right) = \frac{1}{\det \left[ 2\pi^N P_{k+1}^{e(j)} \right]^{1/2}} \exp \left[ \frac{1}{2} (\mathbf{e}_{k+1}^{(j)})^T \left( P_{k+1}^{e(j)} \right)^{-1} \mathbf{e}_{k+1}^{(j)} \right] \quad (9.19)$$

The mean and covariance at time  $t_k$  are then defined as shown in the equations below

$$\hat{\mathbf{x}}_k \approx \sum_{j=1}^N w_k^{(j)} \mathbf{x}_k^{(j)} \quad (9.20)$$

$$P_k \approx \sum_{j=1}^N w_k^{(j)} \tilde{\mathbf{x}}_k^{(j)} \tilde{\mathbf{x}}_k^{(j)T} \quad (9.21)$$

where  $\tilde{\mathbf{x}}_k^{(j)} = \mathbf{x}_k^{(j)} - \hat{\mathbf{x}}_k$ .

### 9.1.3 Resampling

For an importance function of the form shown Equation (9.9) the variance of the importance weights in sequential importance sampling will only increase over time. This will lead to all but one particle to have negligible weight. Moreover, the previously mentioned prediction and update steps are part of a sequential importance sampling algorithm. Consequently, a resampling step can be introduced to address

the degeneration of the particle's importance weights. This step will discard the particles that have negligible weight. Often a roughening step is also included, which increases the particle diversity. It should be noted that these steps are not necessary for the filter to converge, but do improve the BPF performance.

For applying resampling on every cycle Equation (9.4) reduces to Equation (9.22)

$$w_{k+1}^{(j)} = p(\tilde{\mathbf{y}}|\mathbf{x}_{k+1}^{(j)}) \quad (9.22)$$

The purpose of this step is to prevent the effective sample size  $N_{eff}$  from being too small. The effective sample size is defined as shown in Equation (9.23)

$$N_{eff} = \frac{1}{\sum_{j=1}^N (w_{k+1}^{(j)})^2} \quad (9.23)$$

This step is implemented by drawing  $N$  samples (with replacement) from  $\{\mathbf{x}_{k+1}^{(j)}, w_{k+1}^{(j)}\}$  to yield  $N$  equally weighed particles,  $\{\mathbf{x}_{k+1}^{(j)}, 1/N\}$ , where the number of particles remains unchanged. There are many resampling approaches, for this application systematic resampling is utilized as developed in reference [14]. Systematic resampling uses a cumulative sum element of the weights  $z_{k+1}^{(i)}$  as shown below.

$$z_{k+1}^{(i)} = \sum_{j=1}^i w_{k+1}^{(j)} \quad (9.24)$$

This method draws a single uniform sample  $v_{k+1}$  from an interval  $(0, 1]$ , where  $u_{k+1}^{(j)}$  is computed for  $j = 1, 2, \dots, N$

$$u_{k+1}^{(j)} = \frac{(j-1) + v_{k+1}}{N} \quad (9.25)$$

Then for  $i = 1$  the following steps are performed for  $j = 1, 2, \dots, N$  to create the resampled particles [14].

```

if  $u_{k+1}^{(j)} \leq z_{k+1}^{(i)}$  then
  |  $\mathbf{x}_{k+1}^{(j)} \leftarrow \mathbf{x}_{k+1}^{(i)}$   $j \leftarrow j + 1$ 
else
  |  $i \leftarrow i + 1$ 
end

```

## 9.2 Numerical Setup

The initial conditions for the simulated true values are shown Table 9.1. These initial conditions are the same as the ones used for the UKF experiments. The object is selected to be at an attitude that will provide good observability as it orbits. As it was shown in chapter 6, an initial condition which leads to the observer having visibility of all faces provides better observability. In a similar fashion to the UKF experiments, these true values are also used to produce synthetic measurements for azimuth, elevation, and light curve.

The initial conditions for the experiment are shown in Table 9.1. The estimator initial conditions were set as shown in Table 9.2, note that these values are slightly larger than those used for the UKF experiment. The synthetic measurements were created using zero-mean white noise error process with standard deviation of 2 arc-seconds for elevation and azimuth. The light curve measurement has an error process with standard deviation of 0.1 magnitude. The measurements were acquired every 10 seconds. The synthetic measurements were created using the Cook-Torrance BRDF. This same model was used for the estimator measurement model. The results shown were obtained using 800 particles and resampling at each cycle, and are the averaged results of 10 runs.

Table 9.1. Initial Conditions for BPF Joint Estimation

State/Parameter		Initial Value (unit)
Position	$\mathbf{r}_0$	$[4764.48 \ 4764.48 \ 0]^T$ ( $km$ )
Velocity	$\mathbf{v}_0$	$[-5.2533 \ 5.2533 \ 1.9906]^T$ ( $km/s$ )
Angular Velocity	$\boldsymbol{\omega}_0$	$[0 \ 0.00262 \ 0]^T$ ( $rad/s$ )
Attitude	$\mathbf{q}_0$	$[0.23929 \ 0.18930 \ 0.03813 \ 0.95154]^T$
	$[\phi_0 \ \theta_0 \ \psi_0]$	$[30 \ 20 \ 10]^T$ ( $deg$ )
Shape/Size	$\mathbf{p}_0$	$[5 \ 3 \ 4]^T$ ( $m$ )

Table 9.2. Initial Error and Error Covariance for BPF Joint Estimation

State/Parameter		Initial Error (unit)	Error Covariance (unit)
Position	$\mathbf{r}_0$	10 ( $km$ )	$10^2$ ( $km^2$ )
Velocity	$\mathbf{v}_0$	0.1 ( $km/s$ )	$0.1^2$ ( $km^2/s^2$ )
Angular Velocity	$\boldsymbol{\omega}_0$	60 ( $deg/hr$ )	$60^2$ ( $deg^2/hr^2$ )
Attitude	$[\phi_0 \ \theta_0 \ \psi_0]$	5 ( $deg$ )	$5^2$ ( $deg^2$ )
Shape/Size	$\mathbf{p}_0$	0.2 ( $m$ )	$0.2^2$ ( $m^2$ )

Figures 9.1–9.4 show the values for the true position, velocity, attitude, and angular velocity. Similarly to the UKF joint estimation, the perturbation effects for drag, solar radiation pressure, gravity gradient, and aspherical Earth were included as shown in Figures 9.5 and 9.6.

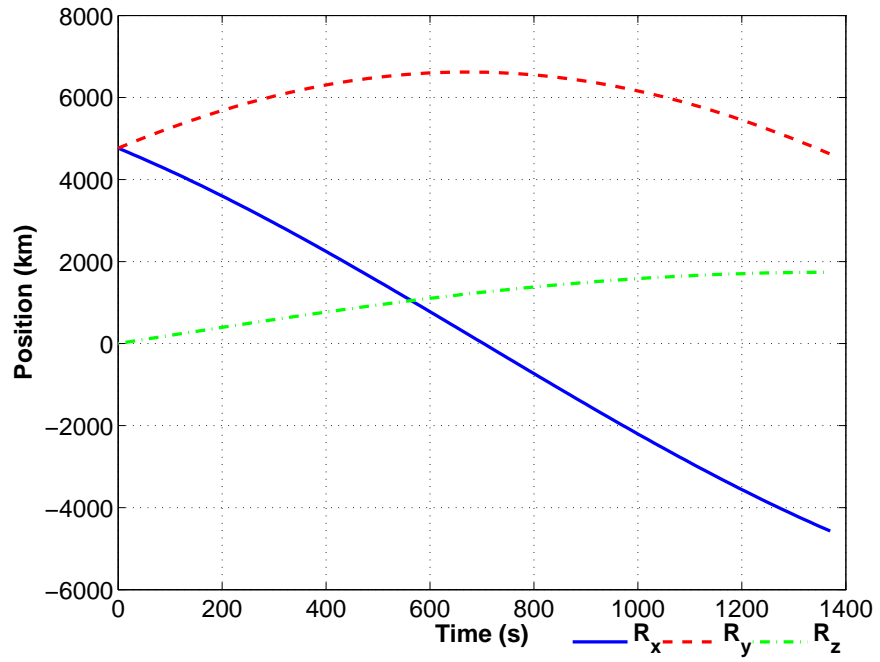


Figure 9.1. BPF Joint Estimation True Object Position.

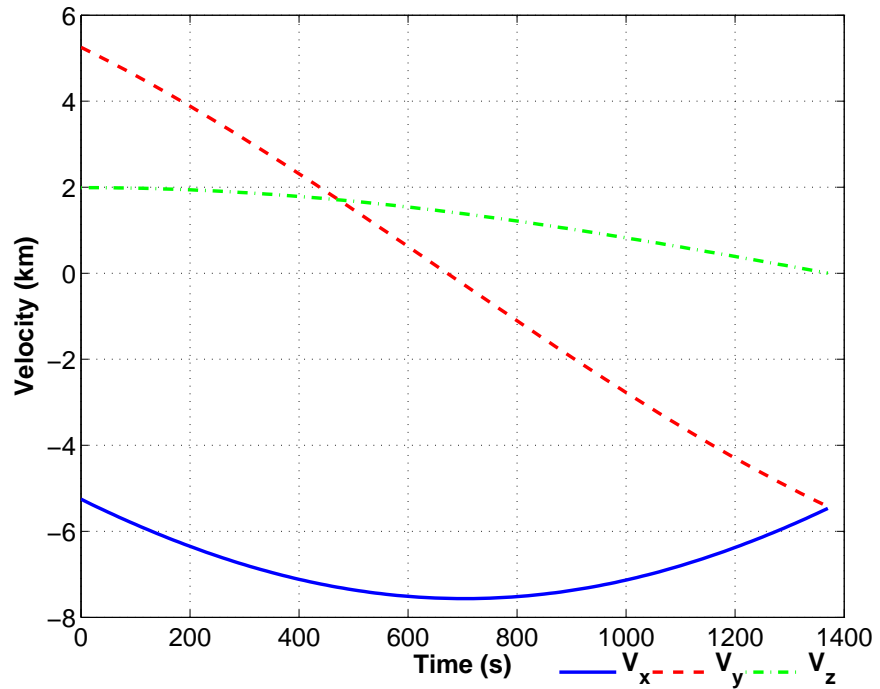


Figure 9.2. BPF Joint Estimation True Object Velocity.

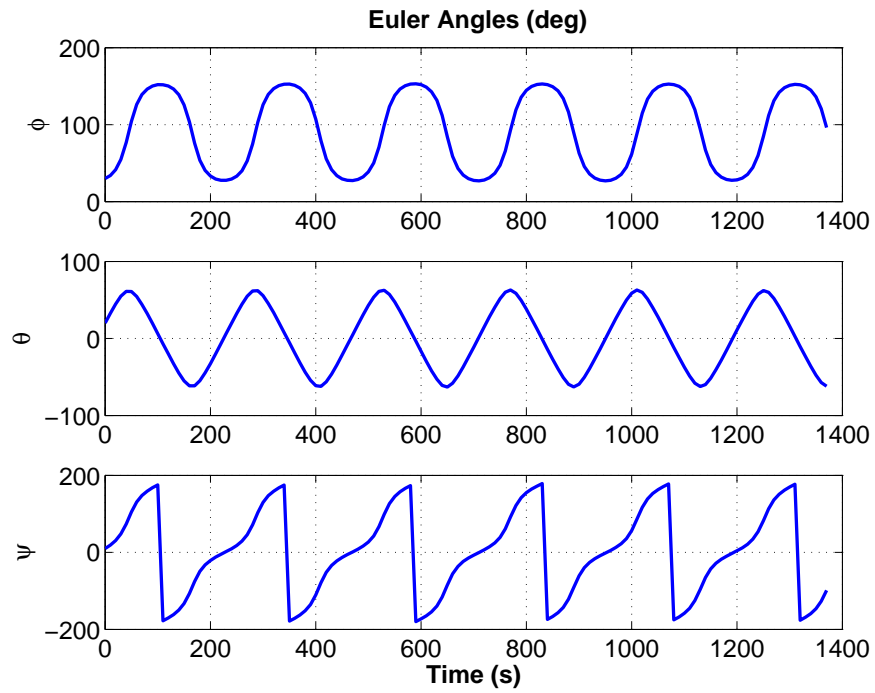


Figure 9.3. BPF Joint Estimation True Object Euler Angles.

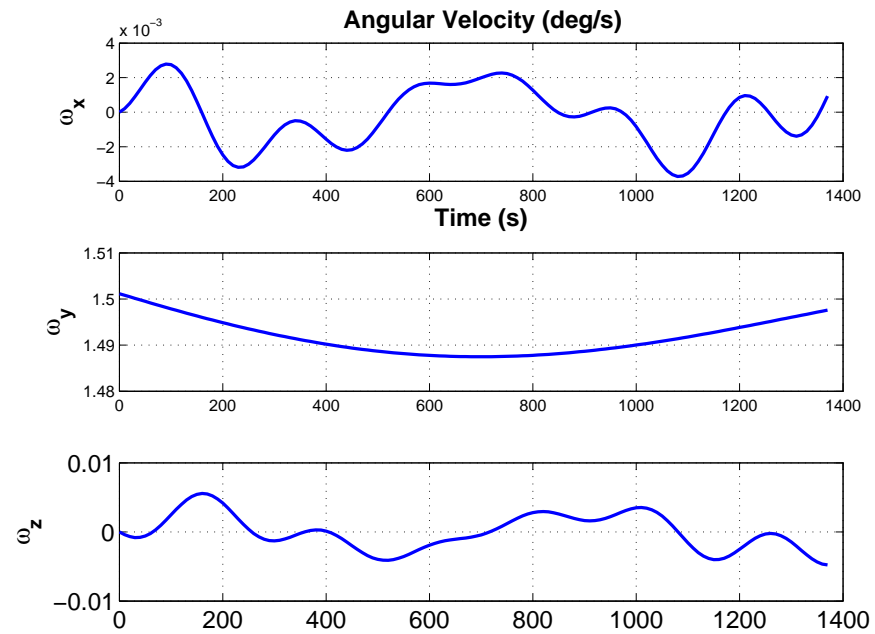


Figure 9.4. BPF Joint Estimation True Object Angular Velocity.

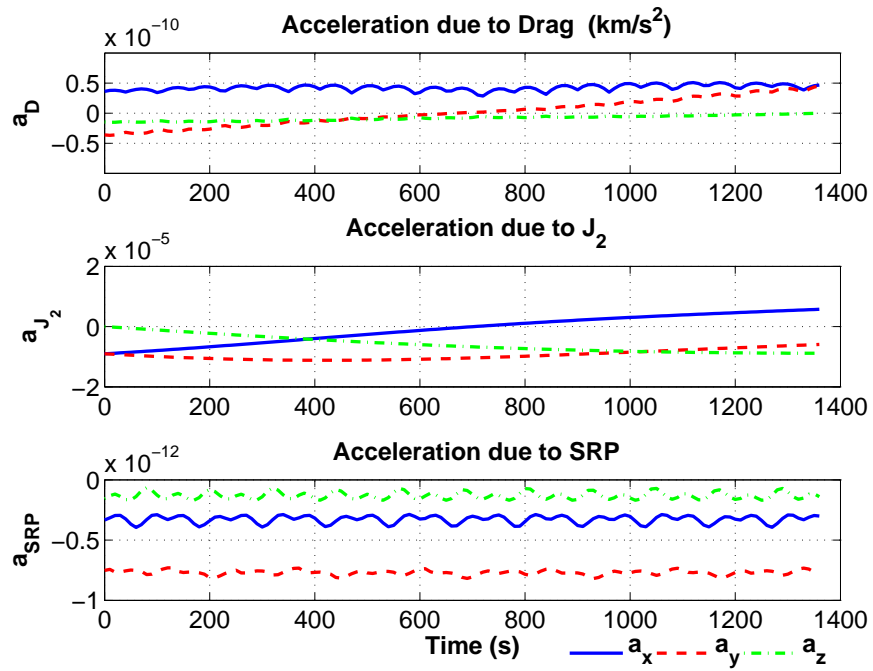


Figure 9.5. BPF Joint Estimation Perturbation Accelerations.

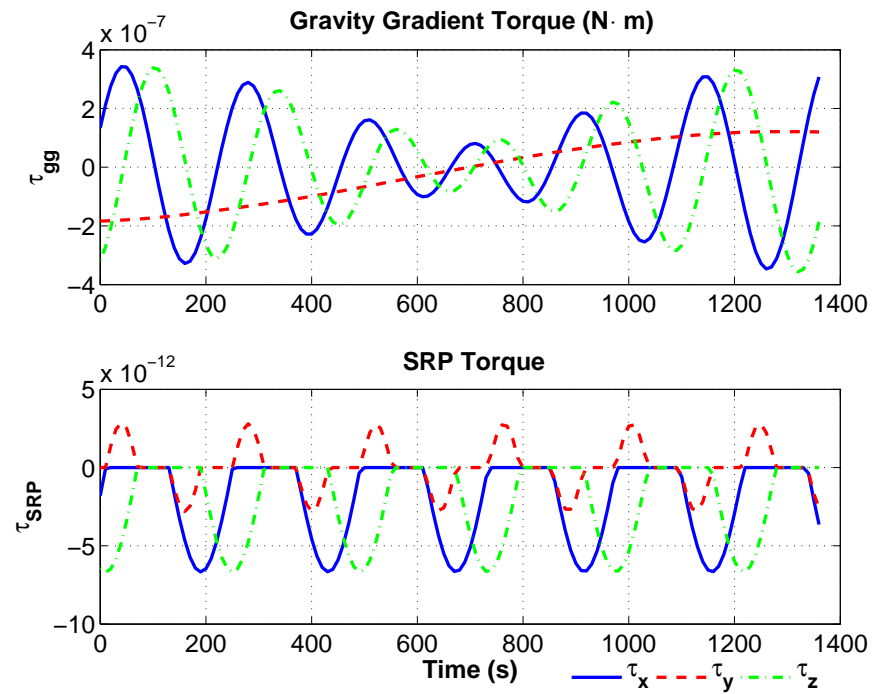


Figure 9.6. BPF Joint Estimation Perturbation Torques.

### 9.3 Results and Discussion

The BPF was used to estimate the states and parameters for the combined direct and inverse problem. Figure 9.7 shows the estimation of the position. The  $3\sigma$  bounds for this state are very large, although the state error for the  $y$  and  $z$  components remains somewhat small. It should be noted that the estimation of the  $x$  position component is poor. On the contrary, the estimation of the velocity for all three components is quite good as shown in Figure 9.8, although the error in the  $x$  component touches the  $3\sigma$  bound it reduces. The bounds grow and reduce with the change in error, but remain bounded. The angular velocity estimation show in Figure 9.9 for MRPs and starts with very small errors of all three parameters but the errors begin to grow every time the MRPs change phase. A similar behavior is seen in Figure 9.10 for Euler angles, where the errors grow after the 800 seconds. This is particularly clear for the yawing angle  $\psi$  where the tracking is out of sync and the errors grow quickly. Nevertheless, the estimation of the angular velocity is very good, the errors remain small and bounded through the entire simulation. Finally, the estimation of the shape/size parameters is good for the length and height where it remains below 5 centimeters for the entire simulation. The width parameter settles at a value of 20 centimeters. Although the results for the position and attitude are are not as good as the ones obtained from the UKF experiments, the BPF is able to estimate the velocity and angular velocity very well. Moreover, two of the object parameters are estimated well. The weights some sample times have been shown in Figure 9.14, to show the effect of resampling. Where the weights are well distributed over all the particles.

Table 9.3 shows the estimation error for all joint estimation approaches: UKF, UKF-bach, and BPF. It can clearly be seen that the UKF-batch with Gauss-Newton algorithm performs the best for the estimation of all the the shape/size parameters.

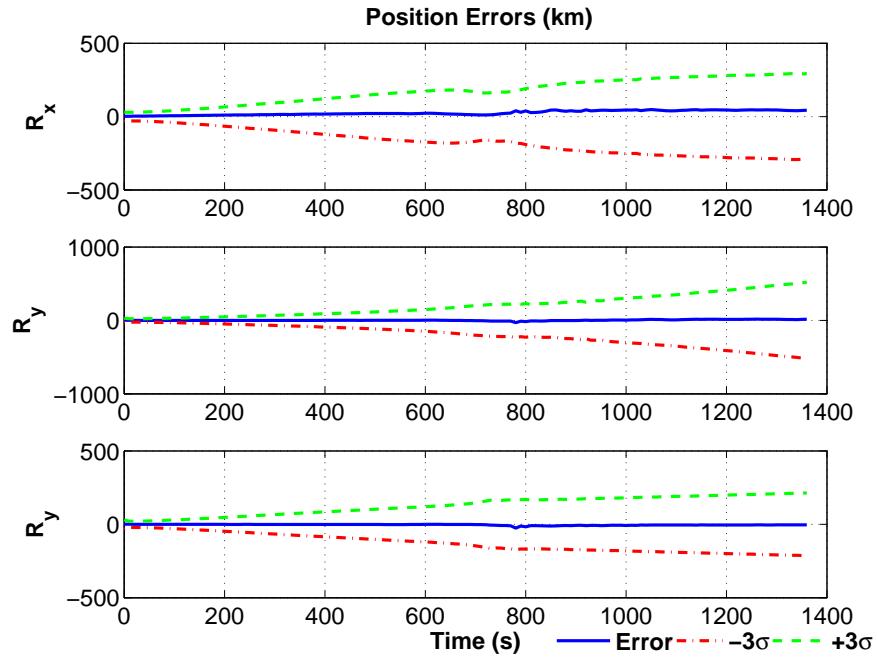


Figure 9.7. BPF Joint Estimation of Position.

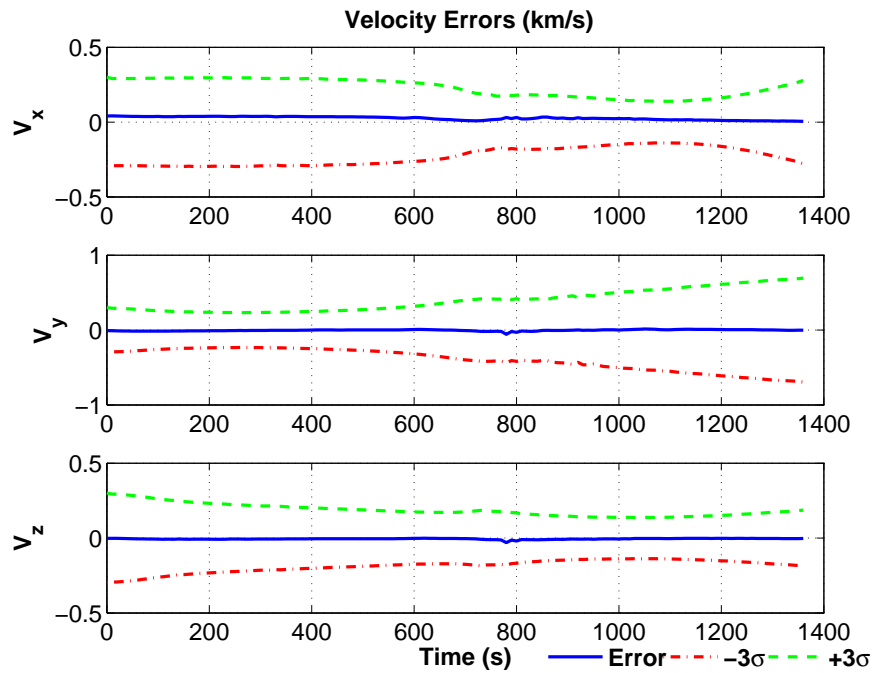


Figure 9.8. BPF Joint Estimation of Velocity.

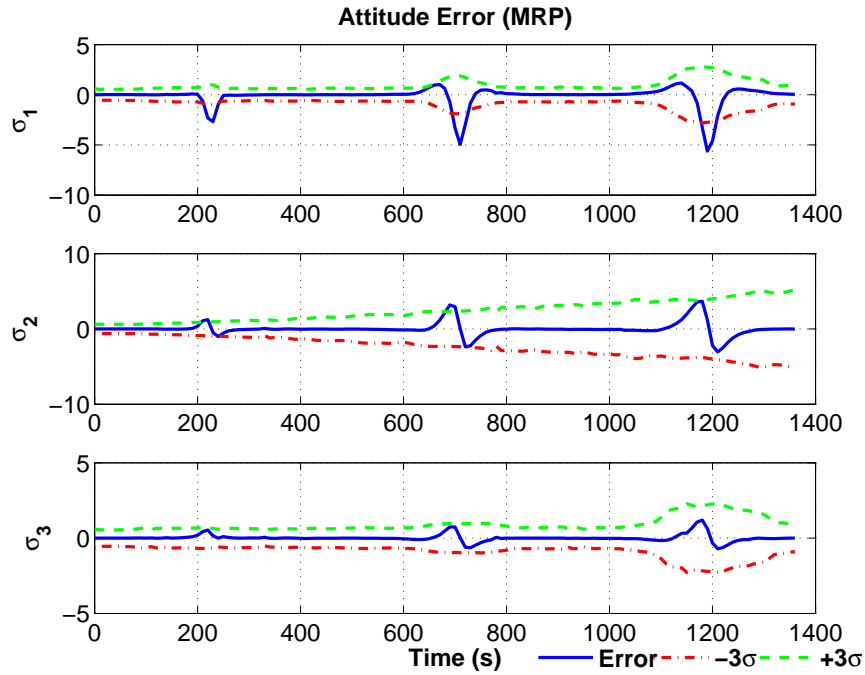


Figure 9.9. BPF Joint Estimation of Attitude (MRPs).

Nevertheless, this is a computationally expensive approach. Moreover, the BPF is able to estimate one of the parameters very well, but fails to have that same performance with the other two. The performance of this filter could be greatly improved with a larger number of particles, as the number of states is large. The performance could be further improved with the added step of roughening, to increase particle diversity. The BPF, similarly to the UKF-batch, is a computationally expensive algorithm. Given the computational price paid to achieve the results yielded by the BPF, it might not be a wise choice as an estimator for this application. The UKF estimates all three parameters with reasonable errors. This approach is the least computationally expensive.

The estimation of the other states is comparable for the UKF and UKF-Batch estimation, where the position, velocity, angular velocity, and attitude are well estimated by all three approaches. On the other hand, it is not able to estimate the

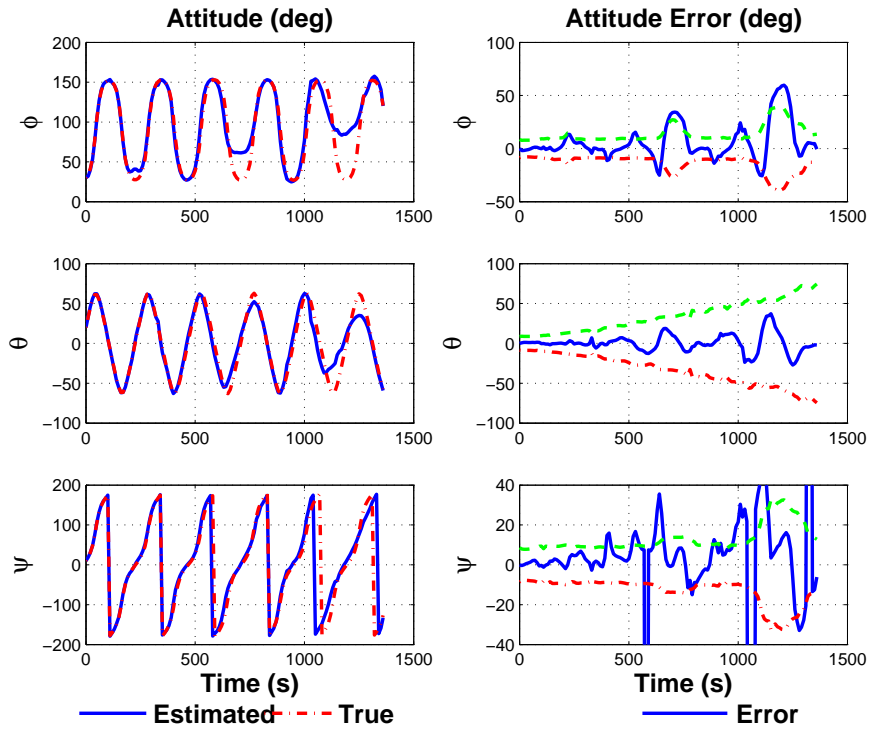


Figure 9.10. BPF Joint Estimation of Attitude (Euler Angles).

Table 9.3. Shape/Size Parameter Final Estimation Error (cm) Summary

<b>p</b>	UKF	UKF-Batch LM	UKF-Batch GN	BPF
Length	2.14	4.69	1.12	0.417
Width	2.02	0.61	1.05	7.49
Height	3.16	1.23	1.26	5.88
Norm	4.32	4.89	1.99	9.53

position and attitude as closely as the UKF based approaches. For this particular application, the UKF has a good performance across all states and parameters and is the least computationally expensive, making it the preferable approach. If computational power is not an issue, the UKF-Batch with the Gauss-Newton cost minimization should be the preferred approach. It should be noted that for all of these experiments the ‘inverse crime’ is committed. As it was shown in the results for

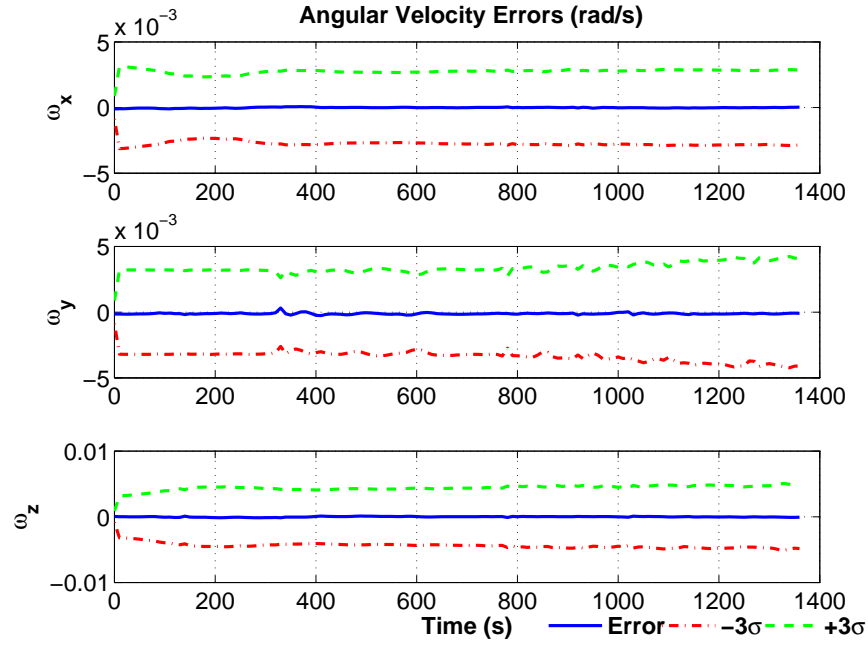


Figure 9.11. BPF Joint Estimation of Angular Velocity.

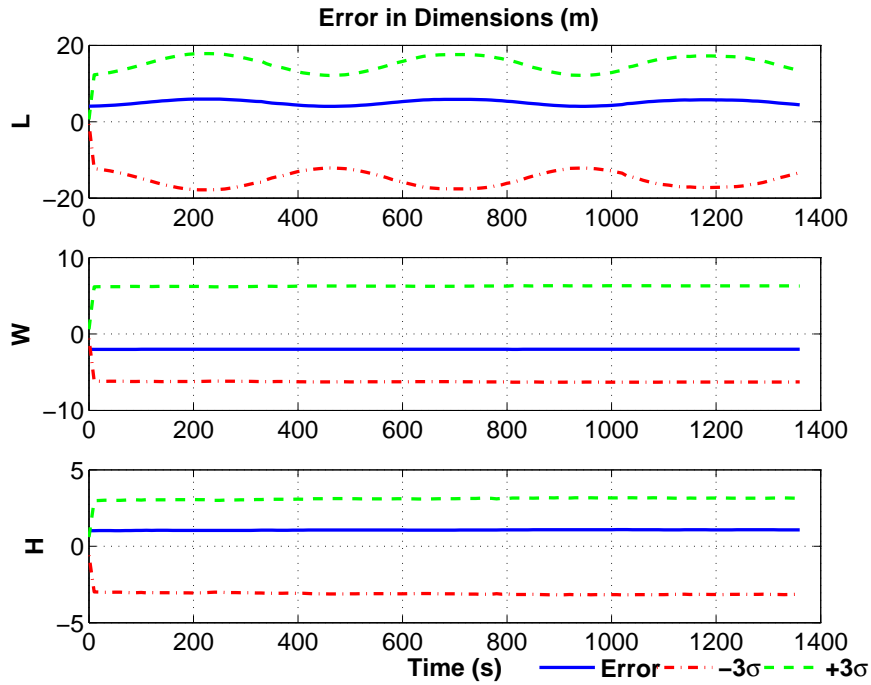


Figure 9.12. BPF Joint Estimation of Shape/Size Parameters.

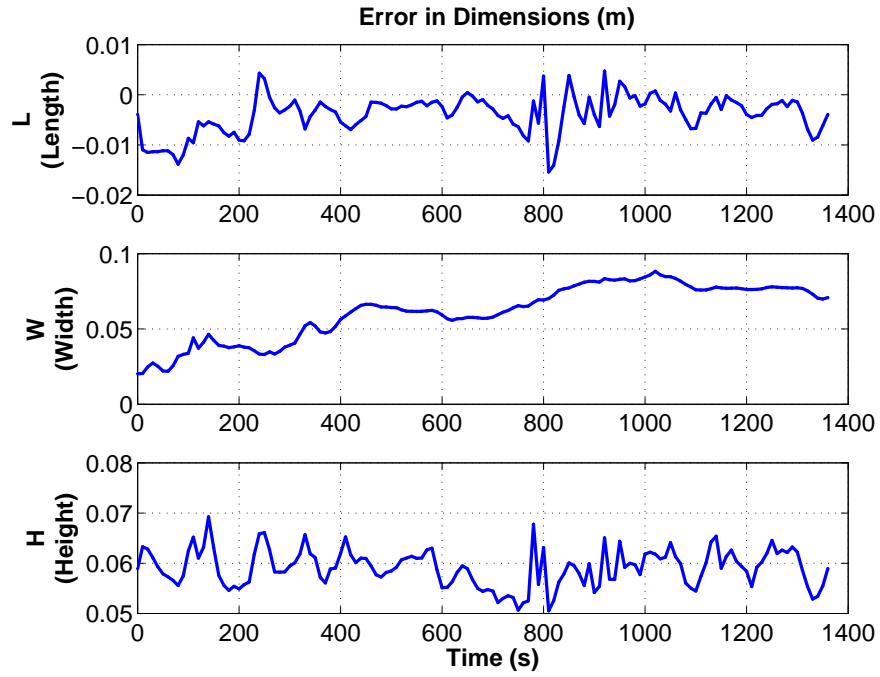


Figure 9.13. BPF Joint Estimation of Shape/Size Parameter (no  $3\sigma$  bounds).

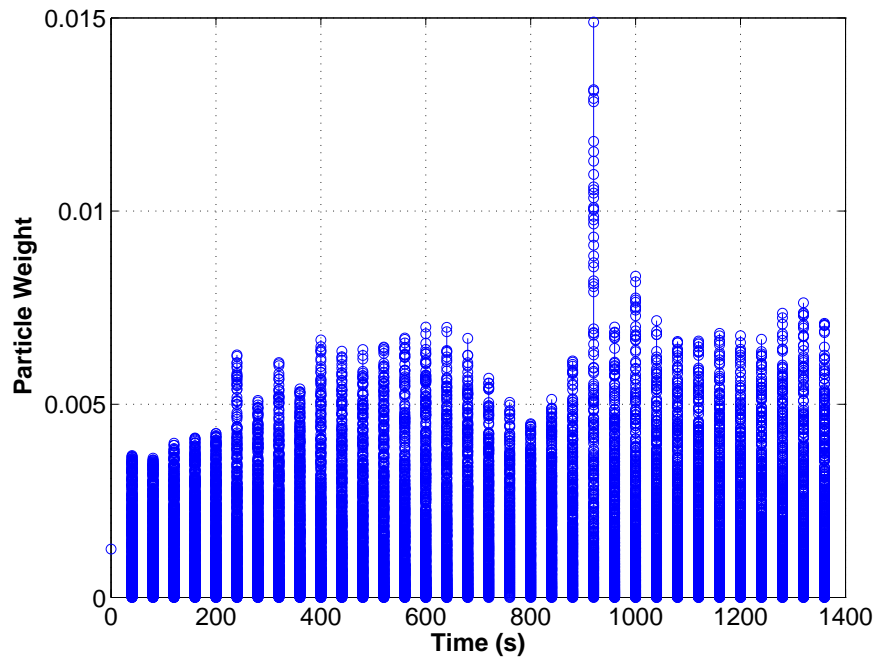


Figure 9.14. BPF Joint Estimation Importance Weights.

chapter 7, if a different model is chosen for the synthetic measurements the results will worsen for all experiments.

## Chapter 10

### Summary and Closing Remarks

This work has shown a comprehensive solution to the combined inverse and direct problem for the estimation of states, shape, and size of a resident space object. Particular detail was given to the modeling of the dynamics, perturbation models, and the measurement models. Sensitivity and observability analyses were performed for the light curve measurement with respect to the angular velocity, attitude, and shape/size parameters. Moreover, three different estimation technique experiments were performed.

A detailed description of the dynamics and kinematics of the resident space object was developed. This model included perturbations due to atmospheric drag, solar radiation pressure, gravity gradient, and aspherical Earth. These models were included as functions of the shape/size parameters of the object in the form of surface area, mass, and inertia matrix.

An extensive study of the light reflection model used in the light curve model was done. This allowed the selection of a well suited BRDF model for the purpose of solving the inverse problem. This light reflectance analysis dealt with a sensitivity and observability analysis. These studies also yielded insight into the light curve measurement and the information it contains. Given the results obtained, it was established that the light curve measurement does not contain information about the angular velocity state. Moreover, it was concluded that information regarding this state is estimated based on the dynamical model given to the estimation algorithm. The attitude and the shape/size parameters sensitivity and observability was also

studied. It was shown that the light curve measurement contains significant information regarding these states and parameters. Nevertheless, the information in this measurement can be greatly affected by the geometry of the observation, as well as, the modeling of the BRDF. The initial conditions, which determine the geometry of the observation, can cause portions of the object to be hidden from the observer on Earth. If part of the object is obscured to the viewer, the information regarding these states and parameters is limited. On the contrary, if the initial conditions allows a full view of the object, the light curve is rich in information and the estimation of these states and parameters will improve significantly.

The first set experiments addressed the inverse problem, where the angular velocity, attitude, and shape/size parameters are estimated while the position and velocity of the object are known (i.e. the orbit is known). The solution to this problem also involved the investigation of the ‘inverse crime’ (model integrity), where the same light curve model is used to produce the synthetic measurements and estimation measurement model. This study yielded results that clearly show that if the so called ‘inverse crime’ is committed, the estimation of the mentioned states and parameters will be significantly better than if two distinct models are used. Consequently, if the same model is used for the synthetic measurements and light curve inversion the problem will be less ill posed and the results will be more optimistic than what is to be expected by using ‘real’ measurements.

The second set of experiments dealt with the estimation of the object’s states and parameters for the combined direct and inverse problem using two estimation algorithms: the unscented Kalman filter and the bootstrap particle filter. The UKF filter has the capability of dealing with nonlinear dynamic models and measurement models. Three experiments were performed for the estimation. The first was a joint estimation of all states and parameters by the UKF. The second and third exper-

iments implemented the UKF along with a batch estimation loop. The shape/size parameters were fed to a batch estimation loop which reduced a cost function. The cost reduction was performed using two different methods: Levenberg-Marquardt and Gauss-Newton. It was shown that the Gauss-Newton method based batch estimation experiments yielded better results for the shape/size parameters than the other two UKF methods. This result indicates the Gauss-Newton batch estimation is a better estimation tool than the UKF alone. Nevertheless, it should be noted this methodology is significantly more computationally expensive than the UKF.

The second estimation approach for the combined problem was the BPF. This filter uses a set of random samples to represent the probability density function of the states. Similarly, to the UKF and UKF-Batch this filter was able to estimate the velocity and angular velocity very well. Nevertheless, it was not able to perform as well in the estimation of the position and attitude. Moreover, the estimation of one of the shape/size parameters was better than the estimate of the UKF and UKF-Batch but the other two shape/size parameters were worse. This can be attributed to the number of particles used. Increasing the number of particles could significantly improve the filter performance. Although this may increase the computational cost, the process can be easily parallelized to mitigate the effect of a large particle population. This filter was implemented to present an alternative nonlinear estimation technique. Further study and improvement of this scheme is left for future work.

The work presented here has demonstrated that the combined direct and inverse problem can be efficiently solved by various estimation techniques. Although the information regarding the attitude and shape/size parameters contained in the light curve can be limited, the estimation algorithms presented here are capable of reaching good estimation values for these states and parameters. Furthermore, it should be

noted that the geometry of the observation, as well as, the light curve model integrity greatly affect the estimation of the attitude and shape/size.

Finally, future work should focus on the development of more efficient and physically accurate light curve models. As previously mentioned, the current models are based on computer graphics rendering. Better light curve models could significantly improve upon the results of the inverse problem. This is especially true when dealing with acquired light curves. In addition, further research should be done regarding the statistics of this system. The solutions for the inverse and direct problem up to now have assumed that the statistics of the system are Gaussian. Nevertheless, this could be a gross simplification.

## APPENDIX A

### Light Curve BRDF Analysis Tables and Plots

## A.1 Light Curve Material Data

The tables below contain the material parameters obtained by reference [1]. The diffuse red, green, and blue are  $d_r$ ,  $d_g$ , and  $d_b$  respectively. The specular components are denoted  $s_r$ ,  $s_g$ , and  $s_b$ . The model specific parameters are listed as  $p_0$ ,  $p_1$  and  $p_2$ .

Table A.1. Brushed Aluminium Experimental Data Model Parameters [1]

Model	$d_r$	$d_g$	$d_b$	$s_r$	$s_g$	$s_b$	$p_0$	$p_1$	$p_2$
Wa	0.0357	0.0304	0.0251	0.0708	0.0537	0.026	0.00845	0	0
Wa-Dü	0.0418	0.0356	0.0272	0.0461	0.0344	0.017	0.00785	0	0
Bl-Ph	0.0335	0.028	0.0244	0.0243	0.0187	0.00893	2.43e4	0	0
La	0.0335	0.0287	0.024	0.0759	0.0576	0.0281	-0.577	0.577	7.51e3
Co-To	0.0418	0.0356	0.0273	0.0799	0.06	0.0294	0.59	0.00776	0
He	0.0326	0.028	0.0241	0.0912	0.0693	0.0332	33.1	0.146	14.4
As-Sh	0.0429	0.0363	0.0277	0.0454	0.0341	0.0167	0.999	3.41e4	0

Table A.2. Black Oxidized Steel Experimental Data Model Parameters [1]

Model	$d_r$	$d_g$	$d_b$	$s_r$	$s_g$	$s_b$	$p_0$	$p_1$	$p_2$
Wa	0.0108	0.00876	0.00596	0.0369	0.0298	0.0194	0.198	0	0
Wa-Dü	0.00929	0.00768	0.00534	0.0265	0.0213	0.0137	0.181	0	0
Bl-Ph	0.0192	0.0156	0.0104	0.00692	0.00559	0.00365	62	0	0
La	0.0264	0.0215	0.0143	0.324	0.257	0.165	-0.608	0.51	72.5
Co-To	0.0186	0.0152	0.0102	0.229	0.182	0.117	0.035	0.19	0
He	0.0194	0.0159	0.0106	0.949	0.757	0.488	4.05	0.481	1.17
As-Sh	0.0165	0.0136	0.00918	0.299	0.237	0.153	0.0488	43.9	0

Table A.3. Black Plastic Experimental Data Model Parameters [1]

Model	$d_r$	$d_g$	$d_b$	$s_r$	$s_g$	$s_b$	$p_0$	$p_1$	$p_2$
Wa	0.00357	0.00288	0.00204	0.0315	0.0259	0.0175	0.331	0	0
Wa-Dü	0.00373	0.00309	0.00221	0.0204	0.0166	0.0112	0.32	0	0
Bl-Ph	0.0173	0.0142	0.00972	0.0014	0.00114	0.000769	192	0	0
La	0.0122	0.01	0.00692	0.11	0.0894	0.0601	-0.638	0.431	14.1
Co-To	0.00601	0.005	0.00352	0.0939	0.0765	0.0515	0.136	0.325	0
He	0.00635	0.00528	0.00371	0.127	0.103	0.0693	11.9	1.73	2.03
As-Sh	7.2e-5	8.58e-5	0.000196	0.0325	0.0266	0.018	0.903	13.6	0

## A.2 Sensitivity Plots

The plots in this section correspond to the numerical and UKF observation matrices as derived in section 6.4 for the BRDF models described in section 6.3. For each of these models a comparison of the observation matrix obtained via the numerical Jacobian  $\mathbf{H}_{NUM}$  and the UKF based observation matrix  $\mathbf{H}_{UKF}$  is shown for the angular velocity, attitude, and shape/size. In addition, plots for the numerically and UKF based Gramian are shown. Each of these plots are shown for the low observability case 1 and high observability case 2, as described in section 6.6.

### A.2.1 Ward Model

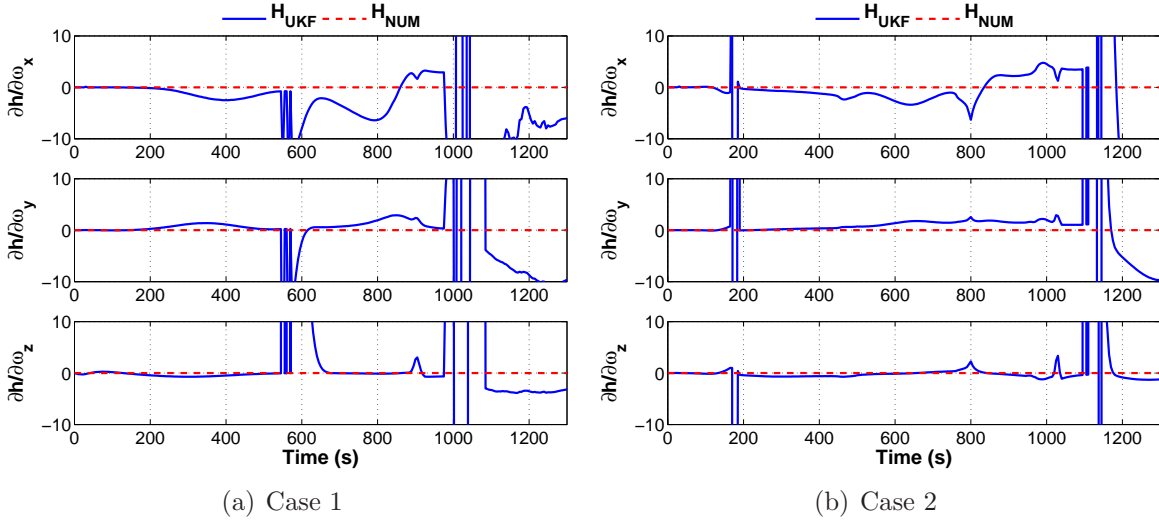


Figure A.1. Ward Model Angular Velocity Sensitivity.

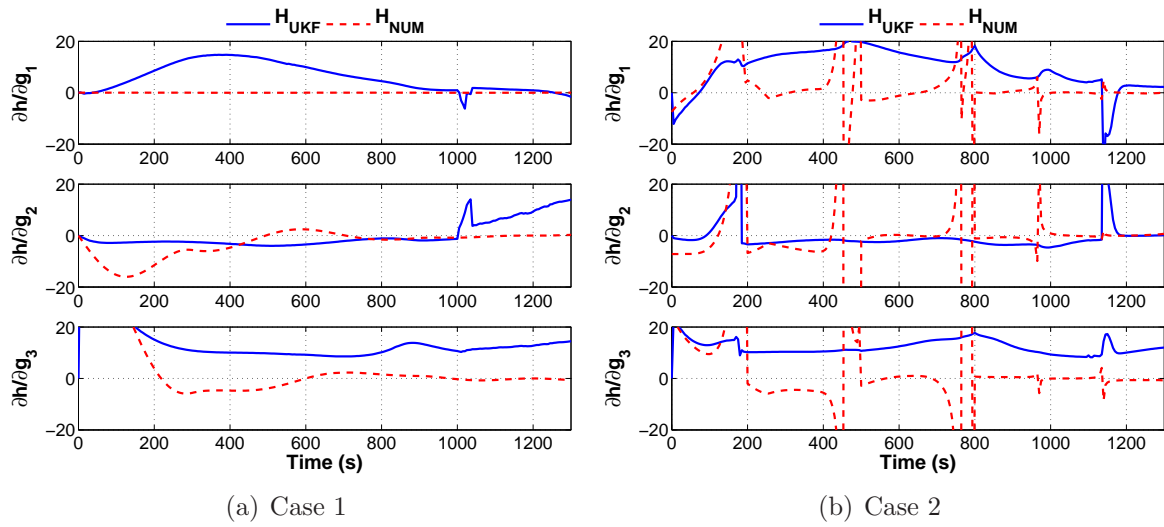


Figure A.2. Ward Model Attitude Sensitivity.

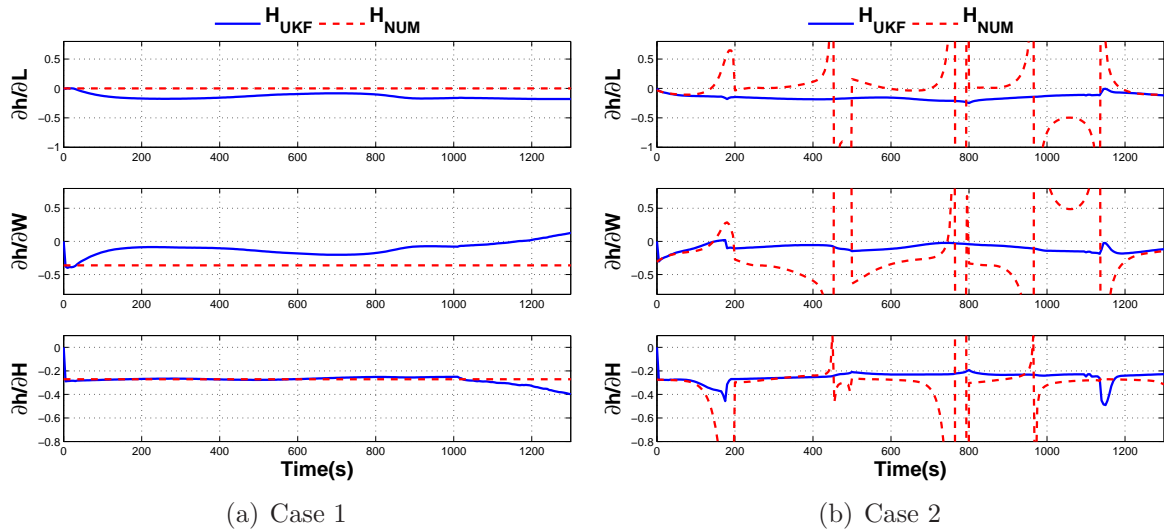


Figure A.3. Ward Model Shape/Size Parameters Sensitivity.

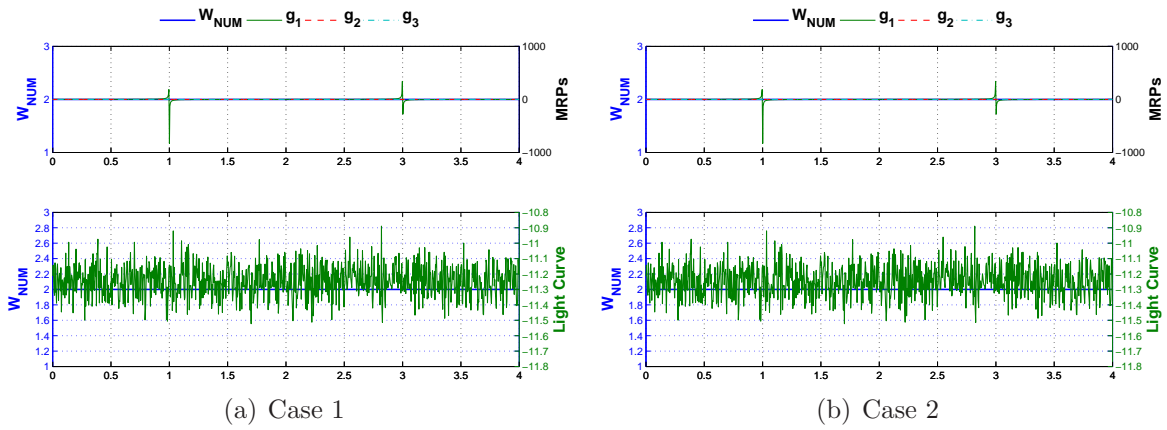


Figure A.4. Ward Model Numerical based Gramian.

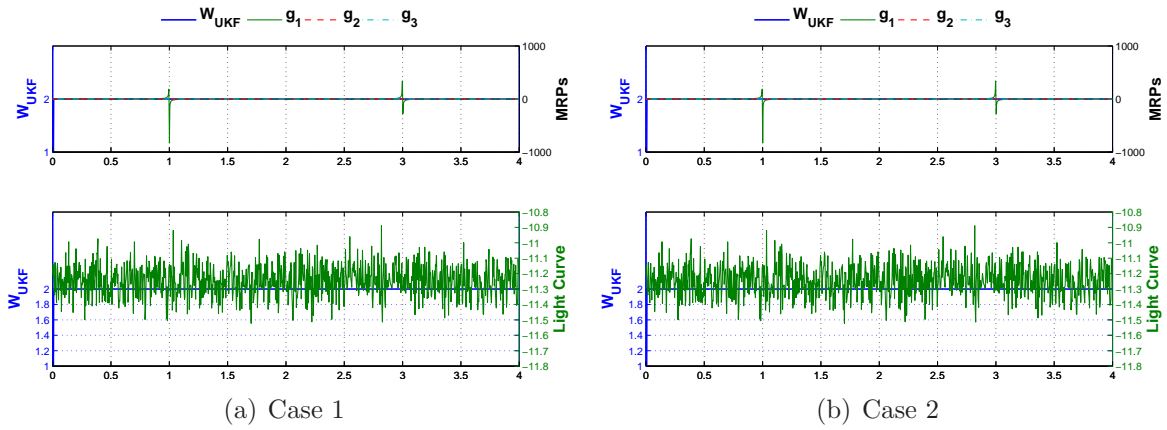


Figure A.5. Ward Model UKF based Gramian.

### A.2.2 Ward-Dür Model

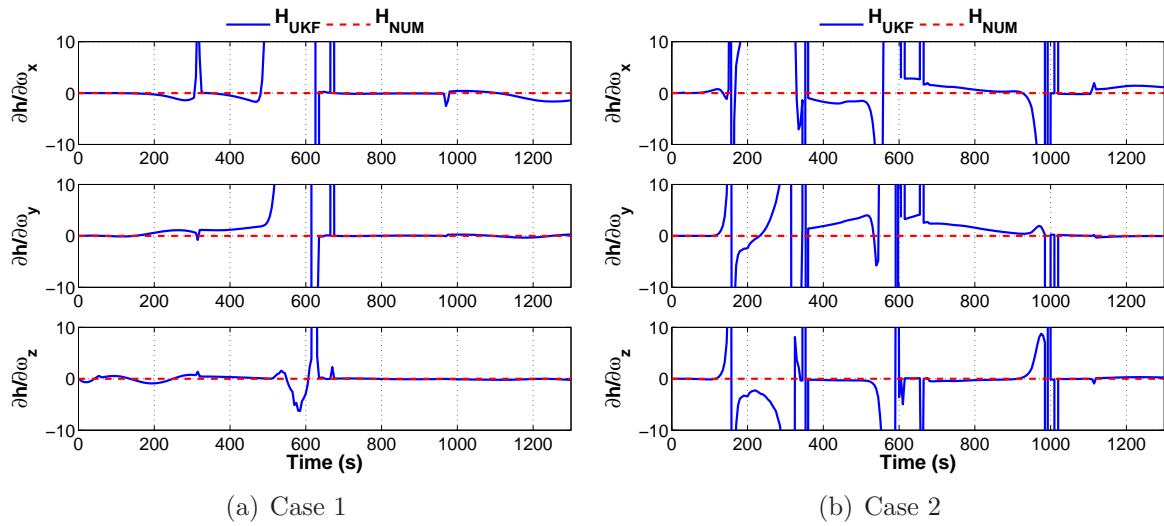


Figure A.6. Ward-Dür Model Angular Velocity Sensitivity.

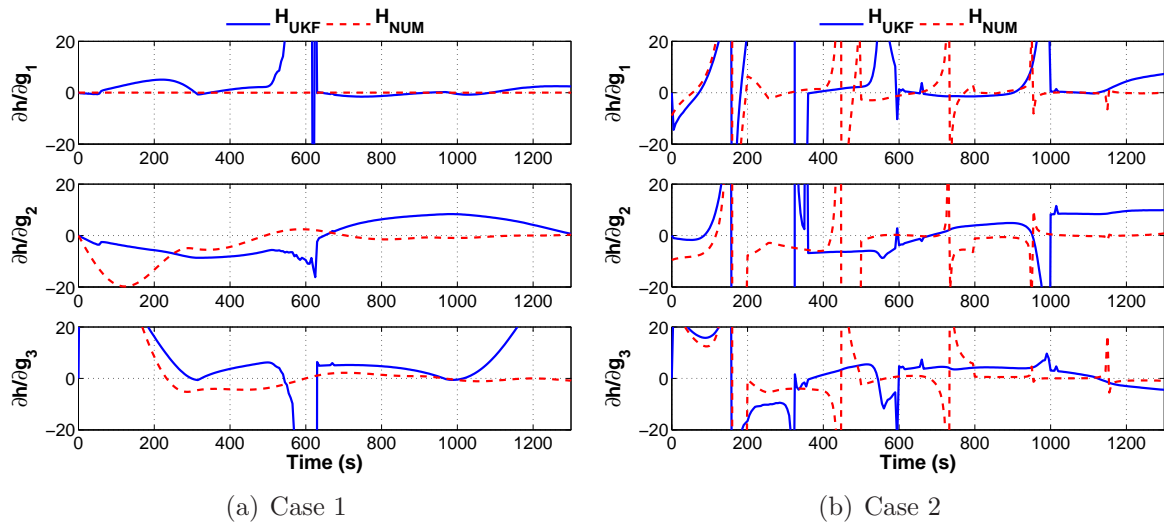


Figure A.7. Ward-Dür Model Attitude Sensitivity.

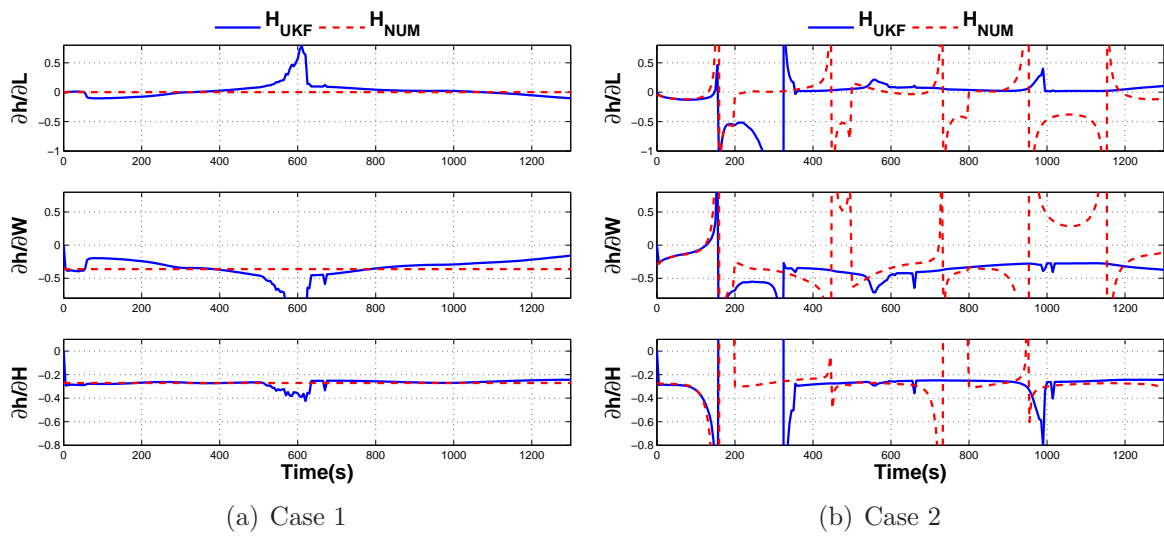


Figure A.8. Ward-Dür Model Shape/Size Parameters Sensitivity.

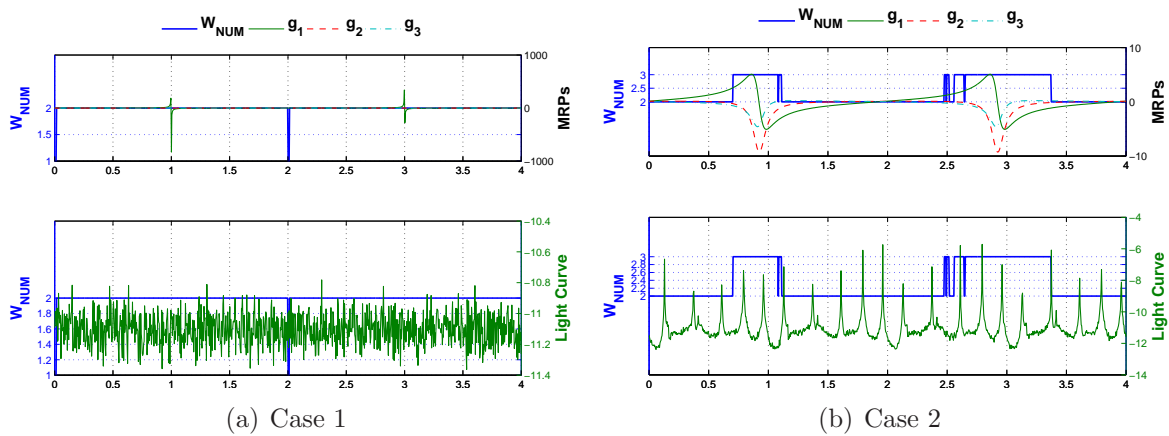


Figure A.9. Ward-Dür Model Numerical based Gramian.

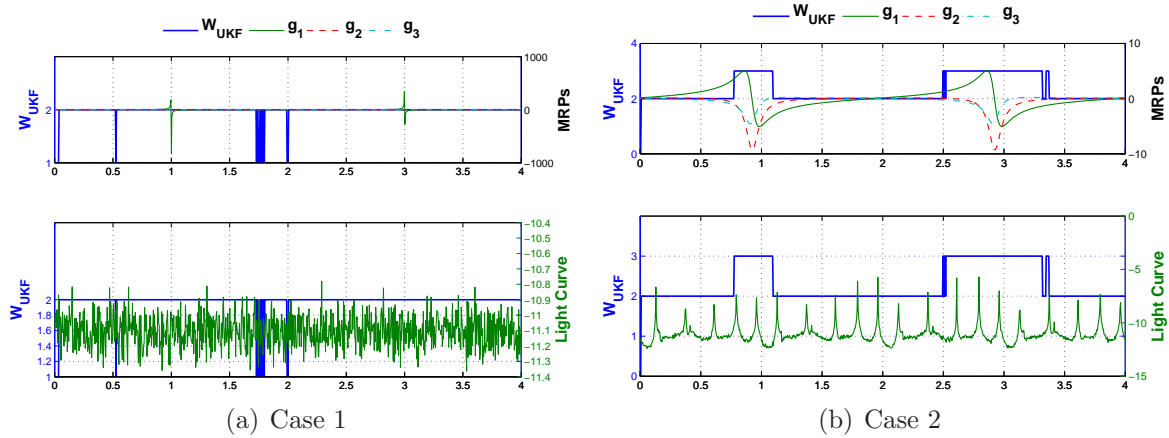


Figure A.10. Ward-Dür Model UKF based Gramian.

### A.2.3 Blinn-Phong Model

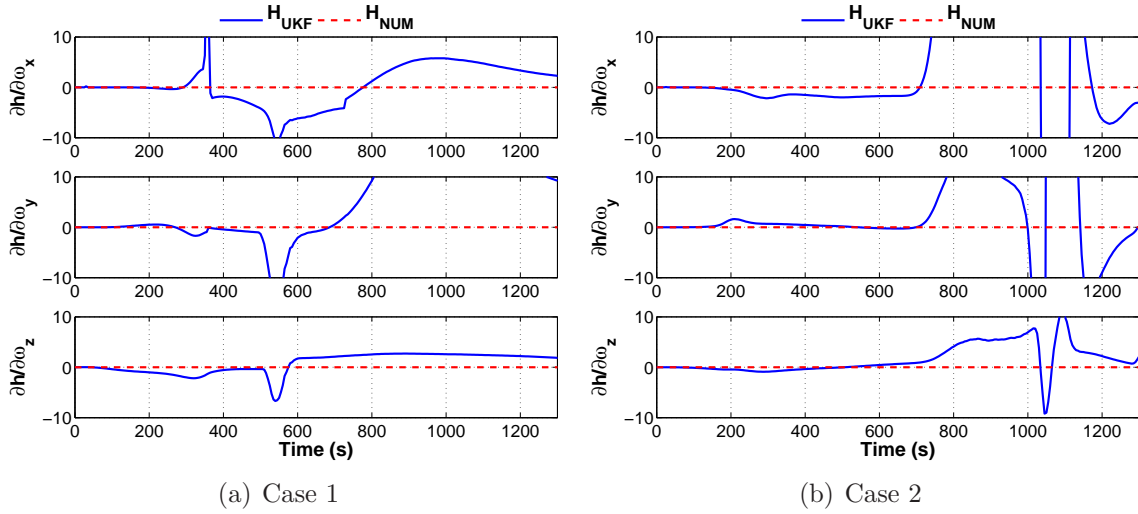


Figure A.11. Blinn-Phong Model Angular Velocity Sensitivity.

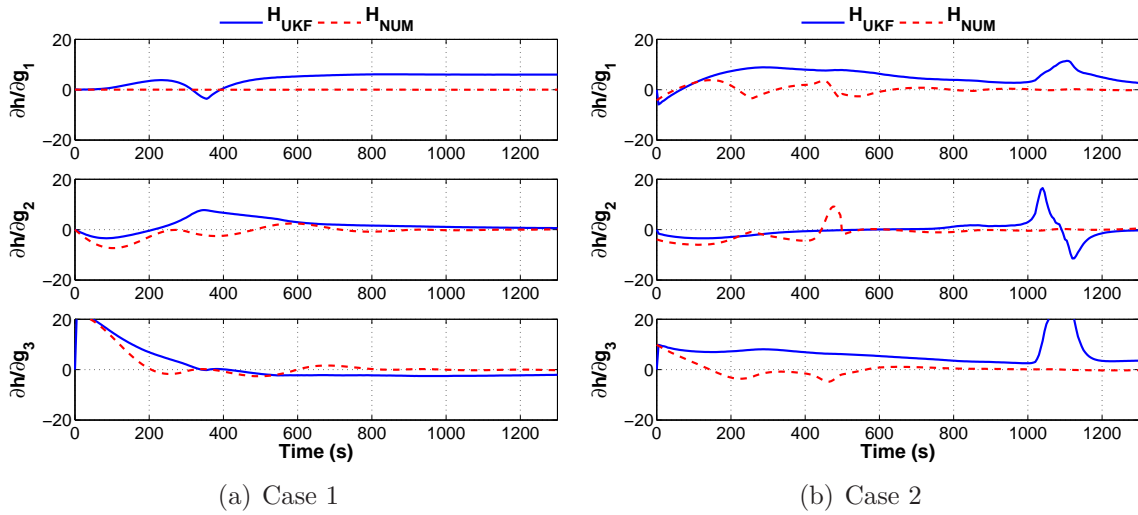


Figure A.12. Blinn-Phong Model Attitude Sensitivity.

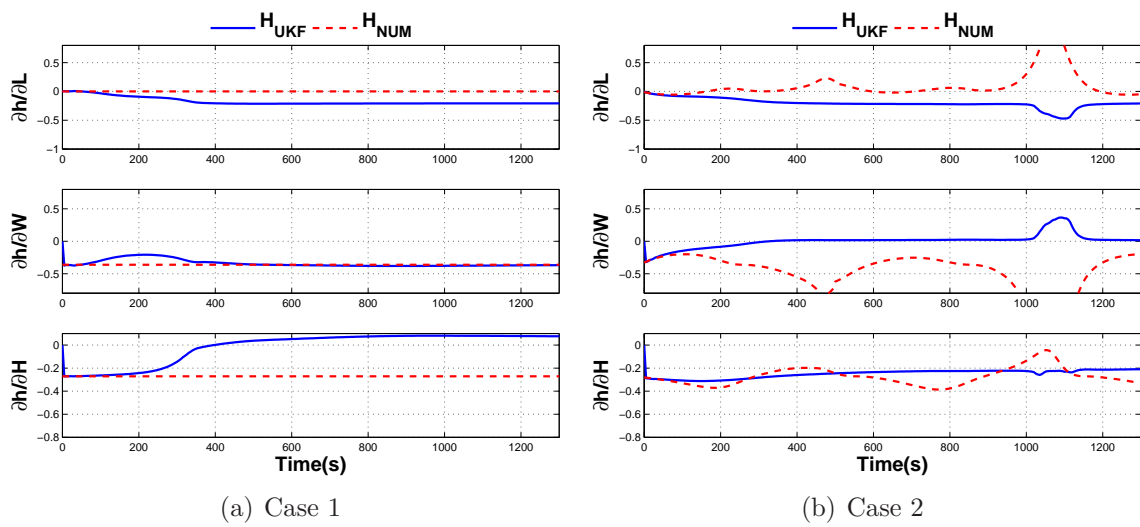


Figure A.13. Blinn-Phong Model Shape/Size Parameters Sensitivity.

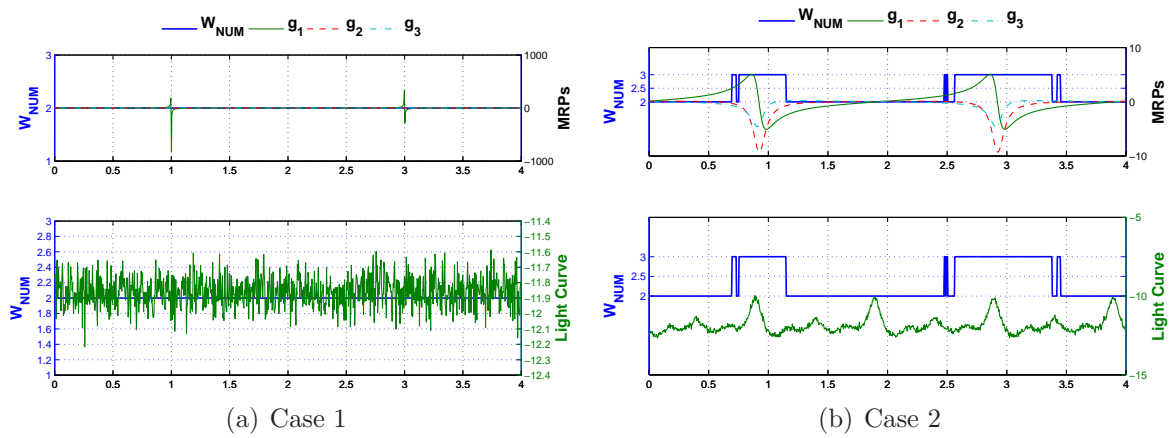


Figure A.14. Blinn-Phong Model Numerical Based Gramian.

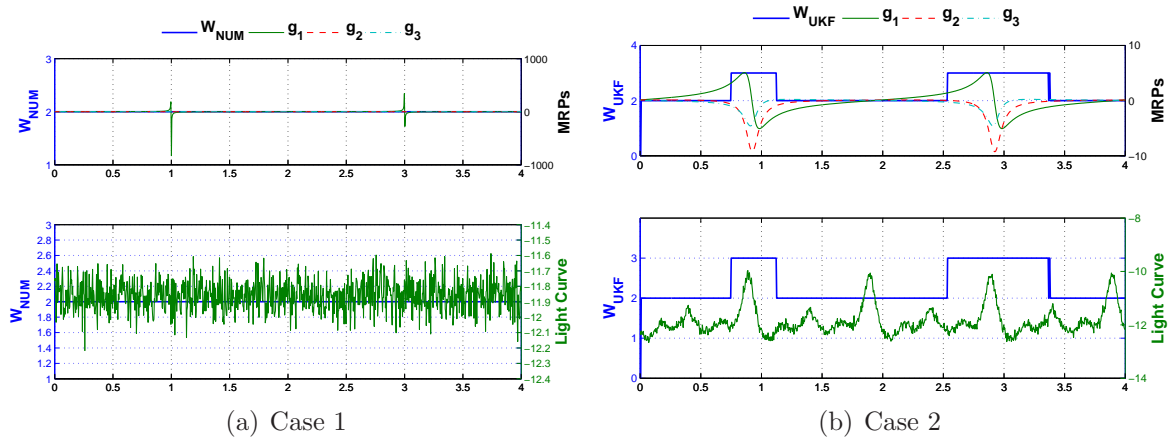


Figure A.15. Blinn-Phong Model UKF based Gramian.

A.2.4 Lafortune et al. Model

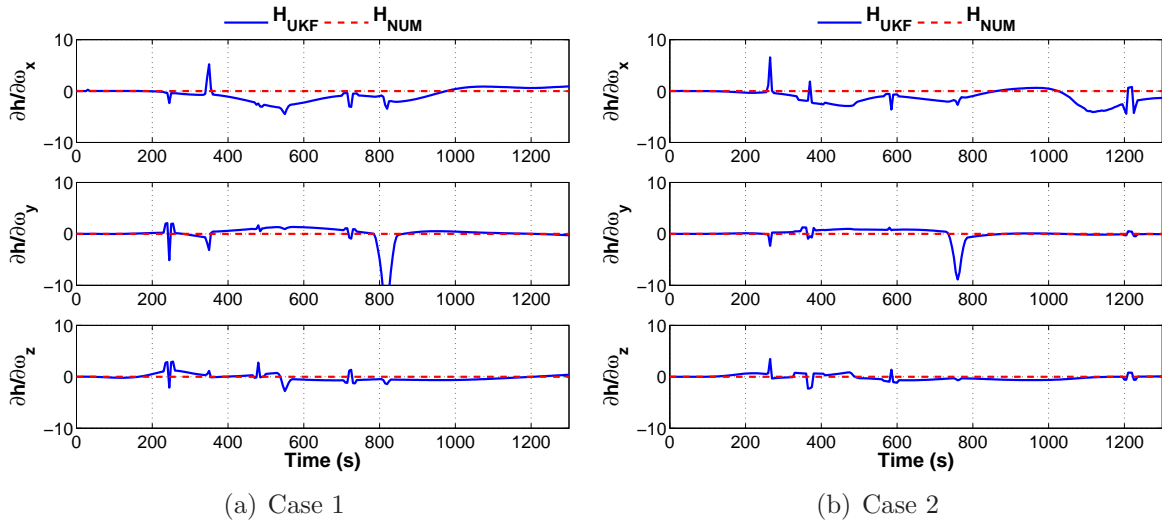


Figure A.16. Lafortune et al. Model Angular Velocity Sensitivity.

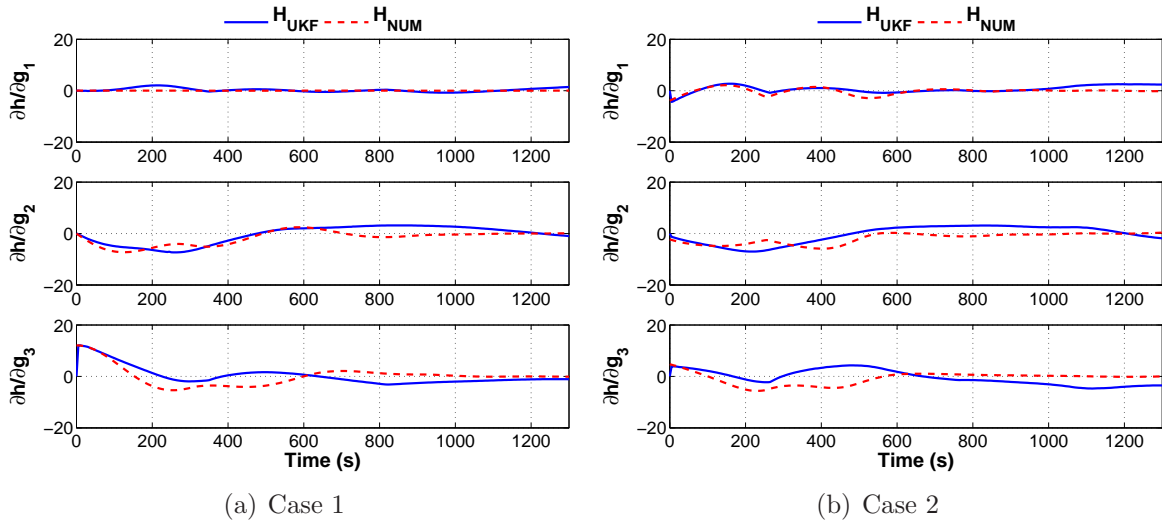


Figure A.17. Lafortune et al. Model Attitude Sensitivity.

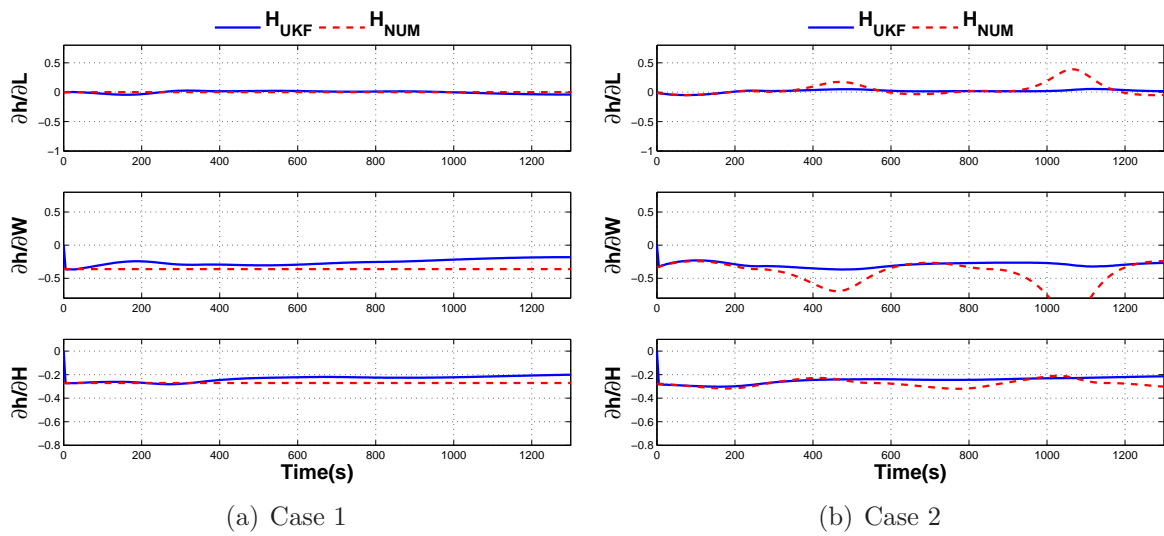


Figure A.18. Lafortune et al. Model Shape/Size Parameters Sensitivity.

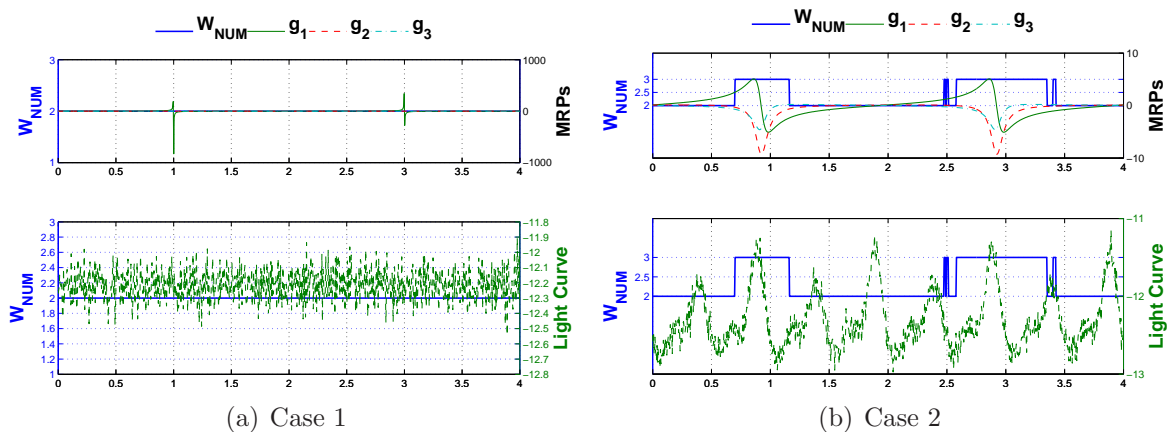


Figure A.19. Lafortune et al. Model Numerical based Gramian.

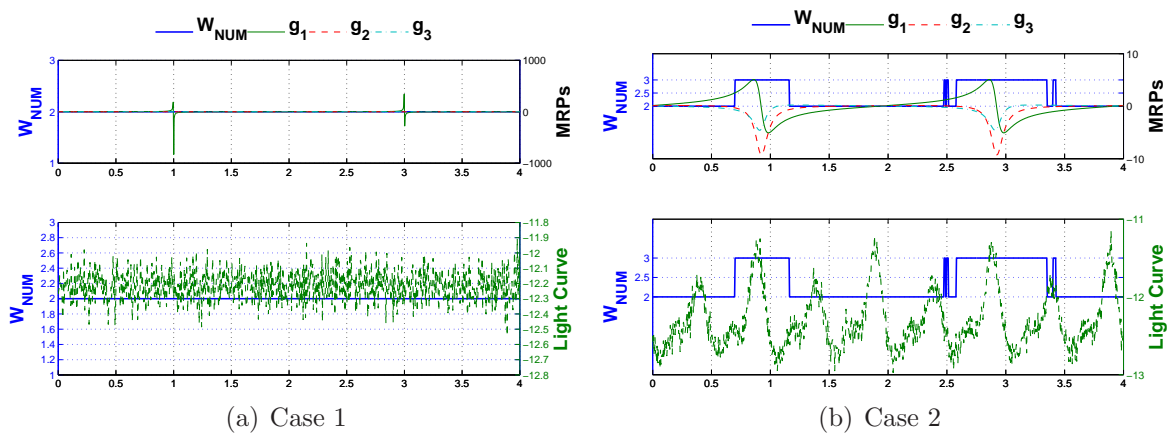


Figure A.20. Lafortune et al. Model UKF based Gramian.

### A.2.5 Cook-Torrance Model

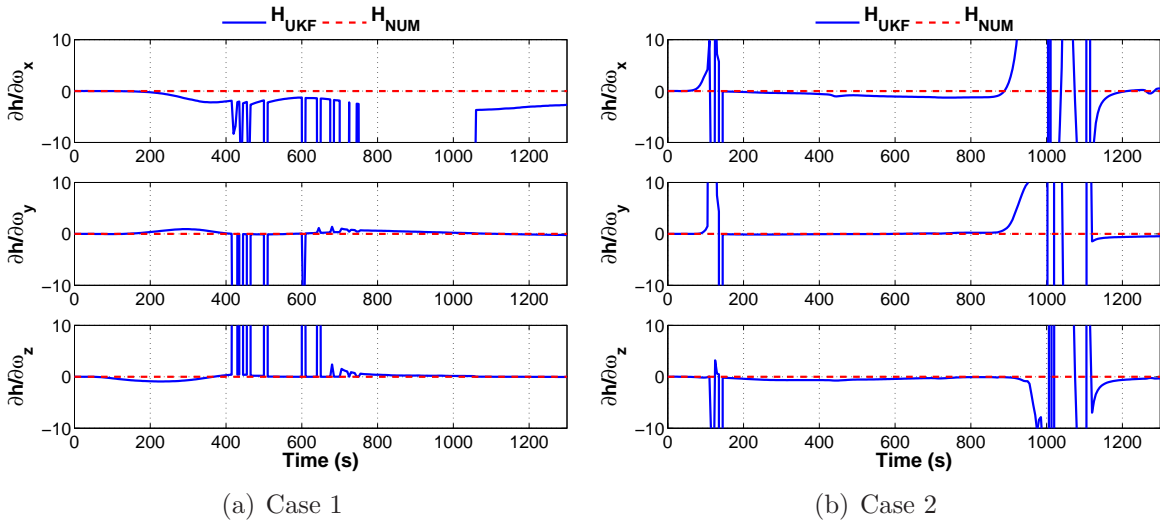


Figure A.21. Cook-Torrance Model Angular Velocity Sensitivity.

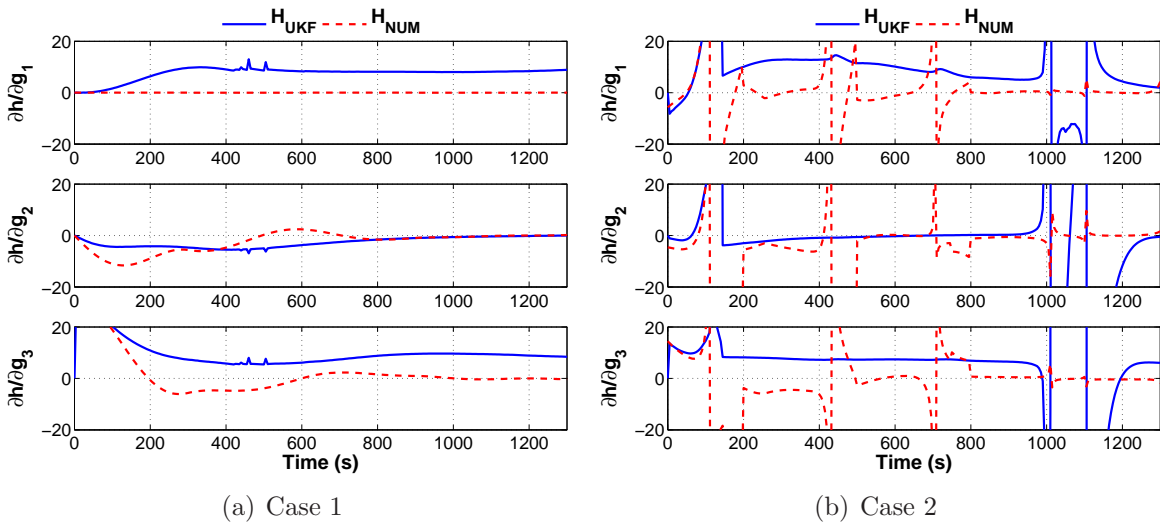


Figure A.22. Cook-Torrance Model Attitude Sensitivity.

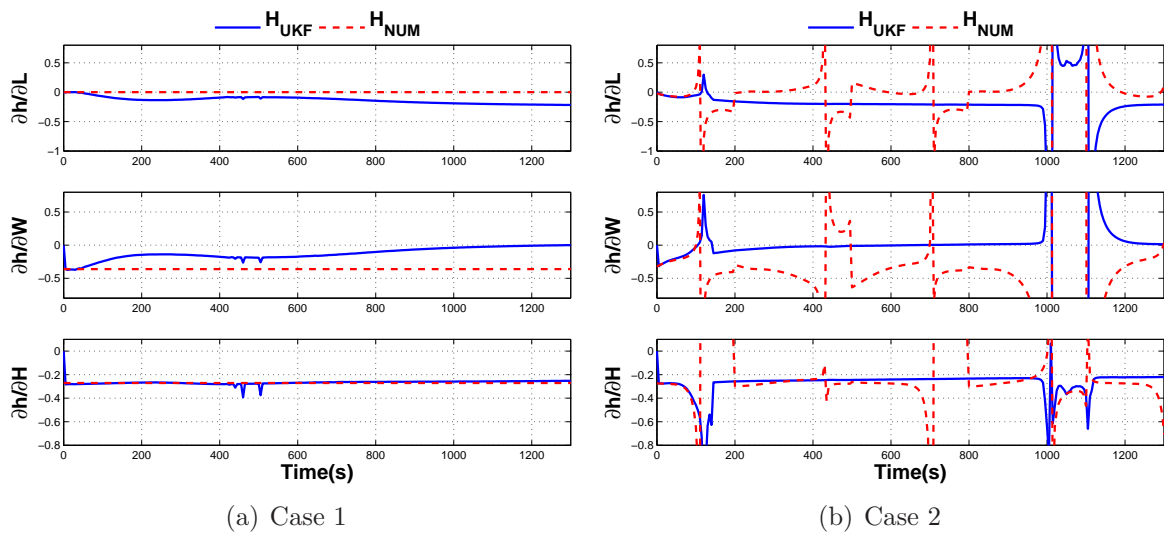


Figure A.23. Cook-Torrance Model Shape/Size Parameters Sensitivity.

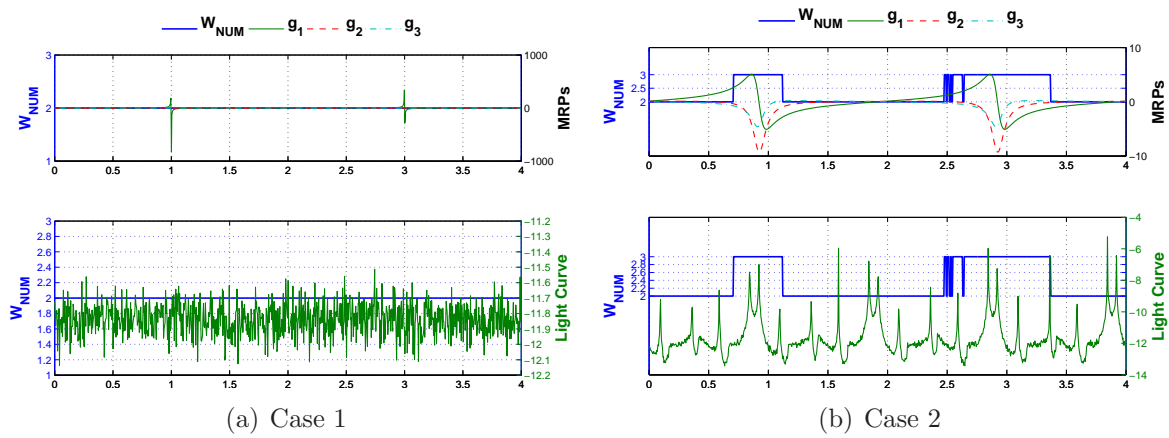


Figure A.24. Cook-Torrance Model Numerical based Gramian.

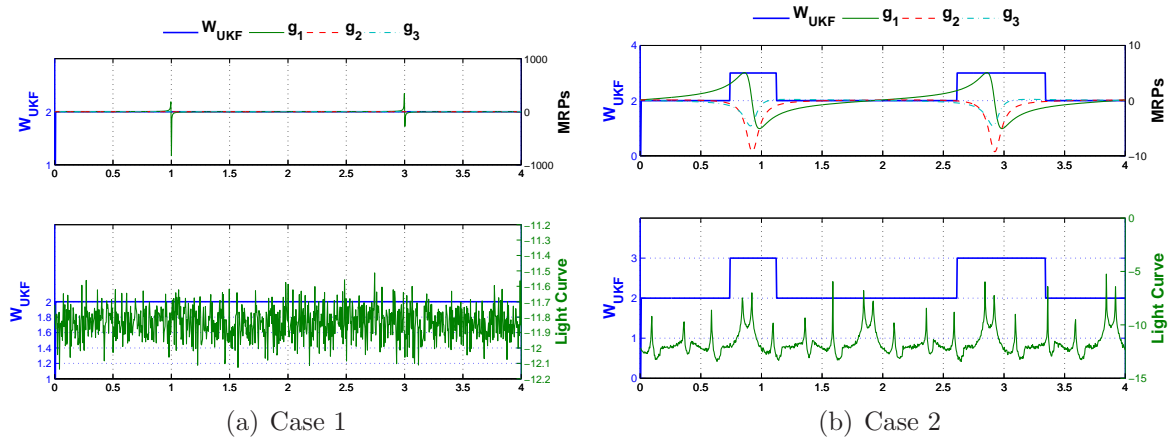


Figure A.25. Cook-Torrance Model UKF based Gramian.

### A.2.6 He Model

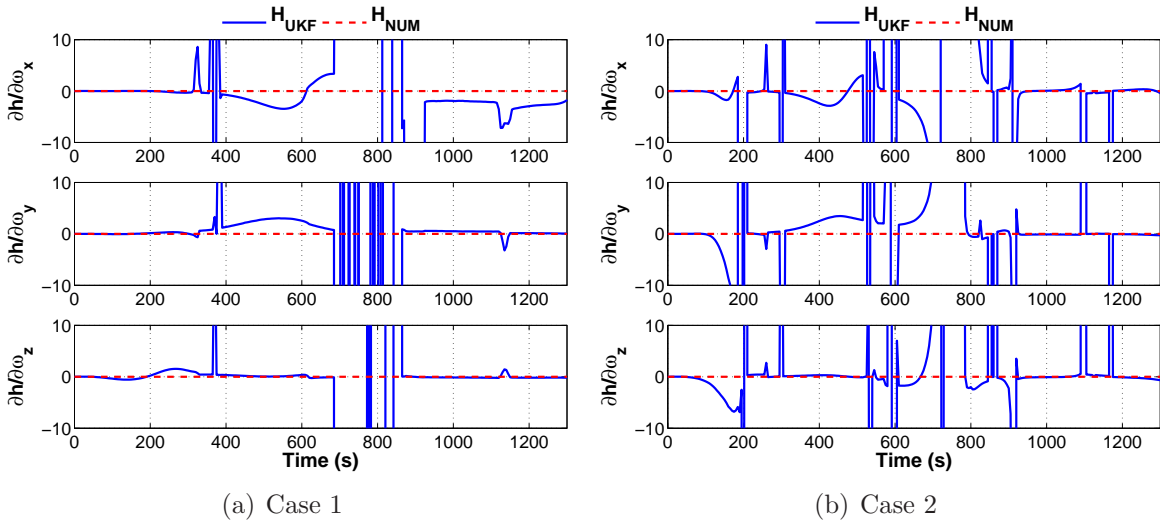


Figure A.26. He Model Angular Velocity Sensitivity.

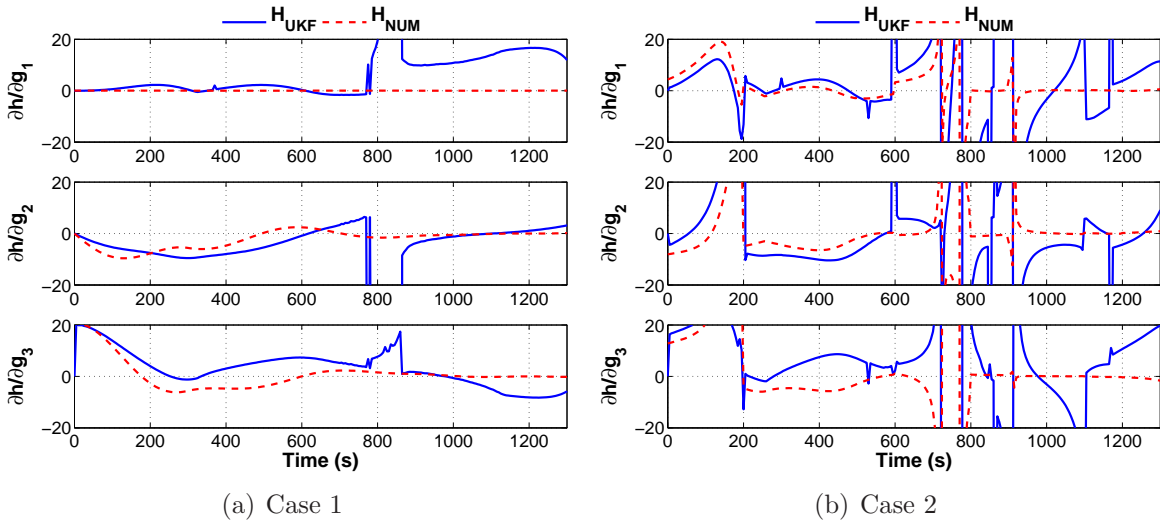


Figure A.27. He Model Attitude Sensitivity.

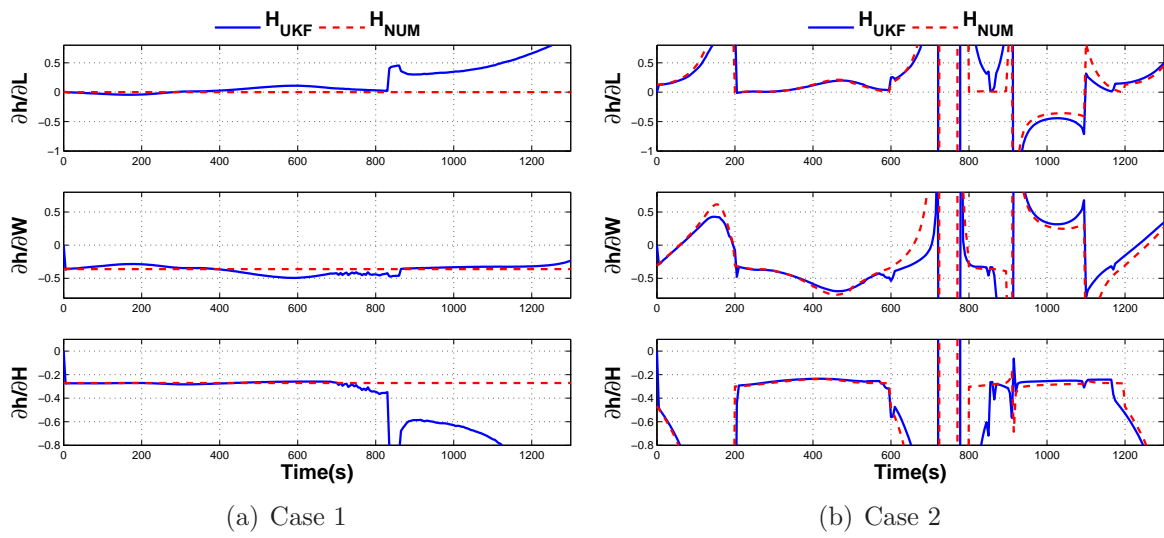


Figure A.28. He Model Shape/Size Parameters Sensitivity.

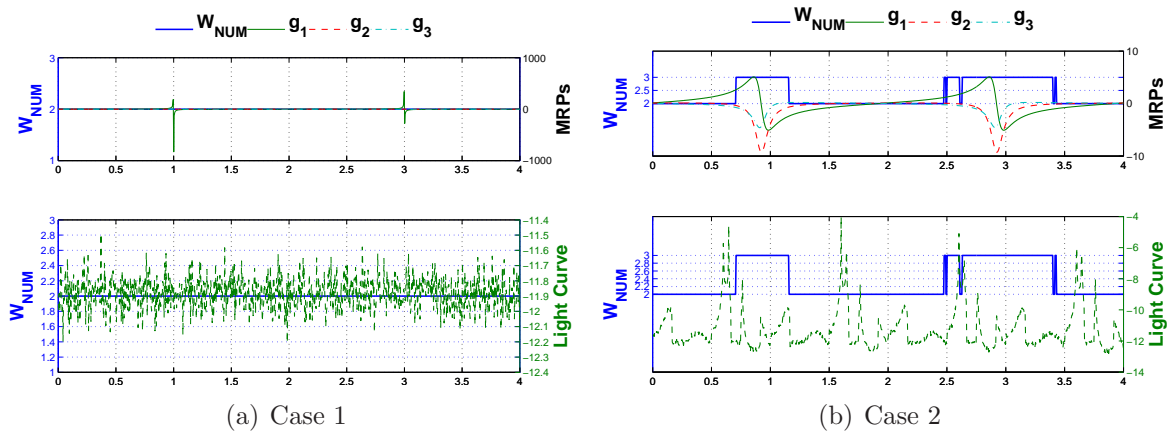


Figure A.29. He Model Numerical based Gramian.

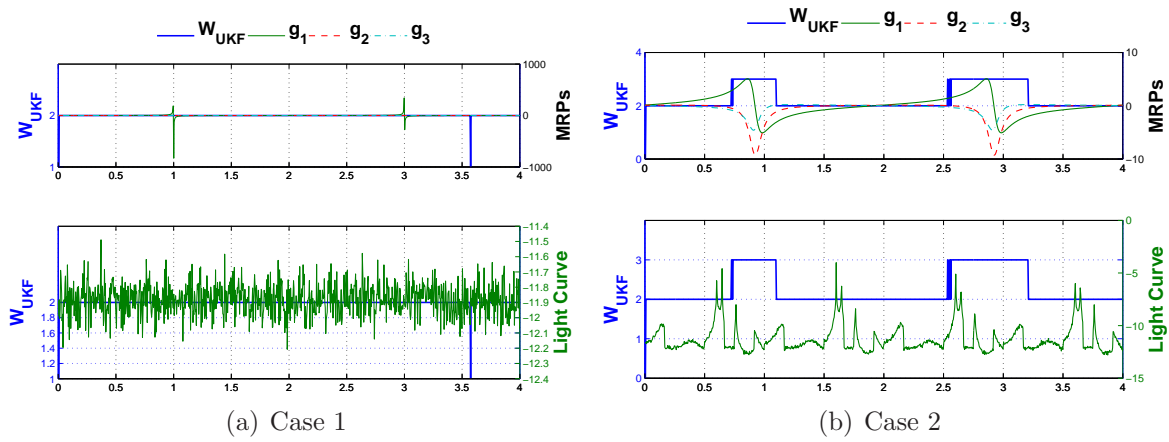


Figure A.30. He Model UKF based Gramian.

### A.2.7 Ashikhmin-Shirley Model

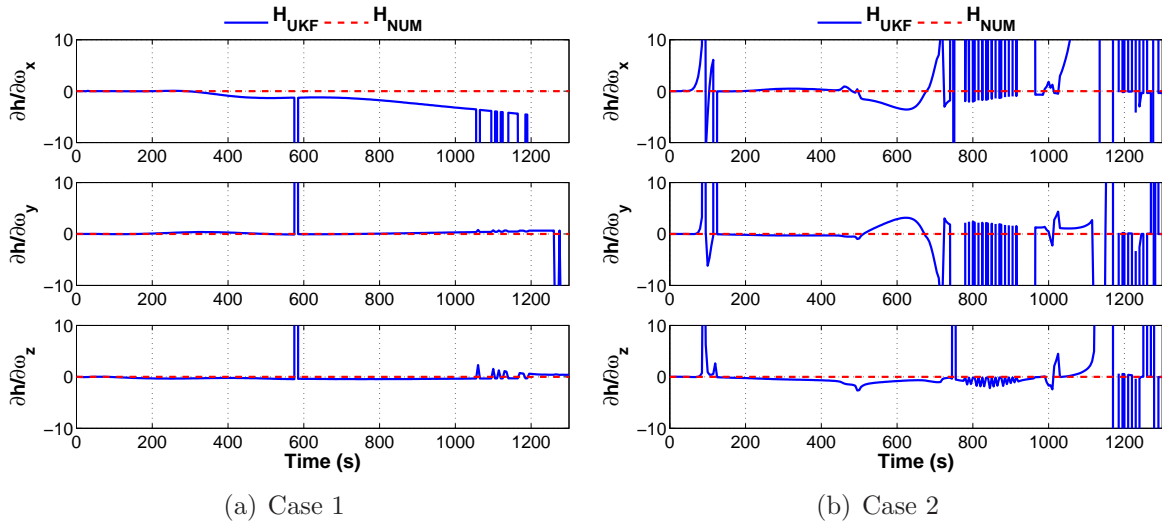


Figure A.31. Ashikhmin-Shirley Model Angular Velocity Sensitivity.

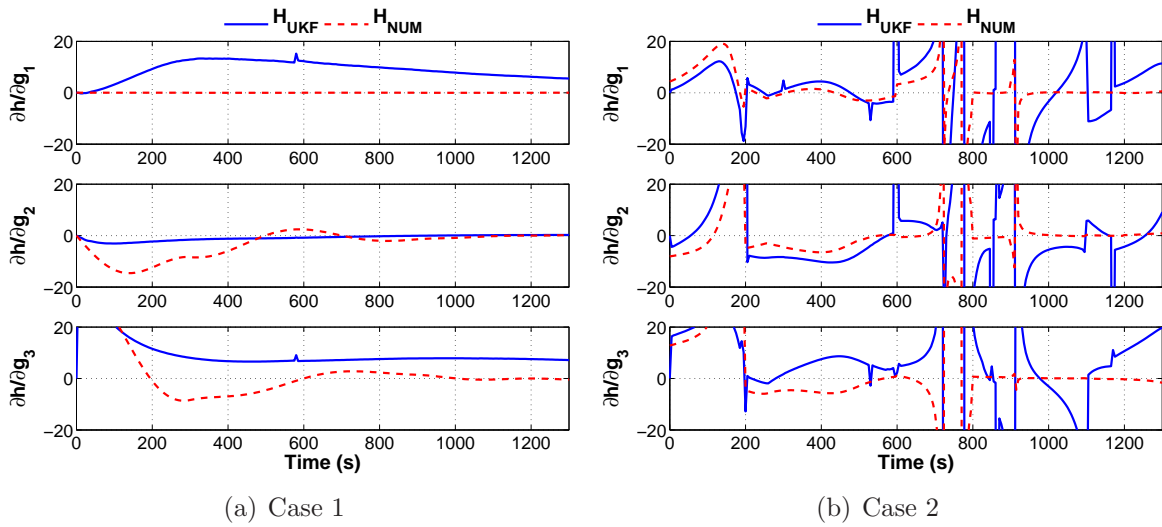


Figure A.32. Ashikhmin-Shirley Model Attitude Sensitivity.

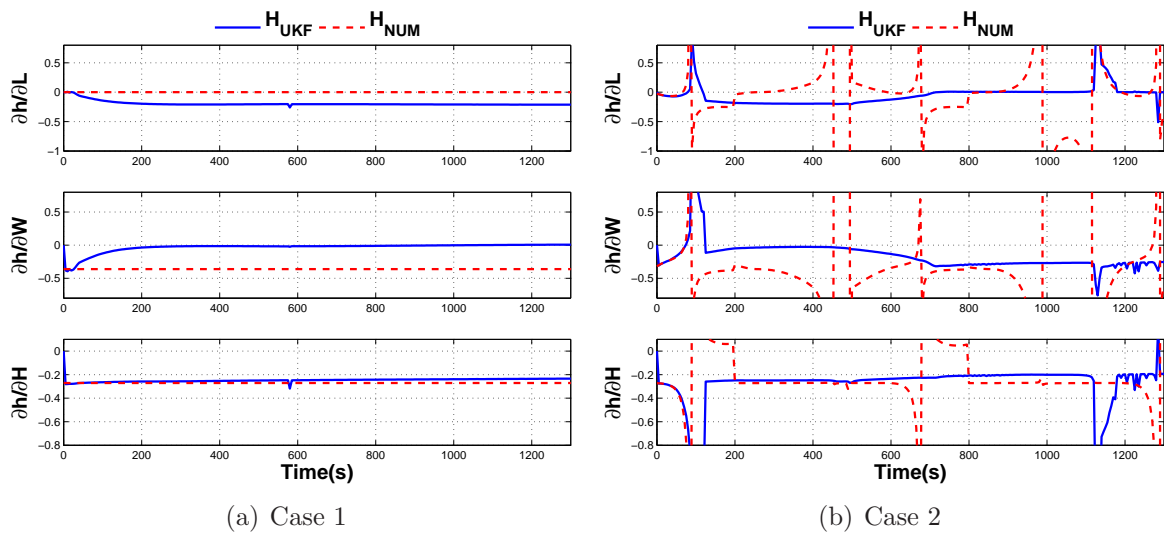


Figure A.33. Ashikhmin-Shirley Model Shape/Size Parameters Sensitivity.

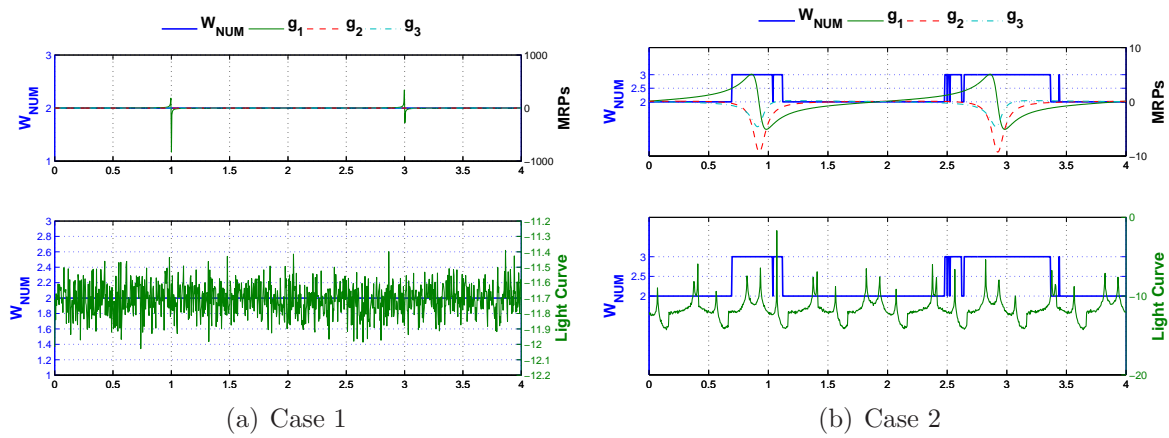


Figure A.34. Ashikhmin-Shirley Model Numerical based Gramian.

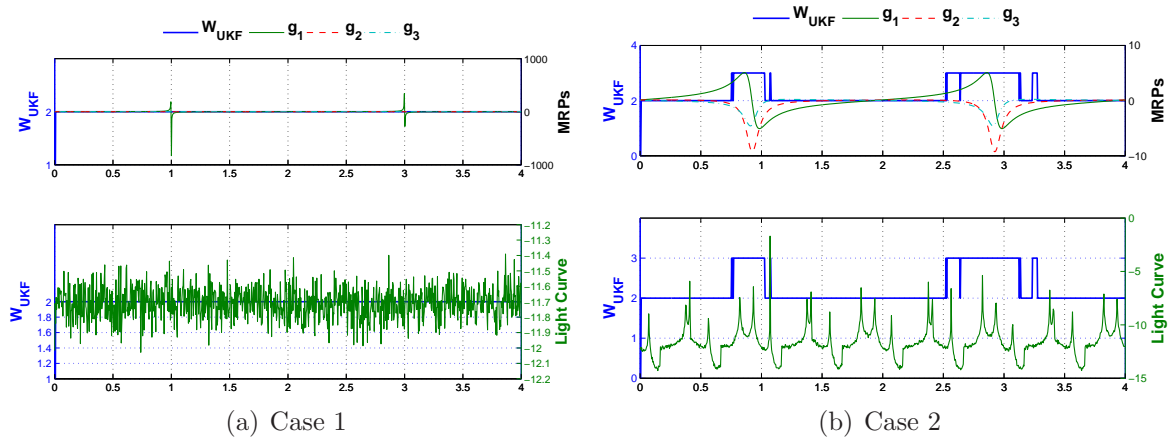


Figure A.35. Ashikhmin-Shirley Model UKF based Gramian.

## References

- [1] A. Ngan, F. Durand, and W. Matusik, “Experimental Analysis of BRDF Models,” in *Proceedings of the Sixteenth Eurographics conference on Rendering Techniques*. Eurographics Association, 2005, pp. 117–226.
- [2] J. L. Foster, J. R. Benbrook, and E. G. Stansbery, “Detection of small radar cross-section orbital debris with the Haystack radar,” *Advances in Space Research*, vol. 35, pp. 1210–1213, 2005.
- [3] J.-C. Liou and N. L. Johnson, “Planetary science. Risks in space from orbiting debris,” *Science*, vol. 311, pp. 340–341, 2006.
- [4] —, “Instability of the present LEO satellite populations,” *Advances in Space Research*, vol. 41, no. 7, pp. 1046–1053, 2008.
- [5] R. Lambour, N. Rajan, T. Morgan, I. Kupiec, and E. Stansbery, “Assessment of orbital debris size estimation from radar cross-section measurements,” *Advances in Space Research*, vol. 34, no. 5, pp. 1013–1020, 2004.
- [6] A. M. Bradley and L. M. Wein, “Space Debris: Assessing Risk and Responsibility,” *Advances in Space Research*, vol. 43, pp. 1372–1390, 2009.
- [7] R. E. Kalman, “A new approach to linear filtering and prediction problems,” *Journal of Fluids Engineering*, vol. 82, no. 1, pp. 35–45, 1960.
- [8] H. Sorenson, “Least-squares estimation: From Gauss to Kalman,” *Spectrum, IEEE*, vol. 7, no. 7, pp. 63–68, 1970.
- [9] J. R. Raol and N. K. Sinha, “On the orbit determination problem,” *IEEE Transaction on Aerospace and Electronic Systems*, no. 3, pp. 274–291, 1985.

- [10] D. A. Vallado, *Fundamentals of Astrodynamics and Applications*. El Segundo, California and Boston, Massachusetts: Microcosm Press and Kluwer Academic Publishers, 2001.
- [11] J. L. Crassidis and F. L. Markley, “Unscented Filtering for Spacecraft Attitude Estimation,” *Journal of Guidance, Control, and Dynamics*, vol. 26, no. 4, pp. 572–542, 2003.
- [12] C. J. Wetterer and M. K. Jah, “Attitude Estimation from Light Curves,” *Journal of Guidance, Control, and Dynamics*, vol. 32, no. 5, pp. 1648–1651, 2009.
- [13] P. S. Williams, D. B. Spencer, and R. S. Erwin, “Coupling of estimation and sensor tracking applied to satellite tracking,” *Journal of Guidance, Control, and Dynamics*, vol. 36, no. 4, pp. 993–1007, 2013.
- [14] J. L. Crassidis and J. L. Junkins, *Optimal Estimation of Dynamic Systems*, 2nd ed. New York, New York: CRC Press, 2012.
- [15] N. Gordon, D. Salmond, and A. Smith, “Novel approach to nonlinear/non-Gaussian Bayesian state estimation,” in *IEE Proceedings F (Radar and Signal Processing)*, vol. 140, no. 2, 1993, pp. 107–113.
- [16] J. Campbell, S. Synnott, and G. Bierman, “Voyager Orbit Determination at Jupiter,” *Automatic Control, IEEE Transactions*, vol. AC-28, no. 3, pp. 256–268, 1983.
- [17] M. Kaasalainen and J. Torppa, “Optimization methods for asteroid lightcurve inversion. I.—Shape determination,” *Icarus*, vol. 153, no. 1, pp. 24–36, 2001.
- [18] J. Āurech, “Shape Determination of the Asteroid (6053) 1993 BW3,” *Icarus*, vol. 159, pp. 192–196, 2002.
- [19] M. Kaasalainen, J. Torppa, and K. Muinonen, “Optimization methods for asteroid lightcurve inversion: II—the complete inverse problem,” *Icarus*, vol. 153, no. 1, pp. 37–51, 2001.

- [20] M. Kaasalainen, P. Pravec, Y. N. Krugly, L. arounov, J. Torppa, J. Virtanen, S. Kaasalainen, A. Erikson, A. Nathues, J. Durech, M. Wolf, J. S. Lagerros, M. Lindgren, C.-I. Lagerkvist, R. Koff, J. Davies, R. Mann, P. Kunirk, N. M. Gaftonyuk, d. Vasiliy G. Shevchenko Vasiliy G. Chiorny, and I. N. B. d, “Photometry and models of eight near-Earth asteroids,” *Icarus*, vol. 167, no. 1, pp. 178–196, 2004.
- [21] C. Fruüh and T. Schildknecht, “Analysis of observed and simulated light curves of space debris,” *International Astronautical Congress*, vol. 6, pp. 1–9, 2010.
- [22] —, “Combination of light curve measurements and orbit determination for space debris identification,” in *Proceedings of the 62nd International Astronautical Congress, International Astronautical Federation*, vol. A6.1.14, 2011, pp. 18733–1881.
- [23] T. Kelecy and M. K. Jah, “Analysis of high area-to-mass ratio (HAMR) GEO space object orbit determination and prediction performance: Initial strategies to recover and predict HAMR GEO trajectories with no a priori information,” *Acta Astronautica*, vol. 69, no. 7, pp. 551–558, 2011.
- [24] T. Yanagisawa and H. Kurosaki, “Shape and motion estimate of LEO debris using light curves,” *Advances in Space Research*, vol. 50, no. 1, pp. 136–145, 2012.
- [25] K. Subbarao and L. Henderson, “Inverse Problems in Unresolved Space Object Identification,” in *AAS/AIAA Space Flight Mechanics Meeting*, no. AAS 11-149, 2011.
- [26] L. S. Henderson, P. Goyal, and K. Subbarao, “Inverse Problem Formulation Coupled with Unscented Kalman Filtering for State and Shape Estimation of Space Objects,” in *AAS/AIAA Space Flight Mechanics Meeting*, no. AAS 12-115, 2012.

- [27] P. Goyal, L. Henderson, and K. Subbarao, “A Preliminary Study in State and Shape Estimation for Space Objects in LEO using the Unscented Kalman Filter,” *Adventures on the Interface of Mechanics and Control*, pp. 299–325, 2012, in Honor of Prof. John L. Junkins on the occasion of his being awarded the ICCES Life-Time Achievement Medal.
- [28] L. Henderson and K. Subbarao, “Sensitivity Analysis of the Lightcurve Measurement Model for use in Attitude and Shape Estimation of Resident Space Objects,” in *AAS/AIAA Space Flight Mechanics Meeting*, no. AAS 13-430, 2013.
- [29] L. S. Henderson and K. Subbarao, “‘Inverse Crime’ and Model Integrity in Unresolved Space Object Identification,” in *AAS/AIAA Space Flight Mechanics Meeting*, no. AAS 14-205, 2014.
- [30] J. L. Crassidis and F. L. Markley, “Attitude Estimation using Modified Rodrigues Parameters,” in *Proceedings of the Flight Mechanics/Estimation Theory Symposium*. NASA Goddard Space Flight Center, 1996, pp. 71–83.
- [31] D. A. Vallado and S. S. Carter, “Accurate orbit determination from short-arc dense observational data,” *Journal of the Astronautical Sciences*, vol. 46, pp. 195–213, 1998.
- [32] M. Kaasalainen, L. Lamberg, K. Lumme, and E. Bowell, “Interpretation of lightcurves of atmosphereless bodies. II— Practical aspects of inversion,” *Astronomy and Astrophysics*, vol. 259, pp. 333–340, 1992.
- [33] —, “Interpretation of lightcurves of atmosphereless bodies. I—General theory and new inversion schemes,” *Astronomy and Astrophysics*, vol. 259, pp. 318–332, 1992.
- [34] M. K. Jah and R. A. Madler, “Satellite Characterization: Angles and Light Curve Data Fusion for Spacecraft State and Parameter Estimation,” in *Proceedings*

of the *Advanced Maui Optical and Space Surveillance Technologies Conference*, vol. 49, 2007.

- [35] J. Matuszewicz, K. Subbarao, and J. Frisbee, “Uncertainty characterization of orbital debris using simulated space surveillance network measurements,” in *AAS/AIAA Astrodynamics Specialist Conference*, no. 388, Mackinac Island, Michigan, August 19-23 2007.
- [36] —, “Uncertainty characterization of orbital debris using the extended kalman filter,” in *AAS/AIAA Astrodynamics Specialist Conference*, no. 389, Mackinac Island, Michigan, August 19—23 2007.
- [37] R. Linares, J. L. Crassidis, M. K. Jah, and H. Kim, “Astrometric and photometric data fusion for resident space object orbit, attitude, and shape determination via multiple-model adaptive estimation,” in *AAS/AIAA Astrodynamics Specialists Conference*, no. AIAA-8341, 2010.
- [38] M. Ashikhmin and P. Shirley, “An Anisotropic Phong BRDF Model,” *Journal of Graphics and Tools*, vol. 5, pp. 25–32, 2000.
- [39] D. Coshes-Meskin and I. Y. Bar-Itzhack, “Observability Analysis of Piece-Wise Constant Systems—Part I : Theory,” *IEEE Transaction on Aerospace and Electronic Systems*, vol. 28, no. 4, pp. 1056–106, 1992.
- [40] Y. Zhou, J. Zhang, and K. Miao, “SVD Based Observability Analysis of Initial Alignment of Inertial Navigation System,” in *IEEE International Symposium on Knowledge Acquisition and Modeling Workshop*, 2008, pp. 444–448.
- [41] R. Long, Q. Yong-yuan, and J. Ji-chao, “Observable Degree Analysis of SINS Initial Alignment Based on Singular Value Decomposition,” in *Knowledge Acquisition and Modeling Workshop 2008. IEEE International Symposium*, 2008, pp. 444–448.

- [42] S. R. Marandi and V. J. Modi, “A preferred coordinate system and the associated orientation representation in attitude dynamics,” *Acta Astronautica*, vol. 15, no. 11, pp. 833–843, 1987.
- [43] M. Shuster, “A survey of attitude representations,” *The Journal of Astronautical Sciences*, vol. 41, no. 4, pp. 439–517, 1993.
- [44] H. Schaub and J. L. Junkins, “Stereographic orientation parameters for attitude dynamics: A generalization of the Rodrigues parameters,” *Journal of the Astronautical Sciences*, vol. 44, no. 1, pp. 1–19, 1996.
- [45] H. Schaub and J. Junkins, *Analytical Mechanics of Aerospace Systems*. AIAA, 2009.
- [46] J. L. Crassidis and J. L. Junkins, *Optimal Estimation of Dynamic Systems*, 1st ed. New York, New York: Chapman and Hall \CRC, 2004.
- [47] C. Sabol, S. S. Carter, and D. A. Vallado, “A fresh look at angles-only orbit determination,” in *AAS/AIAA Astrodynamics Specialist Conference*, no. AAS 99-363, 1999.
- [48] C. Sabol, K. T. Alfriend, and D. Wiese, “Angles-only orbit updates for low-Earth-orbit satellites,” *Journal of Guidance, Control, and Dynamics*, vol. 30, no. 2, pp. 314–321, 2007.
- [49] J. Horwood, A. Poore, and K. Alfriend, “Orbit Determination and Data Fusion in GEO,” in *Proceedings of the Advanced Maui Optical and Space Surveillance Technologies Conference, (September 2011)*. Wailea, Maui, Hawaii: The Maui Economic Development Board, September 13-16 2011, p. E36.
- [50] G. J. Ward, “Measuring and modeling anisotropic reflectection,” in *SIGGRAPH 1992*. ACM Press, 1992.

- [51] D. Geisler-Moroder and A. Dür, “A new Ward BRDF model with bounded albedo,” in *Eurographics Symposium on Rendering 2010*, J. Lawrence and M. Stamminger, Eds., vol. 29, no. 4, 2010, pp. 1391–1398.
- [52] J. F. Blinn, “Models of Light Reflection for Computer Synthesized Pictures,” in *SIGGRAPH 1997*, 1977, pp. 192–198.
- [53] E. P. Lafortune, S.-C. Foo, K. E. Torrance, and D. P. Greenberg, “Non-linear Approximation of Reflectance Functions,” in *Proceedings of the 24th annual conference on Computer graphics and interactive techniques, SIGGRAPH*. ACM Press/Addison-Wesley Publishing Co., 1997, pp. 117–126.
- [54] R. L. Cook and K. E. Torrance, “A reflectance model for computer graphics,” in *SIGGRAPH 1981*. ACM Press, 1981, pp. 307–316.
- [55] X. D. He, K. E. Torrance, F. X. Sillion, and D. P. Greenberg, “A comprehensive physical model for light reflection,” *ACM SIGGRAPH Computer Graphics*, vol. 25, pp. 175–186, 1991.
- [56] A. Dür, “An Improved Normalization for the Ward Reflectance Model,” *Journal of Graphics Tools*, vol. 11, no. 1, pp. 51–59, 2006.
- [57] A. Wirgin, “The Inverse Crime,” *arXiv*, 2004. [Online]. Available: <http://arxiv.org/abs/math-ph/0401050>
- [58] D. Colton and R. Kress, *Inverse Acoustic and Electromagnetic Scattering Theory*. Springer, 1992.
- [59] J. Kaipio and E. Somersalo, *Statistical and Computational Inverse Problems*, S. Antman, J. Marsden, and L. Sirovich, Eds. Springer, 2005.

## Biographical Statement

Originally from Bogotá, Colombia, Laura Suarez Henderson moved to the United States with her family in 2004. She pursued her undergraduate degree in Aerospace Engineering at the University of Texas at Arlington. After graduating Magna Cum Laude with honors, she began a bachelor's to doctoral degree program at this same institution. She was awarded the prestigious National Science Foundation Graduate Research Fellowship in 2012 and the Amelia Earhart Fellowship in 2011 and 2013. Outside of her doctoral pursuit, Laura is working with a team to develop an interactive software that can bring the space exploration experience into the classroom. Mrs. Henderson is married to her husband of five years and they currently live in north Texas. After obtaining her Ph.D. she will join NextGen Aeronautics as a principal investigator for a DARPA SBIR in underwater robotics. She can be reached through the Mechanical and Aerospace Engineering Department at the University of Texas at Arlington.